Development of Portable Sample-In-Answer-Out Microfluidic Systems for On-Site Analyte Detection

Shannon Theresa Krauss
Pelham, New Hampshire

B.S. Chemistry, Keene State College, 2012

A Dissertation presented to the Graduate Faculty of the University of Virginia in
Candidacy for the Degree of Doctor of Philosophy

Department of Chemistry

University of Virginia
May 2018

____

____

____

____

____

Abstract

Microfluidic devices used in the field, whether for clinical or forensic applications, offer many advantages for translating conventional instrumentation to a portable, field-deployable platform. The scaled-down size of these devices offer advantages for rapid analysis, low cost substrates and instrumentation, low reagent and sample consumption, automated sample processing, and simple operating procedures. A core requirement of field technology is that the analysis technique can be performed independently of a centralized facility. To address this requirement, extensive research has been focused on the complete integration of all processes of an analysis technique that would normally be performed in the laboratory into a single microfluidic platform and making the operation of this platform automated for unskilled users. This dissertation presents two specific forensic applications for consideration, illicit drugs and explosives, for developing microfluidic technology.

The chapters that follow describe the development of microfluidic devices, and associated features, for various on-site colorimetric analyses. **Chapter 1** provides the necessary background regarding trends in inexpensive microfluidic device fabrication techniques with discussion of complementary microfluidic platforms. Additionally, various examples of microfluidic devices used for analysis of explosives and illicit drugs are presented. The goal of the work presented in **Chapter 2** was to determine a method towards presumptive on-site testing of illicit drugs using inexpensive, single-use centrifugal microfluidic devices. An objective colorimetric analysis technique for use with a cell phone Android application was evaluated for the detection of cocaine and methamphetamine from an unknown sample. The work described in **Chapter 3** was to explore various chemical reagent storage methods to aid in the complete integration of microfluidic devices for increased portability. Initial chemical storage methods utilizing inkjet printing, custom glass capillary ampules, and hybrid device substrates were evaluated for the integration of the chemicals necessary for different colorimetric reactions. Described reagent storage techniques were utilized in **Chapters 4** and **5** for explosives colorimetric analysis. Towards the development of an on-site analysis technique, a surface swab was determined for sampling residue from a surface to interface sampling with the microfluidic device. The final fully integrated device exhibited 90% success rates for the detection of 8 different explosive compounds within 8 minutes.

Table of Contents

Chapter 1: Introduction

Chapter 2: Objective Method for Presumptive Field-Testing of Illicit Drug Possession Using Centrifugal Microdevices and Smartphone Analysis

Chapter 3: Reagent Storage Techniques for Polyester-based Microfluidic Devices

Chapter 4: Development of a Centrifugal Microfluidic Device with Objective Image Analysis for On-Site Colorimetric Detection of Explosives

Chapter 5: An Integrated Microfluidic Device for *Sample In—Answer Out* Explosives On-Site Detection

Chapter 6: Final Remarks

List of Figures

List of Tables

Abbreviations

AA – Angular acceleration

ACN – Acetonitrile

AN – Ammonium nitrate

ANFO – Ammonium nitrate and fuel oil

ATO - Ammonium titanyl oxalate

A.U. – Arbitrary units

BCG – Bromocresol green

CAD – Computer-aided design

CD – Compact disc

CE – Capillary electrophoresis

Chip – Microfluidic device

CIE - Commission on Illumination color model

COTS – Commercial-off-the-shelf

CZE – Capillary zone electrophoresis

DFSC – Defense Forensic Science Center (Forrest Park, GA)

DNA – Deoxyribonucleic acid

DNT – 2,4-dinitrotoluene

DTL – Double toner layer

FTIR – Fourier transform infrared spectroscopy

HSA – Human serum albumin (Chapter 3 only)

HSA – Heat-sensitive adhesive (Chapters 4 & 5)

HSB – Hue, saturation, and brightness color model

IC – Image capture

IED – Improvised explosive device

IMS – Ion mobility spectrometry

IPA – Isopropyl alcohol

KOH – Potassium hydroxide

LED – Light emitting diode

LIF – Laser-induced fluorescence

LIFM – Laser-irradiated ferrowax microvalve

LOC – Lab-on-a-chip

LOD – Limit of detection

MB – Methylene blue

MDA – 3,4-methylenedioxyamphetamine

MDMA – 3,4-methylenedioxymethamphetamine

MEKC – Micellar electrokinetic chromatography

MeOH – Methanol

Meth – Methamphetamine

NED – N-(1-naphthyl)ethylenediamene dihydrochloride

Oh – Ohnesorge number

OPC – One point cut

PCL – Print, cut, and laminate

PCR – Polymerase chain reaction

PDMS – Polydimethylsiloxane

PET – Poly(ethylene) terephthalate

PMMA – Poly(methyl methacrylate)

POC – Point-of-care

PTFE – Polytetrafluoroethylene

RDM – Rotationally-driven microdevice

RDX – Hexahydro-1,3,5-trinitro-1,3,5-triazine

RGB – Red, green, and blue color model

RNA – Ribonucleic acid

RPM – Rotations per minute

RSD – Relative standard deviation

Sat – Saturation

STL – Single toner layer

TBPB – Tetrabromophenol blue

Tetryl – Methyl-2,4,6-trinitrophenylnitramine

TMAH – Tetramethylammonium hydroxide

TNB – 1,3,5-Trinitrobenzene

TNT – 2,4,6-trinitrotoluene

UN – Urea nitrate

p-DMAC – *para*-dimethylaminocinnamaldehyde

μPAD – Microfluidic paper-based device

μTAS – Micro total analysis system

% TP - % Transparency

Acknowledgements

First, I would like to thank my advisor, Dr. James P. Landers, for the opportunity to work in his research laboratory in addition to his continued guidance as my advisor. I knew working in your lab would be a challenge, which has made these past five years all the more rewarding. Through your invaluable mentorship I was able to grow as a researcher and a writer. I truly appreciate the many times you encouraged me to follow an idea, which has lead to enjoyable research throughout my Ph.D. work. I would also like to thank Dr. Richard E. Tontarski Jr., Dr. Roman Aranda IV, and Mr. Henry P. Maynard III for the collaboration and support early on and throughout my graduate career. I would also like to thank the National Institute of Justice and express my gratitude for the NIJ Graduate Research Fellowship in STEM award. Additionally, I would like to thank all of my peers in the Landers Laboratory that I had the pleasure of working with over the past five years, including the number of undergraduate researchers I was able to work with, for creating an enjoyable and supportive work environment. I would also like to sincerely thank Dr. Brandon L. Thompson for the continued mentorship and friendship throughout my Ph.D. career.

To all of my friends that have made my time in Charlottesville wonderful, thank you for your continued support and welcomed distractions during challenging times throughout this process. I would also like to thank other students within the Department of Chemistry for helping to create a smooth transition into the program. Additionally, I want to express my gratitude to all of the staff within the Department of Chemistry for all that you do and what a pleasure it has been to work with you all.

To Daniel, thank you for your unwavering support throughout this process. You are a wonderful role model as a scientist and a person, and I am lucky to have you in my life. Thank you for always making me laugh and staying positive during challenging times. I truly appreciate all that you do and cannot thank you enough for the countless times you've kept me company working late nights. I'm excited to see our next adventure and what we are able to accomplish in our future endeavors.

And finally, I'd like to thank my family. None of this would be possible without your support. I am so unbelievably lucky to have such a supportive family that keeps me grounded and has taught me the value of hard work. I love you all so much and you all make me strive to be the best I can every day. To Stephanie, Jason, and Braden, thank you for continued encouragement and for always welcoming me to visit. It has been amazing to have family close by and I don't know what I would have done if you hadn't moved to North Carolina. Dad, thank you for your continued encouragement throughout my life. You always know how to shed light on what is truly important. You've taught me invaluable qualities that have made me the person I am today, and I am so lucky to have you as my father.

1. Introduction

1.1 Overview of Microfluidics

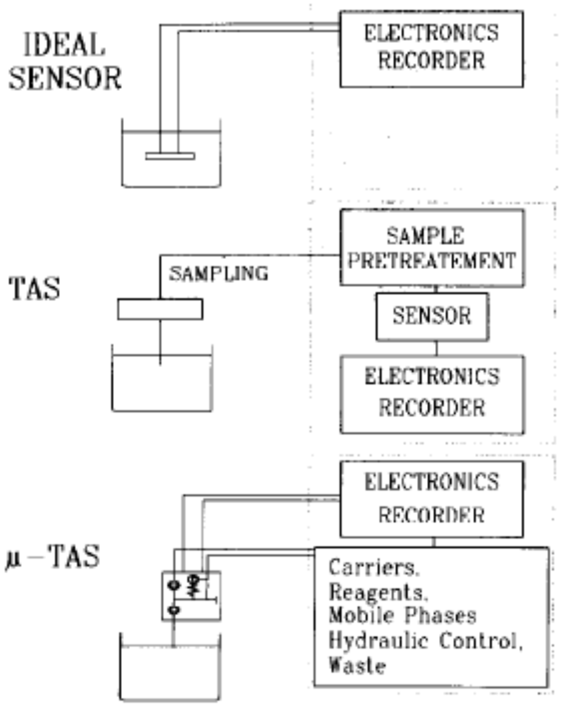

Figure 1-1. Schematic diagram of an ideal chemical sensor, a 'total chemical analysis system' (TAS) and a miniaturized TAS (μ-TAS). Adapted from [1].

The concept of a 'miniaturized total chemical analysis system', or μTAS, was presented by Manz et al. in 1990, and the integration of sample pretreatment, separation, and detection were paramount (**Figure 1-1**).[1] Initially, the motivation for a small-scale analysis system was for enhanced analytical performance, utilizing smaller channel dimensions and shorter channel lengths for improved separations, however, additional advantages of decreased sample consumption and rapid analysis times were presented with continued development throughout the 1990s.[2] Currently, it is well-documented within this independent research field known as microfluidics, or lab-on-a-chip (LOC) systems, effects from the scaling-down of chemical analysis systems to the micrometer or centimeter dimensions lead to new phenomena not accessible with classical liquid handling platforms.[3]

As the field of microfluidics has matured over the past two decades, a major focus has evolved towards decreasing costs and increasing functionality towards a variety of applications. Oftentimes, these applications are those that can benefit from analyses performed outside of a centralized facility, such as point-of-care (POC) testing and diagnostics, including immunoassays, blood analysis, nucleic acid amplification tests, and flow cytommetry.[4] For the success of a microfluidic system as a true LOC platform employing a fully-integrated device rather than a chip-in-a-lab technology providing an enabling tool for research, sample handling, automation, and portability for use with minimal training is essential.[5] The significant demand for LOC systems within the forensic sector, i.e., rapid DNA analysis[6-10] and detection of hazardous material[11-14], has grown rapidly in the last decade.

1.2 Fabrication Techniques Towards Inexpensive, Single-use Microfluidic Devices

Wet etching and photolithography were the dominant fabrication methods early on in the development of microfluidics.[15, 16] These initial methods, however, required expensive cleanroom facilities to create glass and silicon devices. A new generation of fabrication methods reduced the laborious, time consuming, and high cost per device processes through implementing soft lithography with pour-and-cure materials, i.e., polydimethylsiloxane (PDMS).[17-20] Although such pour-and-cure methodologies using a 'master mold' revolutionized microfabrication by providing a simple fabrication procedure complimentary for multilayer devices and large-scale integration, this technique was not ideal for rapid device prototyping. The device fabrication was still dependent on fabricating silicon 'masters' to serve as a device mold for each layer. The implementation of hot embossing and injection molding using thermoplastics, i.e., polystyrene and poly(methyl methacrylate) (PMMA) provided a fabrication process more ideal for mass production, however, this methodology was still not optimal for fabricating multiple prototypes with different designs due to the requirement of a master mold.[15]

Finally, the use of milling, laser ablation, and other direct fabrication processes within polymeric substrates created a method capable of directly patterning device channels and eliminated hazardous reagents.[21-23] Although direct fabrication in this manner approached a method for rapid prototyping, the stepwise process remained lengthy and resulted in rough channels surfaces.

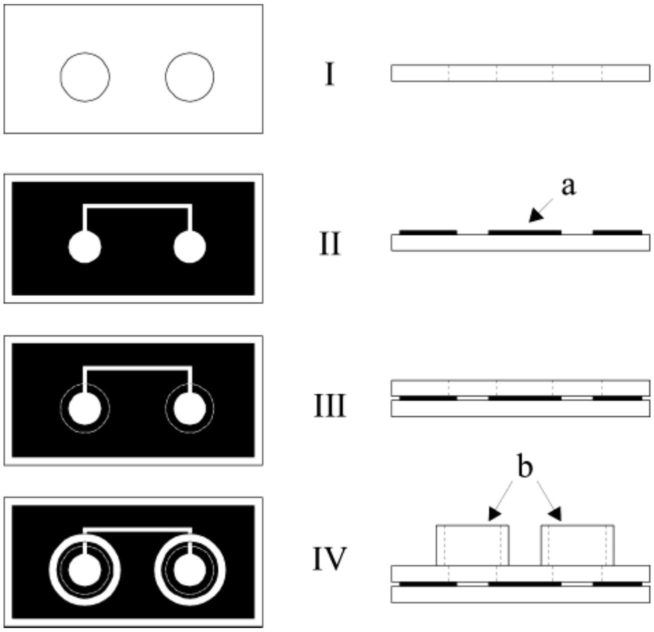

Figure 1-2. Schematic of the main parts generated by the single toner layer (STL) microfabrication process: **I**, perforated polyester cover; **II**, printed polyester base (a, toner layer); **III**, cover (I) and base (II) laminated together; **IV**, the final device (b, liquid reservoirs). Adapted from [25].

Towards rapid fabrication of inexpensive, single-use microfluidic devices, toner and paper-based fabrication methods emerged as promising platforms. Tan et al. first introduced toner as a microfabrication technique as a method for fabricating PDMS microfluidic devices using a master made on transparency film with a photocopying machine.[24] This process was able to decrease the fabrication time for PDMS substrate devices to less than 1.5 hours. Later, do Lago et al. introduced the use of toner for direct device fabrication by combing laser printing and lamination to fabrication devices onto transparency film.[25] This direct-printing process only required a computer with design software, a laser printer, and a laminator. The device channel depths were defined by the printing step, utilizing a single toner layer (STL) as shown in **Figure 1-2** or double toner layer (DTL) for 6 and 12 μm, respectively, and channel width was defined by the printer resolution.

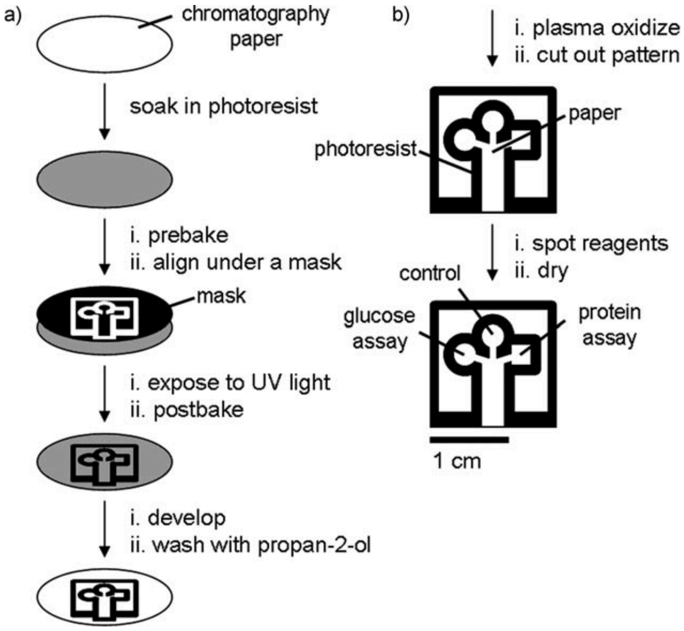

Figure 1-3: Diagram depicting the method for patterning paper into millimeter-sized channels. (**A**) Photolithography was used to pattern SU-8 photoresist embedded into paper; (**B**) the patterned paper was modified for bioassays. Adapted from [26].

Alternatively, when Martinez et al. described the first paper-based device to perform protein and glucose colorimetric bioassays, the described fabrication process followed a traditional photolithography process of patterning channels with SU-8 photoresist onto chromatography paper (**Figure 1-3**).[26] Following this initial method now implemented with paper, the device surface required oxygen plasma pretreatment prior to use to restore the hydrophilic properties effected by the photoresist residue. Later, the same paper-based device pioneers developed a method utilizing direct printing of polymeric barriers, i.e., PDMS and polystyrene, onto various paper substrates to create hydrophobic barriers to define microfluidic channels.[27] Shortly after paper-based devices were introduced, various research groups, in addition to the pioneers, proposed additional fabrication methods owing to the inexpensive and simplistic nature of this restored class of devices from the introduction of the lateral flow assay, ubiquitously known as the at-home pregnancy test. Currently, the most commonly used fabrication method for paper-based devices uses a commercial printer to deposit wax-based ink allowing for rapid prototyping and fabrication.[28-30] Heat is applied after printing to melt the printed wax through the paper to define fluidic channels.

Toner and paper-based fabrication methods have shown potential for both rapid prototyping and inexpensive production of microfluidic devices. A further adaption of the initial method described by do Lago et al. in 2003 resulted in the three-step print, cut, and laminate (PCL) fabrication approach as described by Thompson et al., which offers additional benefits for device fabrication (**Figure 1-4**).[31] As with the first implementation of direct-patterning toner, this method circumvents the need for complex instrumentation, a cleanroom facility, or hazardous reagents, however, the PCL protocol offers a simple method to fabricate more sophisticated, multilayer device architecture. This process uses commercially available transparency sheets composed of poly(ethylene) terephthalate (PET), or broadly polyester film, making this substrate hydrophilic, and printed toner is then used as the hydrophobic component to define channels and valves, and act as an adhesive between layers during device bonding. A

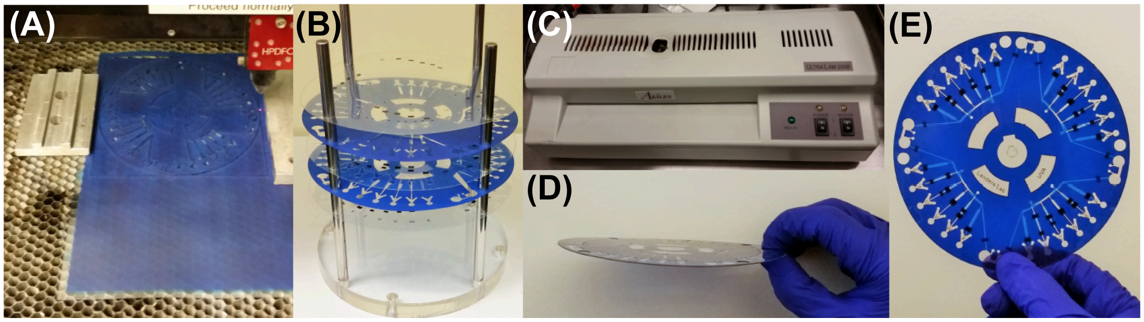

Figure 1-4. Images demonstrating print, cut, and laminate (PCL) device fabrication. (**A**) Toner-coated transparency film anchoring and alignment with the laser head. (**B**) Alignment of layers using a custom-built alignment tool. (**C**) Pass the assembled device through a laminator (standard office version is shown). (**D**) Side view of the laminated device. (**E**) A laminated five-layer microdevice showing final architectural details and ready for use. Adapted from [31].

CO_2 laser (trophy etcher) was used for laser ablation of microfluidic channels within select layers and an office laminator to bond 2-7 layers of transparency film. Ultimately, this method provided a process for rapid prototyping of complex multilayer microfluidic devices in less than 1 hour. The initial implementation of this method was utilized for DNA extraction and PCR amplification[32] in addition to DNA electrophoresis[33]. More recently this method has been applied for centrifugal LOC devices for clinical blood analysis[34-36], pathogen detection[37, 38], and forensic DNA analysis[7, 39-42].

1.3 LOC Microfluidic Platforms

Microfluidic platforms consist of an easily combinable set of microfluidic unit-operations, or fluid handling steps, that enables the miniaturization, integration, and automation of assays laying the foundation of a truly LOC system.[43] Based on the operations for fluidic control, these microfluidic platforms have been broadly categorized as capillary, pressure driven, centrifugal, electrokinetic, and acoustic systems. Although there are advantages and disadvantages of each platform, capillary and centrifugal will be the focus of this chapter as these platforms have been used extensively with the fabrication techniques discussed towards inexpensive, single-use microfluidic devices.

1.3.1 Centrifugal Microfluidics

Using centrifugal forces to automate sample processing was demonstrated in the late 1960s with a centrifugal analyzer for spectrometric analysis[44], and in the early 1900s the company Abaxis developed a portable clinical chemistry analyzer integrating reagent storage, sample processing, and analysis using a plastic rotating cartridge (**Figure 1-5**).[45]

Continued work lead to the next generation of centrifugal devices, modern centrifugal microfluidics, and efforts have increased over the past two decades towards lab-on-a-disc, or lab-on-a-CD, systems. Several reviews highlighting continued advancement of this work towards centrifugal microfluidics for integrated LOC systems have been published.[46-49]

Figure 1-5: Image of the rotor device being placed into the Abaxis instrument. Adapted by [45].

1.3.1.1 Fluidic Movement

The centrifugal microfluidic platform offers a unique advantage to the LOC field due to the ease of automation and portability. Multiple fluidic processing steps can be automated by implementing different rotational frequency protocols, also referred to as spin protocols, which includes speed, direction, and duration. This is advantageous for a LOC system as a simple and compact motor is all that is necessary to create the forces for fluid manipulation, requiring no external connections to syringe or pneumatic pumps[7]. The minimal instrumentation needed for centrifugal devices reduces the cost and expands the potential for an easily portable device.

Sample and reagent handling processes performed on centrifugal devices, including liquid propulsion, mixing, metering, and valving, have been demonstrated for various applications.[46, 49, 50] Pseudo-forces are inertial body forces acting on fluids or particles within a rotating system and are described in **Figure 1-6**.[51] The fundamental movement of fluid as a device spins is caused by centrifugal force driving fluid outward from the center of rotation toward the edge of the device. The basis of this fluid movement relying on the radial force that occurs as the device spins is centrifugal force (F_c), and is defined as:

$$F_c = m\omega^2 r \tag{1}$$

where m is the mass of sample, r is the position, and ω is the angular rotational frequency of the disc. Two additional pseudo-forces that are considered to influence fluid movement are Coriolis force, a velocity dependent force, and Euler force, which is proportional to the angular acceleration. Once fluidic movement within the device is initiated, the different factors that contribute to the fluid average velocity, U, are shown through centrifugal theory:

$$U = \frac{D_h^2 \rho \omega^2 \bar{r} \Delta r}{32 \mu L} \tag{2}$$

where D_h is the diameter of the channel, ρ is the density of the liquid, ω is the angular velocity of the disk, $\bar{r}$ is the average distance of the liquid in the channel from the center of the disk, Δr is the radial extent of the liquid, μ is the viscosity of the fluid, and L is the length of the liquid in the channel. As shown by this equation, the channel dimensions, spin velocity of the device, and properties of the fluid dominate fluid movement. Centrifugal fluid movement is unique compared to other LOC fluid movement methods, e.g., electrokinetic, because movement does not depend on chemical properties of the fluid such as fluid pH, ionic strength, and charge.[49] Additionally, due to the rotational symmetry of the centrifugal flow from the center outwards, the format of a centrifugal microfluidic device is compact disc (CD)-like, resulting in simple replication of identical fluidic architecture around the center of rotation to facilitate parallel sample processing or multiplexing.

1.3.1.2 Valving

Incorporating a microvalving network into any microfluidic platform is considered a critical function for additional control of fluidic movement. Generally, microvalves can be classified as passive or active valves, and typical valves within these categories used in centrifugal microfluidics include capillary, hydrophobic and laser-assisted.

Capillary and hydrophobic valves are considered passive, and these microvalves are actuated within the centrifugal device platform by utilizing centrifugal pressure. Both of these passive valves are based on the general concept that fluid will not move from one microfluidic channel into a subsequent channel connected by a valve until the device reaches a particular rate of rotation, or burst frequency. Capillary burst valves are created when the cross-section of a hydrophilic channel expands abruptly, increasing the liquid-air interface, and have been demonstrated within several centrifugal devices fabricated using various substrates, including PDMS[48], PMMA[52], polycarbonate[53], and

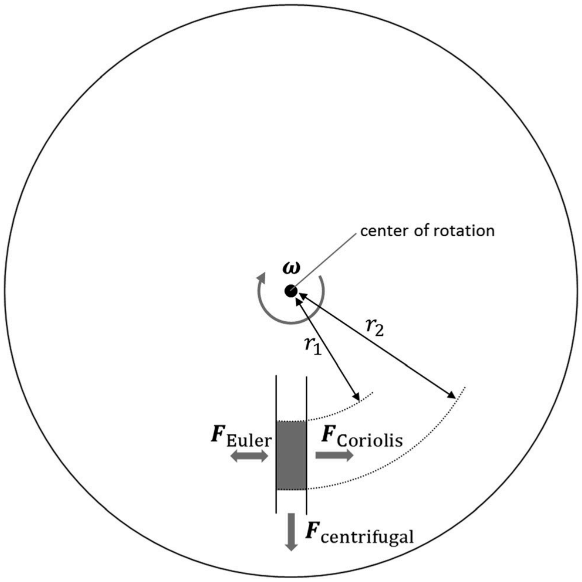

Figure 1-6: Pseudo-forces acting in centrifugal microfluidics. While the centrifugal force always acts radially outward, the Coriolis force acts perpendicular to both ω and the fluid velocity, and the Euler force is proportional to the angular acceleration. Adapted from [51].

polyester[35]. An alternative passive valve includes a hydrophobic valve that relies on a functionalized hydrophobic region within a hydrophilic channel to impede fluid flow.[54] This valve was implemented by Ouyang et al. as the first report of fluidic control within a polyester-based centrifugal device for multistep processes utilizing laser printing lithography.[22] While the burst frequency required for a capillary valve is governed by the aspect ratio of the channel geometries, the burst frequency for a hydrophobic valve is dependent on the nature of the functionalized hydrophobic region. The rate of rotation, in rotations per minute (RPM), required to overcome these valves can be calculated by:

$$f(RPM)=\frac{30}{\pi}\sqrt{\frac{2\gamma(\cos\theta_f-\cos\theta_p)}{\rho h\Delta R\bar{R}}}$$

where γ is the surface tension of the fluid, θ_f is the contact angle of the fluid, θ_p is the contact angle of the functionalized hydrophobic surface, ρ is the fluid density, h is the height of the channel, ΔR is the change in the distance of the fluid from the center of rotation, and $\bar{R}$ is the average distance of the fluid from the center.

Mark et al. described a centrifuge-pneumatic valve for highly wetted liquids, or solutions with a low surface tension, i.e., buffers containing detergents or organic solvents, as most passive valves are best utilized with aqueous solutions.[55] The basis of a centrifuge-pneumatic valve is air compression, which is independent of the fluid properties, and partly surface tension of the fluid. As shown in **Figure 1-7**, the valving structure is comprised of a wide upstream channel with a narrow connecting channel to an unvented downstream receiving chamber.[55] Centrifugal fluid movement is used to fill the wide upstream channel, displacing the air within this channel towards the center of rotation as it fills. Once filled, a meniscus is formed at the bottom of the narrow connecting channel preventing air from displacing from the unvented receiving chamber. The air counter-pressure formed within the receiving chamber reaches equilibrium with the centrifugally generated pressure, ultimately stopping fluid movement. The fluid is then moved into the downstream receiving chamber by increasing the rotational frequency, or burst frequency.

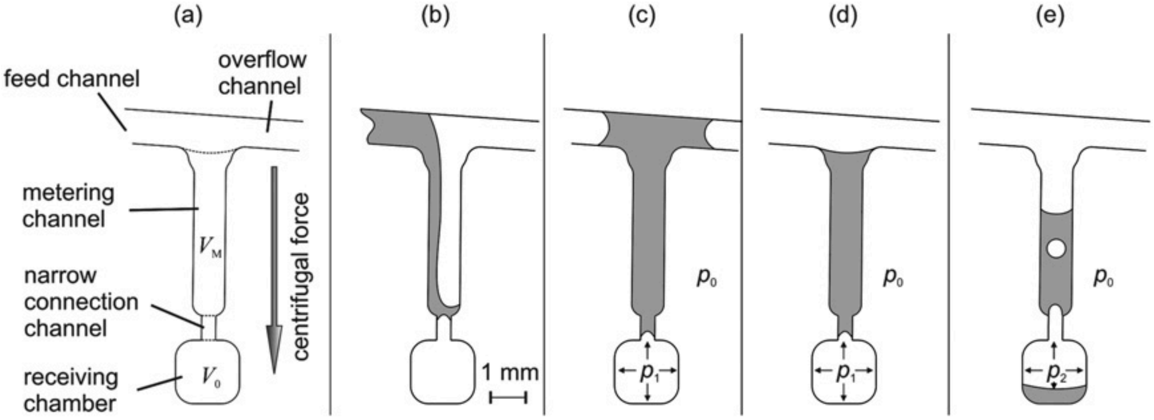

Figure 1-7: Schematic of a metering structure based on the centrifugo-pneumatic valve. (**A**) Liquid can fill the metering channel through the feed channel. The metered volume is defined by the metering channel V_M, the volume of the receiving chamber is V_0. (**B-D**) While liquid is filling the metering channel at a first centrifugal metering frequency, the increased air pressure p_1 stops the liquid from entering the receiving chamber. (**E**) At a higher centrifugal frequency, the liquid is transported to the receiving chamber while leaving air bubbles decrease the air pressure. Adapted from [55].

However, unlike passive valves, active valves are most commonly actuated by mechanical moving parts such as magnetic[56, 57], electric[58, 59], piezoelectric[60, 61], or thermal[62, 63] methods requiring additional interfaces to the device for controlling the valves by external means. An alternative method for active valve actuation consists of no mechanical moving parts and can utilize methods such as phase changes[64-67] and electrochemical[68-70] actuation. The implementation of active valves within centrifugal microfluidic devices has been demonstrated, for example, using paraffin wax and laser-assisted systems. Optofluidic valves actuated by a solid state laser have been described by Garcia-Cordero et al. for use with polyester-based microfluidic devices (**Figure 1-8**).[71]

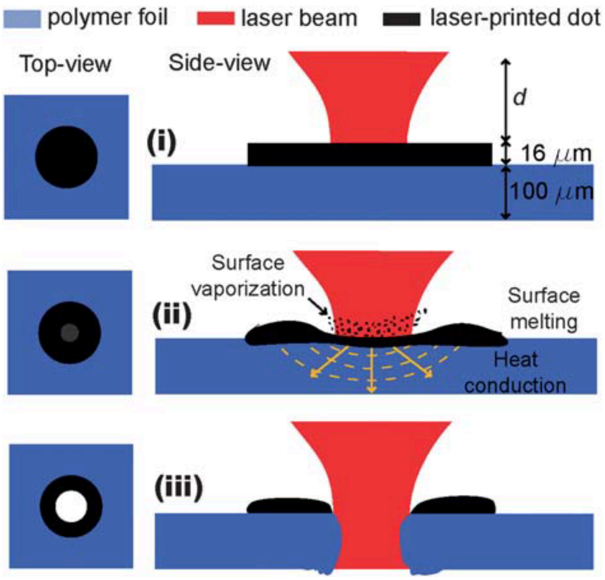

Figure 1-8: Working principle of the one-shot optofluidic valve. (**i**) A dot patterned on a plastic substrate by a laser printer and a laser beam incident on that dot. (**ii**) The optical energy of the beam is converted into thermal energy with multiple consequences: surface vaporization, surface melting, and heat conduction through the plastic substrate. (**iii**) After 0.5 s, the plastic recedes, leaving an orifice. The distance d from the focal point was varied, as was the optical power level, to characterize the one-shot valves. Adapted from [71].

Optically-addressable valves are natively closed valves actuated by melting the device substrate to actuate, or open, the valve to allow fluid to pass. Simply, toner patches are printed onto the polyester layer between channels to increase the light absorbance from the laser and melt the polyester for removal of the physical barrier created by the valve. An alternative to melting the device substrate can incorporate paraffin wax whereby stationary infrared sources were used to melt the wax to actuate, or open, the valve[72, 73], however, the heat applied to melt the wax lead to concerns for the device substrates or integrated reagents. To limit the energy input used for valve actuation, Park et al. demonstrated laser-irradiated ferrowax microvalves (LIFM) utilizing iron oxide nanoparticles within the wax for efficient heating.[74] Unlike optofluidic and paraffin wax valves, LIFMs have been utilized for natively closed, natively open, and reversible valve formats. Ultimately, active valves within a centrifugal microfluidic platform are rotational frequency independent methods.

1.3.1.3 Mixing

Mixing within microfluidic devices is critical to provide homogeneity of sample and reagent for chemical reactions, and is impacted by the laminar flow within small microfluidic dimensions. Similar to valving within microfluidics, mixing can be categorized as active and passive mixing. Initially, centrifugal or batch-wise 'shake-mode' mixing was utilized within centrifugal microfluidic devices as a simple method to apply continuous changes in the spin speed of the device.[75] As continuous changes in spin speed were applied, the angular momentum caused by the acceleration and deceleration resulted in an inversion of the fluids, or twisting motion, for mixing within the microchannel. Although centrifugal mixing is considered active, the requirement of external equipment for actuation is minimal, as a simple spin motor is already utilized for fluidic movement. Methods considered for passive mixing incorporate a micromixer domain into the flow path for enhanced mixing through diffusion or chaotic advection. These methods rely on increasing the contact surface between the different fluids and decreasing the diffusion path.[76]

1.3.1.4 Metering

Precise volume control, or metering, is critical in many sample processing protocols and can depend greatly on the implementation of a valving network. Simply, a metering structure consists of a connection channel to an inlet port, a metering chamber with a defined volume, and an overflow connection to a waste chamber for excess volume (**Figure 1-9**).[51] Any of the valves discussed can be implemented at the radially end of the metering chamber for additional fluidic control. The effectiveness of metering can be impacted by variations in microdevice fabrication and the capillary forces experienced at liquid interfaces.[77, 78] The advantage of centrifugal microfluidics for metering allows for capillary forces to be countered by centrifugal forces for reproducible metering.

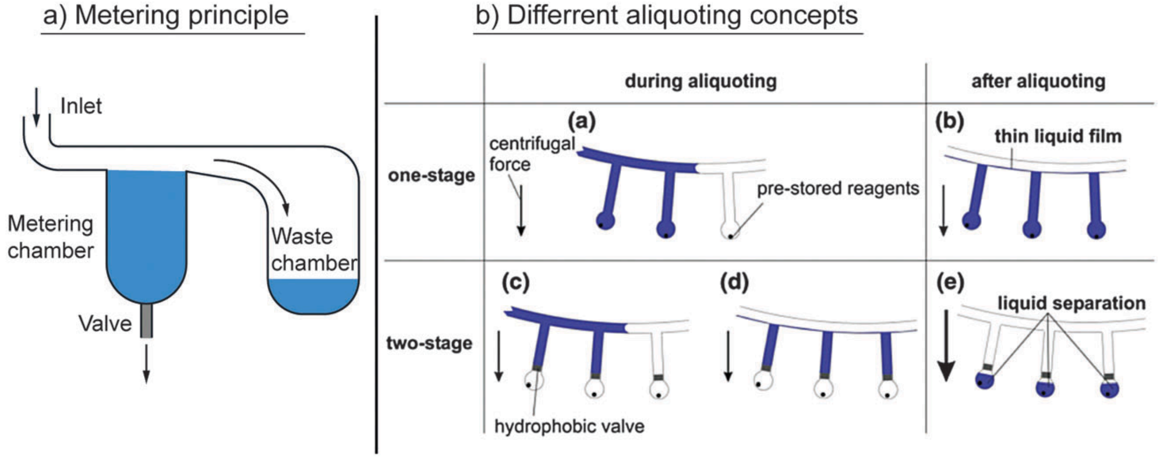

Figure 1-9: Centrifugal microfluidic unit operations for metering and aliquoting. (**A**) Basic principle of metering. A liquid fills a metering chamber with a defined volume. The excess is gated into a waste chamber. The metered volume can subsequently be transferred into the microfluidic network via suitable valves. (**B**) Different aliquoting concepts. Adapted from [51] and [77].

1.3.2 Paper-based Microfluidics

Although the use of paper for analytical testing dates back to the early1800s[30], the first paper-based test, or lateral flow 'dipstick', was commercialized in the 1960s to quantify glucose in urine for diabetes[79]. Broadly, lateral flow assays can be considered the most successful microfluidic LOC platform based on the number of commercialized products, i.e., pregnancy and diabetes testing, however, there are a minimal number of microfluidic reports for these assays.[43] Paper as a substrate for microfluidic devices was more recently introduced in 2007 by Martinez et al. for a protein and glucose biochemical assay (**Figure 1-10**).[26] The advantages of paper that resulted in applications for paper chromatography, lateral flow immunoassays, reactive indicators such as litmus paper, and qualitative spot tests include power-free fluid transport using capillary action, high surface-to-volume ratio for improved detection limits, and the capability for storing reagents within the paper.[30] Significant interest in the use of paper-based microfluidic devices for the developing world and resource-limited areas has been realized for the simplicity and cost-effectiveness of lateral flow test strips with enhanced functionality for diagnostic assays.[80]

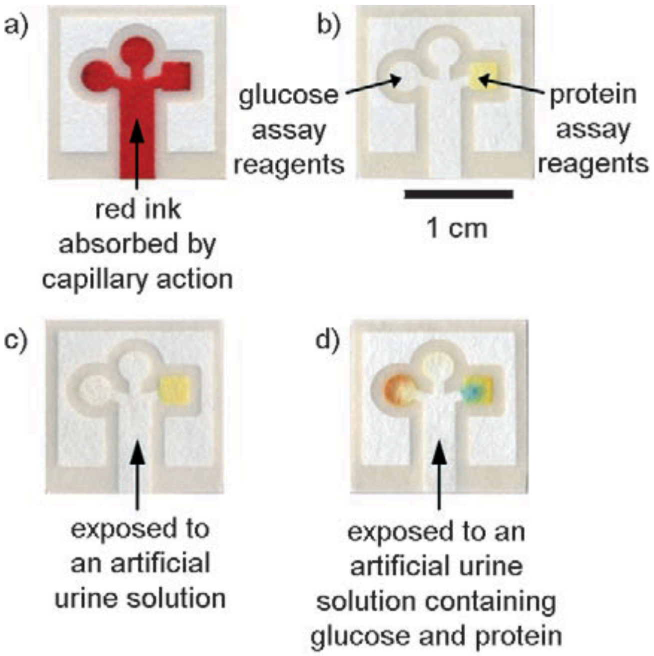

Figure 1-10. Chromatography paper patterned with photoresist. The darker lines are cured photoresist, whereas the lighter areas are unexposed paper. (**A**) Patterned paper whereby the central channel absorbed red ink by capillary action and the pattern directed the sample (ink) into three separate test areas. (**B**) Device after spotting the reagents. The circular region on top was used as a control. (**C**) Negative control for glucose (left) and protein (right) by using an artificial urine solution. (**D**) Positive assay for glucose (left) and protein (right). Adapted from [26].

1.3.2.1 Fluidic Movement

The wicking-based flow exhibited in paper due to capillary action is considered laminar flow. In paper-based microfluidic devices, laminar flow occurs due to the relevant length scale of the membrane pore diameter (<20 μm) resulting in low Reynolds numbers, $\sim 10^3$ at typical flow rates.[81] The different factors that contribute to the fluid flow in a porous media, with a constant cross section, are defined by Darcy law, assuming a fully-wetted paper device:

$$Q = -\frac{\kappa w h}{\mu L}\Delta P \qquad (3)$$

where Q is the volumetric flow rate, κ is the permeability of the paper, wh is the paper cross-sectional area width (w) and height (h), μ is the dynamic viscosity of the fluid, and ΔP is the pressure drop occurring over the length, L, of the paper network. As described by this equation, the microfluidic channel dimensions (width and height), choice of paper material, and properties of the fluid dominate fluidic movement.

The fluid movement within a paper network, driven by capillary force, is considered a form of passive fluid movement. The demonstration of active fluid movement within paper is challenging, however, few groups have accomplished active movement by employing centrifugal force.[82, 83] Cho et al. described the concept of paper-on-a-disc by incorporating paper strips into a centrifugal device platform and characterized the flow within paper at various centrifugal spin speeds.[82] Notably, the flow rate could be precisely controlled through balancing the centrifugal and capillary forces, using the defined equation for determining the equilibrium wicking distance, h_0, against the rotation:

$$h_0 = R_0 - \sqrt{R_0^2 - \frac{2\Delta P_c}{\rho\omega^2}} \tag{4}$$

where R_0 is the radial position of the fluid front, ΔP_c is the capillary pressure, ρ is the density of the fluid, and ω is the angular velocity of the rotating disc. A schematic representation of the balancing forces and hybrid device used is shown in **Figure 1-11**.

1.3.2.2 Fluidic Control

Unlike the centrifugal microfluidic platform, which offers valving, mixing, and metering for additional fluidic control, paper-based microfluidics offer limited control for fluidic movement, i.e., rate and direction of fluid movement, due to the inherent

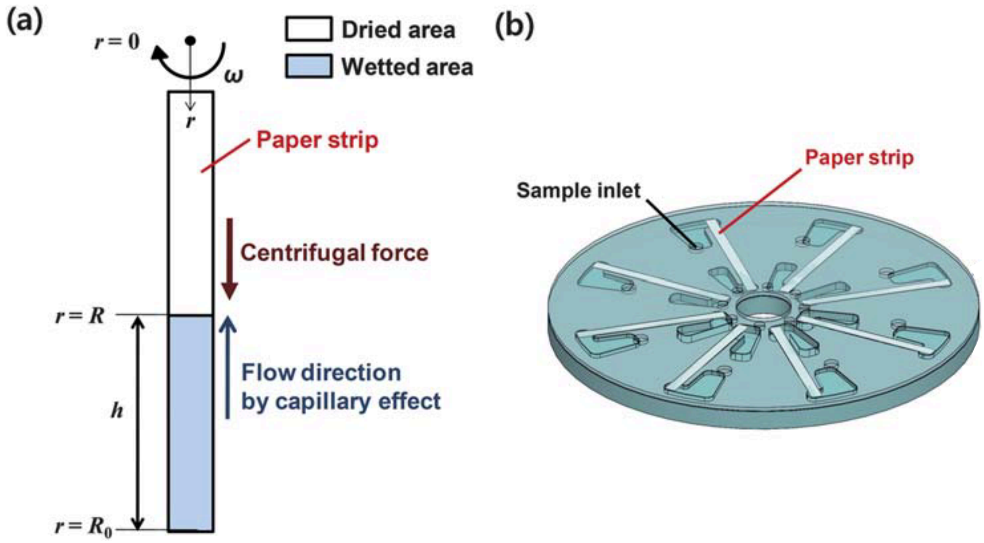

Figure 1-11: Schematic illustrations of (**A**) the force balance in a rotating paper and (**B**) the configuration of a centrifugal device for rotating paper strips. Paper strips were integrated into a plastic disc to demonstrate the control of flow in a paper by balancing capillary-driven flow with a centrifugal force. Adapted from [82].

properties of paper. Limited fluidic control resulted in minimal impact within the microfluidics and analytical communities for paper-based devices due to the lack of functionality towards complex sample matrices and performing multiple sample processing steps. More recently, research groups aim to develop new methods to address these issues regarding fluidic control.

Initial adaptation of the single-strip format of lateral flow strips resulted in 2D[84] and 3D[85] paper devices with a focus on enhanced functionality and multiplexed sample analysis. Further use of these multidimensional paper networks resulted in automation of multistep processes by Fu et al.[86] and Lutz et al.[87] for sequential reagent delivery to a given detection region using paper channel dimensions to control the timing of reagent delivery. Reagent delivery is simply performed using paper-based devices as the sample acts as the rehydration solution for reagents dry-stored at any necessary location within the paper matrix by pipetting the reagent to dry, also referred to as 'spotting'. Additional functionality for paper-based devices has been demonstrated through timing and programming fluid movement,[81, 88, 89] altering the surface chemistry,[90, 91] and incorporating electrodes[92-94].

1.4 Microfluidic Devices for Explosives and Illicit Drug Detection

While substantial efforts have been made for the development of clinical microfluidic devices for POC applications, until recently, less focus has been towards the development of devices for forensic applications.[95] Analogous to the benefits for POC applications, microfluidics offers the same advantages for hand held analysis systems or components of mobile laboratories for on-site forensic analysis including rapid analysis times, decreased sample consumption, portable analysis, and automation for simple operating procedures.

1.4.1 On-Site Detection of Explosives and Illicit Drugs

Rapid, on-site analysis of explosive residues for applications in environmental remediation of decommissioned manufacturing sites[96, 97] to forensic investigation of terrorist-related events[98, 99] can benefit from the development of portable sensing techniques. On-site explosives detection techniques include canines, analytical instrumentation, and colorimetric tests. Although the use of canines for on-site detection is a sensitive technique, this method requires extensive canine training, operation by a skilled handler, and lack of specificity for deciphering between various explosives compounds.[100, 101] Efforts to make analytical instrumentation more portable for field use have resulted in the use of ion mobility spectrometry (IMS)[102, 103], Fourier transform infrared spectroscopy (FTIR) [104], and Raman spectroscopy[105] for on-site analysis.

Methods for standoff or noncontact analysis have been deployed for field use, i.e., handheld Raman spectrometers, as a method for analyzing samples with an internal spectral library for identification.[106] These analytical methods commonly rely on the detection of volatile compounds, require calibration for background interferences, and remain bulky and expensive for field use.

Alternatively, color tests are a common field detection method due to low cost, availability, and simplicity of these methods as the resultant color changes are visual. Current commercial color test kits utilize liquid reagents stored in glass ampules, aerosol sprays for application of the chemical reagents, or swipe pads with reagents stored for use with a portable colorimetric detector. Examples of commercial color test kits include the IDEX[107], Expray Plus[107], and the SEEKERe[108]. Significant limitations that arise with color tests include subjective color interpretation, improper test operation, lighting interferences, and lack of multiplexing requiring multiple individual tests, all providing potential for user error.

While on-site explosives detection is motivated by the desire for a rapid response to potential hazards or explosive-related threats, illicit drug detection is motivated by the growing global need to confront the harm caused by drugs as trends in drug abuse continue to rise and adapt each year.[109] The methods used for illicit drug on-site detection are similar to those used with explosives, and includes canines[110], portable Raman spectroscopy[106], FTIR[111], IMS[112], and colorimetric analysis[108, 113]. However, processing of a collected field sample, or seized drug material, to later convict a suspected individual for the possession of an illicit drug requires more stringent sample processing. The current processing scheme for identifying unknown material for the presence of suspected illicit drugs is multistep. First, an initial presumptive test that can be performed quickly and easily at the scene, and later performed initially in a laboratory setting, is used to determine a course of action *in situ* or for further analysis of a street sample. This initial presumptive test is followed by a confirmatory test of high selectivity and sensitivity performed in a forensic laboratory.

The most commonly used presumptive test for law enforcement is color tests due to strict local and state-level budget limitations. The overly simplistic nature of these color tests has resulted in much concern and media attention[114], highlighting the need to improve these qualitative tests. Common problems that can lead to significant user error discussed with color tests above for explosives are also observed for illicit drugs, with additional limitations from uncontrolled substance additives resulting in false positive and false negative results.[115]

1.4.2 Microfluidic Devices for Explosives

Microfluidic technologies, mainly capillary electrophoresis (CE)- and paper-based devices, have been applied to explosives detection, aiming to address challenges and limitations with current field analysis methods. CE is a class of techniques in which separations are carried out in capillaries under the influence of an electric field. Compounds are separated based on their mass-to-charge ratios, and neutral species are separated using micellar electrokinetic chromatography (MEKC) whereby a surfactant is added to the running buffer to generate micelles for separation of based on differing affinities for the micelle hydrophobic interior. Translation of these separation techniques to microfluidic devices allows for extremely fast separations due to the microchannel dimensions, a notion that was recognized in 1990 during the introduction of 'micro total analysis systems'.[1]

Efforts towards on-site explosives detection utilizing an enclosed microfluidic system were introduced by Sandia National Laboratory to develop a portable Micro-ChemLab system for nitroaromatic explosives, and other biotoxins, with integrated sampling for analysis of both gas and liquid phases.[116] Walenberg and Bailey incorporated a MEKC separation within a glass microfluidic device, microchannel 65 mm in length, for indirect laser-induced fluorescence (LIF) detection of ten different nitroaromatic compounds within 1 minute (**Figure 1-12**).[117]

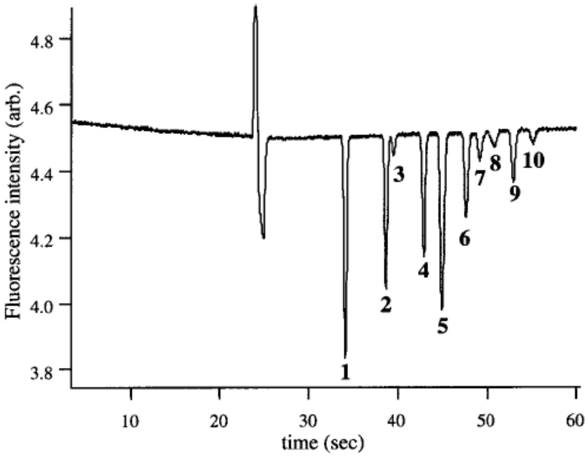

Figure 1-12. Microfluidic-based MEKC – indirect LIF electropherogram of the EPA 8330 mixture of nitroaromatics and nitramines. Analytes: 20 ppm of each TNB (1), DNB (2), NB (3), TNT (4), tetryl (5), 2,4-DNT (6), 2,6- DNT (7), 2-, 3-, and 4-NT (8), 2-Am-4,6-DNT (9), and 4-Am-2,6-DNT (10). Conditions: MEKC buffer, 50 mM borate, pH 8.5, 50 mM SDS, 5 μM Cy7, separation voltage 4 kV, separation distance 65 mm. Adapted from [117].

Alternatively, microfluidic devices for separations with electrochemical detection are advantageous for on-site explosives detection due to the high performance and ease of integration into the microfluidic platform.[118, 119] A microfluidic device for the detection of five nitroaromatic explosives compounds with interchangeable carbon thick-film screen-printed electrodes for amperometric detection with a microfluidic CE device was developed by Wang et al.[120] Later, this method was adapted further by this research group and other groups to explore electrode materials, i.e. gold[121, 122], mercury/gold amalgam[123], and boron-doped diamond electrodes[124], for improved detection limits.

Towards the identification of inorganic explosive compounds, microfluidic CE was coupled with conductivity detection for analysis of ionic species. Additionally, contactless conductivity detection, whereby the electrodes do not contact the sample solution, is advantageous for implementing narrow microchannels, simplified alignment, and elimination of problems associated with solution contact to the electrode.[118, 125] Instead of utilizing MEKC, capillary zone electrophoresis (CZE) is often implemented with contactless conductivity detection for measuring the different electrophoretic mobilities of the corresponding ions. Wang et al. demonstrated analysis of seven different explosive preblast and postblast cationic and anionic species using a microfluidic CZE device and contactless conductivity detection within 1 minute.[126]

Ueland et al. used a commercial microfluidic Agilent Bioanalyzer designed for sizing, quantitation, and purity assessments of DNA, RNA, and proteins, to separate explosives residues in soil with a paper-based microfluidic device for sample processing (**Figure 1-13**).[14] Using this combination of microfluidic systems, a total of eight different nitroaromatic and nitramine explosive compounds were separated using MEKC,

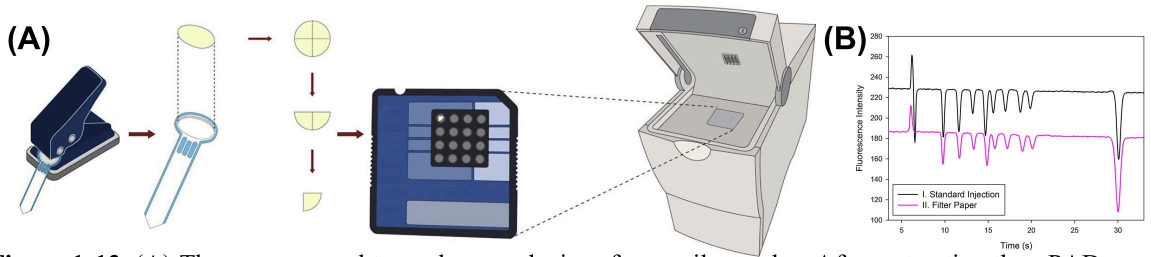

Figure 1-13. (**A**) The process used to analyze explosives from soil samples. After extraction the μPAD was hole-punched. The chad was folded twice and inserted directly into the sample well of the Caliper DNA chip containing buffer for analysis. (**B**) LOC analysis (I) and μPAD chad used for analysis (II) of explosive standards: TNB (1), DNB (2), TNT (3), Tetryl (4), 2,4-DNT (5), 3,4-DNT (6), 2-A-4,6-DNT (7) 4-A-2,6-DNT (8) Experiments were performed using the Agilent Bioanalyzer 2100 (injection 1400 V/40 s, separation 1400 V). Running buffer, 10 mM Borate/50 mM SDS buffer, pH 9.2 with 2%fluorescent DNA Dye®. Adapted from [14].

microchannel 15 mm in length, and identified by fluorescence quenching within 12 minutes from sample extraction and preparation to separation. One limitation of this system was the direct handling of the paper device to punch out the sample paper-based chad to insert into the commercial LOC device chamber with the addition of the separation buffer.

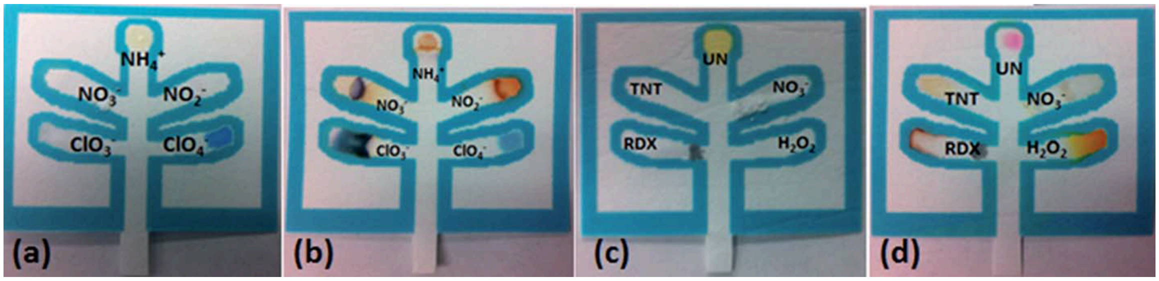

Figure 1-14. The inorganic explosives detection μPAD device prior to analysis (**A**) and following analysis (**B**) of a 1 mg/mL mixture solution of potassium chlorate, ammonium nitrate, potassium nitrite, and potassium perchlorate. The high/organic explosives μPAD prior to analysis (**C**) and following analysis (**D**) of a 1 mg/mL mixture of RDX, TNT, urea nitrate, and hydrogen peroxide solution. Color changes begin to occur after 5 min. with a total run time of ~18 minutes for complete visualization. Adapted from [13].

Additional methods utilized paper-based microfluidic devices for colorimetric detection of explosives. Pesenti et al. developed a simple paper-based device to detect trinitro aromatic explosives by wiping the device on a surface for sample collection, and using one sampling spot for colorimetric detection and removing an additional sampling spot for further confirmatory analysis.[127] Although color change was specific for trinitro aromatic compounds, additional controls for discerning potential environmental contaminants collected during sampling would be valuable. Additionally, multiplexing the described device for the detection of additional explosive compounds would be required for a complete identification system. Peters et al. described two different paper-based microfluidic devices, each capable of simultaneous colorimetric detection of multiple explosives compounds from a single sample input (**Figure 1-14**).[13] Both of these described paper-based devices, however, require subjective visual interpretation of the resultant color change by the user resulting in necessary training for device operation.

1.4.3 Microfluidic Devices for Illicit Drugs

Utilizing LOC microfluidic devices for illicit drug detection has been a greater focus of research groups regarding analysis in biological sample media to detect drug abuse instead of drug possession.[128] Weinberger and Lurie were the first to demonstrate MEKC analysis of illicit drugs by separating 18 drugs within 40 minutes (**Figure 1-15**).[129] Lloyd et al. employed MEKC with a commercial microfluidic Agilent Bioanalyzer to separate amphetamines in a 15 mm channel within 1 min.[130] One limitation of this approach was the derivatization necessary to label analytes prior to separation for LIF detection. Bell et al. demonstrated the first amalgamation of microfluidics and colorimetric testing for the presumptive analysis of illicit drugs.[131] With device architecture wet-etched into glass, this group was able to develop a device to detect methamphetamine, amphetamine, cocaine, and oxycodone within 15 seconds. The glass microdevice, however,

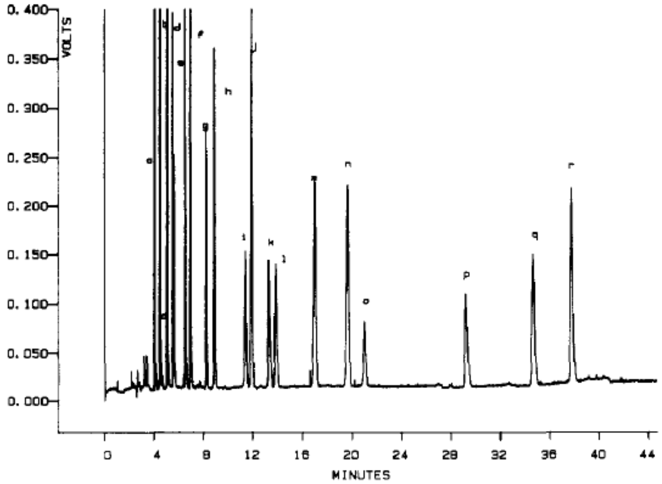

Figure 1-15. MEKC forensic drug screen. Conditions: capillary, 25 cm X 50 µm i.d.; voltage, 20 kV; temperature, 40°C; buffer, 85 mM SDS/8.5 mM phosphate/8.5 mM borate/15% acetonitrile, pH 8.5; detector wavelength, 210 nm; sample concentration, 250 µg/mL of each drug. Key: (a) psilocybin, (b) morphine, (c) phenobarbital, (d) psilocin, (e) codeine, (f) methaqualone, (g) LSD, (h) heroin, (i) amphetamine, (j) librium, (k) cocaine, (I) methamphetamine, (m) lorazepam, (n) diazapam, (o) fentanyl, (p) PCP, (q) cannabidiol, (r) Δ^9-THC. Adapted from [129].

required cleanroom facilities for fabrication, creating manufacturing limitations that translate into expensive microdevices, and detection was still contingent on the subjective analysis of each color change.

Although colorimetric detection using paper-based microfluidic devices continues to receive significant interest by research groups[30], a number of the reagents for illicit drug detection are less compatible for storage on microfluidic devices, such as concentrated acids and volatile reagents, compared to many of the colorimetric microfluidic device applications for POC and resource-limited areas. Musile et al. developed a paper-based microfluidic device for simultaneous presumptive colorimetric detection of cocaine, opiates, ketamine, and various phenethyl amines within 5 minutes, however, it was also recognized that common color tests containing concentrated sulfuric acid, i.e., Marquis and Mecke reagents, and volatile reagents, i.e., Simon's reagent, posed a significant challenge for incorporation into microfluidic devices.[132] The requirement of these reagents has limited the development of LOC microfluidic devices for presumptive colorimetric detection of illicit drugs on-site that are rapid, automated, portable, and cost-effective.

1.5 Conclusions and Future Directions

1.5.1 Conclusions

This chapter introduced the rapidly growing field of microfluidics and the use of microfluidic devices for the development of portable LOC technologies to address current on-site analysis shortcomings. A number of microfluidic device platforms are used as a tool to address various scientific problems, within a wide range of applications including clinical and forensic chemistry. Specifically, centrifugal and paper-based microfluidic device platforms were chosen for discussion within this chapter as advantageous platforms towards portable, single-use microfluidic devices for on-site analyses with complimentary inexpensive and rapid device fabrication techniques. The fundamentals of each platform are described regarding fabrication techniques, fluidic movement, and fluidic control. Many of the examples presented here describe microfluidic advancements for explosives and illicit drug detection. Finally, challenges and future directions are highlighted for the maturing field of microfluidics towards commercial LOC systems.

1.5.2 Future Directions

The field of microfluidics is considered as having close relations with industry and is heavily driven by producing practical devices for real-world applications; however, at the rapid pace microfluidics has matured over the past two decades there is a significant shortage of commercial microfluidic products since the initial excitement and expectations.[133, 134] Although initial efforts in developing microfluidic systems focused on the improvement of current state-of-the-art methods and technologies, within the past several years there has been a growing interest to use microfluidics to solve problems not addressed with macroscale approaches in hopes of addressing the slow uptake of microfluidic technology.[134] A well-known example of this approach is the pregnancy test, broadly recognized as a microfluidic lateral flow assay. This test comprises a biochemical assay using biological sample media to provide immediate results for the end user. While these assays could be performed within the laboratory, the portability and rapid feedback in privacy is transformative for the user.

A series of Focus articles in the journal *Lab on a Chip* by Holger Becker, co-founder and CSO of microfluidic ChipShop GmbH, highlight critical challenges relating to the commercialization of microfluidics from an industry perspective and presents considerations for moving forward.[133] Some of these topics include challenges in manufacturing and mass production of devices, intellectual property issues, lack of standardization, lack of a 'killer application' in microfluidics, and the communication between academia and industry. Significant discussions regarding the state of commercialization for microfluidic technology and future directions have been initiated, for example, the International Conference on Miniaturized Systems for Chemistry and Life Sciences (MicroTAS) introduced a 'Shark Tank' competition at the 2017 meeting and continue to host industry panels to focus on these current issues. Awareness of the gap in the number of available microfluidics publications, referenced by Mark et al. as: "10,000 available publications for microfluidics, offering solutions for almost every problem that might occur…"[3], compared to the number of products in the market is gaining significant attention and will be a focus for the future of this field.

1.6 References

1. A. Manz, N. Graber and H. M. Widmer, *Sensors and Actuators B-Chemical*, 1990, **1**, 244-248.
2. D. R. Reyes, D. Iossifidis, P. A. Auroux and A. Manz, *Analytical Chemistry*, 2002, **74**, 2623-2636.

3. D. Mark, S. Haeberle, G. Roth, F. von Stetten and R. Zengerle, *Chemical Society Reviews*, 2010, **39**, 1153-1182.
4. P. Yager, T. Edwards, E. Fu, K. Helton, K. Nelson, M. R. Tam and B. H. Weigl, *Nature*, 2006, **442**, 412-418.
5. M. I. Mohammed, S. Haswell and I. Gibson, *Proceedings of The 1st International Design Technology Conference, DESTECH2015*, 2015, **20**, 54-59.
6. D. Le Roux, B. E. Root, J. A. Hickey, O. N. Scott, A. Tsuei, J. Y. Li, D. J. Saul, L. Chassagne, J. P. Landers and P. de Mazancourt, *Lab on a Chip*, 2014, **14**, 4415-4425.
7. B. L. Thompson, C. Birch, D. A. Nelson, J. Y. Li, J. A. DuVall, D. Le Roux, A. C. Tsuei, D. L. Mills, B. E. Root and J. P. Landers, *Lab on a Chip*, 2016, **16**, 4569-4580.
8. S. Jovanovich, G. Bogdan, R. Belcinski, J. Buscaino, D. Burgi, E. L. R. Butts, K. Chear, B. Ciopyk, D. Eberhart, O. El-Sissi, H. Franklin, S. Gangano, J. Gass, D. Harris, L. Hennessy, A. Kindwall, D. King, J. Klevenberg, Y. Li, N. Mehendale, R. McIntosh, B. Nielsen, C. Park, F. Pearson, R. Schueren, N. Stainton, C. Troup, P. M. Vallone, M. Vangbo, T. Woudenberg, D. Wyrick and S. Williams, *Forensic Science International-Genetics*, 2015, **16**, 181-194.
9. B. L. LaRue, A. Moore, J. L. King, P. L. Marshall and B. Budowle, *Forensic Science International-Genetics*, 2014, **13**, 104-111.
10. R. S. Turingan, S. Vasantgadkar, L. Palombo, C. Hogan, H. Jiang, E. Tan and R. F. Selden, *Investigative Genetics*, 2016, **7**, 12.

11. M. Saito, N. Uchida, S. Furutani, M. Murahashi, W. Espulgar, N. Nagatani, H. Nagai, Y. Inoue, T. Ikeuchi, S. Kondo, H. Uzawa, Y. Seto and E. Tamiya, *Microsystems & Nanoengineering*, 2018, **4**.
12. H. Lee, S. Lee, I. Jang, J. Kim, G. You, E. Kim, K. Choi, J. H. Lee, S. Choi, K. Shin, M. H. Yoon and H. B. Oh, *Microfluidics and Nanofluidics*, 2017, **21**.
13. K. L. Peters, I. Corbin, L. M. Kaufman, K. Zreibe, L. Blanes and B. R. McCord, *Analytical Methods*, 2015, **7**, 63-70.
14. M. Ueland, L. Blanes, R. V. Taudte, B. H. Stuart, N. Cole, P. Willis, C. Roux and P. Doble, *Journal of Chromatography A*, 2016, **1436**, 28-33.
15. G. S. Fiorini and D. T. Chiu, *Biotechniques*, 2005, **38**, 429-446.
16. W. M. Moreau, *Semiconductor Lithography: Principles, Practices, and Materials*, Spinger Science & Business Media, 1998.
17. Y. N. Xia and G. M. Whitesides, *Angewandte Chemie-International Edition*, 1998, **37**, 550-575.
18. G. M. Whitesides, E. Ostuni, S. Takayama, X. Y. Jiang and D. E. Ingber, *Annual Review of Biomedical Engineering*, 2001, **3**, 335-373.
19. J. C. McDonald, D. C. Duffy, J. R. Anderson, D. T. Chiu, H. K. Wu, O. J. A. Schueller and G. M. Whitesides, *Electrophoresis*, 2000, **21**, 27-40.
20. J. C. McDonald and G. M. Whitesides, *Accounts of Chemical Research*, 2002, **35**, 491-499.
21. C. R. Phaneuf, K. Oh, N. Pak, D. C. Saunders, C. Conrardy, J. P. Landers, S. X. Tong and C. R. Forest, *Biomedical Microdevices*, 2013, **15**, 221-231.

22. Y. W. Ouyang, S. B. Wang, J. Y. Li, P. S. Riehl, M. Begley and J. P. Landers, *Lab on a Chip*, 2013, **13**, 1762-1771.

23. J. A. Lounsbury, A. Karlsson, D. C. Miranian, S. M. Cronk, D. A. Nelson, J. Y. Li, D. M. Haverstick, P. Kinnon, D. J. Saul and J. P. Landers, *Lab on a Chip*, 2013, **13**, 1384-1393.

24. A. M. Tan, K. Rodgers, J. P. Murrihy, C. O'Mathuna and J. D. Glennon, *Lab on a Chip*, 2001, **1**, 7-9.

25. C. L. do Lago, H. D. T. da Silva, C. A. Neves, J. G. A. Brito-Neto and J. A. F. da Silva, *Analytical Chemistry*, 2003, **75**, 3853-3858.

26. A. W. Martinez, S. T. Phillips, M. J. Butte and G. M. Whitesides, *Angewandte Chemie-International Edition*, 2007, **46**, 1318-1320.

27. D. A. Bruzewicz, M. Reches and G. M. Whitesides, *Analytical Chemistry*, 2008, **80**, 3387-3392.

28. Y. Lu, W. W. Shi, L. Jiang, J. H. Qin and B. C. Lin, *Electrophoresis*, 2009, **30**, 1497-1500.

29. E. Carrilho, A. W. Martinez and G. M. Whitesides, *Analytical Chemistry*, 2009, **81**, 7091-7095.

30. D. M. Cate, J. A. Adkins, J. Mettakoonpitak and C. S. Henry, *Analytical Chemistry*, 2015, **87**, 19-41.

31. B. L. Thompson, Y. Ouyang, G. R. M. Duarte, E. Carrilho, S. T. Krauss and J. P. Landers, *Nature Protocols*, 2015, **10**, 875-886.

32. G. R. M. Duarte, C. W. Price, B. H. Augustine, E. Carrilho and J. P. Landers, *Analytical Chemistry*, 2011, **83**, 5182-5189.

33. G. R. M. Duarte, W. K. T. Coltro, J. C. Borba, C. W. Price, J. P. Landers and E. Carrilho, *Analyst*, 2012, **137**, 2692-2698.

34. B. L. Thompson, R. J. Gilbert, M. Mejia, N. Shukla, D. M. Haverstick, G. T. Garner and J. P. Landers, *Analytica Chimica Acta*, 2016, **924**, 1-8.

35. Y. W. Ouyang, J. Y. Li, C. Phaneuf, P. S. Riehl, C. Forest, M. Begley, D. M. Haverstick and J. P. Landers, *Lab on a Chip*, 2016, **16**, 377-387.

36. B. L. Thompson, S. L. Wyckoff, D. M. Haverstick and J. P. Landers, *Analytical Chemistry*, 2017, **89**, 3228-3234.

37. J. A. DuVall, J. C. Borba, N. Shafagati, D. Luzader, N. Shukla, J. Y. Li, K. Kehn-Hall, M. M. Kendall, S. H. Feldman and J. P. Landers, *Plos One*, 2015, **10**.

38. J. A. DuVall, S. T. Cabaniss, M. L. Angotti, J. H. Moore, M. Abhyankar, N. Shukla, D. L. Mills, B. G. Kessel, G. T. Garner, N. S. Swami and J. P. Landers, *Analyst*, 2016, **141**, 5637-5645.

39. B. L. Thompson, C. Birch, J. Y. Li, J. A. DuVall, D. Le Roux, D. A. Nelson, A. C. Tsuei, D. L. Mills, S. T. Krauss, B. E. Root and J. P. Landers, *Analyst*, 2016, **141**, 4667-4675.

40. K. R. Jackson, J. C. Borba, M. Meija, D. L. Mills, D. M. Haverstick, K. E. Olson, R. Aranda, G. T. Garner, E. Carrilho and J. P. Landers, *Analytica Chimica Acta*, 2016, **937**, 1-10.

41. J. A. DuVall, D. Le Roux, A. C. Tsuei, B. L. Thompson, C. Birch, J. Li, D. A. Nelson, D. L. Mills, M. M. Ewing, R. S. McLaren, D. R. Storts, B. E. Root and J. P. Landers, *Analytical Methods*, 2016, **8**, 7331-7340.

42. J. A. DuVall, D. Le Roux, B. L. Thompson, C. Birch, D. A. Nelson, J. Y. Li, D. L. Mills, A. Tsuei, M. G. Ensenberger, C. Sprecher, D. R. Storts, B. E. Root and J. P. Landers, *Analytica Chimica Acta*, 2017, **980**, 41-49.

43. S. Haeberle and R. Zengerle, *Lab on a Chip*, 2007, **7**, 1094-1110.

44. N. G. Anderson, *Science*, 1969, **166**, 317-324.

45. C. T. Schembri, T. L. Burd, A. R. Kopfsill, L. R. Shea and B. Braynin, *Journal of Automatic Chemistry*, 1995, **17**, 99-104.

46. M. Madou, J. Zoval, G. Y. Jia, H. Kido, J. Kim and N. Kim, in *Annual Review of Biomedical Engineering*, Annual Reviews, Palo Alto, 2006, vol. 8, pp. 601-628.

47. M. J. Madou and G. J. Kellogg, *Proc. SPIE Systems and Technologies for Clinical Diagnostics and Drug Discovery*, 1998, ***3259***, 80-93.

48. D. C. Duffy, H. L. Gillis, J. Lin, N. F. Sheppard and G. J. Kellogg, *Analytical Chemistry*, 1999, **71**, 4669-4678.

49. R. Gorkin, J. Park, J. Siegrist, M. Amasia, B. S. Lee, J. M. Park, J. Kim, H. Kim, M. Madou and Y. K. Cho, *Lab on a Chip*, 2010, **10**, 1758-1773.

50. J. Ducree, S. Haeberle, S. Lutz, S. Pausch, F. von Stetten and R. Zengerle, *Journal of Micromechanics and Microengineering*, 2007, **17**, S103-S115.

51. O. Strohmeier, M. Keller, F. Schwemmer, S. Zehnle, D. Mark, F. von Stetten, R. Zengerle and N. Paust, *Chemical Society Reviews*, 2015, **44**, 6187-6229.

52. R. D. Johnson, I. H. A. Badr, G. Barrett, S. Y. Lai, Y. M. Lu, M. J. Madou and L. G. Bachas, *Analytical Chemistry*, 2001, **73**, 3940-3946.

53. T. S. Leu and P. Y. Chang, *Sensors and Actuators a-Physical*, 2004, **115**, 508-515.

54. H. Andersson, W. van der Wijngaart, P. Griss, F. Niklaus and G. Stemme, *Sensors and Actuators B-Chemical*, 2001, **75**, 136-141.

55. D. Mark, T. Metz, S. Haeberle, S. Lutz, J. Ducree, R. Zengerle and F. von Stetten, *Lab on a Chip*, 2009, **9**, 3599-3603.

56. K. Yanagisawa, H. Kuwano and A. Tago, *Microsystem Technologies*, 1995, **2**, 22-25.

57. Z. L. Cai, J. W. Xiang, B. Z. Zhang and W. J. Wang, *Sensors and Actuators B-Chemical*, 2015, **206**, 22-29.

58. K. Sato and M. Shikida, *Journal of Micromechanics and Microengineering*, 1994, **4**, 205-209.

59. J. Schaible, J. Vollmer, R. Zengerle, H. Sandmaier and T. Strobelt, *Transducers '01: Eurosensors Xv, Digest of Technical Papers, Vols 1 and 2*, 2001, 928-931.

60. H. Q. Li, D. C. Roberts, J. L. Steyn, K. T. Turner, O. Yaglioglu, N. W. Hagood, S. M. Spearing and M. A. Schmidt, *Sensors and Actuators a-Physical*, 2004, **111**, 51-56.

61. G. Waibel, J. Kohnle, R. Cernosa, M. Storz, M. Schmitt, H. Ernst, H. Sandmaier, R. Zengerle and T. Strobelt, *Sensors and Actuators a-Physical*, 2003, **103**, 225-230.

62. C. A. Rich and K. D. Wise, *Journal of Microelectromechanical Systems*, 2003, **12**, 201-208.

63. H. Takao, K. Miyamura, H. Ebi, M. Ashiki, K. Sawada and M. Ishida, *Sensors and Actuators a-Physical*, 2005, **119**, 468-475.

64. D. J. Beebe, J. S. Moore, J. M. Bauer, Q. Yu, R. H. Liu, C. Devadoss and B. H. Jo, *Nature*, 2000, **404**, 588-+.

65. A. Richter, D. Kuckling, S. Howitz, T. Gehring and K. F. Arndt, *Journal of Microelectromechanical Systems*, 2003, **12**, 748-753.

66. C. Yu, S. Mutlu, P. Selvaganapathy, C. H. Mastrangelo, F. Svec and J. M. J. Frechett, *Analytical Chemistry*, 2003, **75**, 1958-1961.

67. A. Suzuki and T. Tanaka, *Nature*, 1990, **346**, 345-347.

68. C. R. Neagu, J. G. E. Gardeniers, M. Elwenspoek and J. J. Kelly, *Journal of Microelectromechanical Systems*, 1996, **5**, 2-9.

69. C. R. Neagu, J. G. E. Gardeniers, M. Elwenspoek and J. J. Kelly, *Electrochimica Acta*, 1997, **42**, 3367-3373.

70. H. Suzuki and R. Yoneyama, *Sensors and Actuators B-Chemical*, 2003, **96**, 38-45.

71. J. L. Garcia-Cordero, D. Kurzbuch, F. Benito-Lopez, D. Diamond, L. P. Lee and A. J. Ricco, *Lab on a Chip*, 2010, **10**, 2680-2687.

72. K. Abi-Samra, R. Hanson, M. Madou and R. A. Gorkin, *Lab on a Chip*, 2011, **11**, 723-726.

73. W. Al-Faqheri, F. Ibrahim, T. H. G. Thio, J. Moebius, K. Joseph, H. Arof and M. Madou, *Plos One*, 2013, **8**.

74. J. M. Park, Y. K. Cho, B. S. Lee, J. G. Lee and C. Ko, *Lab on a Chip*, 2007, **7**, 557-564.

75. M. Grumann, A. Geipel, L. Riegger, R. Zengerle and J. Ducree, *Lab on a Chip*, 2005, **5**, 560-565.

76. N. T. Nguyen and Z. G. Wu, *Journal of Micromechanics and Microengineering*, 2005, **15**, R1-R16.

77. D. Mark, P. Weber, S. Lutz, M. Focke, R. Zengerle and F. von Stetten, *Microfluidics and Nanofluidics*, 2011, **10**, 1279-1288.

78. J. Steigert, M. Grumann, T. Brenner, L. Riegger, J. Harter, R. Zengerle and J. Ducree, *Lab on a Chip*, 2006, **6**, 1040-1044.

79. A. H. Free, E. C. Adams, M. L. Kercher, H. M. Free and M. H. Cook, *Clin. Chem.* , **1957**, **3**, 163–168.

80. A. W. Martinez, S. T. Phillips, G. M. Whitesides and E. Carrilho, *Analytical Chemistry*, 2010, **82**, 3-10.

81. J. L. Osborn, B. Lutz, E. Fu, P. Kauffman, D. Y. Stevens and P. Yager, *Lab on a Chip*, 2010, **10**, 2659-2665.

82. H. Hwang, S. H. Kim, T. H. Kim, J. K. Park and Y. K. Cho, *Lab on a Chip*, 2011, **11**, 3404-3406.

83. N. Godino, E. Vereshchagina, R. Gorkin and J. Ducree, *Microfluidics and Nanofluidics*, 2014, **16**, 895-905.

84. E. Carrilho, S. T. Phillips, S. J. Vella, A. W. Martinez and G. M. Whitesides, *Analytical Chemistry*, 2009, **81**, 5990-5998.

85. A. W. Martinez, S. T. Phillips and G. M. Whitesides, *Proceedings of the National Academy of Sciences of the United States of America*, 2008, **105**, 19606-19611.

86. E. L. Fu, S. Ramsey, P. Kauffman, B. Lutz and P. Yager, *Microfluidics and Nanofluidics*, 2011, **10**, 29-35.

87. B. R. Lutz, P. Trinh, C. Ball, E. Fu and P. Yager, *Lab on a Chip*, 2011, **11**, 4274-4278.

88. E. Fu, B. Lutz, P. Kauffman and P. Yager, *Lab on a Chip*, 2010, **10**, 918-920.

89. J. F. Tian, D. Kannangara, X. Li and W. Shen, *Lab on a Chip*, 2010, **10**, 2258-2264.

90. Y. H. Zhu, X. W. Xu, N. D. Brault, A. J. Keefe, X. Han, Y. Deng, J. Q. Xu, Q. M. Yu and S. Y. Jiang, *Analytical Chemistry*, 2014, **86**, 2871-2875.

91. P. D. Garcia, T. M. G. Cardoso, C. D. Garcia, E. Carrilho and W. K. T. Coltro, *Rsc Advances*, 2014, **4**, 37637-37644.

92. W. Dungchai, O. Chailapakul and C. S. Henry, *Analytical Chemistry*, 2009, **81**, 5821-5826.

93. W. J. Lan, E. J. Maxwell, C. Parolo, D. K. Bwambok, A. B. Subramaniam and G. M. Whitesides, *Lab on a Chip*, 2013, **13**, 4103-4108.

94. Z. H. Nie, C. A. Nijhuis, J. L. Gong, X. Chen, A. Kumachev, A. W. Martinez, M. Narovlyansky and G. M. Whitesides, *Lab on a Chip*, 2010, **10**, 477-483.

95. E. Verpoorte, *Electrophoresis*, 2002, **23**, 677-712.

96. P. G. Rieger and H. J. Knackmuss, *Biodegradation of Nitroaromatic Compounds*, 1995, **49**, 1-18.

97. A. Hilmi, J. H. T. Luong and A. L. Nguyen, *Journal of Chromatography A*, 1999, **844**, 97-110.

98. J. S. Caygill, F. Davis and S. P. J. Higson, *Talanta*, 2012, **88**, 14-29.

99. R. L. Wang, G. Yang, J. Q. Zhang, Q. Li, R. X. Fu, J. C. Ye, T. Z. Wang, Y. Lu, H. Zhou and G. L. Huang, *Analytical Methods*, 2014, **6**, 9628-9633.

100. K. G. Furton and L. J. Myers, *Talanta*, 2001, **54**, 487-500.

101. S. Singh, *Journal of Hazardous Materials*, 2007, **144**, 15-28.

102. R. G. Ewing, D. A. Atkinson, G. A. Eiceman and G. J. Ewing, *Talanta*, 2001, **54**, 515-529.

103. M. Najarro, M. E. D. Morris, M. E. Staymates, R. Fletcher and G. Gillen, *Analyst*, 2012, **137**, 2614-2622.

104. A. Banas, K. Banas, M. Bahou, H. O. Moser, L. Wen, P. Yang, Z. J. Li, M. Cholewa, S. K. Lim and C. H. Lim, *Vibrational Spectroscopy*, 2009, **51**, 168-176.

105. M. Lopez-Lopez and C. Garcia-Ruiz, *Trac-Trends in Analytical Chemistry*, 2014, **54**, 36-44.

106. E. L. Izake, *Forensic Science International*, 2010, **202**, 1-8.

107. http://www.fieldforensics.com, (accessed April 2, 2018).

108. https://www.detectachem.com, (accessed 23 February 2018).

109. U. United Nations Office on Drugs and Crime, *Journal*, 2014.

110. T. Jezierski, E. Adamkiewicz, M. Walczak, M. Sobczynska, A. Gorecka-Bruzda, J. Ensminger and E. Papet, *Forensic Science International*, 2014, **237**, 112-118.

111. J. M. E. Chalmers, Howell G. M. and M. D. Hargreaves, *Infrared and Raman Spectroscopy in Forensic Science*, 2012.

112. G. A. Eiceman, Z. Karpas and H. H. Hill, *Ion Mobility Spectrometry, 3rd Edition*, 2014, 1-400.

113. NIK Narcotics Field Drug Test Kits, http://www.alternateforce.net).

114. R. Gabrielson and T. Sanders, *Journal*.

115. Y. Tsumura, T. Mitome and S. Kimoto, *Forensic Science International*, 2005, **155**, 158-164.
116. D. Lindner, *Lab on a Chip*, 2001, **1**, 15N-19N.
117. S. R. Wallenborg and C. G. Bailey, *Analytical Chemistry*, 2000, **72**, 1872-1878.
118. M. Pumera, *Electrophoresis*, 2006, **27**, 244-256.
119. J. Wang, *Analytica Chimica Acta*, 2004, **507**, 3-10.
120. J. Wang, B. M. Tian and E. Sahlin, *Analytical Chemistry*, 1999, **71**, 5436-5440.
121. A. Hilmi and J. H. T. Luong, *Environmental Science & Technology*, 2000, **34**, 3046-3050.
122. A. Hilmi and J. H. T. Luong, *Analytical Chemistry*, 2000, **72**, 4677-4682.
123. J. Wang and M. Pumera, *Talanta*, 2006, **69**, 984-987.
124. J. Wang, G. Chen, M. P. Chatrathi, A. Fujishima, D. A. Tryk and D. Shin, *Analytical Chemistry*, 2003, **75**, 935-939.
125. M. Pumera, *Talanta*, 2007, **74**, 358-364.
126. J. Wang, M. Pumera, G. Collins, F. Opekar and I. Jelinek, *Analyst*, 2002, **127**, 719-723.
127. A. Pesenti, R. V. Taudte, B. McCord, P. Doble, C. Roux and L. Blanes, *Analytical Chemistry*, 2014, **86**, 4707-4714.
128. E. Al-Hetlani, *Electrophoresis*, 2013, **34**, 1262-1272.
129. R. Weinberger and I. S. Lurie, *Analytical Chemistry*, 1991, **63**, 823-827.
130. A. Lloyd, L. Blanes, A. Beavis, C. Roux and P. Doble, *Analytical Methods*, 2011, **3**, 1535-1539.
131. S. C. Bell and R. D. Hanes, *Journal of Forensic Sciences*, 2007, **52**, 884-888.

132. G. Musile, L. Wang, J. Bottoms, F. Tagliaro and B. McCord, *Analytical Methods*, 2015, **7**, 8025-8033.

133. H. Becker, *Lab on a Chip*, 2009, **9**, 1659-1660.

134. C. D. Chin, V. Linder and S. K. Sia, *Lab on a Chip*, 2012, **12**, 2118-2134.

2. Objective Method for Presumptive Field-Testing of Illicit Drug Possession Using Centrifugal Microdevices and Smartphone Analysis

2.1 Introduction

The outcome of cases concerning illegal possession of controlled substances is heavily reliant on confirmation that the suspected individual possessed the substance in question. Presumptive tests are critical in providing prompt qualitative identification of a controlled substance, enabling immediate action to be taken at the scene. These presumptive tests allow law enforcement to seize material for confirmatory testing and arrest the suspected individual. Due to budget limitations supporting presumptive field tests for local and state-level law enforcement, current methods are commonly colorimetric and include a number of commercial, prepackaged individual tests or "reagent ampule pouches" to accommodate the large screening demand. Noncolorimetric field techniques that can be used to screen for illicit drugs include portable Raman spectroscopy[1], Fourier transform infrared spectroscopy[2] (FTIR), and ion mobility spectrometry[3] (IMS). While portability issues concerning these conventional techniques have been addressed, making field-testing achievable, these techniques remain expensive for law enforcement to carry out for initial screenings. In addition, these methods have obvious disadvantages. For example, with Raman spectroscopy, fluorescent signals corresponding to common drug cutting agents and impurities lead to inconsistent results. Similar interference issues are observed using FTIR for the presence of water.[4] Finally, challenges arise with IMS from saturation of the instrument with bulk sample, resulting in carry-over during sequential analyses or unpredictable results due to charge depletion at high sampling amounts.[5]

Microfluidic technologies are the focus of increasing interest in the forensic sector[6-8] due to low reagent and sample consumption, fast analysis times, inexpensive materials, and increased portability for on-site analyses.[9] Over the past decade, the use of centrifugal force identified by Duffy et al. for fluid flow control in microfluidic devices has led to significant effort by numerous research groups to explore centrifugally driven microfluidics.[10, 11] The centrifugal microfluidic "lab-on-a-disc", or rotation-driven microdevice (RDM) platform, comprises unique features that are advantageous to the user when automation and ease of portability are desired, as fluid movement requires only a simple motor. Using this platform, it is possible to automate multiple fluidic processing steps, in parallel or in series, by controlling rotation speed, direction, and duration, ultimately allowing for fluid manipulation without the need for syringe-based or pneumatic pumps.[12] This increases the compatibility of the RDM platform for rapid presumptive drug detection whereby multiple colorimetric reactions could be performed simultaneously. Currently, the standard colorimetric approach incorporates multiple test ampules, each filled with a different selective reagent to test for its associated drug, which must be broken in situ.

While colorimetric kits for illicit drugs have some advantages over conventional instrumentation, the reliance on proper operation and subjective analysis by the user is a substantial concern. Common complications that arise during field-testing result from subjective color interpretation, improper test operation, incorrect results reported for the test used, on-site environmental limitations (e.g., poor lighting or reflecting color from flashing police vehicle lights), and sequential tests needed, increasing the opportunity for user error. There is an increased awareness that individuals with normal vision (i.e., without color blindness) perceive various colors differently,[13-15] which can lead to the reporting of erroneous results. Additionally, these problems can also lead to several individual pouches, or tests, being used in an attempt to verify results.

At present, the majority of the illicit drugs encountered by law enforcement contain additional uncontrolled substances.[16-18] These additives, or drug-cutting agents, add a layer of complexity and cannot be adequately accounted for with current colorimetric tests, as they can interfere with color changes. Strictly, only color changes that directly match the kit instructions are considered positive for a particular drug. All other results, including partial color changes or insufficient color changes, require additional on-site analysis or remain inconclusive at the scene. The amount of sample used to conduct these tests is critical for correct identification and can lead to false negative and positive results due to the sensitivity of the colorimetric reactions.[19] Frequently, cutting agents affect the amount of controlled substance being tested, requiring additional test pouches to be used while varying the sample amounts applied to each pouch to verify results. Existing on-site detection kits can place an additional burden on local and state laboratories to alleviate inconclusive or inaccurate results reported. This susceptibility demands a new detection approach: a technology that provides a chemical analysis system with an electronic colorimetric detector as an objective detection method that can determine subtle variations in color change by examining image parameters not easily distinguishable with visual observation.

While a microfluidic device for detection of illicit drugs using capillary electrophoresis has been described,[20] it represents an instrument-intensive approach that is not likely compatible with field analyses. However, while also employing microfluidic technologies, Bell et al. described a more practical, minimalist approach, reporting the first amalgamation of microfluidics and colorimetric testing for the presumptive analysis of illicit drugs.[21] With device architecture wet-etched into glass, they were able to develop a device to detect methamphetamine, amphetamine, cocaine, and oxycodone in an impressive 15 seconds.[21] The glass microdevice, however, required cleanroom facilities for fabrication, creating manufacturing limitations that translate into expensive microdevices and was still contingent on the subjective analysis of color change.

We propose that the problems discussed above can be obviated by employing the laser print, cut, and laminate (PCL) protocol that the Landers Lab has previously described.[22] This method offers a means to fabricate sophisticated microfluidic architecture using inexpensive, commercial, off-the-shelf materials and instrumentation to ultimately combine multiple colorimetric tests into a single device for a cost-effective and rapid on-site detection technique. The devices are fabricated from polyester overhead transparencies[23] using a laser printer, laser cutter, and office laminator. In an effort to enhance current subjective field methods, a polyester-toner RDM with a simple protocol for device operation, requiring minimal training and a smartphone-based image analysis method for interpreting results is described here. This detection utilizes threshold values associated with image parameters from colorimetric reactions in the presence of specific drugs to identify unknown samples. Common illicit drugs found in law enforcement, such as cocaine and methamphetamine, were used for proof-of-principle. We aim to eliminate the need for using multiple tests on-site with this described device design, leading to a detection platform with an elevated rate of success when translated to field analyses.

2.2 Materials and Methods

2.2.1 Reagents

Cocaine, methamphetamine, codeine, and amphetamine standard solutions were purchased from Cerilliant (Round Rock, TX). Cobalt(II) thiocyanate, sodium nitroprusside, acetaldehyde, sodium carbonate, caffeine, lidocaine, acetylsalicylic acid, starch, and dextrose were purchased from Sigma-Aldrich (St. Louis, MO).

2.2.2 Preparation of Drug Samples and Reagents

Purchased drug standards were concentrated in an Eppendorf Vacufuge 5301 (Westbury, NY) and then serial diluted to various concentrations when necessary. Ethanol was used as the solvent during dilutions. Cobalt thiocyanate and Simon's reagent solutions were prepared as described previously.[24]

2.2.3 Fabrication of Polyester-Toner Devices

The laser PCL method used for polyester-toner device fabrication has been previously described by Thompson et al.[22] The microfluidic devices for determining threshold values and drug detection were designed in CorelDraw CAD software. Both devices were five layers, comprised of alternating polyester and toner-coated polyester layers. The toner-coated layers were made by printing two layers of black toner using a

HP LaserJet 4000 printer onto both sides of a single transparency sheet. Device features including channels, inlets, mixing wells, detection chambers, and air vents were then laser-ablated into each layer using a VersaLASER system (Scottsdale, AZ), defining device architecture. To prepare the drug detection device for detecting cocaine and methamphetamine, using cobalt thiocyanate and Simon's colorimetric reagents, respectively, cobalt thiocyanate (0.75 μL), and sodium carbonate (1.5 μL) were spotted and dried onto the device before bonding. The device was bonded during lamination (three passes) at >160 °C using an UltraLam 250B.

2.2.4 Laser Valve Actuation

Two layers of black toner patches were printed onto the middle transparency layer before laser ablation to use for valves. A 1000 mW 532 nm Green Portable Laser Pointer Pen (Model LT-HJG0087) was purchased from www.laserpointerpro.com and positioned 1.5 cm above the RDM. The laser was turned on for 10 s to open each valve.

2.2.5 Microdevice Control

A Sanyo Denki Sanmotion series stepper motor controlled by a Pololu DRV8825 stepper motor driver in full step mode was utilized for the spin system. Motion control profiles were generated using a Parallax Propeller microcontroller and a printed circuit board was designed with EAGLE CAD software containing the microcontroller, motor drivers, and associated components for power regulation, heat sinking, and serial communication with an external computer terminal. A poly(methyl methacrylate) (PMMA) custom support structure immobilized the motor during rotation.

All spin parameters were saved with Parallax Propeller software and performed using the "automated mode". After sample addition, the device spin protocol for determining threshold values using the one-step design was as follows: spin 1000 RPM for 3 s with 100 angular acceleration (AA), followed by 1000 RPM, four replicate spins, for 5 s (200 AA). Complete backfilling of the sample into the detection chambers via capillary action was achieved before each consecutive spin as described previously by Ouyang et al. for the 'spin-stop' mixing protocol.[25] Image capture was taken at 3 min.

The spin protocol for determining threshold values using the two-step device design was as follows: spin 500 RPM for 3 s with 250 AA, then three alternating repeats of 1000 RPM and –1000 RPM for 3 s (500 AA) for mixing. The laser valve was opened and the device was spun at 1000 RPM, 10 s (250 AA), and six replicates of alternating 1000 RPM and −1000 RPM for 5 s each (500 AA) for another mixing cycle. Image capture was taken at 5 min total time, 3 min after valves were opened. The drug detection device spin protocol was the same as the two-step protocol used for threshold determination.

2.2.6 Image Analysis

To perform image analysis with a desktop scanner, the device was removed from the spin system and scanned after the completed spin protocol using an EPSON Perfection V100 Photo Scanner with 1200 dpi resolution. The scanned images were saved as TIFF files and the device detection chambers were cropped using ImageJ. RGB values were evaluated with ImageJ. The hue and saturation of the cropped images were measured using a Mathematica algorithm. For smartphone image capture, a PMMA holder was fabricated to position the smartphone 5 cm above the RDM for consistent image capture. Analysis with the Android smartphone was performed using a custom-written smartphone application.

2.3 Results and Discussion

2.3.1 Objective Image Analysis

To develop an automated and objective detection system for illicit drugs, a means of quantitatively measuring drug-specific colorimetric reactions to correlate with a qualitative readout for the user was essential. Initially, resulting color changes from each reaction were analyzed using several image parameters, including RGB (red, green, and blue color model), and HSB (hue, saturation, and brightness). The RGB channels of an image were analyzed individually to determine the dynamic range associated with specific color changes, which is illustrated in **Figure 2-1**. The HSB color model is derived from RGB with hue describing the color, independent of intensity and brightness, and saturation as the color intensity. Individually, hue or saturation can be used to analyze all color changes, defining the shade and intensity of the color change, while the brightness of the image is

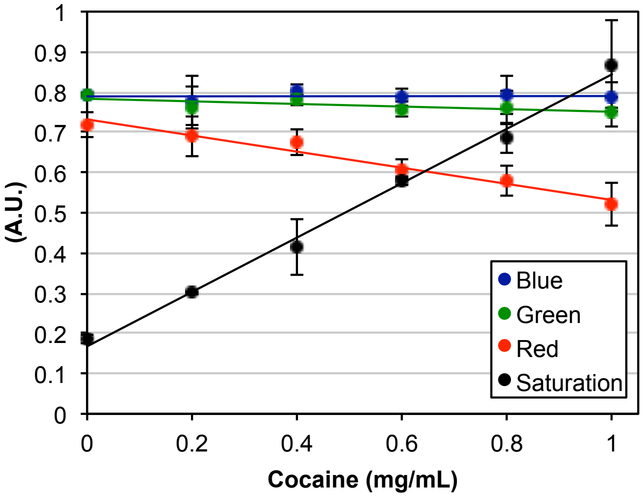

Figure 2-1. Cocaine image analysis with RGB. Comparing saturation as the image analysis parameter for cocaine with RGB color analysis. The color change for cocaine is blue-green which is mostly comprised of blue and green color at each concentration, resulting in small dynamic ranges. There is more variability in the amount of red color, but the dynamic range is substantially smaller than the saturation analysis parameter.

held constant by the detector or lighting. Ultimately, of the initial image parameters evaluated, the large dynamic range associated with hue and saturation made them the most promising parameters to use for analysis.

The most appropriate parameter, hue or saturation, then needed to be defined for each colorimetric reaction, cocaine using cobalt thiocyanate[18, 26] and methamphetamine using the Simon's reagent.[27, 28] Various concentrations of cocaine and methamphetamine were analyzed using the threshold determination RDM (**Fig. 2-2**) to measure both the hue and the saturation associated with the resulting color changes. Initially, image capture with a $50 desktop scanner provided a high level of control over image settings and resolution to develop a comparative standard method to smartphone image capture.

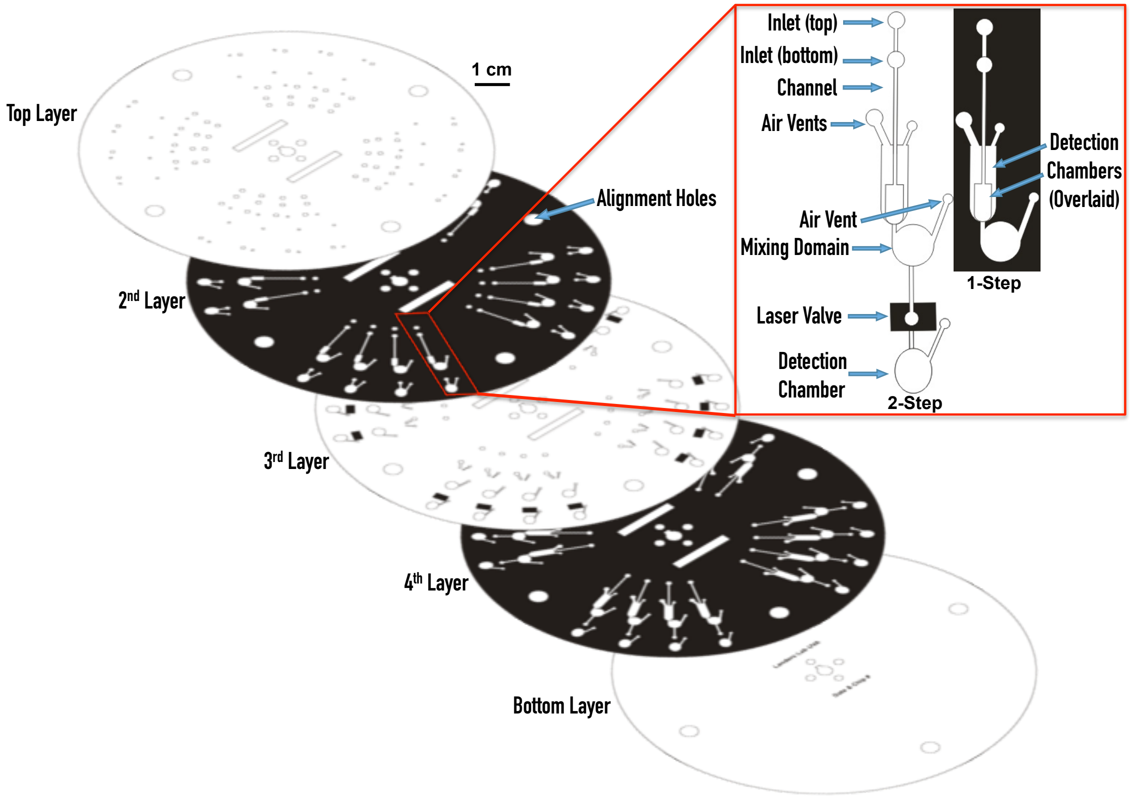

Figure 2-2. Schematic of the device design for threshold determination. CAD design of microfluidic device used to define detection threshold values for methamphetamine (2-step architecture) and cocaine (1-step architecture) with inset describing each feature of one domain.

2.3.2 Threshold Determination Device Fluidic Control

A threshold determination device was designed and fabricated (**Fig. 2-2**) for a multilayer format to induce mixing by the balancing of centrifugal-driven flow and capillary action, as described by Ouyang et al.[25] To summarize, this involved two nearly identical channel architectures, overlaid in a five-layer system (features described in **Fig. 2-2**; dimensions described in **Fig. 2-3**), for holding the requisite volumes of sample and reagent, with detection chambers ~124 µm deep (one laser-ablated toner sheet). For the initial scan for detection of cocaine using the device design without a valve (one-step design, **Fig. 2-2** inset), the cobalt thiocyanate reagent (1 µL) was pipetted into the top inlet and sample (3 µL) into the bottom inlet, where capillary action facilitated the filling of each structure. A mixing chamber at the base of both overlaid detection chambers consisted of three laser-ablated polyester layers to hold the combined volume of reagent and sample (4 µL) for mixing. A passive capillary valve[29, 30] held each solution in the

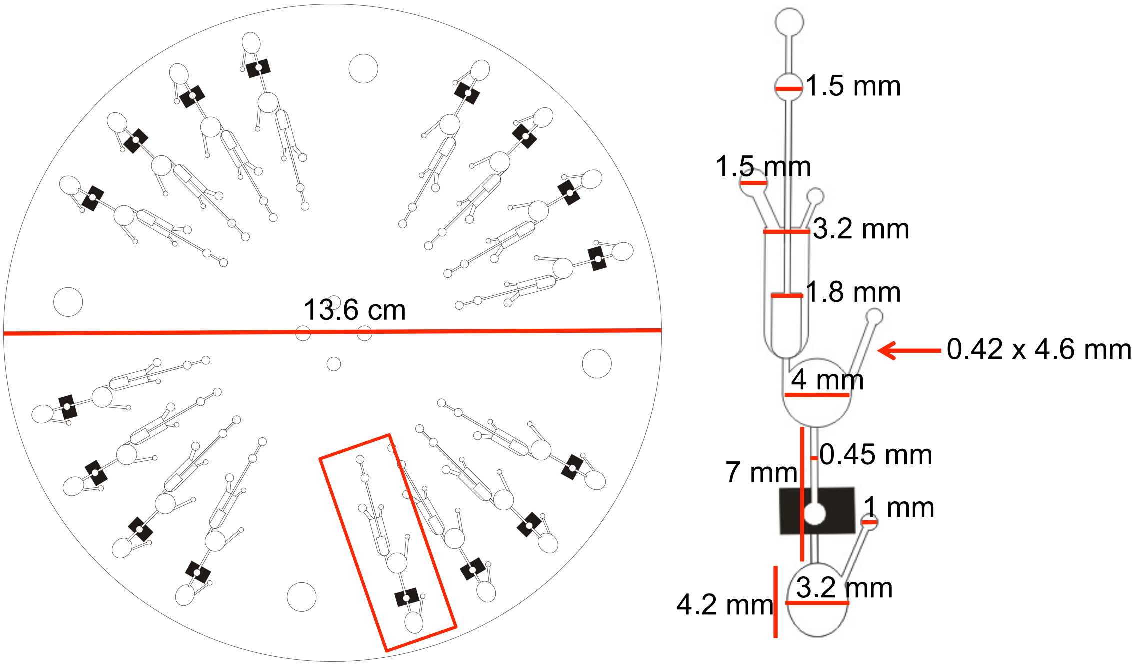

Figure 2-3. Device design with dimensions. CAD design of one microfluidic device layer used for defining detection thresholds with features labeled to describe design dimensions.

separate (overlaid) detection chambers until centrifugal force was substantial enough to drive the solutions to the peripheral mixing domain to mix the sample and reagent. Alternatively, when device spinning was stopped, capillary action moved the solution back into the detection chambers. The device was spun at 1000 RPM, to overcome the resistance of the capillary valve, and stopped repeatedly to perform the 'spin-stop' reciprocal protocol for thorough mixing of sample and reagent.

Once initial color analysis was performed (initial scan), the fabrication process was then adapted for on-board reagent storage (**Fig. 2-4**). RDMs fabricated using the PCL method allow for nonvolatile reagents to be concentrated on the device through pipetting and drying, similar to paper-based device fabrication. Cobalt thiocyanate (for cocaine) and sodium carbonate (for methamphetamine) reagents were pipetted and allowed to dry on the bottom layer of the device in the 'mixing domain'. Once dried, the top layer of the device was added and bonded, thus, enclosing the dried reagents. This approach was then used for subsequent scanner and smartphone analysis.

When valving was necessary for the two-step methamphetamine colorimetric reaction, a laser valve that was originally described by Garcia-Cordero et al. was implemented.[31] A black toner patch printed onto the topside of the middle device layer would act as the closed valve (**Fig. 2-5A**). When the laser was turned on to actuate the valve, the toner patch absorbed the energy from

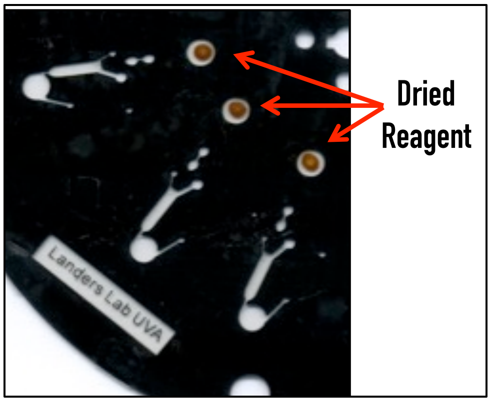

Figure 2-4. Image of dried reagent within a test device. Device image showing cobalt thiocyanate solution pipetted and allowed to dry within device chambers. Cover layer was added and device bonded to enclose the reagent within the completed device.

the laser and melted the polyester layer to produce an open hole (**Fig. 2-5B**). Once the device was spun, the solution passed though the hole and interacted with the reagent dried in a second chamber (**Fig. 2-5C**). The core device architecture for the one-step design was used for the two-step design with an additional mixing domain below the laser valve added for the "detection chamber" (two-step design, **Fig. 2-2**, inset).

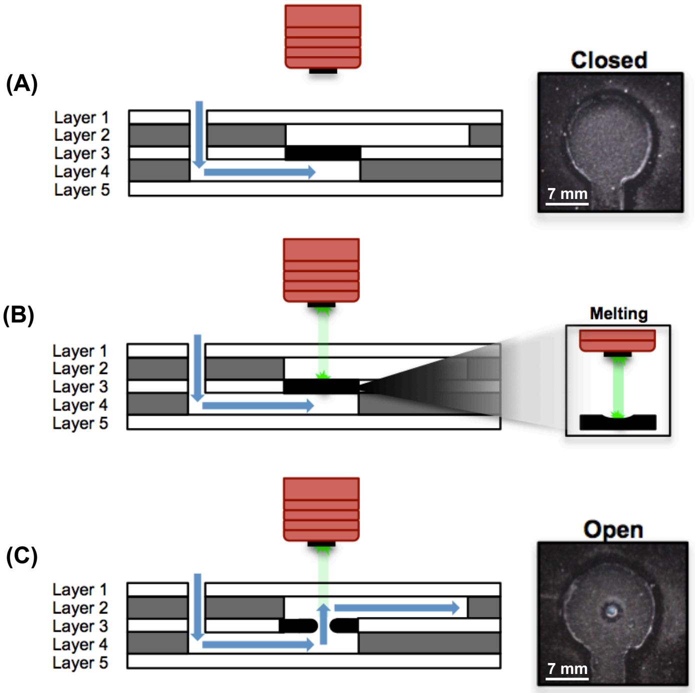

Figure 2-5. Schematic of laser valve operation. (**A**) Solution is held in the bottom channel by a closed laser valve (image shown). (**B**) Toner patch absorbs laser energy and melts polyester layer 3. (**C**) Laser valve is open (image shown) and solution can move into the top channel when the device is spun.

For the 'initial scan' analysis of methamphetamine to verify that the color change could be detected on-chip, the simpler one-step design was used. Sodium nitroprusside was added to methamphetamine in-tube and pipetted into the top inlet (3 µL) and sodium carbonate was pipetted into the bottom inlet (1 µL). Once initial tests were performed, the device design was adapted to account for the two-step reaction with sodium carbonate stored on the device in the detection chamber. Sodium nitroprusside reagent solution was pipetted (1 µL) into the top inlet and sample (3 µL) into the bottom inlet. The two-step spin protocol was performed, opening the laser valve to mix methamphetamine with the reagent in the lower detection chamber for scanner and smartphone image capture.

2.3.3 Threshold Determination for Qualitative Analysis

The results for the reaction of cocaine and cobalt thiocyanate for the initial scan, and final analysis with stored reagents using the scanner and cell phone analysis are given in **Figure 2-6**. These results explore the relationship between cocaine concentration and the magnitude of either hue or saturation, reported as arbitrary units (A.U.) from 0 to 1, derived from dividing hue values by 360° and saturation values by 100%. The hue values for samples containing or devoid of cocaine (respectively, referred to as positive and negative) were not significantly different (**Fig. 2-6A**) for any imaging modality. This was likely due to a small path length of the detection chamber (248 μm).

The subtle variations between hue values made it difficult to define an absolute threshold value indicative of a sample positive for cocaine. Hence, saturation was evaluated using the same images (**Fig. 2-6B**). When the saturation was initially assessed for pipetted reagent onto the device with scanned images for analysis, referred to as 'initial scan' in **Figure 2-6**, the empirically derived limit of detection (LOD) for cocaine was 1 mg/mL. Then, the device was operated with cobalt thiocyanate stored onboard and

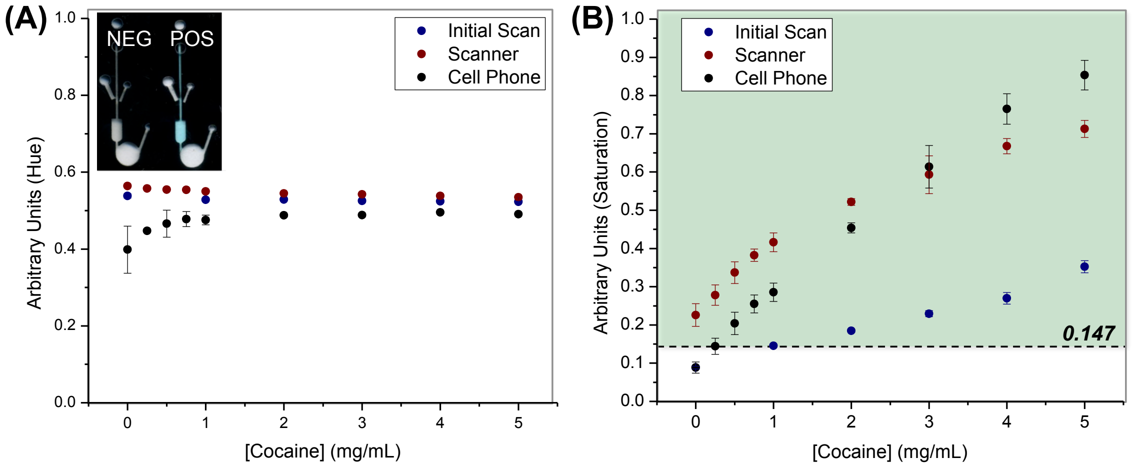

Figure 2-6. Cocaine threshold determination. (**A**) Hue was not adequate to define a threshold for the presence of cocaine due to small hue differences. (**B**) A saturation threshold at 0.147 A.U. was used for determining the presence of cocaine with smartphone analysis and on-board reagent.

the image capture was performed with the desktop scanner and smartphone. The LOD was determined to be 0.50 mg/mL with the scanned images, due to the increased concentration of reagent when the reagent is dried. The lowest LOD was seen with smartphone analysis at 0.25 mg/mL, where each data point represents n = 9 from three separate devices and three replicates of each cocaine concentration for each device. Additionally, the largest dynamic range (0.144−0.853 A.U.) across cocaine concentrations of 0.25 to 5 mg/mL was seen with smartphone analysis using on-board reagent storage.

An additional comparison of the smartphone and standard scanner method was performed, and the values were in good correlation shown through the R^2 and slope values, 0.9805 and 1.599 for saturation and hue results, respectively (**Fig. 2-7**). This gave us confidence that the 5 MP smartphone camera has adequate resolution for image analysis. To further evaluate consistent smartphone results, a lighting condition 20% brighter than ambient lighting was used and compared (**Fig. 2-8**), and these results were in good correlation, shown with the R^2 and slope values, 0.9873 and 0.960 for saturation

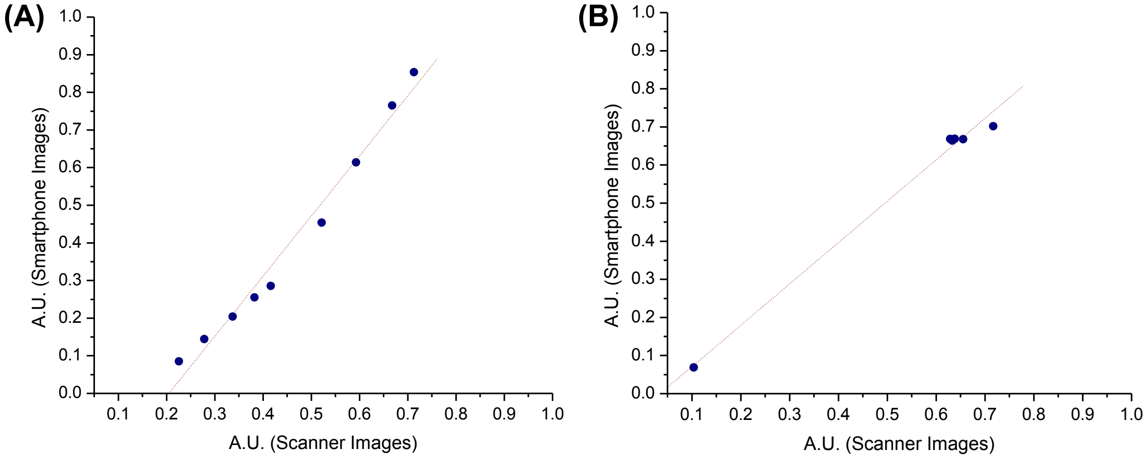

Figure 2-7. Comparison of smartphone and scanner image analysis. (**A**) Comparing smartphone and scanner saturation results for cocaine detection. (**B**) Comparing smartphone and scanner hue results for methamphetamine detection.

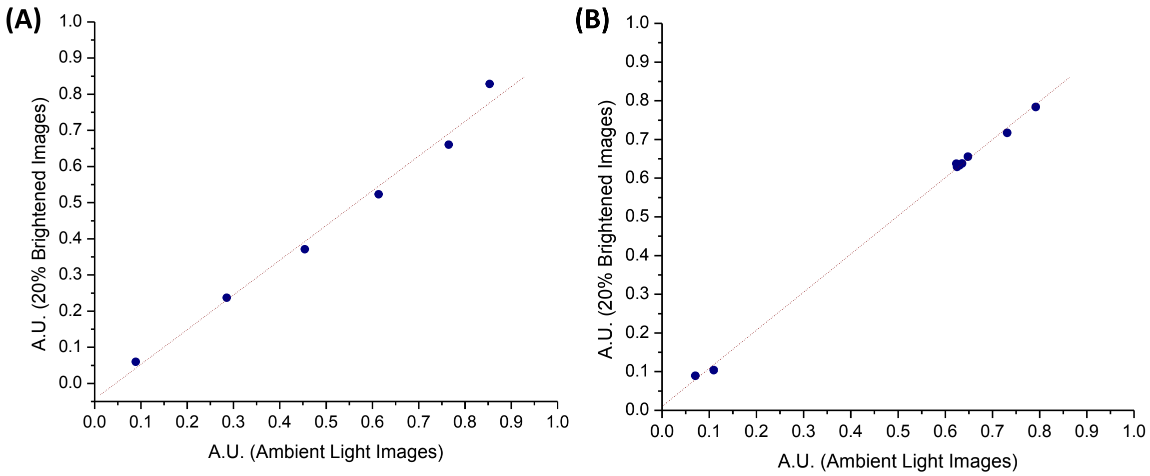

Figure 2-8. Comparison of 20% lightened and ambient-lighted smartphone image analysis. (**A**) Comparison of saturation results for cocaine detection with smartphone for ambient lighted and 20% brightened images. (**B**) Comparison of hue results for methamphetamine detection with smartphone for ambient lighted and 20 % brightened images.

and hue results, respectively. In the future, lighting in this range can be implemented into a final enclosed prototype system.

When considering the operational environment, the common sampling mass collected in the field using a commercial sampling scoop[32] typically results in drug concentrations in the 4– 6 mg/mL concentration range. Drug concentrations from lower than those typically encountered in the field were assessed to provide some insight into drugs that may contain impurities. This could improve current field-testing protocols where equivocal results require further analysis using a larger mass of the seized material and more reagent. A threshold value was defined from the average saturation of 0 mg/mL cocaine plus 3X the standard deviation (+3σ) for 99.7% confidence that cocaine is present. That threshold value was 0.147 A.U. for analysis with the smartphone, and all samples with a saturation value greater than this value were considered positive for cocaine; conversely, samples with saturation values below the threshold were considered negative for cocaine.

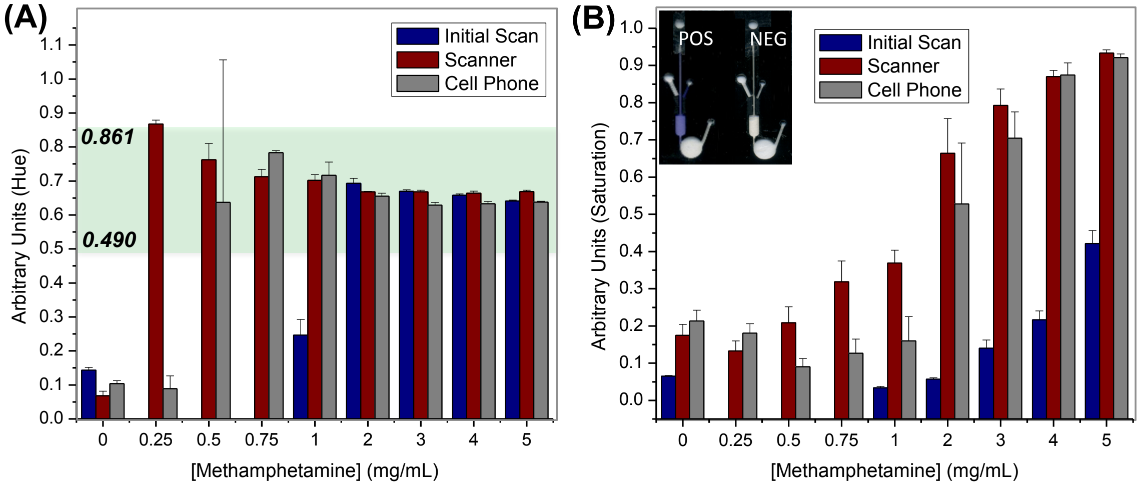

Figure 2-9. Methamphetamine threshold determination. (**A**) Hue was adequate to define a “meth-positive zone” with an upper limit, 0.861 A.U., and lower limit, 0.490 A.U. for smartphone analysis and dry-stored reagents. (**B**) Due to a lower LOD, saturation was not used for drug detection.

This same analytical approach was applied to methamphetamine for reaction with Simon’s colorimetric reagent to define appropriate threshold values. The hue analysis for methamphetamine over a concentration range for each imaging technique is given in **Figure 2-9A**. The initial data from pipetted reagents and scanner analysis (initial scan) demonstrated that hue is an acceptable parameter for judging the presence or absence of methamphetamine. An increased response in hue was observed across concentrations between 2 and 4 mg/mL, with 2 mg/mL determined as the LOD. The device was then operated with sodium carbonate (the second Simon’s reagent) stored on-board and sodium nitroprusside in acetaldehyde (the first Simon’s reagent) pipetted onto the device. The sodium nitroprusside solution was pipetted due to the incompatibility to be stored dry, and future alternatives to dry storage may include commercial blister packs.[33] Image capture was then performed with the desktop scanner and smartphone across three different devices (n = 9 overall). Although both smartphone and scanner analysis with on-board sodium carbonate resulted in lower LODs compared to both reagents pipetted,

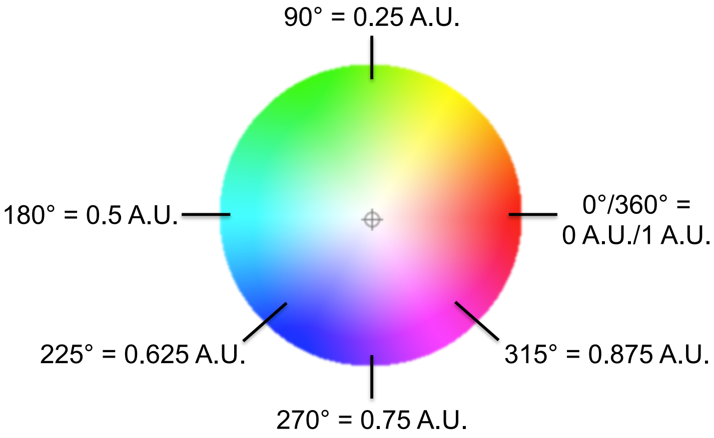

Figure 2-10. Correlating hue values and colors to arbitrary units.

the LOD was lowest for scanned images at 0.25 mg/mL methamphetamine compared to 0.75 mg/mL for smartphone analysis. The large error bar for 0.5 mg/mL with smartphone analysis is due to the reddish-purple color change observed, where 1 and 0 A.U. both represent red using this hue y-axis (**Fig. 2-10**). Analyzing the same images for saturation resulted in higher LODs for methamphetamine detection relative to that obtained with hue analysis across all imaging modalities (**Fig. 2-9B**). At higher concentrations, saturation could be used in combination with hue to further validate the presence of methamphetamine, but hue remains more valuable as a single identification method.

In contrast to cocaine detection, where one saturation threshold value was sufficient for defining cocaine-positive samples, methamphetamine detection required a methamphetamine-positive detection zone (referred to as meth-positive zone). The need for a detection 'zone' rather than a single detection 'threshold' is due to the 360° nature of the hue scale. The expected hue output for methamphetamine is roughly 0.6A.U. (blue-purple color), and unlike saturation, as the hue value increases, the associated color also changes. As hue approaches 1 A.U., the associated color becomes a more intense red color, moving away from the expected color (0.6 A.U.). Simply, a hue value too low or too high would not be indicative of the appropriate color change (**see Fig. 2-10** for an example of this color breakdown). The range of hue values for a meth-positive zone using dried reagent and smartphone analysis was defined by the average hue for concentrations 0.75−5 mg/mL ±3σ, and was determined to be 0.490−0.861 A.U. Additionally, the specificity of this assay for methamphetamine was shown by analyzing amphetamine using the Simon's reagent and observing a "negative" output for methamphetamine (**Fig. 2-11**).

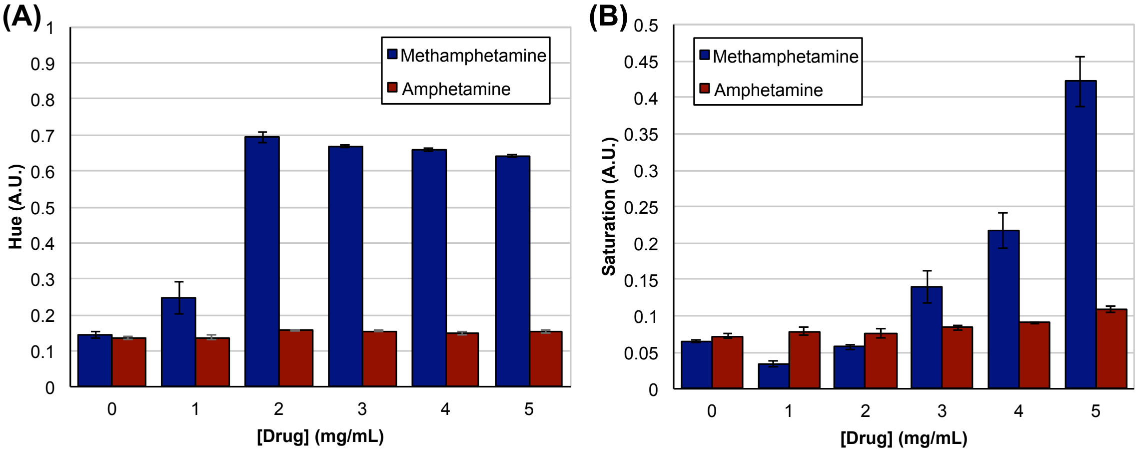

Figure 2-11. Scanner image analysis for methamphetamine and amphetamine with Simon's reagent. (**A**) Hue was adequate to define a 'meth-positive zone' with an upper limit, 0.810 A.U., and lower limit, 0.532 A.U. (**B**) Due to a lower LOD, saturation was not used for drug detection.

2.3.4 Timing for Image Capture and Analysis

There is a temporal component to the development of color for the reaction of methamphetamine with the Simon's reagent making timing of image capture critical (**Fig. 2-12**). In order to define optical postreaction image capture (IC) time, images were captured using standard scanner detection at 3, 6, and 12 min time points after initiation of the Simon's reagent colorimetric reaction at varying methamphetamine concentrations.

The largest impact on color change was seen with hue values at concentrations lower than 1 mg/mL, causing 0.25 and 0.5 mg/mL hue values to fall outside of the meth-positive zone. At 0.5 mg/mL the average hue values were 0.7622, 0.8039, and 0.8551

A.U. at 3, 6, and 12 min, respectively. In contrast, the average hue values at 5 mg/mL were 0.6686 A.U., 0.6812 A.U., and 0.6927 A.U., respectively. At higher concentrations of methamphetamine, the image capture time is shown to be less critical, with smaller changes in hue observed. Each data point was performed with n = 9 over three different devices. As shown in **Figure 2-12**, the most stable hue values were obtained with the shortest IC time (3 min). This is favorable for reducing the operational time and minimizing the effect of drug concentration on color development.

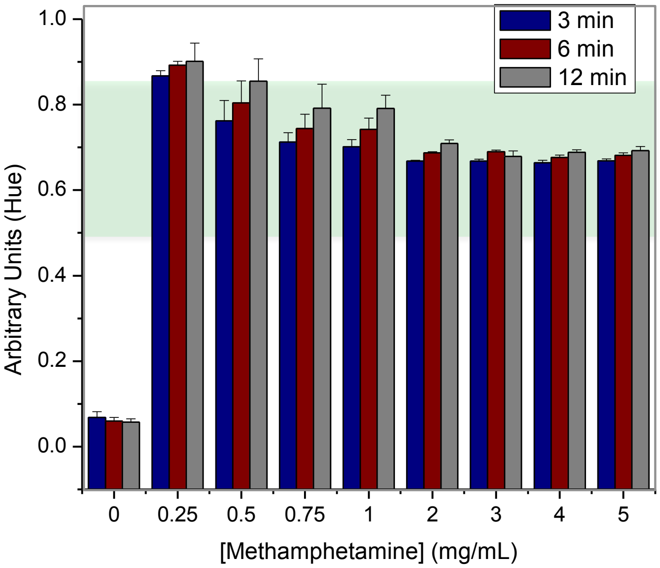

Figure 2-12. Image capture (IC) time assessment for methamphetamine at 3−12 min.

2.3.5 Drug-Cutting Agents as Colorimetric Interferents

Seized illicit drugs are often "cut" with other substances that can include inert compounds or an additional active ingredient. Common cutting agents act as fillers and, for methamphetamine, compounds like starch and dextrose have been reported, while lidocaine, aspirin, and caffeine are often used as adulterants with cocaine.[18, 34] Given this fact, it was critical to evaluate the color change and image analysis of methamphetamine and cocaine after spiking with these common drug additives.

Using the standard scanner approach for initial analysis, methamphetamine, ranging from 1 to 4 mg/mL, was spiked 1:1 with either starch or dextrose (equal w/w for 1−4 mg/mL) and reacted with Simon's reagent for n = 9 across three devices. As conveyed in **Figure 2-13A**, the hue values obtained with methamphetamine in the presence of either additive did not differ significantly from those containing only methamphetamine in the 2−4 mg/mL concentration range, indicating no false negative effect. At 1 mg/mL, the hue values vary around the lower threshold value of this meth-positive zone. Negative controls at 0 mg/mL methamphetamine included no additive (blank) or starch and dextrose at an increased concentration (10 mg/mL) and showed no false positive results. Ultimately, these experiments showed no false positive or negative results for methamphetamine in the presence of these two common additives.

For cocaine, a threshold value was defined for the standard scanner approach from the saturation values obtained from a cocaine blank (0.127 A.U.). The negative controls containing lidocaine and caffeine, individually at 10 mg/mL, resulted in false positives. To alleviate any doubt in the results, a potential second threshold value was assessed by the average saturation for all 0 mg/mL data (0.148 A.U), which included the three additives at 10 mg/mL concentration recorded as 0 mg/mL cocaine. These values (0.127 – 0.148 A.U.) defined the upper and lower limits of a 'threshold zone', or what we define as the 'equivocal zone'; this is shown in yellow in the main plot in **Figure 2-13B**. Cocaine was then spiked 1:1 (w/w for 1−4 mg/mL) with each of the additives (lidocaine, caffeine, or aspirin) individually; for example, the 2 mg/mL cocaine data with lidocaine represents cocaine spiked with lidocaine to yield a final concentration of 2 mg/mL for both the cocaine and lidocaine. Over a concentration range where both are present at 1−4 mg/mL, colorimetric reaction with cobalt thiocyanate was performed and the associated saturation values are given in the main plot in **Figure 2-13B**.

The values increased linearly over the 2−4 mg/mL concentration range, and all values were greater than the upper limit of the equivocal zone. However, all

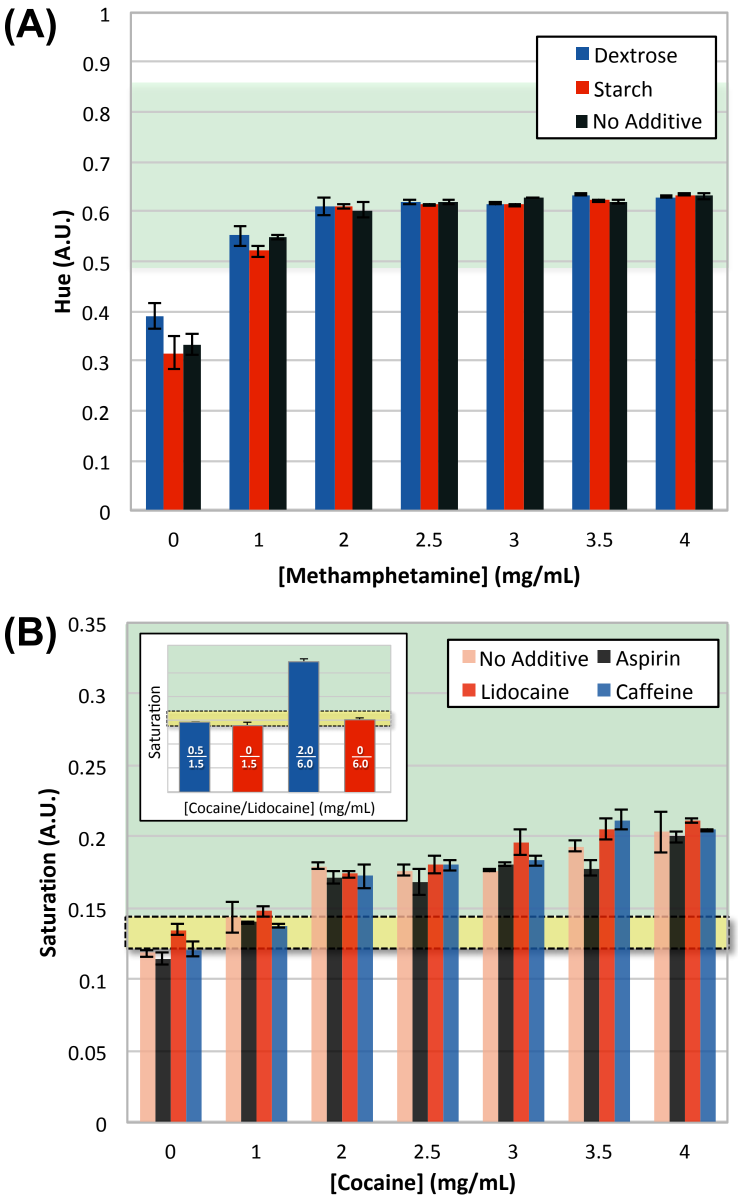

Figure 2-13. Evaluation of drug-cutting agents on analysis. (**A**) Hue values for methamphetamine at various concentrations with additive. (**B**) Saturation values for cocaine concentrations with additive. An 'equivocal zone' (yellow) is used to reveal potential false positive and negative results. Inset demonstrates a 3:1 ratio of lidocaine and cocaine that falls in this equivocal zone. A 4× increase in sample amount, in the same volume, leads to an increased response with cocaine present.

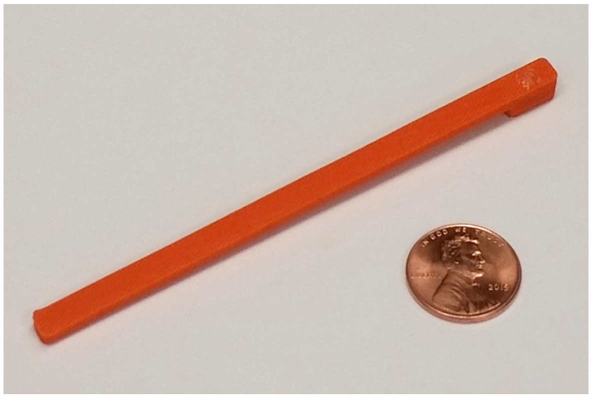

Figure 2-14. Image of 3D-printed sampling scoop.

concentrations of 1 mg/mL cocaine with 1 mg/mL of each additive (individually) produced saturation values that fell squarely in the equivocal zone. This indicates that an unknown substance cut 1:1 with an additive could potentially be read as a false negative. It is for this reason that the "equivocal zone" (as opposed to a single-value threshold) can be critical. If an unknown sample contains cocaine, but the sample analyzed on the RDM is at a low concentration such that the saturation value falls in (not below) the equivocal zone, this could objectively trigger the need for repeat analysis where the mass of unknown substance analyzed was increased by a factor of 2−4X. If cocaine is indeed present, the saturation value obtained with a higher mass of input sample should clear the equivocal zone. This is shown in **Figure 2-13B inset**, with cocaine cut 1:3 with lidocaine, a cutting agent known to produce false positive results.[19] At low concentrations, saturation values are equivocal for the cut cocaine sample and for lidocaine alone (with lidocaine at the same concentration for both samples). However, when 4X the sample mass is used (in the same volume), the saturation value for cocaine cut with lidocaine increases beyond the equivocal zone, while the solution of lidocaine-only remains within the equivocal zone.

To augment results that fall in the equivocal zone and require higher concentrations to define a positive result, a 3D-printed prototype sampling scoop was designed that, when added to 1 mL of ethanol, results in a concentration that would always fall above the equivocal zone (**Fig. 2-14**). This sampling scoop was designed for the final detection device and was initially evaluated for ten separate mass trials using lidocaine, resulting in 8.122 ± 0.001 mg of sample obtained. If the user sampled excess unknown material using the designed scoop, it would lead to concentrations outside of the desired sensitivity range. The methamphetamine sample chambers were designed to hold different sample and reagent volumes (1 and 3 µL) in order to carry out a crude titration of the sample (**Fig. 2-15**). The same-to-reagent ratio for low concentrations was included with the sample-to-reagent ratio for high concentrations. This was used to confirm that the sampling mass would fall within the sensitivity range of the reaction and should eliminate the need to perform replicate analyses using multiple devices.

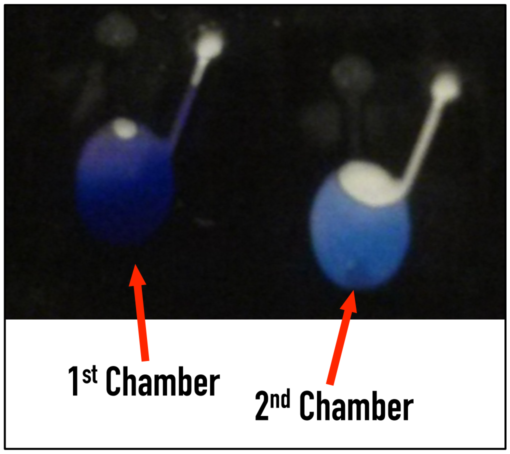

Figure 2-15. Image of microfluidic device to account for both high and low concentrations of methamphetamine. At high concentrations of methamphetamine, the color change was too dark for detection (1st chamber) with the sample-to-reagent ratio determined for 0.75 mg/mL LOD. A dilution chamber was added (2nd chamber) for optimized detection at high concentrations.

2.3.6 Microfluidic Flow Control and Detection of Unknown Samples

A drug detection device was designed where two separate colorimetric reactions could be carried out simultaneously from a single input (**Fig. 2-16**). The core of this device design is the initial threshold device architecture, replicated and connected to incorporate redundancies for increased accuracy. Sodium carbonate was dry-stored in the methamphetamine detection chambers and cobalt thiocyanate was dry-stored in the cocaine reagent chambers, using the same technique as for the threshold determination

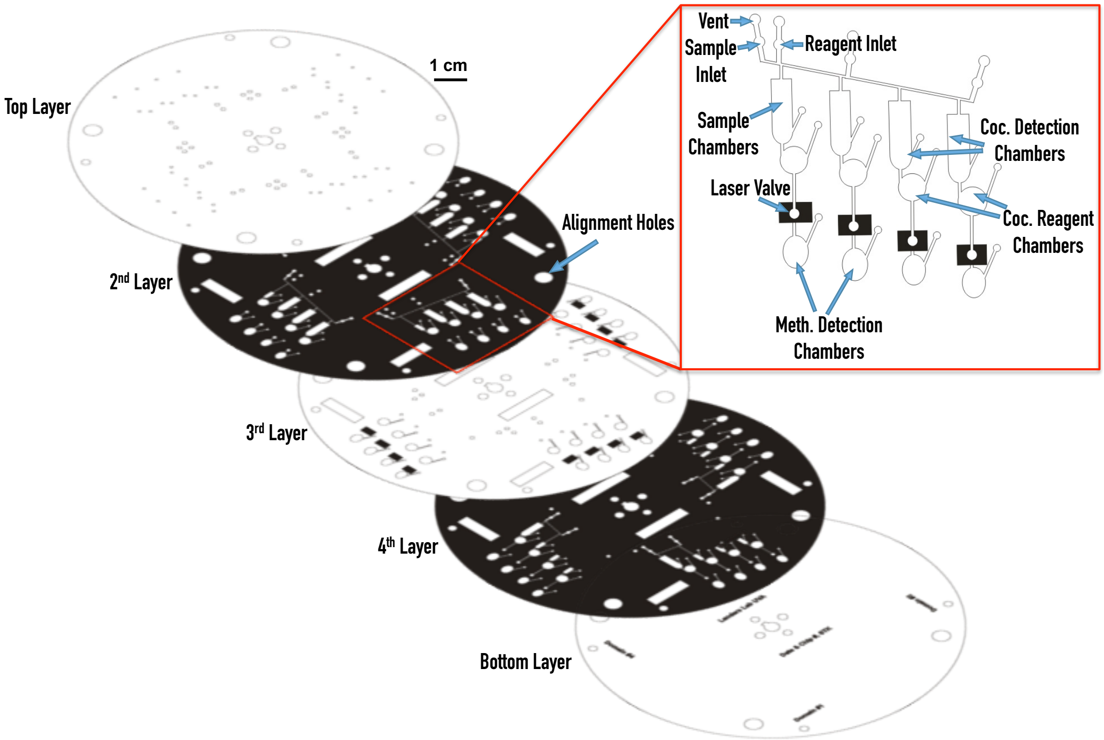

Figure 2-16. Unknown sample device design. Microfluidic device design for drug detection from a single sample input with inset describing methamphetamine and cocaine detection architecture for one domain.

device, providing similar reagent stability as current methods. For use of the device, cocaine detection was a single-step and methamphetamine was a two-step reaction. Implementing a two-step reaction required additional fluidic control to allow the sample to react with each reagent sequentially. As a result, a simple laser valving network utilizing an inexpensive laser pointer was implemented.

For device operation, the sample solution was added to the 'sample inlet' for the top device level (of the two levels obtained using a five-layer device), while the first Simon reagent, sodium nitroprusside in acetaldehyde, was added to the bottom level 'reagent inlet' (**step 1, layer 2 and layer 4, Fig.2-17**). Due to the volatility of this reagent it could not be dry-stored on the device; the architecture inherently allows for this to be addressed by a commercial blister pack[33] in the future. The blister pack would be punctured during the addition of the sample scoop, releasing the first Simon reagent. Once added, the solutions filled the device architecture via capillary action into the sample chambers. The solutions were contained in each sample chamber by utilizing a capillary valve. The device was spun using the reciprocal ‘spin-stop’ mixing protocol. The smartphone application has a generic tab labeled “Hue”, with drop-down options for either “Cocaine” or “Methamphetamine” detection using the predefined threshold values 0.147 and 0.490−0.861 A.U., respectively (**Fig. 2-18**).

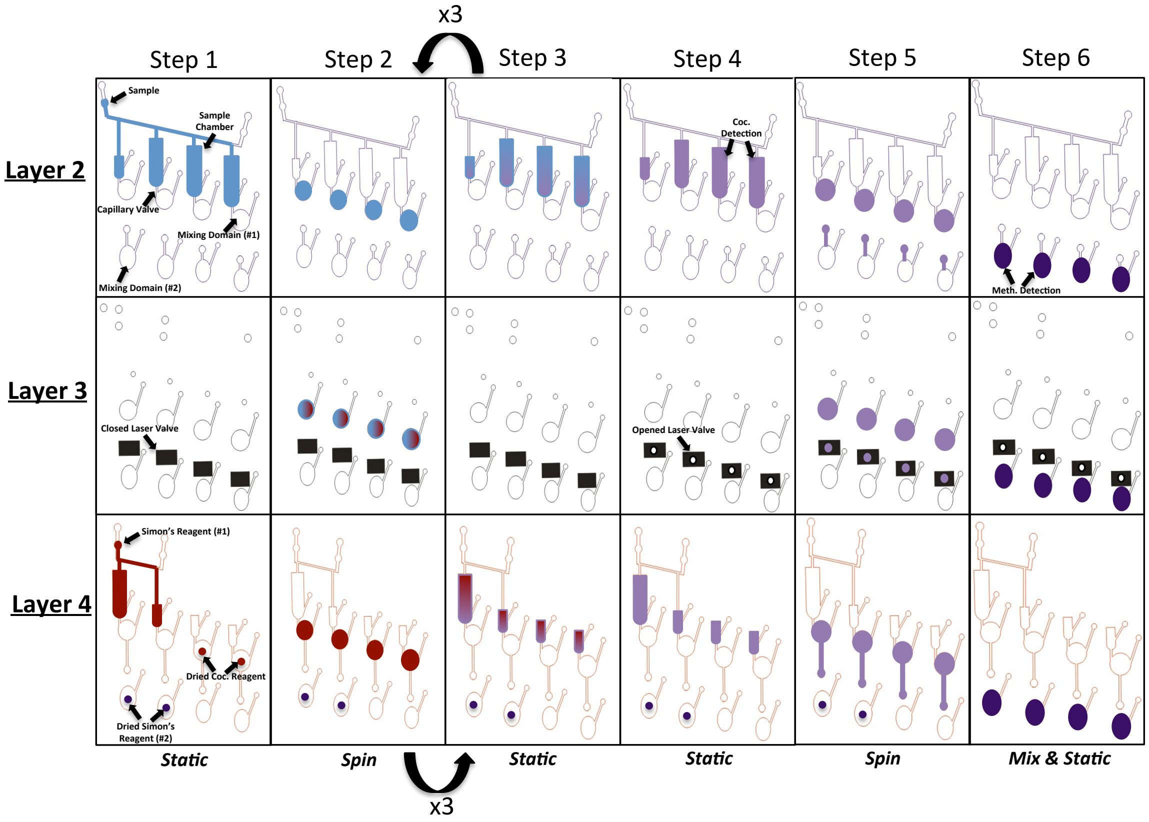

Figure 2-17. Schematic of the step-wise spin protocol for the drug detection device. (**Step 1**) Sample is added to the layer 2 inlet and the first Simon’s reagent is added to the layer 4 inlet. (**Step 2**) The device is spun to allow sample to interact with reagent in the circular chambers. (**Step 3**) The device is stopped to allow the partially mixed sample and reagent to back-fill due to capillary action. Steps 2 and 3 are repeated, alternating between the two steps, to perform the ‘spin-stop’ mixing protocol. (**Step 4**) An image is captured with the cell phone and then the laser valve is opened. (**Step 5**) The device is spun to move all of solution into the bottom circular chambers. (**Step 6**) The device is alternated between spinning and static positions, spinning clockwise and counterclockwise, for agitated mixing of sample with the final Simon’s reagent.

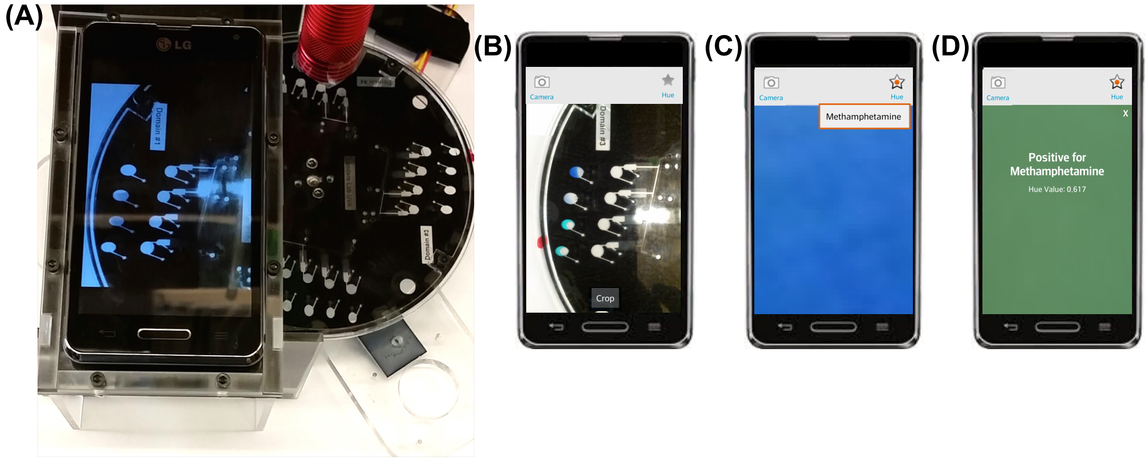

Figure 2-18. Image analysis setup. (**A**) Image of device, spin system with PMMA base, PMMA stand and smartphone for imaging, and laser (in red) positioned above device. (**B**) Image capture of device using smartphone camera. (**C**) Cropped color change analyzed using custom application. (**D**) Results reported qualitatively for a particular drug using defined thresholds, methamphetamine here.

Threshold values provide an effective method for qualitative assessment and, in this case, for detecting cocaine and methamphetamine. To evaluate the RDM and objective analysis technique 30 samples containing methamphetamine, cocaine, both drugs (equal w/w), no drug, and lidocaine or codeine as interferents, were de-identified by a colleague so the analyst had no knowledge of the content prior to, or during, analysis. Each sample was tested (n = 3 devices) and analyzed using the smartphone

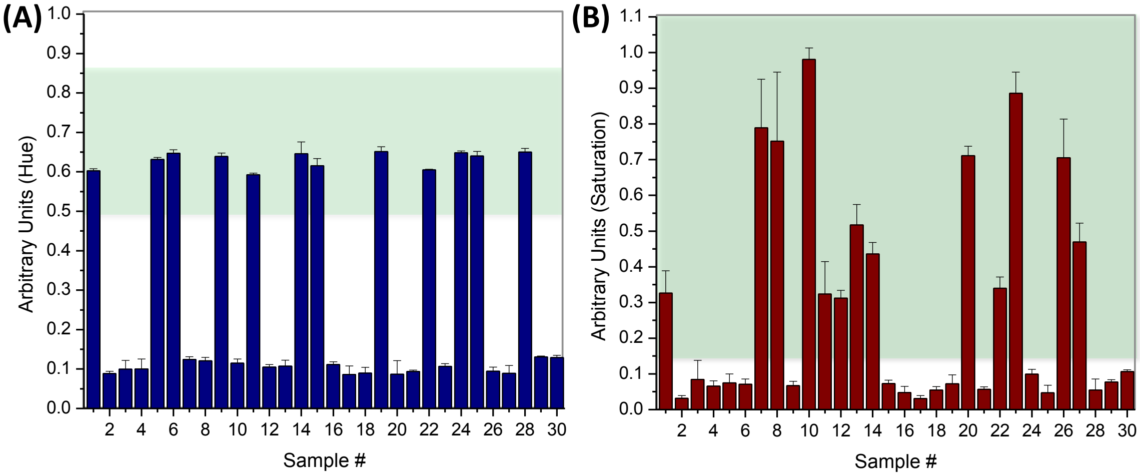

Figure 2-19. Thirty de-identified samples analyzed for methamphetamine and cocaine. (**A**) The hue threshold values predefined for methamphetamine detection were used to assess each methamphetamine detection chamber. (**B**) The saturation threshold values predefined for cocaine detection were used to assess each cocaine detection chamber.

application (**Fig. 2-19**). Based on the predefined thresholds, a 'call' was made for each unknown (**Table 2-1**).

Table 2-1. Unknown sample contents. The 'experimental readout' for 30 unknown samples including the actual composition of each sample and score for the experimental readout given by a colleague.

Unknown Sample	Experimental Readout	Actual Composition	Correct Call?
U1	Cocaine, Methamphetamine	2.5 mg/mL Cocaine; 2.5 mg/mL Meth.	Yes
U2	None	5 mg/mL Lidocaine	Yes
U3	None	Ethanol	Yes
U4	None	5 mg/mL Codeine	Yes
U5	Methamphetamine	5 mg/mL Meth.	Yes
U6	Methamphetamine	10 mg/mL Meth.	Yes
U7	Cocaine	5 mg/mL Cocaine	Yes
U8	Cocaine	10 mg/mL Cocaine	Yes
U9	Methamphetamine	8 mg/mL Meth.	Yes
U10	Cocaine	8 mg/mL Cocaine	Yes
U11	Cocaine, Methamphetamine	5 mg/mL Cocaine; 5 mg/mL Meth.	Yes
U12	Cocaine	1 mg/mL Cocaine	Yes
U13	Cocaine	1 mg/mL Cocaine	Yes
U14	Cocaine, Methamphetamine	1 mg/mL Cocaine; 1 mg/mL Meth.	Yes
U15	Methamphetamine	1 mg/mL Meth.	Yes
U16	None	Ethanol	Yes
U17	None	10 mg/mL Lidocaine	Yes
U18	None	10 mg/mL Codeine	Yes
U19	Methamphetamine	7 mg/mL Meth.	Yes
U20	Cocaine	7 mg/mL Cocaine	Yes
U21	None	Ethanol	Yes
U22	Cocaine, Methamphetamine	6 mg/mL Cocaine; 6 mg/mL Meth.	Yes
U23	Cocaine	6.90 mg/mL Meth.	Yes
U24	Methamphetamine	6.75 mg/mL Cocaine	Yes
U25	Methamphetamine	0.5 mg/mL Meth.; 3.5 mg/mL Caffeine.	Yes
U26	Cocaine	8 mg/mL Cocaine	Yes
U27	Cocaine	6.5 mg/mL Cocaine; 3.5 mg/mL Lidocaine	Yes
U28	Methamphetamine	8 mg/mL Meth.	Yes
U29	None	10 mg/mL Caffeine	Yes
U30	None	10 mg/mL Amphetamine	Yes

All samples were correctly confirmed (scored by a colleague knowledgeable of the contents). Unknown samples U1, U5, U6, U9, U11, U14, U15, U19, U22, U24, U25, and U28 were positive for methamphetamine and U1, U7, U8, U10− 14, U20, U22, U23, U26, and U27 were positive for cocaine. Samples U2, U4, U17, and U18 contained lidocaine and codeine, respectively, and neither were above the positive threshold for cocaine. Saturation was also used to analyze the methamphetamine sample chambers to confirm sample titration occurred. The second detection chamber resulted in a more dilute sample and is shown in the decreased saturation response in **Figure 2-20**.

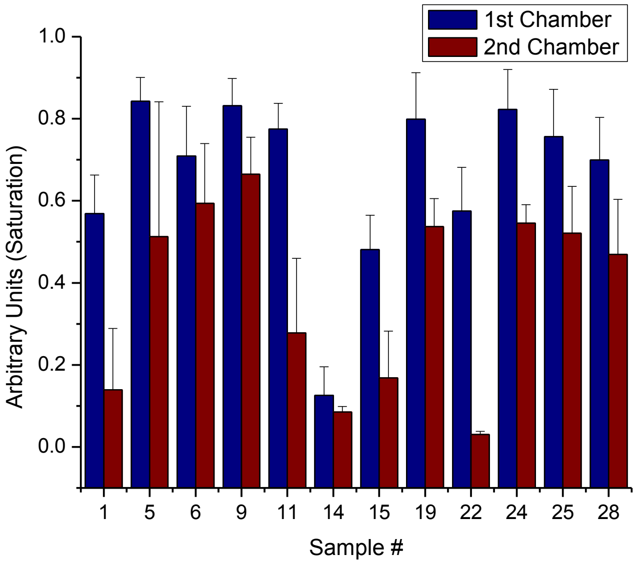

Figure 2-20. Comparing saturation results for redundant methamphetamine detection chambers to confirm sample dilution.

2.4 Conclusions

An enhanced objective detection method for presumptive colorimetric field-testing of illicit drugs was demonstrated that utilizes an image to determine subtle variations in color. The device integrated methods for detection of cocaine and methamphetamine had LODs of 0.25 and 0.75 mg/mL, respectively, when analyzed using a smartphone. Common sampling amounts in the field are 4−6 mg/mL and detection thresholds were determined from analyzing similar and lower concentrations. The defined thresholds were used for cocaine and methamphetamine detection in the presence of common drug-cutting agents. The proposed sampling amount was adjusted and final detection device to account for known false positive and negative results due to additives, an advantageous method compared to subjective on-site methods currently used.

A total of 30 unknown samples were correctly identified for the presence of cocaine and methamphetamine using the drug detection RDM. To date, 565 laser valves have been opened with 100% success. With the total device operation time of ~6 min, this RDM has the potential for a 4-fold reduction in time with a technology that could be compatible with cost-effective mass production in comparison to current tests (depending on the number of pouches used on-site). Overall, smartphone analysis reduced the nine-step scanner procedure to four steps (sample addition, spin protocol, image capture, and analysis). Further advances of this fieldable device will involve a more portable image analysis modality, such as a completely enclosed, 3D printed system with lighting. Also, integration of more detection chambers and reagents will allow for screening of additional illicit drugs, and on-board storage of concentrated acids with polyester-toner devices will need to be addressed.

2.5 References

1. E. L. Izake, *Forensic Science International*, 2010, **202**, 1-8.
2. J. M. E. Chalmers, Howell G. M. and M. D. Hargreaves, *Infrared and Raman Spectroscopy in Forensic Science*, 2012.
3. G. A. Eiceman, Z. Karpas and H. H. Hill, *Ion Mobility Spectrometry*, CRC Press, Third edn., 2016.

4. C. Y. Goh, W. van Bronswijk and C. Priddis, *Applied Spectroscopy*, 2008, **62**, 640-648.
5. J. R. Verkouteren and J. L. Staymates, *Forensic Science International*, 2011, **206**, 190-196.
6. D. Le Roux, B. E. Root, J. A. Hickey, O. N. Scott, A. Tsuei, J. Y. Li, D. J. Saul, L. Chassagne, J. P. Landers and P. de Mazancourt, *Lab on a Chip*, 2014, **14**, 4415-4425.
7. K. M. Horsman, J. M. Bienvenue, K. R. Blasier and J. P. Landers, *Journal of Forensic Sciences*, 2007, **52**, 784-799.
8. J. Wang, *Analytica Chimica Acta*, 2004, **507**, 3-10.
9. D. R. Reyes, D. Iossifidis, P. A. Auroux and A. Manz, *Analytical Chemistry*, 2002, **74**, 2623-2636.
10. D. C. Duffy, H. L. Gillis, J. Lin, N. F. Sheppard and G. J. Kellogg, *Analytical Chemistry*, 1999, **71**, 4669-4678.
11. M. J. Madou and G. J. Kellogg, *Proc. SPIE Systems and Technologies for Clinical Diagnostics and Drug Discovery*, 1998, **3259**, 80-93.
12. R. Gorkin, J. Park, J. Siegrist, M. Amasia, B. S. Lee, J. M. Park, J. Kim, H. Kim, M. Madou and Y. K. Cho, *Lab on a Chip*, 2010, **10**, 1758-1773.
13. J. Neitz and G. H. Jacobs, *Nature*, 1986, **323**, 623-625.
14. J. Neitz, J. Carroll and M. Neitz, *Optics & photonics news*, 2001, **33**, 26-33.
15. G. Jordan and J. D. Mollon, *Vision Research*, 1995, **35**, 613-620.

16. *Recommended methods for the Identification and Analysis of Cocaine in Seized Materials* United Nations Office on Drugs and Crime (UNODC), Vienna, Austria, 2012.
17. S. L. Mikkelsen and K. O. Ash, *Clinical Chemistry*, 1988, **34**, 2333-2336.
18. R. Haddoub, D. Ferry, P. Marsal and O. Siri, *New Journal of Chemistry*, 2011, **35**, 1351-1354.
19. Y. Tsumura, T. Mitome and S. Kimoto, *Forensic Science International*, 2005, **155**, 158-164.
20. E. Al-Hetlani, *Electrophoresis*, 2013, **34**, 1262-1272.
21. S. C. Bell and R. D. Hanes, *Journal of Forensic Sciences*, 2007, **52**, 884-888.
22. B. L. Thompson, Y. Ouyang, G. R. M. Duarte, E. Carrilho, S. T. Krauss and J. P. Landers, *Nature Protocols*, 2015, **10**, 875-886.
23. C. L. do Lago, H. D. T. da Silva, C. A. Neves, J. G. A. Brito-Neto and J. A. F. da Silva, *Analytical Chemistry*, 2003, **75**, 3853-3858.
24. C. L. O'Neal, D. J. Crouch and A. A. Fatah, *Forensic Science International*, 2000, **109**, 189-201.
25. Y. W. Ouyang, J. Y. Li, C. Phaneuf, P. S. Riehl, C. Forest, M. Begley, D. M. Haverstick and J. P. Landers, *Lab on a Chip*, 2016, **16**, 377-387.
26. L. J. Scott, *Microgram*, 1973, **6**, 179-181.
27. F. Feigel and V. Anger, *Spot Tests in Organic Analysis*, Elsevier, Amsterdam, 1966.
28. K.-A. Kovar and M. Laudszun, *Chemistry and Reaction Mechanisms of Rapid Tests*

for Drugs of Abuse and Precursors Chemicals, Vienna, 1989.

29. M. Madou, J. Zoval, G. Y. Jia, H. Kido, J. Kim and N. Kim, in *Annual Review of Biomedical Engineering*, Annual Reviews, Palo Alto, 2006, vol. 8, pp. 601-628.
30. H. Cho, H.-Y. Kim, J. Y. Kang and T. S. Kim, *Journal of Colloid and Interface Science*, 2007, **306**, 379-385.
31. J. L. Garcia-Cordero, D. Kurzbuch, F. Benito-Lopez, D. Diamond, L. P. Lee and A. J. Ricco, *Lab on a Chip*, 2010, **10**, 2680-2687.
32. http://www.safariland.com/, (accessed 8 February 2018).
33. M. Focke, D. Kosse, C. Mueller, H. Reinecke, R. Zengerle and F. von Stetten, *Lab on a Chip*, 2010, **10**, 1365-1386.
34. D. Ciccarone, *Primary Care*, 2011, **38**, 41-58.

3. Reagent Storage Techniques for Polyester-based Microfluidic Devices

3.1 Introduction

Microfluidic devices used in the field, whether for clinical or forensic applications, have been of increasing interest due to the scaled-down size of these devices allowing for rapid analysis, small volumes, and simple operation.[1-4] In order to make microfluidic devices field-deployable for many applications, an automated procedure that can be performed independently of a centralized facility needs to be achieved. Applications for developing countries and limited resource settings exhibit an additional demand for cost-effective devices.[5, 6]

This last characteristic of cost-effective devices is particularly challenging when fabricating microfluidic devices with complex multilevel architectures. Wet etching and photolithography[7], the dominant fabrication methods early on in the development of the microfluidics field, have been supplanted by soft lithography, hot embossing, and injection molding[8], where a reduction in the laborious and time-consuming nature of the fabrication has lowered the cost per device substantially. While 'pour-and-cure' methodologies using a master mold are ideal for mass production, these methods remain costly for device prototyping.

Alternative fabrication protocols for generating inexpensive lab-on-a-chip (LOC) devices have been defined using paper and polyester-based materials.[9] Paper-based analytical devices (µPADs) exploiting the inherent capillary action of paper to drive fluid movement have been explored more extensively.[10-12] While simple in fabrication, fluidic processes such as volume metering, fluid flow control, mixing, sequential reagent addition, and incorporating controls are still being developed. In contrast, microfluidic devices fabricated from polyester film (overhead transparencies) embedded with toner[13], approaches the fabrication simplicity and operation costs that make μPADs attractive. Moreover, these devices circumvent the fluidic control limitations associated with μPADs, retain the ability to exploit capillary action, and can be augmented for more highly-controlled fluidic movement, i.e., centrifugally-driven flow. This allows for a unique melding of the simple laser print, cut and laminate (PCL) fabrication protocol[14] with Lab-on-a-CD[15] systems, for developing field deployable devices.

Several reviews have advocated for centrifugally-driven microdevices with advantages of simplicity, portability and automation.[16-18] A simple motor is used to provide centrifugal force to drive fluid flow, with controllable parameters such as rotation speed, direction, torque, and duration used for additional control.[19] Colorimetric assays are attractive for field-tests where a rapid qualitative readout of color is desired (‘yes/no’ response) or quantitative information is required based on an on-board calibration curve. Both scenarios are well-suited to use of a smartphone for image capture and color analysis, and provides a low-cost and portable detection system for field analysis.[20, 21] A core requirement of microfluidic devices for on-site analysis is effective storage of reagents in a stable form prior to use at the scene. The capability to store multiple reagents on a single device offers additional advantages for multiplexed analysis from a single field sample. This chapter describes the development of three different reagent storage methods that require simple, inexpensive fabrication, complimentary to the PCL fabrication method for use with polyester-based microfluidic devices, that includes inkjet printing reagents, storing reagents within filter paper, and capillary ampule storage.

3.1.1 Printing Reagents

At the core of the PCL fabrication method is the exploitation of printing technology that has been refined over three decades to provide low-volume (pL-nL) dispensing with remarkably accurate spatial resolution (sub-100 µm). The spatial accuracy of inkjet printers has been reported to be less than 30 µm.[22] With the PCL method, printing toner is critical for defining device architecture and aiding in device bonding. The hydrophobic toner printed onto the film acts as a barrier around areas of hydrophilic overhead transparency, absent of toner, to create various device features including channels, inlets, mixing chambers, and air vents. Printed toner is also exploited to create hydrophobic patches within hydrophilic regions to control fluid movement, allowing printed toner of various gray scales to create a passive valving network of different hydrophobicity.[23]

Inkjet printing was first used for complete µPAD fabrication in 2008[24], where patterning paper and reagent deposition was demonstrated; an extensive review on inkjet-printing µPADs has recently been published.[25] The inkjet deposition of reagents onto paper-based devices is not dissimilar to normal printer function (printing onto absorbent paper), and the fact that overhead transparencies specifically made for printing exist suggests that it should be possible to deposit reagents onto a polyester film. The ability to do so opens up new avenues for reagent deposition and storage on polymer microdevices, providing the possibility for the PCL protocol to facilitate the comprehensive fabrication of devices with high architectural complexity and embedded reagents.

The Ohnesorge number (Oh) has been reported expansively as the critical dimensionless parameter for describing inkjet printability, with an Oh number between 0.02 and 1.50 described as optimal printability.[22, 26, 27] In the equation that defines the Ohsenorge number:

$$Oh = \frac{\mu}{\sqrt{\rho d \sigma}} \tag{1}$$

where µ is the viscosity of the printed fluid, ρ is the density of the fluid, d is the diameter of the printer nozzle, and σ is the surface tension of the liquid. An obstacle that is not addressed using the Ohnesorge number equation, is the nature of the substrate onto which reagent is printed. The formation of an 'elongated liquid bridge' between the droplet ejected from the printer nozzle and the substrate is disrupted upon contact with the substrate allowing for deposition.[28] Printing onto paper is a nonissue because the absorbent nature of paper allows for increased tolerance to droplet size, enhancing the ability to disrupt the liquid bridge upon contact. Additionally, the porosity allows the deposited material to be immediately absorbed into the paper to aid in drying, which prevents events such as conjoining or satellite droplet formation and streaking. Polyester film lacks this intrinsic absorbency, leaving the Oh number defined for good printability on paper as non-optimal with a polyester surface that is flat and homogenous; this shifts the printing optimization focus to the substrate. Laserjet printing, more commonly associated with printing onto overhead transparencies, is not viable due to the cost in comparison to inkjet printers when considering cartridge sizes for printing limited reagent volumes or expensive reagents. Additionally, refillable ink cartridges are readily available for inkjet printers.

Here, we report on the incorporation of inkjet printing reagents into the PCL fabrication method, complimentary for mass production and prototyping, to enhance the fabrication of polyester-toner microfluidic devices that remains simple and cost-effective. The ability to store reagents long-term on these devices allows for a complete LOC device, with automated operation, that only requires a single sample input. Once optimization and polyester-film selection was accomplished, the cohesive fabrication for microfluidic devices was achieved for standard colorimetric analysis of human serum albumin.

3.1.2 Paper-based Reagent Storage

Paper-based microfluidic devices have provided a benchmark for simple deposition and inexpensive storage of reagents. When Martinez et al. described the first paper-based device, reagents were spotted and dried at room temperature for a protein and glucose colorimetric bioassay.[29] This was the first of many paper-based devices developed with reagents integrated in this manner[30-32], owing to the very characteristics of paper that allow reagents to be spotted and easily absorbed into a cellulose matrix. The enhanced surface area offered by the woven cellulose fibers facilitates rapid drying of the spotted reagents. In addition, small volumes of reagent can be deposited onto paper, easily allowing the mass delivered to be controlled by the reagent concentration. Similarly, the mass of reagent stored is tuned to the volume of sample used to reconstitute the reagent during the assay procedure. For colorimetric reactions, which have been the most widely used paper-based device assays[10], color intensity can be easily optimized on paper by changing the mass of reagent deposited while color homogeneity can be controlled by selecting a paper matrix with appropriate flow rate and porosity for the desired reaction.

A reagent method of comparable simplicity to paper storage has not been fully defined for centrifugal microfluidic devices where more complex fluidic control can be maintained outside of a capillary-driven paper network. Here, we describe a method for exploiting the advantages of paper for reagent integration and storage within a polymeric microdevice, providing a wider bandwidth for assay development than the ever-developing paper microdevice platform currently offers.[33] For example, aside from pre-concentration, many paper devices do not yet incorporate sample preparation, requiring sample processing to be performed off-chip.[34] The ability to maintain centrifugal fluidic control allows many opportunities for complex device use. Several processes can be performed on centrifugal microdevices for heightened fluidic control, including radial movement, capillary priming, capillary valving, siphoning, metering, splitting, and batch-mode mixing.[17, 35]. Outside of fluidic control, other processes that have been performed on polymeric devices that are not widely used with paper devices include integrating paramagnetic beads[36, 37], sample removal after device use for additional off-chip analyses[38] (comparison or confirmatory), and heating with minimal volume loss to evaporation.[39] Kim et al. describe a fully integrated centrifugal device for performing DNA extraction, amplification, and detection of food-borne pathogens in 30 min, employing an enrichment step using antibody-coated magnetic beads.[40] Another example from Nwankire et al. involves a fully-integrated centrifugal device for a five-parameter liver assay panel from whole blood using colorimetric reactions.[41] These are just two examples from over 300 papers published on centrifugal microdevices[42], and many of these devices could benefit from a simple, paper-based reagent storage method. Godino et al. describe a polymeric centrifugal device that integrated paper utilized as a siphon for fluidic control, but in the later stages of the assay protocol, add colorimetric reagents via pipet for detection.[43]

Here, a centrifugal polyester-paper hybrid microfluidic device is utilized with proof-of-principle colorimetric assays for a wide range of analytes that include total serum protein, serum albumin, an explosive (2,4,6-trinitrotoluene, or TNT), a narcotic (cocaine), and iron. At the core of our hybrid devices is a polyester film-toner device fabricated using the laser *print, cut and laminate* (PCL) technique we have previously described.[14] Device fabrication incorporates inexpensive, commercial materials and instrumentation, and allows for reagent-saturated paper to be readily integrated, in a multiplexed format if desired. This allows for various assays to be performed on a single centrifugal microdevice, cost-effectively, to compliment device development in an academic setting, prototyping, and commercialization.

3.1.3 Liquid Reagent Storage

Liquid reagent storage methods explored as blister packs[44, 45], glass ampules[46, 47], and syringes[48] have been implemented for microfluidic devices. Glass ampules are advantageous due to the vapor barrier and inert properties of glass for long-term reagent storage. Glass ampules are more commonly used as a large-scale format outside of the microfluidic device, where commercial one point cut (OPC) ampules aid in transportation of standards and reagents. The contents are released by locally applying mechanical force to break the ampule. This notion of liquid reagent storage has been briefly explored for small-scale microfluidic platforms for on-board reagent storage. Blister or foil packs utilize flexible sheets of polymer to enclose reagents. These packs can be pierced and deformed to release the contents, similar to blister packages used to access pills in pharmaceuticals. Unlike blister packs and glass ampules, syringes have been utilized within the instrumentation rather than within the microfluidic device to act as a dispensing unit.[48] Dispensing reagents in this manner can increase costs due to additional dispensing instrumentation, introduce cross-contamination from syringe contact with each microfluidic device, and allow for user error from replacing reagents after each device is used.

The implementation of glass ampules and blister packs within microfluidic devices requires small dimensions compatible with the substrates used. Oftentimes, blister packs and ampules are used for storing rehydration buffers to solvate dry sample or dry reagents for point-of-care devices, such as lyophilized enzymes or dried oligonucleotides. Commercial blister packs between 150 µL and 5 mL are available from thinkXXS.[44] Additionally, glass ampules of 50 µL and 100 µL of buffer have been used for reagent storage within centrifugal microfluidic devices for nucleic acid analysis[46] and DNA extraction[47], respectively. These liquid reagent storage options are not ideal for handling low reagent volumes, i.e., 1-10 µL, for performing colorimetric reactions, where additional metering and disposal architecture of excess hazardous reagent would be necessary.

Here, we propose a simple custom glass ampule method for storage of small reagent volumes that is compatible with both concentrated acids and volatile reagents for colorimetric detection of illicit drugs. The Marquis and Simon’s reagents are used as proof-of-principle colorimetric assays that contain sulfuric acid and acetaldehyde reagents. Ampules are fabricated from thin glass capillaries and do not require a thermal sealing method, which can impact the effectiveness of the stored reagents. Glass ampules are stored within polyester-based centrifugal microfluidic devices fabricated using the laser print, cut and laminate (PCL) fabrication method.[14] The simplicity of PCL fabrication and the described glass capillary ampule fabrication method, offers an overall cost-effective device fabrication method using commercial, off-the-shelf materials. Additionally, the small size of the capillary ampules allow for the integration of multiple colorimetric reagents into a single device for enhanced unknown sample screening.

3.2 Materials and Methods

3.2.1 Inkjet Printing Reagents

3.2.1.1 Reagents and Materials

Unless otherwise indicated, all reagents were purchased from Sigma-Aldrich (St. Louis, MO). TRANSNS Copier/Laser transparency sheets were purchased from Film Source, Inc. (Maryland Heights, MO) and Apollo Quick-Dry Universal, 3M CG3489, 3M PP2200, Staples Multipurpose, and HP Premium Inkjet transparency sheets were all purchased from a third party vendor (Amazon.com). Artificial plasma was made using a protocol defined previously.[49] Albumin from human serum lyophilized powder in artificial plasma (pH 7.4) was used for human serum albumin (HSA) standards. A protein-sensitive reagent was prepared by mixing 3.3 mM tetrabromophenol blue (TBPB) purchased from Alfa Aesar (Ward Hill, MA) in ethanol with a citrate buffer solution (pH 1.8) in a 1:1 volume ratio. Similarly, an albumin-sensitive reagent was prepared by mixing 3.3 mM bromocresol green (BCG) in ethanol with citrate buffer (pH 1.8) in a 1:1 ratio.

3.2.1.2 Fabrication of Polyester-Toner Devices

Polyester-toner device fabrication using the laser PCL method has been previously outlined extensively by Thompson et al.[14] The device is made up of alternating polyester and toner-coated polyester layers. The toner-coated layers are made by printing two layers of toner onto both sides of a single transparency sheet. These toner layers define the architecture of the device and also act as an adhesive for bonding during lamination. All device features were laser-ablated using a VersaLASERVLS3.50 system with compatible CAD software. Inlets and air vents were cut into the capping layer, device features were cut out of the fluidic layers (2 and 4), and the middle device layer was used as a via layer for optimal fluidic mixing between all layers. Reagents were printed onto the bottom side of the capping layer and the topside of the bottom layer. The chambers for printed reagents spanned three layers to allow sample access to both printed reagent areas.

3.2.1.3 Inkjet Printer Modifications

Printing was performed using an EPSON R280 printer with modifications described previously.[50, 51] Refillable ink cartridges were purchased through a third-party vendor (inkproducts.com) for modifications in place of the stock EPSON ink cartridges. The refillable ink cartridges were modified using a Dremel® drill to fit a P200 pipette tip. The ink cartridge connector that extends from the bottom of the cartridge to the print nozzle was removed. A hole was then drilled into the front of the ink cartridge above the connector hole, approximately 25 mm tall and 12 mm wide. The ink cartridge embedded chip and plastic support to hold the cartridge together were kept intact to guarantee that the cartridge fits normally into the printer. The end of a P200 pipette tip was cut until the tip fit tightly over the print nozzle to become the new reservoir to hold printing solutions.

3.2.1.4 Print Preparation

The printer was cleaned and conditioned between each device-printing session. To clean the printer, a 12 mL plastic syringe (inkproducts.com) and silicon tubing (5 mm o.d.) were used to drive cleaning solutions through the print head nozzle onto a paper towel placed below the print head. Ethanol, isopropyl alcohol, ethanol, water, and air were sequentially used to flush the print head. Once cleaned, a new P200 pipette tip was cut to fit tightly around the nozzle over the print head, acting as a reservoir to hold the reagent solution. Reagent was added to the reservoir and a P200 pipette was placed on the pipette tip reservoir to push reagent through the print head nozzle onto a paper towel for conditioning. The printing reservoir was filled again with 150 μL of reagent for printing. Ink cartridges were returned to the appropriate printer compartment and situated into the ‘home position’ to lock in place. No error messages were confirmed when the printer was turned on before printing reagents.

3.2.1.5 Polyester Layer Preparation

A compact disc (CD) was placed in the printing tray designated for CD labels. P5 filter paper (11 cm diameter) purchased from Fisher Scientific (Pittsburg, PA) was taped on top of the CD. Dye solution was printed onto the filter paper using the EPSON Print CD software. The printed dye regions were used to align the pre-cut polyester capping and bottom device layers for printing. Different ink cartridges were chosen (e.g. black and cyan) to print two different reagents simultaneously, when necessary. The designed printing regions in the EPSON Print CD Software were coordinated with each ink cartridge for cyan (0 red, 0 green, and 255 blue) and black (0 red, 0 green, 0 blue).

3.2.1.6 Examination of Printing onto Different Polyester Films

A reagent-mimic solution of ethanol and citrate buffer (pH 1.8) in a 1:1 volume ratio with added green dye was prepared for printing. The solution was printed ten successive times onto a TRANSNS transparency film layer and an Apollo Quick-Dry Universal transparency film layer simultaneously. Bright field microscopy at 4X magnification was used to image the interface of each printed spot with the substrate surface. Characterization of the substrate surface was performed using a Zygo® Newview™ 7200/7300 Optical Profilometer (Middlefield, CT). MountainsMap® (Digital Surf), WSxM and Matlab were used for image processing.

3.2.1.7 Microfluidic Device Stability

Three replicate chambers, on three devices (n = 9), were tested at each time point. Devices were stored at room temperature in a dark area until analysis. Standard 50 mg/mL HSA aliquots were stored at -20°C until analysis on day 1, immediately after device fabrication, and at weeks 1, 2, 3, 4, and 8.

3.2.1.8 Centrifugal Spin Protocol and Microdevice Control

The device spin system consisted of a Sanyo Denki Sanmotion series stepper motor controlled by a Pololu DRV8825 stepper motor driver in full step mode. The motor was mounted on a custom made 3-arm support structure cut from poly(methyl methacrylate) to immobilize the motor during rotation. Motion control profiles were generated using a Parallax Propeller microcontroller, programmed in the native programming language. A printed circuit board was designed using EAGLE CAD software. The device spin protocol after sample addition for reciprocal mixing[52] was as follows: spin 1000 RPM with 50 angular acceleration (AA) for 10 s, 1000 RPM, three replicates, for 10 s (500 AA), 1000 RPM for 20 s (500 AA), and 1000 RPM for 20 s (1000 AA).

3.2.1.9 Colorimetric Detection with Printed Devices

To monitor the colorimetric reactions, devices were scanned using an EPSON Perfection V100 Scanner with 1200 dpi resolution. The scanned images were saved as TIFF files for further analysis using a Mathematica algorithm, in terms of hue and saturation.

3.2.2 Paper-hybrid Devices

3.2.2.1 Reagents

Bromocresol green (BCG), albumin from human serum lyophilized powder, cobalt thiocyanate, tetramethylammonium hydroxide, hydroxylamine, 1,10-phenanthroline, iron (III) chloride, ethanol, tartrazine dye, sodium hydroxide, acetic acid, and hydrochloric acid were all purchased from Sigma-Aldrich (St. Louis, MO). Cocaine and 2,4,6-trinitrotoluene (TNT) standard solutions (1.0 mg/mL) were purchased from Cerilliant (Round Rock, TX). Tetrabromophenol blue (TBPB) was purchased from Alfa Aesar (Ward Hill, MA).

3.2.2.2 Preparation of Reagents and Standards

A protein-sensitive reagent was prepared by mixing 3.3 mM TBPB in ethanol with citrate buffer solution (pH 1.8) in a 1:1 volume ratio. Similarly, an albumin-sensitive reagent was prepared by mixing 3.3 mM BCG in ethanol with citrate buffer (pH 1.8) in a 1:1 ratio. Cobalt thiocyanate reagent was prepared in 10% acetic acid to make a 20 g/L solution. Tetramethylammonium hydroxide reagent was used as is. Hydroxylamine and 1,10-phenanthroline reagents were prepared separately in acetate buffer, 8 mg/mL and 0.1 g/mL respectively, using a protocol described previously.[53]

Albumin from human serum lyophilized powder in artificial plasma (pH 7.4) was used for human serum albumin (HSA) standards. Artificial plasma was made using a method defined previously.[49] Upon addition of HSA, TBPB changes from yellow to blue depending on protein concentration. Similarly, BCG changes from yellow to green depending on the HSA albumin content. Purchased standard solutions of cocaine and TNT were used as is. Iron (III) chloride was prepared in a 10 mg/mL aqueous solution.

3.2.2.3 Hybrid Device Fabrication

Devices were fabricated from TRANSNS Copier/Laser transparency sheets purchased from Film Source, Inc. (Maryland Heights, MO), with five alternating layers of uncoated (lays 1, 3, and 5) and toner-coated sheets (layers 2, and 4). For the toner-coated sheets, two layers of black toner were printed onto each side of the sheet. The toner acts as an adhesive when heated during device bonding.

Reagents were added to Whatman filter papers in 5 µL increments. The first reagent spot was allowed to dry for 10 min and then a sequential reagent spot was added. Once dried, reagents were either punched out using a 2 mm Acu-Punch disposable biopsy punch (Acuderm, Fort Lauderdale, FL) or laser cut using a VersaLASERVLS3.50 system (Scottsdale, AZ) with compatible CAD software. Device layers 2-5 were combined, and then the reagent punches were added to the corresponding reagent chambers. Layer 1 was combined, enclosing the reagent punches, and laminated at >160 °C.

3.2.2.4 Spin System

A Sanyo Denki Sanmotion series stepper motor controlled by a Pololu DRV8825 stepper motor driver in full step mode was utilized for the spin system. Motion control profiles were generated using a Parallax Propeller microcontroller and a printed circuit board was designed with EAGLE CAD software containing the microcontroller, motor drivers, and associated components for power regulation, heat sinking, and serial communication with an external computer terminal. A poly(methyl methacrylate) (PMMA) custom support structure immobilized the motor during rotation.

3.2.2.5 Image Analysis

After each completed spin procedure, the reaction chambers within each device were imaged using an Android smartphone or an EPSON Perfection V100 Photo Scanner with 1200 dpi resolution. Images were taken at 5 cm above the microdevice for consistent image capture with the smartphone. Scanned images were saved as TIFF files and smartphone images were taken 5 cm above the microdevice for consistent image capture. Color changes in the device detection windows of each image were cropped using ImageJ. The cropped images were then analyzed to determine color hue and saturation (HSB color model) as image analysis parameters, using a Mathematica algorithm. The hue and saturation values were both reported as arbitrary units (A.U.) by dividing the hue results by 360° and the saturation results by 100%.

3.2.3 Capillary Ampules

3.2.3.1 Reagents

Cocaine, codeine, heroin, methamphetamine, 3,4-methylenedioxymethamphetamine (MDMA) and 3,4-methylenedioxyamphetamine (MDA) standard solutions were purchased from Cerilliant (Round Rock, TX). Sulfuric acid, formaldehyde, sodium carbonate, and methanol were purchased from Fisher Scientific (Waltham, MA). Acetaldehyde, sodium bicarbonate, and cobalt (II) thiocyanate were purchased from Sigma-Aldrich (St. Louis, MO). Sodium nitroprusside dihydrate was purchased from MP Biomedicals (Santa Ana, CA). All solutions were prepared in Nanopure™ water (Barnstead/Thermolyne, Dubuque, IA).

3.2.3.2 Preparation of Drug Samples and Reagents

Purchased drug standards were concentrated in an Eppendorf Vacufuge 5301 (Westbury, NY) when necessary. Methanol was used as the solvent for dilutions.

Simon's reagent was prepared by dissolving 0.1 g sodium nitroprusside in 10% acetaldehyde (v/v, acetaldehyde:water) for solution A, and dissolving 0.2 g sodium carbonate in 10 mL H_2O for solution B.[54] Solution A and B were used sequentially. Modified cobalt thiocyanate reagent was prepared by dissolving 2.0 g cobalt (II) thiocyanate in a 10% acetic acid solution (v/v, acetic acid:water).[55, 56] Marquis reagent was prepared by carefully adding 10 mL concentrated sulphuric acid and 0.5 mL of 37% formaldehyde (v/v, formaldehyde/water).[57]

3.2.3.3 Fabrication of Custom Capillary Ampules

Capillary tubes, 1.5-1.8 mm diameter, were cut to the desired length using a diamond tip glass cutter tool. PTFE thread seal tape (manufactured to MIL Spec T27730A) or QUIK-CURE™ 5 min epoxy (Bob Smith Industries) was used to seal the ends of cut capillary segments.

3.2.3.4 Fabrication of Centrifugal Microfluidic Devices

Devices were fabricated using the print, cut and laminate (PCL) protocol previously described in detail.[14] Using the PCL method, device layers were fabricated using TransNS Copier/Laser transparency sheets (Film Source, Inc., Maryland Heights, MO) and heat-sensitive adhesive (EL7970-39, Adhesives Research, Glen Rock, PA) was used in place of toner to bond the layers of the device together. Five-layer device designs consisting of alternating layers of uncoated (layers 1,3, and 5) and adhesive-coated transparency sheets (layers 2, and 4) were used as the core centrifugal device for studies with dye, Simon's reagent, and Marquis reagent. This five-layer core device format was adapted for the neutralization studies by implementing a toner-coated transparency sheet for layer 3. This toner-coated layer (printed black toner using HP LaserJet 4000 printer) was used for additional fluidic control through laser valving as described previously[58, 59], whereby energy from a short pulse of a red laser (2 s) is absorbed by a patch of toner to provide a simple mechanism for opening a path for fluid flow.

All device architecture was designed in CorelDraw software (Coreldraw V9). A CO_2 laser system (VLS3.50, Universal® Laser Systems, Scottsdale, AZ, USA) was used to laser ablate the microfluidic architecture into each device layer. Cut device layers were combined and laminated at >160 °C for device bonding. Chambers within the device for containing capillary ampules were cut to be exposed (open chambers). To accommodate the custom capillary ampules, 0.8 mm poly(methy methacrylate) (PMMA) sections were adhered to the core polyester-based centrifugal device for both device formats, five-layer with and without toner-coated layer 3. PMMA chambers were laser cut and adhered to the microfluidic device using pressure-sensitive adhesive. Once the capillary ampule was placed in the PMMA reinforced chamber, another layer of pressure-sensitive adhesive with a transparency sheet cover layer were used to enclose the ampule. For neutralization studies, an additional 1.5 mm PMMA section was incorporated for added depth to the sodium bicarbonate chamber.

3.2.3.5 Spin System

The rotation system was composed of a FAULHABER Coreless Technology series 2232_SR motor controlled by a Pololu DRV8801 Single Brushed DC Motor Driver Carrier and aligned by a TT Electronics wide gap slotted optical switch. The laser system was composed of a Thorlabs 638nm red laser diode, a Thorlabs LT230260P-B laser diode focusing tube, a Thorlabs SR9F electrostatic discharge (ESD) protection and strain relief cable, a Thorlabs MTS50-Z8 motorized translation stage, and two Wavelength Electronics FL500 laser diode drivers. The lighting system was composed of a RadioShack three-light emitting diode (LED) Waterproof Flexi Strip. A custom PMMA support structure and spin system enclosure immobilized the motor during rotation and permitted consistent imaging.

The custom-made printed circuit boards (PBCs) were designed in Easily Applicable Graphical Layout Editor (EAGLE) and were comprised of the multicore microcontroller, motor drivers, laser diode drivers, N-Channel metal-oxide-semiconductor field-effect transistors (MOSFETs), high efficiency linear voltage regulators, and various passive electronic components and connectors. Control of the multipurpose microfluidic spin system was accomplished through the Parallax Serial Terminal (PST) program running on a Microsoft Windows based personal computer that was connected to the Parallax Propeller multicore microcontroller by a universal serial bus (USB) cable. The PST allowed the user to manually control all aspects of the system.

3.2.3.6 Image Analysis

After each completed spin procedure, the reaction chambers within each device were imaged using an Android smartphone or an EPSON Perfection V100 Photo Scanner with 1200 dpi resolution. Images were taken at 5 cm above the microdevice for consistent image capture with the smartphone. Color changes in the device detection chambers of each image were cropped using ImageJ. The cropped images were then analyzed to determine the hue (HSB color model), using either ImageJ or a Mathematica algorithm. The hue values were reported as arbitrary units (A.U.).

3.3 Results and Discussion

3.3.1 Inkjet Printing Reagents for Storage with Polyester-Toner Devices

An obvious addition to the PCL fabrication method was to define a print-based delivery and reagent storage method. This was accomplished using an inkjet printer, modified for printing reagents instead of toner, to carry out automated spatial patterning of multiple reagents onto polyester layers. This method has the potential to springboard device advancement towards fully integrated systems by the addition of a single fabrication step at a minimal cost.

3.3.1.1 Initial Printing Attempts

Since inkjet printing of reagents had been successfully applied to paper-based microfluidic devices[63, 64] and agarose media,[22, 50, 65] an obvious discriminator between those substrates and the polyester films used for microfluidic devices described here was the porosity of the substrate. Meanwhile, the nature of the surface onto which the droplet is ejected does not factor into the equation for the Ohnesorge number, requiring a new approach for increasing reagent printability. Commonly, polyester-toner microdevices have been fabricated using smooth, dual-purpose transparency films,[13, 14, 66, 67] i.e., TRANSNS Copier/Laser transparency sheets (Film Source). Initial attempts to print directly onto the smooth TRANSNS transparency film were unsuccessful due to the non-absorbent characteristic of the film. Initiating the printing process onto paper and transitioning the print onto the transparency by overlaying the transparency film onto the printed paper circumvented this limitation and once a print stream was created using paper, it was maintained when moved onto transparency (**Fig. 3-1**). This methodology could not be used moving forward, because it made printing more complex device designs difficult. Patterning onto paper between each printing event wasted valuable reagents and increased device fabrication time. Additionally, this method limited the device layer designs, requiring reagent-patterning spots to be positioned for intermittent printing onto the alignment filter around the transparency film.

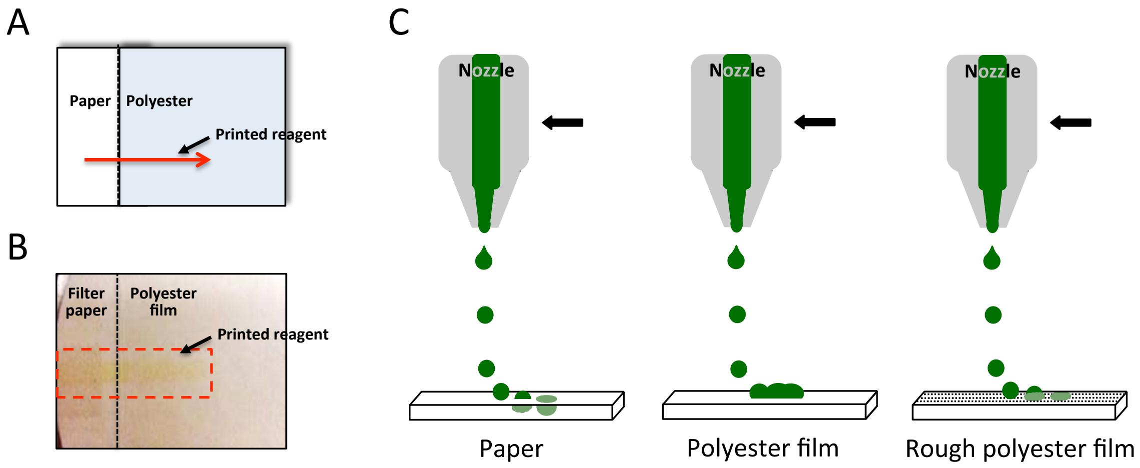

Figure 3-1. Inkjet printing droplets onto various substrate material. (**A**) Diagram describing initial attempts of printing reagent onto polyester film by overlapping with paper, starting the print stream on paper to maintain printing onto polyester. (**B**) Actual image of printed TBPB reagent (yellow) onto polyester film using paper to initiate printing. (**C**) Schematic demonstrating droplet interactions with different microdevice material during inkjet printing. Droplets are absorbed into the porous cellulose-based substrate (paper) and dry. Non-porous polyester film does not absorb the printed droplets causing multiple droplets to combine on the surface and no drying occurs. Inkjet polyester film with a rough surface allows more surface area for the printed droplet to interact with and dry onto the surface.

Secondary attempts to print directly onto transparency films involved the addition of additives to the reagent matrix. The Ohnesorge number (**Equation 1**) was used to predict printability of solutions, defining good printability as a ratio of reagent properties and inkjet print head diameter.[60, 61] Various additives were used following the Ohnesorge parameters, including polyethylene glycol and glycerol to increase solution density and viscosity, and surfactants to decrease surface tension. If the viscosity of the solution was too high, the force generated by the piezo was insufficient to eject the droplet and make contact with the substrate, thus causing the droplet to retract into the print nozzle and dry.[62] Once the droplet dried, this became a common source for clogging of the print head and would require substantial syringe pressure and cleaning to dislodge the dried print solution. When the concentration of surfactant was in excess, adjacent droplets would combine and result in a droplet that was too large to dry onto the printing surface (**Fig. 3-1**). Although some success resulted from using additives incorporated into the reagent solution, overall printing was inconsistent and, frequently, the printer nozzle would become clogged.

3.3.1.2 Optimization for Various Print Solutions and Polyester Films

Plasma surface treatment for polymeric films has been reported to increase the surface energy for patterning inks[68], but techniques were avoided that would increase the complexity and time for device fabrication, leading to employment of commercial inkjet-compatible transparencies with a rough surface. The enhanced surface area and energetic interaction provided by the roughness was considerably more effective at disrupting the liquid bridge for droplet deposition. Additionally, the trapped droplets within cavities from the roughness

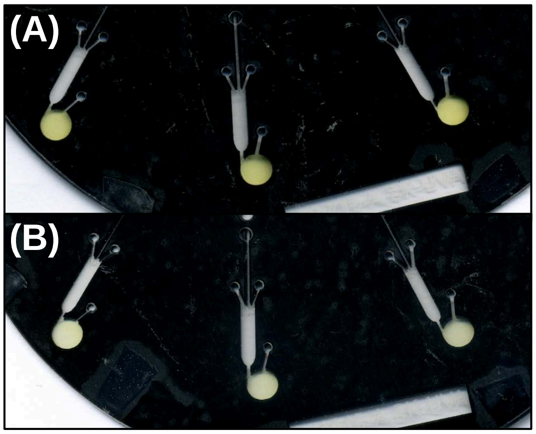

Figure 3-2. A commercial inkjet-compatible transparency with a rough surface was employed for printing TBPB indicator onto multiple devices. Printed devices resulted in dark (**A**) and light (**B**) colored printed regions through visual examination.

dried more rapidly in comparison to the larger droplets, formed by adjoining individual droplets, onto the TRANSNS film (**Fig. 3-1**).

Table 3-1. Hue and saturation analysis results for the five devices printed with TBPB and categorized as light and dark colored prints.

Number of Devices	Number of Print Cycles	Visual Print Appearance	Hue	Saturation
3	5	Light	0.521 ± 0.007	0.235 ± 0.007
2	5	Dark	0.516 ± 0.002	0.386 ± 0.054

Strictly moving to an inkjet-compatible transparency with a rough surface was not sufficient for obtaining consistent printing. Five separate devices were each printed with TBPB indicator to visualize differences in printing allowed by the yellow colored TBPB solution. While each device had consistent printing for the replicate chambers (n = 3 for each device), inconsistencies with printing were observed amongst the five different devices. Through visual examination, the five devices could be divided into either a light yellow or dark yellow printing result (**Fig. 3-2**). Color analysis was performed using hue and saturation from the HSB color model to evaluate the differences in printing between the light and dark printed device (**Table 3-1**). Each device was printed with five print cycles of TBPB and resulted in similar hue values for both light and dark printed devices as the shade of color for the printed indicator did not differ. Comparing the saturation analysis between the light and dark printed devices best demonstrates the variation in printing, as saturation analysis is sensitive to the amount of printed solution deposited onto the film. A number of variables relating to printer preparation needed to be optimized. To generate consistent printing, it was critical to clean and condition the printer between each device printing session using pressure and solvent to assure no clogging of the print head.

The printability of solutions containing water, detergent and buffer, commonly used in biological assays, was assessed with different commercial inkjet transparency films with rough and smooth surfaces denoted, including TRANSNS (smooth), Apollo Quick-Dry Universal, (rough), 3M CG3480 (rough), HP Premium (rough), Staples® Multipurpose (Rough), and 3M PP2200 (smooth). A qualitative assessment of 'printability' was defined by a '0', '0.5' or '1' designation, where '0' represented failed printing and '1' for effective printing. With an assessment of '1', the film was no longer optically transparent at the spot of printing (**Table 3-2**). For '0.5', the film seemed transparent under direct light, as the printed spot was only visible under specific lighting conditions, i.e. rotating the film at various angles. Each of these results was significantly different from an assessment of '0' where there was no indication of reagent printed on the transparency. Each individual solution was printed in three different locations on

Table 3-2. Printing various biologically relevant solutions onto different commercial transparency films to determine optimal printing parameters. Along the top row for each film, contact angles of each solution measured on the surface of the film are given. Along the bottom row for each film, the print quality was assessed using 0, 0.5, and 1 as a qualitative method to report when the solutions did not print, faintly printed, or printed well.

Commercial Transparency Films	Water	Tween 20 (%Vol/vol)				TBPB	Citric acid Buffer	Dye
		0.1 %	0.3 %	2.00 %	10.00 %			
TRANS-NS (smooth)	67° ± 1.0	47° ± 0.2	46° ± 1.5	41° ± 0.2	40° ± 1.3	72° ± 0.9	32° ± 1.0	38° ± 1.2
	0	0	0	0.5	0.5	0	0.5	0.5
Apollo Universal (rough)	43° ± 0.1	24° ± 0.3	26° ± 0.3	28° ± 0.1	27° ± 0.3	32° ± 0.2	13° ± 2.0	18° ± 0.3
	0	0.5	0.5	1	1	0	1	1
3M CG3480 (rough)	75° ± 3.8	48° ± 0.9	49° ± 0.2	47° ± 0.4	49° ± 1.0	79° ± 0.5	31° ± 2.0	35° ± 4.3
	0	0	0	0.5	1	0	1	1
HP Premium (rough)	Surface coating is water soluble							
	0.5	0	1	1	0.5	0.5	1	1
Multipurpose Transparency film (rough)	44° ± 1.0	26° ± 0.2	19° ± 1.5	19° ± 0.6	19° ± 0.5	46° ± 2.2	10° ± 4.1	11° ± 0.3
	0.5	0.5	0.5	0.5	0.5	0.5	1	1
3M PP2200 (smooth)	43° ± 1.3	32° ± 0.5	24° ± 0.6	21° ± 1.0	23° ± 0.2	14° ± 0.4	38° ± 1.0	13° ± 1.4
	0	0	0	0.5	0.5	0	0.5	1

three separate device layers for n = 9. Additionally, three separate droplets were used to measure contact angles of each solution used to assess printability. One obvious influence on droplet formation is the surface tension of the fluids involved; high surface tension leads to a higher resistance in droplet formation at the print nozzle exit.[69] Printing fails when the droplet jetted from the nozzle exit fails to detach effectively. Unfortunately, measuring the wetting angle of the fluids on the print nozzle exit surface is extremely difficult, and even if the precise composition of the nozzle exit is known, processing conditions can significantly affect wettability. The data in **Table 3-2** suggests a trend where fluids with low surface tension generally print better. This trend is inferred by low wetting angles across a variety of thermoplastic surfaces, and is used as a proxy for wetting of the print nozzle material. This is illustrated, for example, in the comparison of a color dye and TBPB versus water and low concentrations of Tween 20, with the only significant deviation from this trend being PP2200.

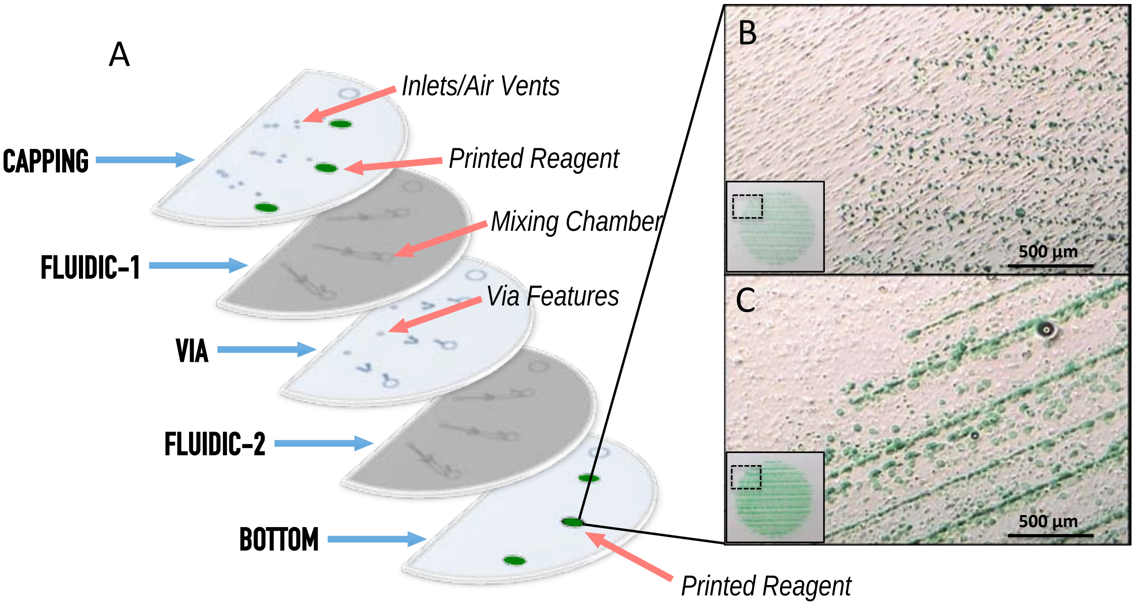

Figure 3-3. (**A**) Schematic of a 5-layer mixing device describing the role of each polyester and toner-coated polyester layer, with top and bottom layers for printed reagents. Bright field microscopy image (4X magnification) of a reagent spot printed ten times on (**B**) TRANSNS smooth and (**C**) Universal Apollo inkjet films.

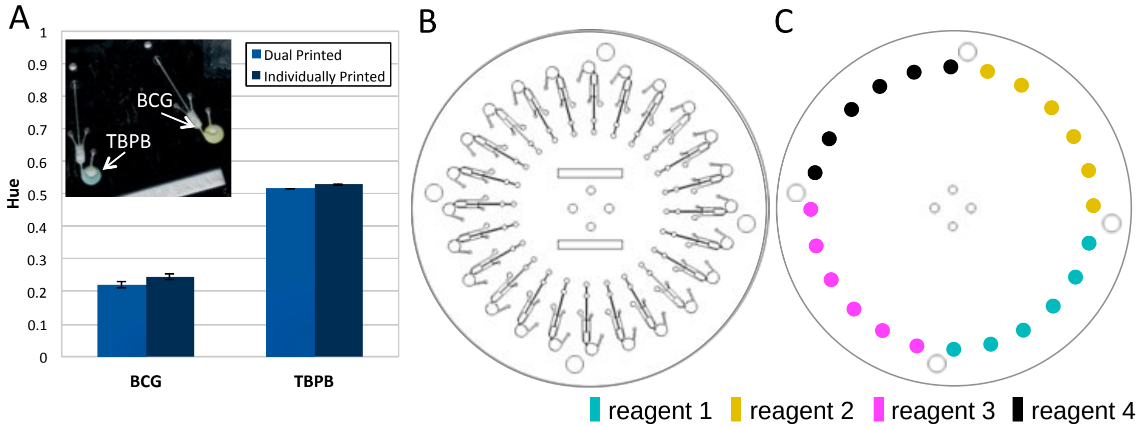

Figure 3-4. (**A**) HSA was added to devices printed simultaneously with TBPB and BCG, and analyzed for hue. An image of the color change is shown in the graph inset. (**B**) CorelDraw image describing the device design used for reciprocal mixing where each ink cartridge (cyan, yellow, magenta, and black) can be used to individually print different reagents onto a polyester device layer. (**C**) The printed reagent layer can be aligned to multiple reaction chambers on the device

3.3.1.3 Microdevice Fabrication with Rough Polyester Film

Devices are fabricated from alternating layers of untreated polyester and toner-coated polyester, allowing for features that include inlets, air vents, channels, and mixing chambers (**Fig. 3-3A**). With a view to more complex LOC devices, the printed layers can be aligned to allow each printed reagent region to match an appropriate reaction chamber for multiplexing (**Fig. 3-4**). Reagents can even be printed simultaneously without cross-contamination of reagents to reduce fabrication time (**Fig. 3-4A**), primarily because each reagent is obtained from a separate 'cartridge'. This fabrication technique allows reagents to be stored on-board in an enclosed manner for transport and storage after fabrication.

As described in **Table 3-2**, moving to an inkjet-compatible rough transparency film such as the Apollo Quick-Dry Universal film chosen here, with an average roughness of 10.2 µm (**Fig. 3-5A**), immediately improved the printability of the reagents compared to the smooth transparencies, average roughness of 0.126 µm (**Fig. 3-5B**), that

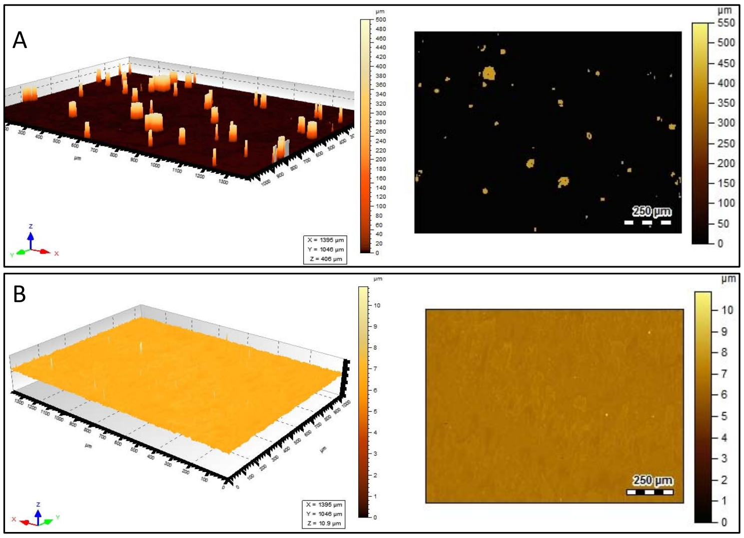

Figure 3-5. Optical profilometry images of substrate surfaces. (**A**) Surface images, 3D (left) and top-down (right) of Apollo Universal inkjet transparency film, root mean square (rms) roughness is 45.3 mm and average roughness (ra) is 10.2 mm. (**B**) Surface images, 3D (left) and top-down (right) of TRANSNS transparency film, rms = 0.171 mm and ra = 0.126 mm.

were traditionally used with PCL fabrication. **Figure 3-3B** shows the edge of the printed reagent spot on the TRANSNS transparency film (smooth), and in **Figure 3-3C**, similarly onto Apollo Universal transparency film (rough); insets show the entire printed spot. Introducing rough surfaces for the top and bottom microdevice layers, however, had an affect on fluid movement required for the spin-stop centrifugal mixing protocol[52], which relies on capillary action for back-filling. Parameters such as channel length, channel diameter, and fluid viscosity effect how long it will take a solution to fill a channel by capillary action. The greater surface area introduced by the rough channel walls increased the channel length and slightly decreased the channel diameter, hindering efficient movement of viscous HSA via capillary action. To overcome this, a five-layer device design was used that incorporated a smooth transparency film as the middle layer to promote back-filling for mixing. The smooth transparency film permitted only one of the channel walls to be comprised of the rough film.

The printer specifications for individual droplet size and resolution are 1.5 pL and 5760 x 1440 dpi, respectively. Using these values and dimensions of the designed printed reagent area, it was determined that nanoliters of reagent are deposited onto our devices during the initial pass of the print head, or initial print event. To deposit more volume of reagent, several successive print events were performed onto the same area. The number of successive print events was optimized using TBPB by varying the number of events and evaluating the printed area with image analysis. Increasing the volume of TBPB deposited should produce an increasingly darker, or more intense, yellow-colored area. Saturation, an image parameter of the HSB color model, referring to color intensity, was chosen to analyze the printed area and is reported from 0 to 1 by dividing the saturation values by 100%. Hue cannot be used for analysis because the shade of the color will not change with an increased mass of printed reagent. **Figure 3-6A** shows that the relationship between the number of print events and the magnitude of the saturation was linear. The less-than-optimal fit is most likely a result of slight printer tray misalignment during printing. Given that the printer was designed to print CD labels, the manual repositioning of the tray after each print event, and prior to the next successive print event, is outside the parameters of normal use for this hardware. This leads to shifts in the tray position that causes variability in the location of printed reagent. As a result, rather than successive prints over the same precise band locations, the end result was a series of random reagent and reagent-free bands within the printed spot. After a given number of printing events, the position of these individual ‘reagent bands’ varied between each printed reagent spot causing variability in the overall color intensity, i.e. saturation. Given that saturation can be significantly impacted by even the smallest change in color intensity, variability in the location of the reagent bands would result in larger error bars. This is in comparison to hue analysis where the hue value associated with a given color is not susceptible to changes color intensity, and would therefore be unaffected by variability in reagent band location. A total of ten successive print events was chosen because the saturation value was 17.5% greater than the average saturation resulting from print events 5-8, overcoming affects from print tray misalignment. This is most likely due to the decreased chance for reagent-free regions within the overall reagent spot as the number of print events is increased. Reagents were simultaneously printed onto the capping and bottom microdevice layers (**Fig. 3-3A**) to double the mass of reagent incorporated into each device without doubling the fabrication time for printed reagents.

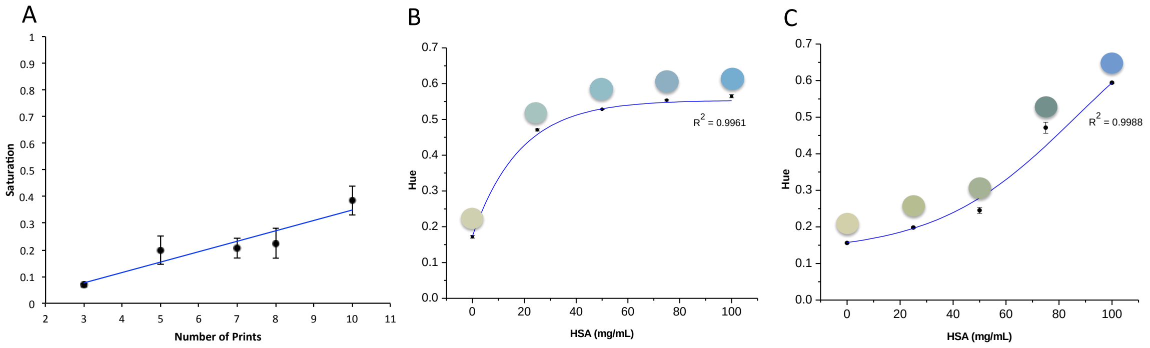

Figure 3-6. (**A**) TBPB was printed onto the reagent layers for polyester–toner device integration and the printed reagent spots were analyzed for saturation to show an increase in amount of reagent deposited. (**B**) Hue analysis for various concentrations of HSA in artificial plasma added to TBPB printed devices. (**C**) Hue analysis for various concentrations of HSA in artificial plasma added to BCG printed devices. Above the points on each graph shows the color associated with that point.

3.3.1.4 Human Serum Albumin Concentration Measurements

Printing total protein and albumin sensitive reagents were chosen as proof of principle colorimetric reactions because the resulting color changes are well defined and pertinent for point-of-care testing. Devices printed with TBPB and BCG were evaluated over a range of relevant HSA concentrations and analyzed for the color change using hue (three printed regions on three devices for n = 9). **Figure 3-6B,C** shows the color change with addition of HSA on the printed TBPB and BCG devices. Results are reported from

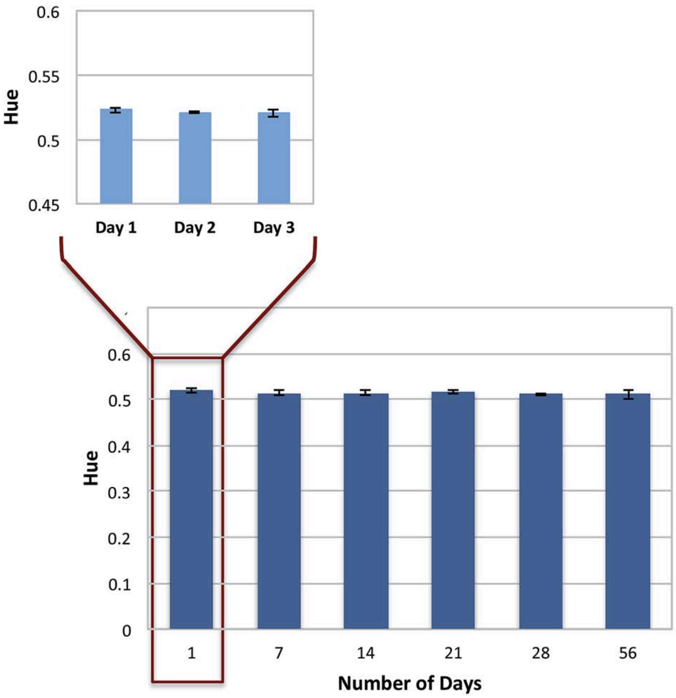

Figure 3-7. TBPB-printed devices were stored at room temperature and analyzed for hue over eight weeks with graph inset showing the initial three day stability.

0 to 1 derived by dividing the hue values by 360°. The calibration generated from printed TBPB devices resulted in an exponential curve with good correlation (R^2 = 0.9961). Results suggest that the assay is less sensitive at higher concentrations of HSA. Printed TBPB produced a larger dynamic range for detecting 0-50 mg/mL HSA, which has been seen previously.[20] This range could be expanded, where some reagent-limited results are observed, by more successive print events or increasing reagent concentration.[52] The calibration for printed BCG devices resulted in a sigmoidal curve (R^2 = 0.9988), with increased sensitivity for HSA concentrations between 50-75 mg/mL. No loss in activity from the transparency surface coating or device bonding was seen for both assays. The good fit of each curve demonstrates adequate mixing of reagent and standard. Efficient mixing, resulting in homogenous color, was addressed by incorporating six mixing events using a spin protocol that alternates the device between a spinning and stopped position.[52] The device architecture allows capillary action to move the solution back towards the center of the device when spinning is stopped, while centrifugal force mobilizes the fluid into the mixing domain when the device is spun.

3.3.1.5 Printed Reagent Stability

Device stability was initially measured over three days and subsequently expanded into a longer shelf life analysis (**Fig. 3-7**). It is critical for point-of-care microfluidic devices to have stability over time for storage and transportation. The devices utilized here had minimal storage requirements allowing printed TBPB devices to be stored at room temperature and kept in a drawer, as indicated in the reagent MSDS. Reagent exposure to lamination during fabrication and the microdevice material during storage seemed to have no effect on stability. At each time point, the addition of HSA to the devices resulted in a blue color change and quantitatively, minimal detection changes occurred. **Figure 3-7** shows a low percent relative standard deviation (%RSD) over 8 weeks, 0.652 %, indicating no loss in activity of the printed reagent

3.3.2 Simple Paper-Polyester Hybrid Devices for Reagent Storage

Reagent storage on paper is a simple and inexpensive method for integrating reagents into microfluidic devices, and has been exploited extensively in paper-based microfluidics. This approach is adapted here for centrifugal microfluidic devices, providing a successful reagent storage method when integrated into polyester device fabrication for polyester-paper hybrid devices.

3.3.2.1 Device Fabrication

A schematic illustration of the fabrication process for polyester-toner and paper hybrid devices is shown in **Figure 3-8**. The reagent of interest is pipetted onto Whatman-1 filter paper and then removed using an Acu-Punch disposable biopsy punch (2 mm diameter). The reagent punch was added to a designated reagent chamber in the device, enclosed by a capping layer and sealed by thermal bonding using lamination. If mass production and fabrication time are critical, the paper can be soaked with reagent, allowed to dry, and then laser cut to the desired reagent punch shape and size. **Figure 3-8D** shows a sheet of filter paper (125 mm diameter) that has been soaked in BCG reagent, and then laser cut into 380 reagent punches 2 mm in diameter.

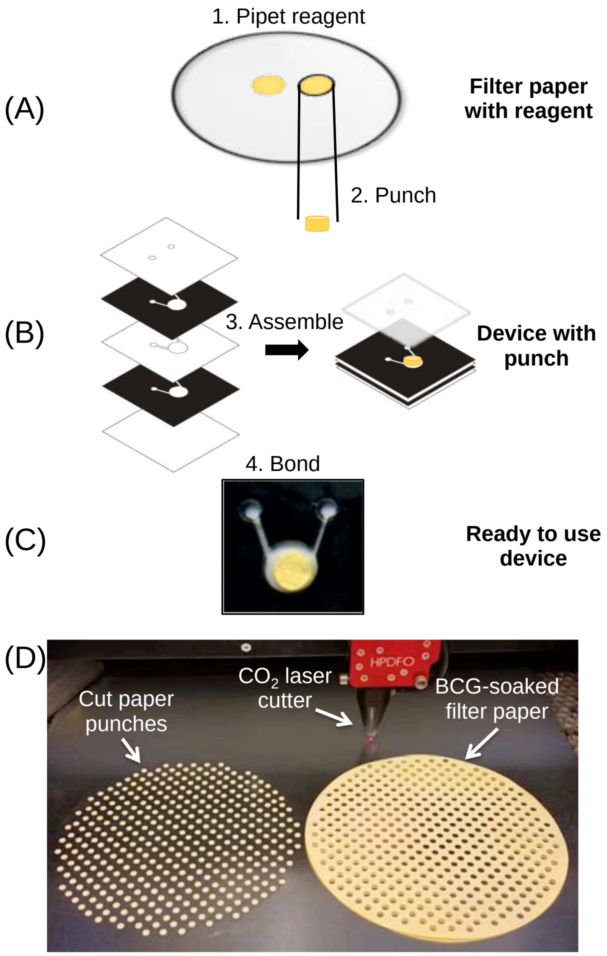

Figure 3-8. Schematic describing steps to fabricate paper/PET hybrid devices. (**A**) Reagents are pipetted onto filter paper and left to dry. Dried reagent spots on filter paper are removed using Acu-Punch tool. (**B**) Device layers are assembled without the top 'cover layer'. Reagent filter paper punches are added to device and the toplayer is combined. (**C**) Device is thermal bonded to enclose reagent punches. (**D**) Filter paper soaked in BCG reagent, dried, and laser cut into 380 2 mm diameter paper reagent punches to integrate into microdevices.

3.3.2.2 Colorimetric Analysis and Reagent Stability

The utility of this approach was examined for colorimetric reactions of different applications, including clinical, forensic, and environmental applications. The ability to detect total serum protein, serum albumin, cocaine, TNT, and Fe^{3+} colorimetrically was examined using TBPB, BCG, cobalt thiocyanate, tetramethylammonium hydroxide, and hydroxylamine with 1,10-phenanthroline, respectively. The color changes associated in the presence or absence of each analyte with reagents on 2 mm paper punches are also shown in **Figure 3-9**. All reactions were successful, with the expected color changes observed for 50 mg/mL HSA, 1 mg/mL cocaine, 1 mg/mL TNT, and 1 mg/mL $FeCl_3$. Color changes to blue-green for protein, yellow-green for albumin, blue for cocaine, purple for TNT, and red-orange for Fe^{3+} were observed. Adsorbed reagent to the paper matrix still undergoes a colorimetric reaction when the sample solution is introduced. The color generated by the reagents in the absence of each analyte is shown in **Figure 3-9**, with citrate buffer, ethanol, and water as negative analyte solutions.

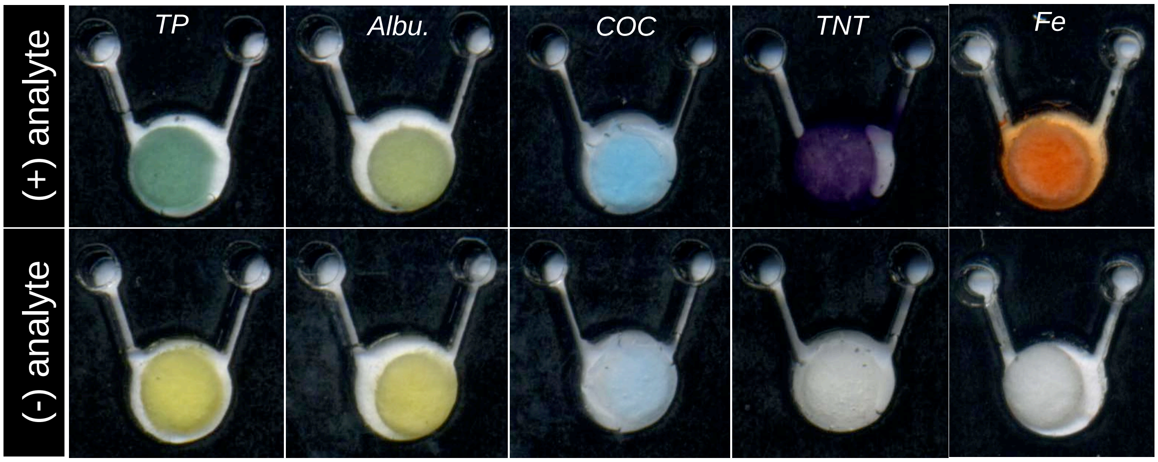

Figure 3-9. Images (Day 7) of the color change with, and without, total protein (TP), albumin (Albu.), cocaine, TNT, and Fe with TBPB, BCG, cobalt thiocyanate, tetramethylammonium hydroxide, and hydroxylamine and 1,10-phenanthroline reagents, respectively.

With the goal of detecting Fe in either whole blood or in the environment, the reaction of Fe^{3+} with hydroxylamine and 1,10-phenanthroline colorimetric reagents overlaid on a single paper punch is shown in **Figure 3-10**. In this study, each device with multiple reagent chambers (for n = 9 using 3 devices) was stored to test the long-term storage amenability for Fe^{3+} reagents. Since 1,10-phenanthroline is hygroscopic, the effectiveness over time when the reagent is embedded in a polyester chamber having an

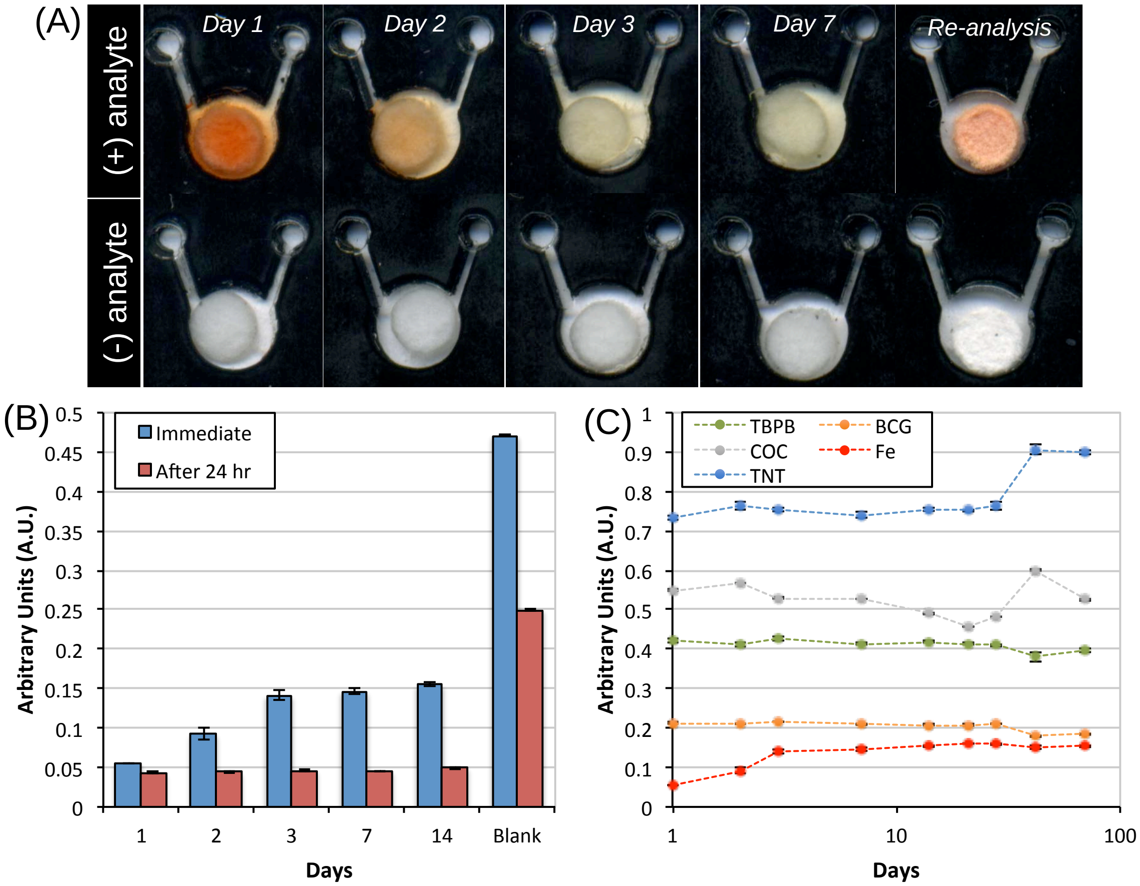

Figure 3-10. (**A**) Images of FeCl3, and blank solutions, added to reagent paper punches with hydroxylamine and 1,10-phenanthroline dried reagents at Day 1, 2, 3, 7, and re-imaging Day 7 after 24 h. (**B**) Image analysis using hue of FeCl3and blank solution added to reagent punches at Day 1, 2, 3, 7, and 14 as well as re-imaging of the same punches >24 h after initial reaction. (**C**) Total protein, albumin, cocaine, iron, and TNT reagents stored on paper punches over 10 weeks.

inlet port and air vent (1 mm diameter) needed to be evaluated. Fe(III) is first reduced to Fe(II) using hydroxylamine and changes from colorless to a red/orange color in the presence of 1,10-phenanthroline, upon formation of the ferroin complex.[70] The expected color change is observed on day 1 in the presence of 1 mg/mL $FeCl_3$. Due to 1,10-phenanthroline being hygroscopic, the resulting color change with the addition of $FeCl_3$ differed over seven days, and the reagent punch failed to turn red for Fe^{3+} when used after day 1. The reaction turned orange on day 2, and then turned a consistent brown color from days 3-7. The reacted devices were left overnight, allowing the solvent to evaporate from the chamber. The color change observed after 24 hr was consistently pink, analogous to the expected red hue color. The resulting pink color (not expected red color) was most likely due to the lack of solvent. When a negative (aqueous) solution was added to each of the punches from days 1-7 and left to dry overnight, the resulting color remained white (**Fig. 3-10A**). This demonstrated that the pink color change was not due to the reagents alone, and only occurred when Fe^{3+} was present. Either color change, immediate brown color or pink color observed upon re-analysis, can be used for Fe^{3+} detection as both resulting hue values differ from a negative analyte solution. This provided a possible alternate method for Fe^{3+} detection, using hydroxylamine and 1,10-phenanthroline reagents, with confirmatory analysis performed 24 hr later. The hue results corresponding to each color change observed in **Figure 3-10A** with the re-analysis after 24 hr for each is shown in **Figure 3-10B**. Image analysis to determine hue values utilized a desktop scanner and analysis of color with ImageJ using the HSB color model.

To assess the long-term storage capabilities for TBPB, BCG, cobalt thiocyanate, tetramethylammonium hydroxide, hydroxylamine and 1,10-phenanthroline for detection of total serum protein, serum albumin, cocaine, TNT, and Fe, respectively, devices were fabricated to store reagent punches in 2.3 mm diameter chambers with a vent and inlet port. The dry reagent-saturated devices were stored at room temperature, and the respective analytes for each added at days 1, 2, 3, 7, 14, 21, 28, 42, and 70 (for $n = 9$, using 3 devices). Hue analysis was performed for each colorimetric reaction, with the exception of cocaine where saturation was used due to methods described previously.[59] This is not a significant change in the detection protocol, as saturation is measured with the same process used for hue analysis where the device is scanned and analyzed using

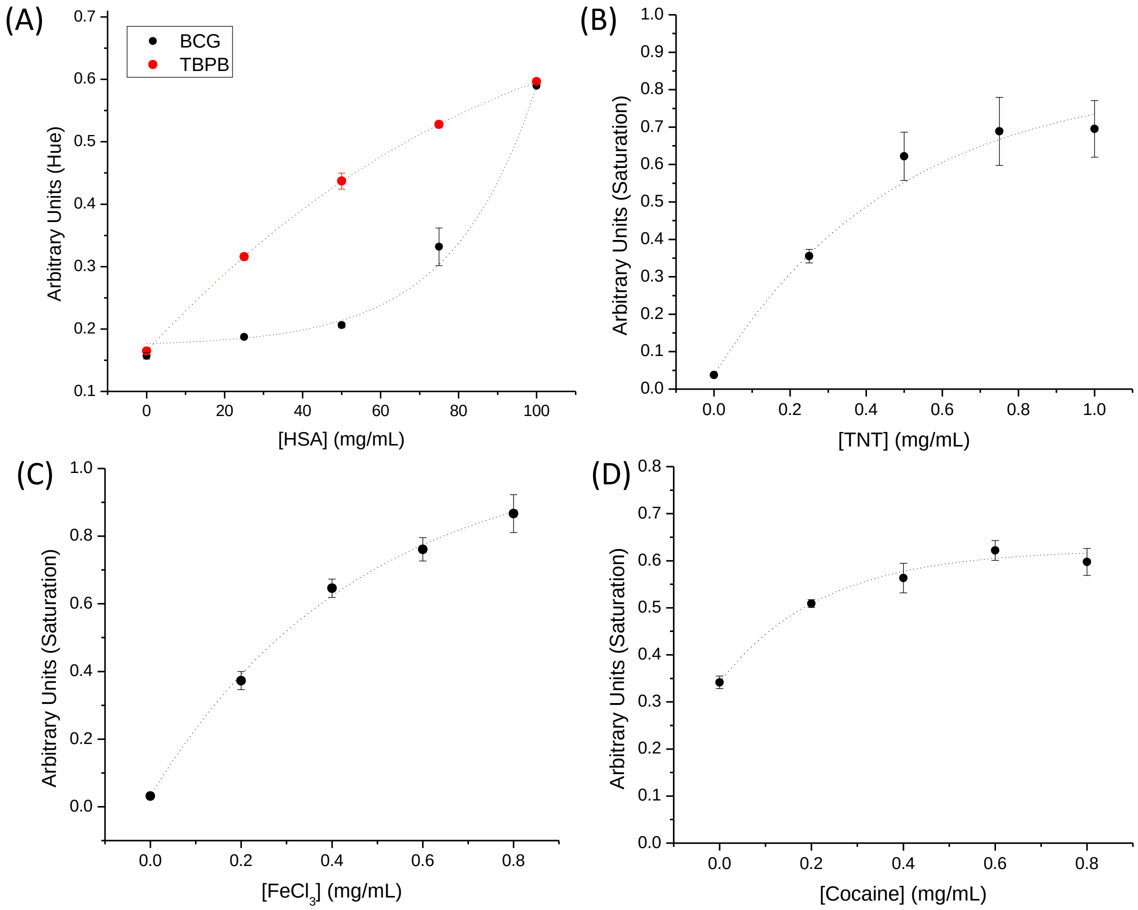

Figure 3-11. Image analysis of the color change for various concentrations of (**A**) total protein and albumin, (**B**) TNT, (**C**) $FeCl_3$, and (**D**) cocaine.

the HSB color model with ImageJ. **Figure 3-10C** shows that no loss in activity was observed over 70 days for each of the reagents.

In addition to the qualitative color changes seen in **Figure 3-9A** and **Figure 3-10A**, the reagent punches are also compatible for quantitative analysis. **Figure 3-11** demonstrates the change in either hue or saturation upon image analysis, with each colorimetric reaction over a range of analyte concentrations. All curve fits were exponential, and show excellent R^2 values ranging from 0.9931 to 0.9999 for all five analytes (protein, HSA, cocaine, TNT, and Fe). This reagent-paper method has the potential for quantitative analysis by using calibration curves to relate known analyte

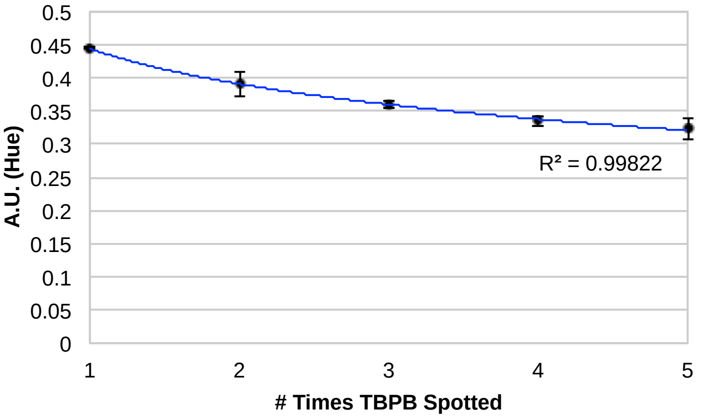

Figure 3-12. Increasing TBPB reagent for HSA analysis. TBPB was spotted onto filter paper and dried an increasing number of times to increase the mass of reagent deposited for each paper punch. The punches were added to a device for bonding and HSA was used to analyze the color change with hue to show the difference in the color change.

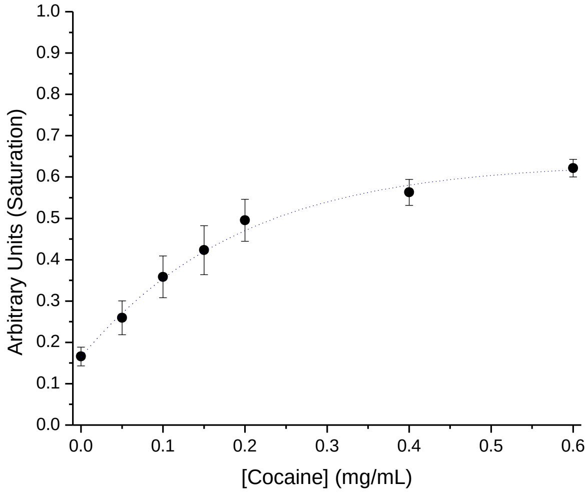

Figure 3-13. Cocaine analyzed using saturation with 0.1 mg/mL defined as the limit of detection (exponential fit; $R^2 = 0.9997$).

concentrations to specific changes in hue/saturation, and can be exploited for unknown sample analysis. If a given response is reagent-limited, the spot/dry protocol for reagent delivery can be repeated to increase the mass of reagent deposited onto a paper punch (**Fig. 3-12**). This allows for commercial reagents purchased at a given concentration to be easily concentrated within the paper matrix to improve (lower) limits of detection (LOD) by increasing the mass of reagent. For example, with cocaine, which is commonly cut with other adulterants[71], the LOD identified previously for pipetting reagent (used in liquid form) and dry-depositing reagent directly onto a polyester layer (without a paper matrix) was 1 mg/mL and 0.25 mg/mL, respectively.[59] The LOD for cocaine using a polyester-paper hybrid device was empirically determined to be 0.1 mg/mL (**Fig. 3-13**), thus representing a 2.5-fold decrease in the LOD. This was defined by a saturation value greater than 3X the standard deviation (+3σ) of the saturation for 0 mg/mL cocaine (0.234 A.U.). The saturation of 0.1 mg/mL cocaine was 0.35 A.U. ± 0.05, above the defined threshold value of 0.234 A.U.

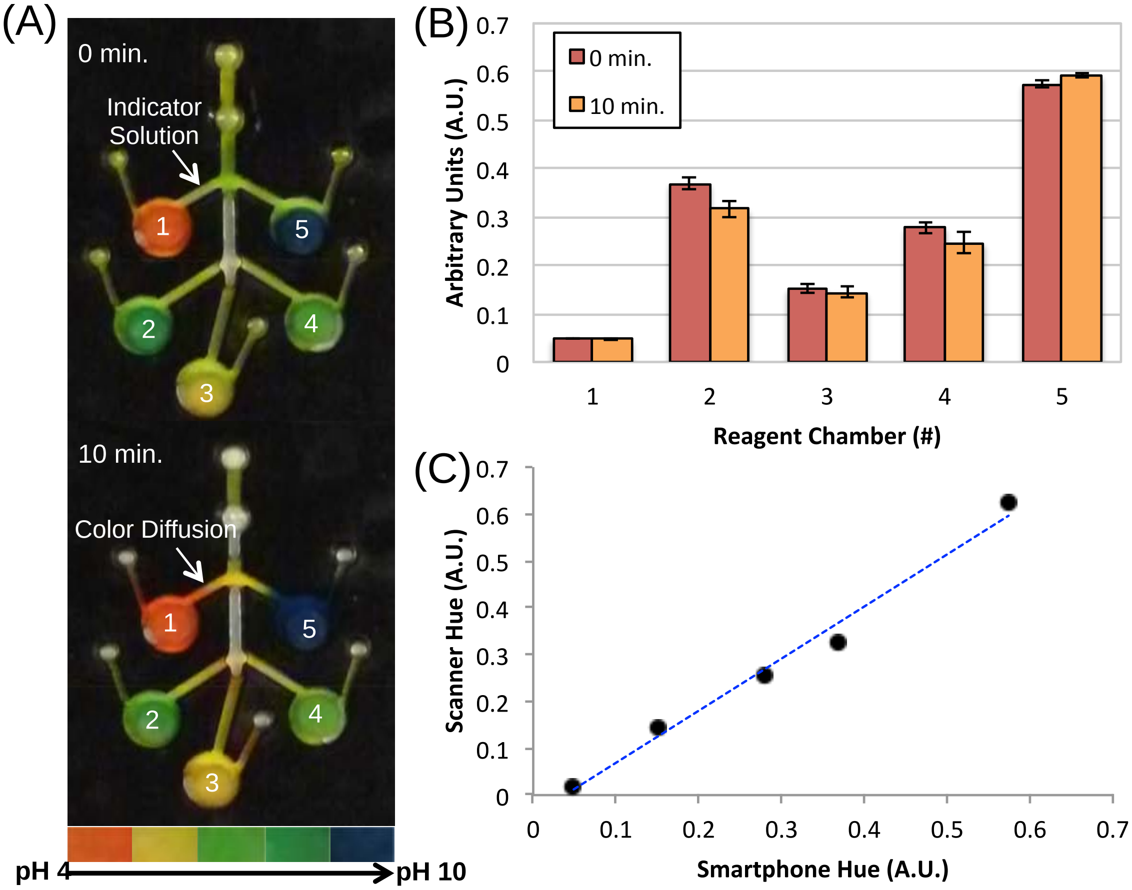

Figure 3-14. (**A**) Images of polyester-toner device at 0 and 10 min with a universal pH indicator added to 5 different reagent storage wells holding filter papers with various dried pH solutions. (**B**) Corresponding hues of the different reagent storage wells in (**A**) at 0 and 10 min. (**C**) Comparison of hue values obtained from smartphone and desktop photo scanner images.

3.3.2.3 Multiplexed Reagent Analysis

It was essential to determine that a multiplexed device containing numerous reagents for the detection of various different analytes could function without reaction crosstalk. A microdevice was designed with a single sample inlet connected to five different reaction chambers (**Fig. 3-14A**). Solutions of varying pH were added to Whatman-1 paper to simulate different reagents. A universal indicator containing methyl red, bromothymol blue, and phenolphthalein was added though a sample port, generating a unique color change at each of the reagent punches. The resulting color change for each reagent punch was associated with the original pH of the solutions added to the punches. An image was taken immediately following addition of the indicator and after 10 min. Immediately after indicator was added, no color change was seen in the channels connecting each reagent chamber to the inlet channel. Over the course of 10 min, color change from each reagent punch had only diffused partially into the connecting channels (see arrows in **Fig. 3-14A**). This indicated that the different pH solutions stored in punches were not diffusing quickly enough into the channel to impact the color change at any other pH punch. This was further validated by analyzing the hue values for each reagent chamber, and, as shown in **Figure 3-14B**, the color was unaffected by the pH of other reagent punches.

Finally, with a view to replacing the ImageJ image analysis on a scanner with that on a smartphone, and utilizing a custom smartphone application ('app') to evaluate hue and saturation, the image analysis results were compared from a scanned image and a smartphone image (**Fig. 3-14C**). The correlation of data obtained with each analysis method is excellent (slope of 1.11, $R^2 = 0.9850$), indicating that a smartphone camera, despite having a lower resolution than a desktop scanner, is adequate for image analysis in this case.

Table 3-3. The flow rate, thickness, and pore size for various Whatman filter papers tested for reagent storage potential.

Flow Rate	Brand	Grade	Thickness (μm)	Pore Size (μm)
Slow	Whatman	42	200	2.5
Medium	Whatman	1	180	11
Medium	Whatman	3	390	6
Fast	Whatman	41	220	20-25

3.3.2.4 Volume Recovery from Paper Punches

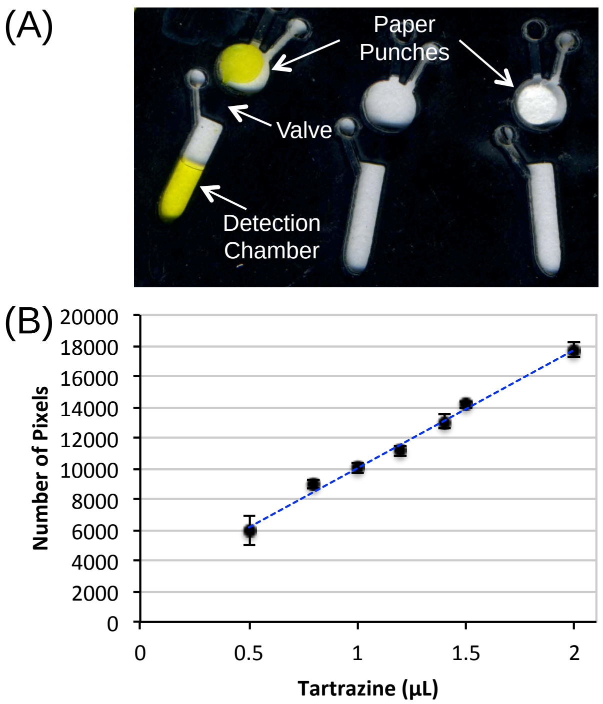

Figure 3-15. (**A**) Image of device after tartrazine added to paper and spun down to recover volume from paper punches. (**B**) Average number of pixels associated with a particular volume of tartrazine.

While most colorimetric reactions are single step, two-step colorimetric reactions exist, e.g., the Simon's Reagent with methamphetamine[72], the Griess test with nitrate[73], the bicinchoninic acid protein assay[74], and the modified Lowry assay[75]. With two-step reactions, it is imperative that an adequate volume of liquid from the sample is recovered for the second analytical step, or for sample recovery to perform other confirmatory or comparative analyses. In order to evaluate this, different Whatman filter papers with varying thicknesses and pore sizes (**Table 3-3**) were embedded into a centrifugal microdevice and the efficiency of volume recovery from the paper punch determined. Known volumes between 0.5 and 2µL of tartrazine dye solution (n = 3) were added to each paper punch chamber (without paper added) and spun into the detection chamber for 60 s at 2,000 RPM. A final scanned image of the device with tartrazine in the detection chambers was taken (**Fig. 3-15A**), and a custom Mathematica algorithm was used to count the number of pixels in the detection chamber that are of a particular color/hue (yellow color of tartrazine). These results were used to generate a calibration curve (linear, $R^2 = 0.9940$) to relate to unknown volume amounts (**Fig. 3-15B**).

Once the calibration curve was generated, the various paper punches from **Table 3-3** were added into the top circular chambers of the device, as seen in **Figure 3-15A**. A hydrophobic valve[23] was printed at the base of the paper punch chamber to prevent fluid flow after 2 µL of tartrazine was added. The device was spun for 2 min at 2,000 RPM to draw tartrazine solution absorbed by the paper out of the paper punch, and transport it to the lower detection chamber. Pixel counting in the detection chamber was used to calculate the volume of tartrazine recovered, based on the calibration curve. Recovery results are shown in **Table 3-4**, with Whatman-1 filter paper providing the most consistent volume recovery from the punch (1.25 ± 0.07 µL), with Whatman-1 and 41 associated with the largest volume recovery (1.25 µL each).

Table 3-4. Volume recovered from each paper was determined by relating the number of pixels associated with tartrazine to a volume using the calibration fit equation.

Whatman Paper Grade	Average Number of Pixels	Calculated Volume (µL)
1	11965.25 ± 578.03	1.25 ± 0.07
3	9717.50 ± 1109.05	0.96 ± 0.14
41	11946.75 ± 643.60	1.25 ± 0.08
42	10142.50 ± 1138.50	1.01 ± 0.15

3.3.3 Custom Capillary Ampules for Low-Volume Storage of Reagents

Glass ampules have been routinely used in conventional color tests for illicit drugs as a chemically inert material for colorimetric reagent storage. Traditionally, ampules are manufactured by melting the ends of glass tubing using a gas flame. For a laboratory setting, empty glass ampules can be purchased, filled with the desired storage solution, and sealed in a similar manner. Glass ampules have been adapted here for small volumes using glass capillaries and non-thermal sealing methods.

3.3.3.1 Capillary Ampule Fabrication

A schematic illustration of the fabrication process for custom capillary ampules with images of completed ampules is shown in **Figure 3-16**. A glass capillary of 1.5-1.8 mm diameter is cut using a glass cutter tool. This capillary diameter was chosen as a complimentary diameter to allow an extended length micropoint pipet tip (Fisher Scientific, Waltham, MA) to be used for adding reagent to the ampule and to allow for air displacement (~0.6 mm at pipet tip and ~1.25 mm at 1st marking). The capillary was cut to the desired length, depending on the amount of volume needed for storage. A segment of capillary ~6-8 mm in length was chosen for 4-6 µL of reagent to provide excess area to seal the ends of the capillary.

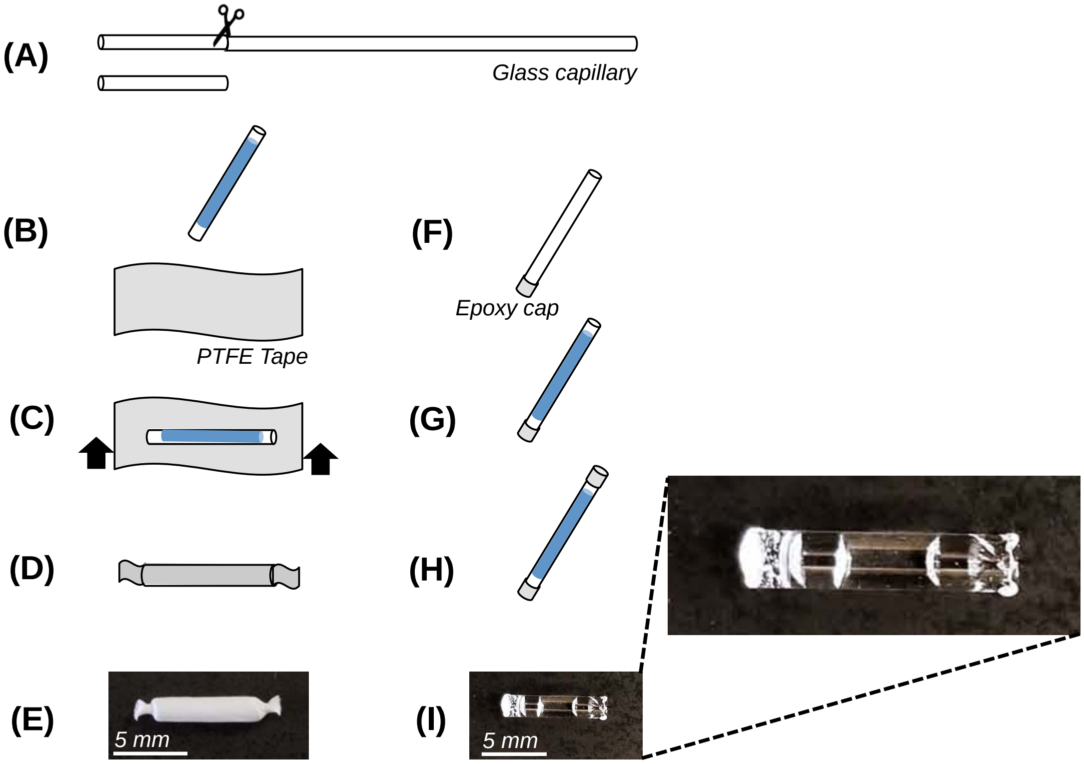

Figure 3-16. Schematic of custom ampule fabrication for PTFE-sealed ampules (**B-E**) and epoxy-sealed ampules (**F-I**). (**A**) Glass capillary were cut for desired volume. (**B**) The cut capillary section was filled with desired solution for storage. (**C**) Filled ampule was wrapped in PTFE seal tape. (**D**) PTFE seal tape ends were twisted and excess was cut from the ends. (**E**) Image of PTFE-sealed ampule. (**F**) One end of cut capillary section was sealed with epoxy. (**G**) Epoxy-sealed capillary was filled with desired solution for storage. (**H**) The remaining open end of capillary was sealed with epoxy to enclose solution. (**I**) Image of epoxy-sealed ampule with 3 µL enclosed.

For corrosive reagents, i.e., concentrated sulfuric acid, polytetrafluoroethylene (PTFE) thread tape was used to seal the capillary ampule after the reagent was added (**Fig. 3-16B-E**). The PTFE tape was wrapped around the capillary to enclose the reagent. For volatile reagents, i.e., acetaldehyde, an airtight method to seal the capillary ampule was required. Quick-dry epoxy was used to seal one end of the cut capillary piece, prior to adding reagent and sealing the other end of the capillary with epoxy (**Fig. 3-16F-I**).

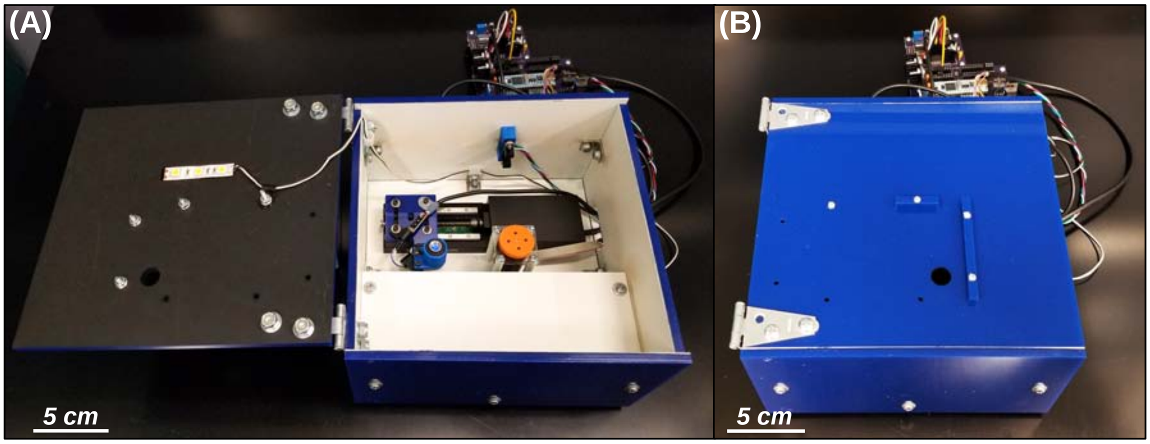

Figure 3-17. Images of the centrifugal microfluidic spin system enclosure for controlling the device rotation, laser valving, and imaging. (**A**) Image of open enclosure with center spin motor, linear actuator for laser diode position, white LED strips on the lid for consistent lighting during image capture. (**B**) Image of the device enclosure in the lid closed showing the laser-ablated hole for device imaging with cell phone.

3.3.3.2 Volume Released from Capillary Ampules

The capillary ampules were crushed mechanically by applying force to the capillary through the polyester capping layer of the 0.8 mm PMMA device chamber. The released solution, tartrazine dye here for evaluation of volume recovery, remained in the ampule chamber until centrifugal force was applied. The recovered volume from the capillary ampule was measured after a centrifugal spin protocol of 60 s at 3000 RPM using the spin system enclosure (**Fig. 3-17**). The channel at the base of the ampule chamber was 0.7 mm, width, and prevented movement of the broken glass into the subsequent chamber. After the spin protocol, a scanned image of the device was taken, with tartrazine in the subsequent chamber for image analysis. This process was performed with known amounts of tartrazine from 0-10 µL (n = 3) added to each capillary ampule, released, and scanned. Using the scanned images, a custom Mathematica algorithm was used to count the number of pixels in the detection chamber that are of a particular color (yellow color of tartrazine), and compared to a calibration curve (**Fig. 3-18**) generated without ampules, to determine the released volume. Recovered volumes using both epoxy and PTFE ampule seal methods were evaluated (**Table 3-5**). For both ampule seal methods, a higher volume recovery was observed when more volume was added to the ampules. Overall, the epoxy-seal method allowed for higher recoveries than the PTFE-seal method, aside for 2.5 µL where the PTFE method released more volume. This is demonstrated using the correlation plot in **Figure 3-19**, resulting in slopes of 1.06 and 1.19 for epoxy and PTFE seals, respectively.

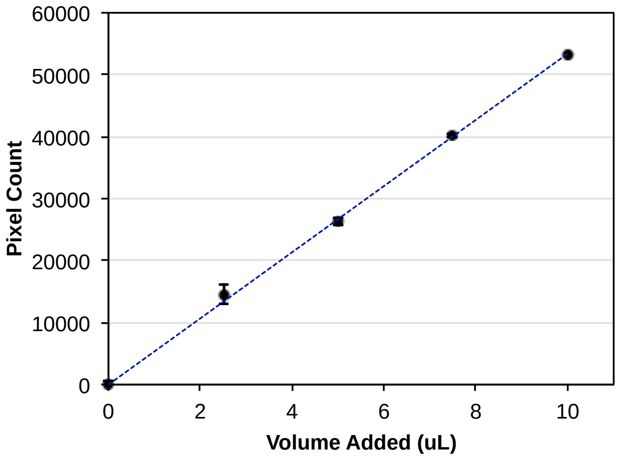

Figure 3-18. Calibration curve for determining volume recovery from ampules. A calibration curve was generated associating the number of pixels for a given volume of tartrazine added to the microfluidic device.

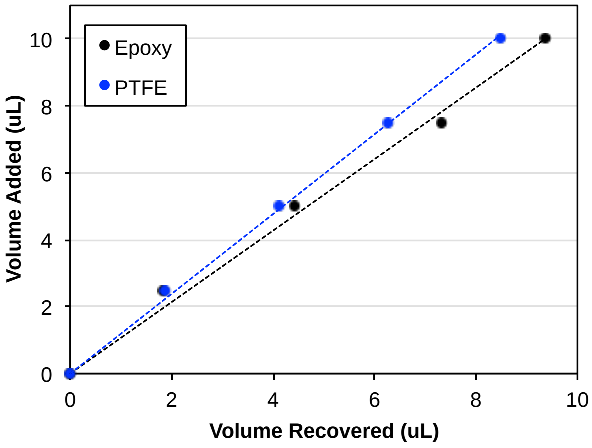

Figure 3-19. Correlation plot for volume recovered from ampules. A correlation plot for comparing the amount of volume added to the amount of volume recovered for both epoxy-sealed and PTFE-sealed ampules, with relative slopes of 1.06 and 1.19.

This is likely due to the PTFE tape wrapped around the ampule, preventing a small amount of the released solution after breaking the ampule from entering the subsequent chamber for analysis.

Table 3-5. Volume Recovered from Ampules. Volume recovered from epoxy-sealed and PTFE-sealed ampules was determined by relating the number of pixels associated with tartrazine to an unknown volume using the calibration fit equation. Recovery values (%) were calculated using the average recovered volumes.

Volume Added (µL)	Epoxy	Teflon
2.5	1.82 ± 0.20	1.88 ± 0.12
5.0	4.41 ± 0.16	4.11 ± 0.30
7.5	7.31 ± 0.27	6.27 ± 0.25
10.0	9.35 ± 0.48	8.48 ± 0.35

3.3.3.3 Colorimetric Analysis using Capillary Ampules

The utility of this reagent storage approach for colorimetric detection for the possession of illicit drugs was evaluated using Simon’s and Marquis colorimetric reagents commonly used in commercial field-testing kits. Colorimetric detection of methamphetamine using the Simon’s reagent consists of a solution of sodium nitroprusside and acetaldehyde (A), followed by reaction with sodium carbonate (B). Due to the volatility of acetaldehyde, 4 µL of solution A was stored in capillary ampules using the epoxy seal method. Sodium carbonate was stored using a paper reagent dry-storage method previously described.[76] To assess the detection of methamphetamine with the Simon’s reagent stored in capillary ampules, varying concentrations of methamphetamine from 0-10 mg/mL (n = 3) were evaluated for the colorimetric response using image analysis. The capillary ampule was crushed within the ampule chamber in the microfluidic device and 4 µL of methamphetamine sample was added to the ampule chamber. A centrifugal mixing protocol was then performed for 10 s at 1000 RPM, followed by centrifugal mixing for 3 s each replicate rotation of clockwise and counter clockwise spins at 3000 RPM and -3000 RPM, respectively, for 6 replicate spins. Once the spin protocol was complete, an image of the detection chamber was taken using a cell phone and analyzed for hue with ImageJ.

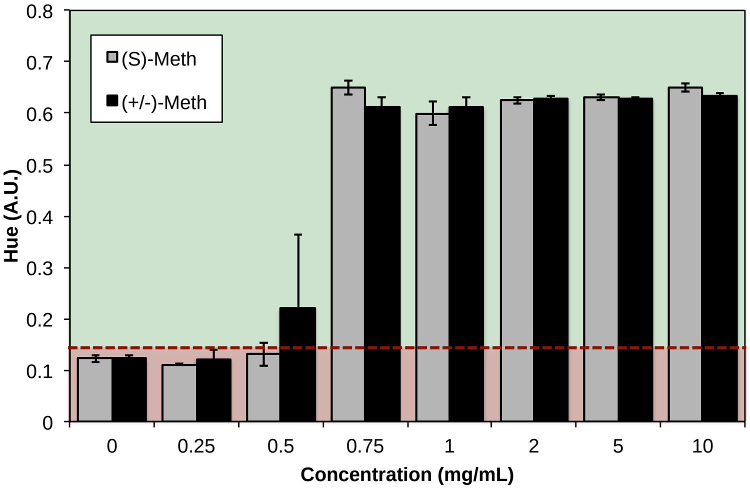

Figure 3-20. Hue analysis for methamphetamine detection. Methamphetamine was detected using the Simon Reagent with the organic reagent component stored in epoxy-sealed ampules. The detection threshold defined by +3σ was 0.142 A.U. (red dashed line) with an empirically-determined detection limit of 0.75 mg/mL for (S)-methamphetamine and (+/-)-methamphetamine.

The hue results for each methamphetamine concentration are shown in **Figure 3-20**. Threshold values were utilized as a simple, objective method for the qualitative detection of illicit drugs to notify the user that the drug of interest is present. The threshold value for detection of methamphetamine was defined as 0.142 A.U., a value +3σ of the negative response (0 mg/mL) for 99.7% confidence that methamphetamine is present. Samples resulting in a hue value greater than this threshold are considered positive for methamphetamine. The empirically derived limit of detection (LOD) for methamphetamine was 0.75 mg/mL. These results were comparable to those reported previously with reagents not stored, i.e., pipetted onto microfluidic devices.[59]

In contrast to the Simon's reagent, the Marquis reagent contains concentrated sulfuric acid. The Marquis reagent has been recognized as a presumptive color test for the detection of opioids.[77] Colorimetric detection of opioids using the Marquis reagent consists of a solution of concentrated sulfuric acid and formaldehyde. Due to the incompatibility of sulfuric acid and the 5 min epoxy, PTFE tape was used to seal 6 µL of

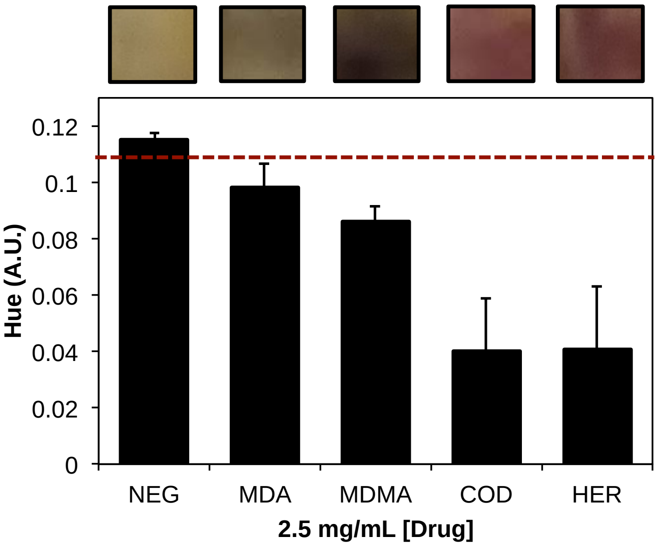

Figure 3-21. Hue analysis for illicit drug detection with the Marquis reagent. MDA, MDMA, codeine, and heroin were detected colorimetrically using the Marquis Reagent stored in PTFE-sealed ampules using hue analysis, with exemplary images of the color changes above each corresponding data point. The detection threshold defined by -3σ was 0.108 A.U. (red dashed line).

stored Marquis reagent in capillary ampules. To assess the utility of the Marquis reagent stored in capillary ampules and reacted within a polyester-based microfluidic device, various opioid compounds were chosen. Codeine, heroin, MDMA, and MDA were evaluated using the Marquis reagent for the colorimetric response on-chip using image analysis. Each sample was added to the device (6 µL) and then the capillary ampule was crushed within the ampule chamber. A centrifugal mixing protocol was then performed for 10 s at 2000 RPM, followed by centrifugal mixing for 3 s each replicate rotation of clockwise and counter clockwise spins at 3000 RPM and -3000 RPM, respectively, for 3 replicate spins. Once the spin protocol was complete, an image of the detection chamber was taken using a cell phone and analyzed for hue with ImageJ.

The hue results for each opioid are shown in **Figure 3-21** with exemplary images for each color change. No degradation of the microfluidic device from concentrated sulfuric acid was observed with the Marquis reagent stored in ampules before use and image capture <1 min after release of the reagent. The same approach for defining a threshold value for methamphetamine detection with Simon's reagent was used for defining a threshold value for the qualitative detection of the presence of an opioid substance. The threshold value for detection of an opioid was defined as 0.108 A.U., a value +3σ of the negative response (0 mg/mL) for 99.7% confidence that an opioid is present.

3.3.3.4 Fluid Movement Towards the Center of Rotation

The dominant centrifugal fluidic movement is outward from the center of rotation. This presents a disadvantage for centrifugal microfluidics when sequential processing steps are desired as the radial dimension of the microfluidic disc limits the number of steps. Recent work has shown the exploitation of capillary action within polyester-based centrifugal devices to move fluid inward towards the center of rotation for mixing.[52] Additional work in centrifugal microfluidics has explored pneumatic pumping[78, 79], passive centrifugal pumping[80], and even capillary wicking with paper[81] for moving fluid inwards.

Here, we report on a method for moving fluid towards the center of rotation using CO_2 formation from a neutralization reaction. The overall device design is described in **Figure 3-22**. A

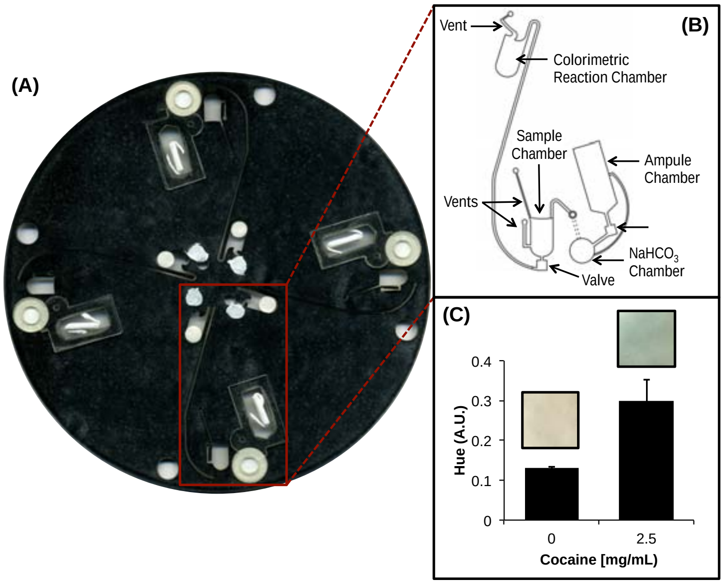

Figure 3-22. Microfluidic device for moving fluid against centrifugal force with CO_2 formation. (**A**) Microfluidic device used for CO_2 forming neutralization reaction to move fluid towards the center of rotation. (**B**) Inset CAD design describing the device architecture. (**C**) Colorimetric reaction used with neutralization reaction to show no inhibition from CO_2 released.

capillary ampule containing 6 µl concentrated sulfuric acid was sealed with PTFE tape and added to the PMMA ampule chamber. A subsequent 1.5 mm PMMA chamber was used to contain 0.018±0.003 g sodium bicarbonate. A 10 mm diameter section of PTFE was inserted into layer 3 within the open sodium bicarbonate chamber of the core centrifugal device. The PTFE was used as a filter, to prevent the reaction solution from contaminating the sample while allowing CO_2 gas to permeate through the membrane. A laser valve was utilized to control acid movement into the sodium bicarbonate chamber once the ampule was crushed. Once formation of CO_2 occurs in the sodium bicarbonate channel, the gas then moved through the PTFE filter, into the PMMA gas transfer channel (4 mm length, represented as dotted line in **Figure 3-22B inset**) connecting to the sample chamber of the core polyester-based centrifugal device to move the sample solution inward towards the center of rotation for detection in the colorimetric reaction chamber.

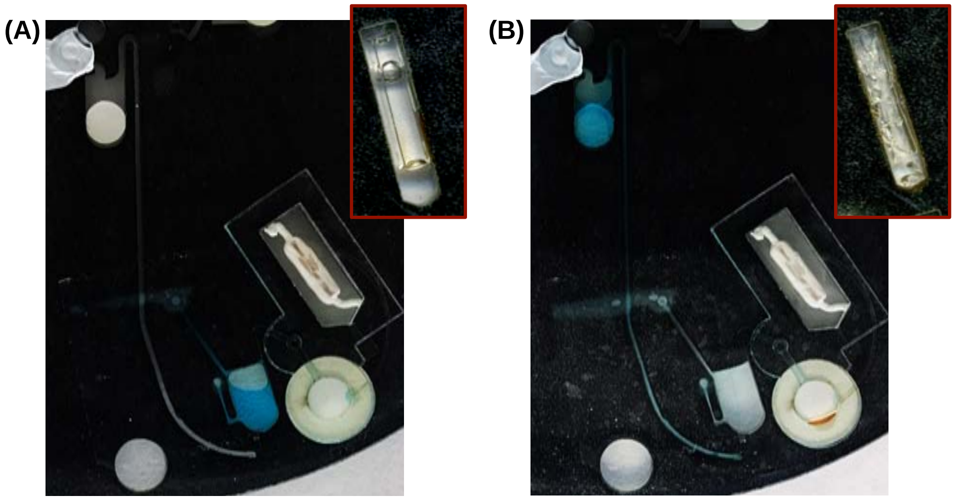

Figure 3-23. Images showing fluid movement toward microdevice center of rotation with CO_2 formation. (**A**) Image before performing the microdevice spin protocol with dye solution in the sample chamber, concentrated sulfuric acid in a PTFE-sealed ampule, and sodium bicarbonate dried on the microfluidic device. (**B**) Image after performing the spin protocol where the neutralization reaction with sulfuric acid and sodium bicarbonate formed CO_2 gas that was used to move the dye solution from the sample chamber into the colorimetric reaction chamber at the center of the disc. Insets showing ampule without PTFE to demonstrate the state of the ampule sealed within the PTFE seal.

Initial evaluation of the neutralization reaction to move fluid over a radial distance of 50 mm was assessed using 10 µL of aqueous- and methanol-based dye solutions (**Fig. 3-23**). Successful fluid movement inward toward the center of rotation was determined using methanol-based dye to visually see the simulated movement of drug sample. The centrifugal spin protocol was performed for 10 s at 2000 RPM. Once the ampule was crushed, the spin protocol began and acid was instantaneously moved from the ampule chamber into the sodium bicarbonate chamber. Within 3 seconds the bulk solution was moved from the sample chamber to the colorimetric reaction chamber during the initial spin event. After validation of fluid movement with dye, the colorimetric detection of cocaine with cobalt(II) thiocyanate was used to show that no undesirable affects from CO_2 formation were observed on the colorimetric reaction. **Figure 3-22C** shows the hue response with exemplary images for cocaine colorimetric detection (n = 3).

3.4 Conclusions

3.4.1 Printed Reagent Devices

We have demonstrated the utility of depositing reagents with a modified commercial inkjet printer onto polyester devices. Devices with printed reagents were evaluated using total protein and albumin colorimetric assays. Device shelf life was determined as at least eight weeks at room temperature after device fabrication, which involves printed reagents subjected to heat during lamination, with no loss of activity. Incorporating reagent printing into the fabrication process for polyester-toner microdevices offers a unique advantage for mass production, storage and handling, cost, and device simplicity of operation. Integrating reagent storage can allow these devices to be more compatible for various point-of-need diagnostics. In the future, direct observations of droplet formation would be desirable, and in particular, confirmation that a liquid bridge forms between the nozzle and the surface. This requires high speed cameras integrated within the confines of the print system to directly observe the formation of a droplet at the exit of the print nozzle.

3.4.2 Polyester-Paper Hybrid Devices

We have demonstrated the utility of depositing reagents onto filter paper and integrating them into polyester-toner microfluidic devices fabricated using the PCL method. Exploiting polyester-paper hybrid microfluidic devices offers an advantage for reagent storage that is simple and inexpensive while also being amenable to centrifugally driven fluid flow and control. Using numerous reagent/analyte combinations, the robustness of the colorimetric assays on these devices was evaluated, both qualitatively and quantitatively; no loss in color reactivity was seen over 10 weeks. Additionally, with endpoint colorimetric detection or for a multi-step process, Whatman-1 filter paper provided superior results. Incorporating dry reagent-soaked paper punches into centrifugal or polyester-based devices is simple and inexpensive, presenting the possibility for facile adoption with many applications. In the future, calibration curves should be generated using real-world samples to better associate unknown results with a curve for quantitative analysis. Overall, this technique offers a simple and inexpensive means of integrating reagents for use with more complex device networks, thus, allowing for increased device portability and automation.

3.4.3 Reagent Ampule Devices

We have demonstrated the utility of a simple custom capillary ampule fabrication method for low-volume storage of volatile and corrosive chemical reagents. This liquid storage method represents a simple approach to addressing the recognized challenge of reagent storage for field-deployable and point-of-care devices[82, 83], outside of rehydration and washing buffer storage made available by commercial blister packs and glass ampules.

The described approach was used to address the limitations associated with developing a centrifugal microfluidic device for the colorimetric detection of illicit drugs. Common colorimetric reagents, i.e., Simon's and Marquis reagents, used in the field for presumptive drug detection were applied here. Methamphetamine detection with the Simon's reagent showed no loss in detection (0.75 mg/mL LOD) with reagent stored in ampules compared with work previously described with pipetted reagents. Additionally, the Marquis reagent was stored in ampules and used on a polyester-based device for the detection of various opioids such as codeine, heroin, MDMA, and MDA. The utility of this approach was additionally assessed for the enhancement of fluid movement within a centrifugal device platform, allowing for more complex processing. Using the described custom capillary ampules to store concentrated acids, a neutralization reaction was performed, utilizing CO_2 formation for inward fluid displacement towards the center of rotation. Fluid movement was achieved over a radial distance of 50 mm within 3 s for cocaine colorimetric detection. In the future, this approach should be used to apply other colorimetric reactions, such as the Mandelin reagent, for additional illicit drug detection.

3.4.4 Comparison of Reagent Methods

Overall, three different simple and inexpensive means of integrating reagents, complimentary to the PCL fabrication for polyester-based devices, were developed for increased portability and automation of complex centrifugal microfluidic device networks. All three methods were effective for colorimetric reagent storage with inherent advantages and disadvantages for various device applications. The inkjet printing-based reagent storage method is advantageous for an automated device fabrication protocol, where reagents are incorporated using simple commercial instrumentation (office inkjet printer). Inkjet printing provides a method for reagent deposition for volumes in the picoliter range, however, this can be time consuming if microliter volumes of reagent are required. In addition, corrosive reagents can damage components of the printer, making this an ineffective method for many reagent storage applications, i.e., explosives and narcotics detection. Print-based reagent storage is better suited for clinical colorimetric assays where reagent composition has shown to be compatible. Paper and capillary ampule-based reagent storage methods demonstrate a more simplistic fabrication approach, where the required equipment consists of basic laboratory equipment (pipets) and consumables (pipet tips, filter paper, glass capillaries). Where dry-storage of reagents is possible, paper-polyester hybrid devices offer an enhanced method for stable reagent storage with the ability to increase colorimetric response due to the reagent-saturated paper format and ability for the color change to dye the paper for later analysis. Where corrosive or volatile reagents prevent dry-storage, capillary ampules provide a compatible method for integrating reagents into polyester-based microfluidic devices.

3.5 References

1. C. D. Chin, V. Linder and S. K. Sia, *Lab on a Chip*, 2012, **12**, 2118-2134.
2. X. L. Mao and T. J. Huang, *Lab on a Chip*, 2012, **12**, 1412-1416.
3. K. M. Horsman, J. M. Bienvenue, K. R. Blasier and J. P. Landers, *Journal of Forensic Sciences*, 2007, **52**, 784-799.
4. J. Wang, *Analytica Chimica Acta*, 2004, **507**, 3-10.
5. G. M. Whitesides, *Nature*, 2006, **442**, 368-373.
6. P. Yager, T. Edwards, E. Fu, K. Helton, K. Nelson, M. R. Tam and B. H. Weigl, *Nature*, 2006, **442**, 412-418.
7. G. S. Fiorini and D. T. Chiu, *Biotechniques*, 2005, **38**, 429-446.
8. G. M. Whitesides, E. Ostuni, S. Takayama, X. Y. Jiang and D. E. Ingber, *Annual Review of Biomedical Engineering*, 2001, **3**, 335-373.
9. W. K. T. Coltro, D. P. de Jesus, J. A. F. da Silva, C. L. do Lago and E. Carrilho, *Electrophoresis*, 2010, **31**, 2487-2498.
10. P. Lisowski and P. K. Zarzycki, *Chromatographia*, 2013, **76**, 1201-1214.
11. M. N. Costa, B. Veigas, J. M. Jacob, D. S. Santos, J. Gomes, P. V. Baptista, R. Martins, J. Inacio and E. Fortunato, *Nanotechnology*, 2014, **25**.
12. A. W. Martinez, S. T. Phillips, G. M. Whitesides and E. Carrilho, *Analytical Chemistry*, 2010, **82**, 3-10.
13. C. L. do Lago, H. D. T. da Silva, C. A. Neves, J. G. A. Brito-Neto and J. A. F. da Silva, *Analytical Chemistry*, 2003, **75**, 3853-3858.
14. B. L. Thompson, Y. Ouyang, G. R. M. Duarte, E. Carrilho, S. T. Krauss and J. P. Landers, *Nature Protocols*, 2015, **10**, 875-886.

15. M. J. Madou and G. J. Kellogg, *Proc. SPIE Systems and Technologies for Clinical Diagnostics and Drug Discovery*, 1998, ***3259***, 80-93.

16. D. Mark, S. Haeberle, G. Roth, F. von Stetten and R. Zengerle, *Chemical Society Reviews*, 2010, **39**, 1153-1182.

17. M. Madou, J. Zoval, G. Y. Jia, H. Kido, J. Kim and N. Kim, in *Annual Review of Biomedical Engineering*, Annual Reviews, Palo Alto, 2006, vol. 8, pp. 601-628.

18. R. Gorkin, J. Park, J. Siegrist, M. Amasia, B. S. Lee, J. M. Park, J. Kim, H. Kim, M. Madou and Y. K. Cho, *Lab on a Chip*, 2010, **10**, 1758-1773.

19. D. C. Duffy, H. L. Gillis, J. Lin, N. F. Sheppard and G. J. Kellogg, *Analytical Chemistry*, 1999, **71**, 4669-4678.

20. A. W. Martinez, S. T. Phillips, E. Carrilho, S. W. Thomas, H. Sindi and G. M. Whitesides, *Analytical Chemistry*, 2008, **80**, 3699-3707.

21. L. Shen, J. A. Hagen and I. Papautsky, *Lab on a Chip*, 2012, **12**, 4240-4243.

22. B. Derby, *Journal of Materials Chemistry*, 2008, **18**, 5717-5721.

23. Y. W. Ouyang, S. B. Wang, J. Y. Li, P. S. Riehl, M. Begley and J. P. Landers, *Lab on a Chip*, 2013, **13**, 1762-1771.

24. K. Abe, K. Suzuki and D. Citterio, *Analytical Chemistry*, 2008, **80**, 6928-6934.

25. K. Yamada, T. G. Henares, K. Suzuki and D. Citterio, *Angewandte Chemie-International Edition*, 2015, **54**, 5294-5310.

26. J. Tai, H. Y. Gan, Y. N. Liang and B. K. Lok, *Electronics Packaging Technology Conference, 2008*, 2008, **10**, 761 - 766.

27. J. B. Durkee, *Cleaning with Solvents: Science and Technology*, 2014, 1-755.

28. S. Kumar, in *Annual Review of Fluid Mechanics, Vol 47*, eds. S. H. Davis and P. Moin, Annual Reviews, Palo Alto, 2015, vol. 47, pp. 67-94.

29. A. W. Martinez, S. T. Phillips, M. J. Butte and G. M. Whitesides, *Angewandte Chemie-International Edition*, 2007, **46**, 1318-1320.

30. W. Dungchai, O. Chailapakul and C. S. Henry, *Analytica Chimica Acta*, 2010, **674**, 227-233.

31. A. W. Martinez, S. T. Phillips and G. M. Whitesides, *Proceedings of the National Academy of Sciences of the United States of America*, 2008, **105**, 19606-19611.

32. S. J. Vella, P. Beattie, R. Cademartiri, A. Laromaine, A. W. Martinez, S. T. Phillips, K. A. Mirica and G. M. Whitesides, *Analytical Chemistry*, 2012, **84**, 2883-2891.

33. D. M. Cate, J. A. Adkins, J. Mettakoonpitak and C. S. Henry, *Analytical Chemistry*, 2015, **87**, 19-41.

34. A. K. Yetisen, M. S. Akram and C. R. Lowe, *Lab on a Chip*, 2013, **13**, 2210-2251.

35. J. Ducree, S. Haeberle, S. Lutz, S. Pausch, F. von Stetten and R. Zengerle, *Journal of Micromechanics and Microengineering*, 2007, **17**, S103-S115.

36. D. C. Leslie, J. Y. Li, B. C. Strachan, M. R. Begley, D. Finkler, L. A. L. Bazydlo, N. S. Barker, D. M. Haverstick, M. Utz and J. P. Landers, *Journal of the American Chemical Society*, 2012, **134**, 5689-5696.

37. Y. K. Cho, J. G. Lee, J. M. Park, B. S. Lee, Y. Lee and C. Ko, *Lab on a Chip*, 2007, **7**, 565-573.

38. J. A. DuVall, S. T. Cabaniss, M. L. Angotti, J. H. Moore, M. Abhyankar, N. Shukla, D. L. Mills, B. G. Kessel, G. T. Garner, N. S. Swami and J. P. Landers, *Analyst*, 2016, **141**, 5637-5645.

39. M. Amasia, M. Cozzens and M. J. Madou, *Sensors and Actuators B-Chemical*, 2012, **161**, 1191-1197.

40. T. H. Kim, J. Park, C. J. Kim and Y. K. Cho, *Analytical Chemistry*, 2014, **86**, 3841-3848.

41. C. E. Nwankire, M. Czugala, R. Burger, K. J. Fraser, T. M. O'Connell, T. Glennon, B. E. Onwuliri, I. E. Nduaguibe, D. Diamond and J. Ducree, *Biosensors & Bioelectronics*, 2014, **56**, 352-358.

42. O. Strohmeier, M. Keller, F. Schwemmer, S. Zehnle, D. Mark, F. von Stetten, R. Zengerle and N. Paust, *Chemical Society Reviews*, 2015, **44**, 6187-6229.

43. N. Godino, E. Vereshchagina, R. Gorkin and J. Ducree, *Microfluidics and Nanofluidics*, 2014, **16**, 895-905.

44. http://www.thinxxs.com/main/produkte/microfluidixxs/blister-on-a-chip.html, (accessed 8 February 2018).

45. M. Focke, D. Kosse, C. Mueller, H. Reinecke, R. Zengerle and F. von Stetten, *Lab on a Chip*, 2010, **10**, 1365-1386.

46. S. Lutz, P. Weber, M. Focke, B. Faltin, J. Hoffmann, C. Muller, D. Mark, G. Roth, P. Munday, N. Armes, O. Piepenburg, R. Zengerle and F. von Stetten, *Lab on a Chip*, 2010, **10**, 887-893.

47. J. Hoffmann, D. Mark, S. Lutz, R. Zengerle and F. von Stetten, *Lab on a Chip*, 2010, **10**, 1480-1484.

48. L. K. Lafleur, J. D. Bishop, E. K. Heiniger, R. P. Gallagher, M. D. Wheeler, P. Kauffman, X. H. Zhang, E. C. Kline, J. R. Buser, S. Kumar, S. A. Byrnes, N. M. J. Vermeulen, N. K. Scarr, Y. Belousov, W. Mahoney, B. J. Toley, P. D. Ladd, B. R. Lutz and P. Yager, *Lab on a Chip*, 2016, **16**, 3777-3787.

49. L. Liu, C. L. Qiu, Q. Chen and S. M. Zhang, *Journal of Alloys and Compounds*, 2006, **425**, 268-273.

50. D. J. Cohen, R. C. Morfino and M. M. Maharbiz, *Plos One*, 2009, **4**, 8.

51. P. Yager, E. Fu, B. Lutz and D. Stevens, Microfluidics 2.0, http://www.mf20.org/).

52. Y. W. Ouyang, J. Y. Li, C. Phaneuf, P. S. Riehl, C. Forest, M. Begley, D. M. Haverstick and J. P. Landers, *Lab on a Chip*, 2016, **16**, 377-387.

53. M. M. Mentele, J. Cunningham, K. Koehler, J. Volckens and C. S. Henry, *Analytical Chemistry*, 2012, **84**, 4474-4480.

54. C. L. O'Neal, D. J. Crouch and A. A. Fatah, *Forensic Science International*, 2000, **109**, 189-201.

55. L. J. Scott, *Microgram*, 1973, **6**, 179-181.

56. D. A. Kidwell and S. A. Athanaselis, in *Handbook of Forensic Drug Analysis*, ed. F. Smith, Elsevier, 2004, pp. 235-276.

57. *Recommended methods for the identification and analysis of amphetamine, methamphetamine and their ring-substituted analogues in seized materials*, United Nations Office on Drugs and Crime (UNODC), Vienna, Austria, 2006.

58. J. L. Garcia-Cordero, D. Kurzbuch, F. Benito-Lopez, D. Diamond, L. P. Lee and A. J. Ricco, *Lab on a Chip*, 2010, **10**, 2680-2687.

59. S. T. Krauss, T. P. Remcho, S. M. Lipes, R. Aranda, H. P. Maynard, N. Shukla, J. Li, R. E. Tontarski and J. P. Landers, *Analytical Chemistry*, 2016, **88**, 8689-8697.

60. B. Derby, *Annual Review of Materials Research, Vol 40*, 2010, **40**, 395-414.

61. M. Singh, H. M. Haverinen, P. Dhagat and G. E. Jabbour, *Advanced Materials*, 2010, **22**, 673-685.

62. J. T. Delaney, Jr., P. J. Smith and U. S. Schubert, *Soft Matter*, 2009, **5**, 4866-4877.

63. K. Abe, K. Kotera, K. Suzuki and D. Citterio, *Analytical and Bioanalytical Chemistry*, 2010, **398**, 885-893.

64. K. Maejima, S. Tomikawa, K. Suzuki and D. Citterio, *Rsc Advances*, 2013, **3**, 9258-9263.

65. E. A. Roth, T. Xu, M. Das, C. Gregory, J. J. Hickman and T. Boland, *Biomaterials*, 2004, **25**, 3707-3715.

66. G. R. M. Duarte, C. W. Price, B. H. Augustine, E. Carrilho and J. P. Landers, *Analytical Chemistry*, 2011, **83**, 5182-5189.

67. G. R. M. Duarte, W. K. T. Coltro, J. C. Borba, C. W. Price, J. P. Landers and E. Carrilho, *Analyst*, 2012, **137**, 2692-2698.

68. R. Wolf and A. C. Sparavigna, *Engineering*, 2010, **2**, 5.

69. J. Eggers, in *Nonsmooth Mechanics and Analysis.*, eds. P. Alart, O. Maisonneuve and R. T. Rockafellar, Springer, Boston, MA, 2006, vol. 12.

70. W. W. Brandt, F. P. Dwyer and E. Gyarfas, *Chemical Reviews*, 1954, **54**, 959-1017.

71. D. Ciccarone, *Primary Care*, 2011, **38**, 41-58.

72. F. Feigel and V. Anger, *Spot Tests in Organic Analysis*, Elsevier, Amsterdam, 1966.

73. P. Griess, *European Journal of Inorganic Chemistry*, 1879, **12**, 426-428.

74. P. K. Smith, R. I. Krohn, G. T. Hermanson, A. K. Mallia, F. H. Gartner, M. D. Provenzano, E. K. Fujimoto, N. M. Goeke, B. J. Olson and D. C. Klenk, *Analytical Biochemistry*, 1985, **150**, 76-85.

75. B. Frolund, T. Griebe and P. H. Nielsen, *Applied Microbiology and Biotechnology*, 1995, **43**, 755-761.

76. S. T. Krauss, V. C. Holt and J. P. Landers, *Sensors and Actuators B-Chemical*, 2017, **246**, 740-747.

77. *Rapid testing methods of drugs of abuse. Manual for use by national law enforcement and narcotics laboratory personnel*, United Nations International Drug Control Programme, Vienna, Austria, 1994.

78. R. Gorkin, L. Clime, M. Madou and H. Kido, *Microfluidics and Nanofluidics*, 2010, **9**, 541-549.

79. M. C. R. Kong and E. D. Salin, *Analytical Chemistry*, 2010, **82**, 8039-8041.

80. S. Zehnle, F. Schwemmer, G. Roth, F. von Stetten, R. Zengerle and N. Paust, *Lab on a Chip*, 2012, **12**, 5142-5145.

81. H. Hwang, S. H. Kim, T. H. Kim, J. K. Park and Y. K. Cho, *Lab on a Chip*, 2011, **11**, 3404-3406.

82. Y. Huang, E. L. Mather, J. L. Bell and M. Madou, *Analytical and Bioanalytical Chemistry*, 2002, **372**, 49-65.

83. M. Hitzbleck and E. Delamarche, *Chemical Society Reviews*, 2013, **42**, 8494-8516.

4. Development of a Centrifugal Microfluidic Device with Objective Image Analysis for On-Site Colorimetric Detection of Explosives

4.1 Introduction

Proper response to potential threats and hazards, including those relating to explosives compounds, requires rapid, on-site analysis for applications ranging from environmental remediation of decommissioned testing and manufacturing sites[1-3] to forensic and defense investigation of terrorist-related events[4-6]. Additionally, the increased terrorist use of improvised explosives devices (IEDs)[7] has led to the investigation of portable sensing techniques for the detection of homemade explosives. Some conventional analytical instrumentation has been made more portable and utilized for the detection of explosives compounds in the field. Handheld Raman spectrometers have been deployed for field use as a noncontact method for analyzing samples with an internal spectral library for identification.[8] Ion mobility spectrometry (IMS) instruments are widely deployed for screening applications, however, IMS relies on analyte ionization prior to analysis, which can lead to difficulties with competitive ionization.[9] Ultimately, without reducing the cost of these portable systems, a barrier remains for implementing these techniques as an ideal field test. An explosive detection platform that is rapid, inexpensive, portable, and user-friendly is desired.

Color tests are a widely used method for field detection due to the low cost, availability, and simplicity of these tests.[10] The presence or absence of an analyte of interest can be defined by a visual color change or color intensity, providing a qualitative ‘yes/no’ response. Associated drawbacks of this type of subjective analysis include variations in human color perception and differences in lighting that affect the perceived color.[11, 12] Quantitative analysis can also be achieved with colorimetry by circumventing subjective visual interpretation and, instead, using objective color analysis based on empirically defined calibration curves for color change or color intensity.

Colorimetry has been routinely used as a sensing mechanism in portable microfluidic devices, with applications that range from on-site or at-home analysis, to limited-resource testing. Microfluidic technologies offer advantages from the scaled-down size of these devices that include portability, rapid analysis times, low cost substrates, and low sample consumption. The centrifugal microfluidic platform offers additional advantages for field analysis in which inexpensive instrumentation can be used and easily automated, requiring only a single programmable motor for fluid movement allowing for simple operating procedures for ease-of-use. Where current color tests used in the field are not multiplexed[10], requiring additional time and sample for analyte identification, centrifugal microfluidics can perform multiple fluidic processing steps or colorimetric reactions in parallel about the center of rotation.

Objective imaging approaches, including the use of small cameras, can easily be interfaced with microfluidic devices and used for spatial and temporal image capture where chemistry-induced color changes have occurred.[13] The resulting color change can be quantified using a number of color ‘spaces’, or color models, and different research groups have explored red/green/blue intensity and absorbance (RGB)[14, 15], hue/saturation/brightness (HSB, HSV or HSL)[16, 17], and the International Commission on Illumination (CIE) color space[18, 19] as useful approaches to detection. Performing colorimetric analysis objectively from an image of a microfluidic device allows for a more automated device format, where the operating procedure and color analysis are encoded. A fully automated procedure after the addition of sample provides a user-friendly detection system requiring minimal training in the field for a rapid response to potential explosive threats. The use of programmed threshold values associated with the color analysis can provide definitive results regarding the presence of an explosive compound without requiring on-site data interpretation by the user.

4.1.1. Objective Image Analysis and Color Adjustments

Scenarios arise with objective color analysis where it can be challenging to discriminate between colors that are only subtly different and have similar numerical color values, e.g., a change in color from yellow-to-orange. To address these limitations, some researchers have developed components that reduce lighting influences[14, 20], account for image-to-image variation[16, 21], and generate more reliable calibration data.[22] When altering lighting/background proves ineffective, however, other approaches to color enhancement are needed.

Multispectral images, or images that contain a wide range of colors, are easily enhanced digitally using contrast exaggeration or by expanding the highlight and shadow areas. Color enhancement of a monochromatic image (image displaying similar colors) often serves to only increase the range of saturation intensities instead of enhancing the discrimination between the colors.[23] While color enhancement can be performed by altering the saturation and brightness[23], this needs to be specifically customized for each color change. Additionally, variations in the colorimetric reaction can result from contamination when using field samples, e.g., soil, and thus, generate false positive results from unintended changes in the saturation and brightness of the color change. Instead, similar to the manipulation of images as they are being perceived using polarized lenses[24, 25], color enhancement methods that manipulate, or alter, the perceived color can provide front-end color interpretation rather than utilizing back-end processing. This can be accomplished by introducing a colored component over or around the detection area to create the appearance of an alternative color change, one that enhances the native color change, provides more discrimination between colors, and improves detection. For example, a yellow-to-red bitonal color change (difference in hue of ~60°) can be manipulated to appear as a green-to-purple color change (difference in hue of ~180°) by tinting the detection area blue or introducing external blue lighting on the detection background.

Most devices capable of color detection (e.g., scanners, cameras, cell phones) use the RGB color space, which represents color as an additive combination of red, green and blue.[26] Analysis with RGB can also be performed using individual R, G, or B channel intensities to measure a color response independent of the other channels. Using individual RGB intensities, however, does not account for the entire color spectrum, thus, other image parameters need to be considered. The HSB color space (hue, saturation, brightness) is derived from recasting RGB data from a Cartesian coordinate system into spherical coordinates and can provide more robust parameters for color analysis. Hue is an alternative image analysis parameter that is particularly useful, as color is represented by a single numerical value more closely related to the perceived color, rather than the sum of individual RGB values. Hue is typically reported as an angle that varies between

0° and 360°, and can be converted to values between 0 and 1 in arbitrary units (A.U.); both ranges cover the entire spectrum of colors.[26]

Typically, a monotonal color change (i.e., colorless-to-colored) can present significant challenges when using hue analysis because the hue spectrum does not contain white as a color. This is problematic for situations where the background of an image with a colorless solution would appear white, such as with paper microfluidics.[27] Manipulating the color of a natively white background, resulting in an overall bitonal color change, would increase the ability to use hue to analyze monochromatic color changes. With the goal of leveraging smartphones as COTS (commercial-off-the-shelf) detectors, we present a method that involves the use of three different color manipulation/tinting methods that can be used for heightened colorimetric detection for hue analysis. Hybrid polyester-paper devices, fabricated via *print-cut-laminate* (PCL)[28] and paper utilized for reagent storage[29] methods (described in **Chapter 3**), have associated tinting advantages from both the paper and polyester substrates used. Both fabrication-based and external tinting approaches were explored, with the former involving 'dyed' reagent-saturated paper or print-based tinting of the device itself. External tinting options involved the use of background LED-based color infusion from a variety of sources during image capture. This approach to color manipulation provides a simple technique to enhance colorimetric analysis with microfluidic devices of various substrates. While the effectiveness of all explored tinting methods was assessed via colorimetric hue analysis for detection of hydrogen peroxide (H_2O_2), a detectable byproduct of IEDs[30-32], what is described here has broad applicability to any analyte-of-interest where colorimetric chemistry exists.

Overall, this chapter describes the optimization of colorimetric reactions for the detection of eight different explosives compounds for the centrifugal microfluidic platform. Each reaction was translated to the microfluidic devices, and the resultant color change for each reaction within the device was then analyzed to determine the optimal image analysis parameter, tinting methods for enhanced analysis, and threshold values for objective detection with a cell phone. The microfluidic device design was later adapted for multiplexed detection towards the goal of a sample-in-answer-out explosive identification system that is portable and automated for on-site use with minimal training for system operation.

4.2 Materials and Methods

4.2.1 Reagents

2,4,6-Trinitrotoluene (TNT), 2,4-dinitrotoluene (DNT), methyl-2,4,6-trinitrophenylnitramine (Tetryl), and urea nitrate (UN) were provided by Signature Science (Austin, TX). Hydrogen peroxide (35%), phosphoric acid, and isopropyl alcohol were purchased from Fisher Scientific (Waltham, MA). Nessler's reagent was purchased from La-Mar-Ka, Inc. (Baton Rouge, LA). Ammonium nitrate (AN), potassium nitrate, sodium perchlorate, glycerol, acetonitrile, methanol, ethanol, acetone, water, tetramethylammonium hydroxide (TMAH), methylene blue (MB), sulfanilamide, zinc powder, ammonium titanyl oxalate (ATO), N-(1-naphthyl)ethylenediamene dihydrochloride (NED), 4-(dimethylamino) cinnamaldehyde (*p*-DMAC), and erioglaucine were purchased form Sigma-Aldrich (St. Louis, MO).

Acetonitrile, methanol, ethanol, and water were purchased as high-performance liquid chromatography grade solvents. Tetramethylammonium hydroxide, methylene blue, and Nessler's reagent were used as is. A 1M aqueous solution of ammonium titanyl oxalate was prepared. For the Griess reaction, 8% sulfanilamide and 0.5% N-(1-naphthyl)ethylenediamene were prepared in 8.5% phosphoric acid either separately or combined. A 0.45 mM aqueous solution of erioglaucine was used for dye-based tinting.

4.2.2 Device Fabrication

Devices were fabricated using the PCL protocol[28] from TRANSNS Copier/Laser transparency sheets purchased from Film Source, Inc. (Maryland Heights, MO). Devices were fabricated using five layers of polyester overhead transparency sheets, with layers 2 and 4 as toner-coated layers (act as adhesive for device bonding) fabricated with two layers of black toner printed onto each side of the polyester film using an HP LaserJet 4000 printer. Color was printed onto the device layer 1 for print tinting using a Brother HL-4570CDW printer. Device architecture was cut out of each device layer using a VersaLASERVLS3.50 system (Scottsdale, AZ) with compatible CAD software. Reagents stored on Whatman filter paper, or reagent-saturated paper, were added prior to device bonding using a method previously described.[29] Devices were laminated at >160 °C for device bonding using an office laminator (Akiles UltraLam 250B).

Devices fabricated using heat-sensitive adhesive (HSA) instead of printed toner with the PCL method that has been described previously.[33] HSA (EL-7970-39) was purchased from Adhesives Research (Glen Rock, PA) and bonded to both sides of a polyester layer simply using lamination for HSA-coated layers in replace of toner-coated layers 2 and 4. Subsequent PCL steps are the same as with toner devices.

4.2.3 Spin System

A Sanyo Denki Sanmotion series stepper motor controlled by a Pololu DRV8825 stepper motor driver in full step mode was utilized for the spin system. Motion control profiles were generated using a Parallax Propeller microcontroller and a printed circuit board was designed with EAGLE CAD software containing the microcontroller, motor drivers, and associated components for power regulation, heat sinking, and serial communication with an external computer terminal. A poly(methyl methacrylate) (PMMA) three-arm custom support structure immobilized the motor during rotation for initial analyses. A simple PMMA enclosure was laser-cut and assembled for all lighting studies and tinting experiments using MakerCase (http://www.makercase.com), a web-based application for designing laser-cut project cases.

The device centrifugal spin protocol for the one-step device design was as follows: spin 500 RPM for 5 s, 0 RPM for 5 s, and 2000 RPM for 45 s. The device protocol for the two-step design was the same as the one-step protocol with three subsequent additional steps. The first subsequent step was a centrifugal mixing protocol performed for 3 s each replicate rotation of clockwise and counterclockwise spins at 3000 RPM and -3,000 RPM, respectively, for 3 replicate spins. The next step involved opening the laser valve used for additional fluidic control through laser valving as described previously.[34, 35] Once the laser valve was opened, an additional spin step for 10 s at 3000 RPM followed by another centrifugal mixing protocol was performed.

4.2.4 Lighting

White light was provided by a three LED Waterproof Flexi Strip (RadioShack) powered by a benchtop DC voltage power supply. The intensity of the white light was controlled by varying the voltage from 8-9 V with current up to 100 mA. RGB light was provided by a three Pololu Addressable RGB LED strip powered by a 5V LM1085 voltage regulator using 15V, 2A AC to DC converter. The intensity of the RGB light was controlled by a single 25 turn 10k ohm 0.5 watt potentiometer, wired as a variable resistor. The red, green, and blue elements of the RGB LEDs were controlled by a Parallax Propeller Mini. A custom Spin code program was written to control the individual R, G, and B values. The input RGB values were 255, 0, 0 (red); 0, 255, 0 (green); 0, 0, 255 (blue); 0, 255, 255 (cyan).

4.2.5 Image Analysis

After device operation of each centrifugal spin protocol, the reaction chambers within each device were imaged using an Android cell phone positioned above the microdevice using a standalone PMMA phone holder or PMMA enclosure for consistent image capture. Resulting color changes observed in each image were cropped and analyzed with HSB or RGB color spaces using ImageJ. Images of the microfluidic device with an array of chambers for additional control over analysis parameters were taken using an EPSON Perfection V100 Photo Scanner with 1200 dpi resolution.

4.3 Results and Discussion

4.3.1 Microfluidic Device

An inexpensive microfluidic device capable of detecting a number of explosive materials was designed and evaluated for rapid, objective colorimetric detection. Microfluidic devices were fabricated using the previously described PCL fabrication technique as an inexpensive centrifugal device platform.[28] The five-layer device was utilized for colorimetric assay optimization and was comprised of alternating layers of uncoated and coated polyester film, or overhead transparency sheets. The coated polyester layers were coated with either printer toner or heat-sensitive adhesive (HSA) for defining the fluidic architecture and for device bonding. The overall toner-based device design used for initial studies is shown in **Figure 4-1** and allowed for sample to be added to the inlet and distributed to various reaction chambers (one-step reaction format used here). Paper substrate was utilized within each reagent chamber as a simple reagent storage method compatible with polyester-based devices, as described previously.[29]

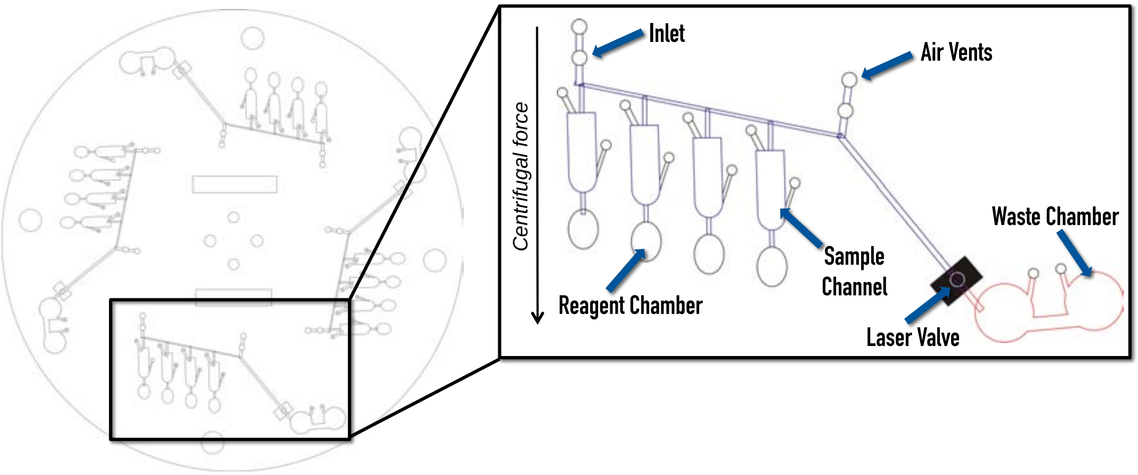

Figure 4-1. Device design used to evaluate and optimize each colorimetric reaction. The inset describes each feature of one domain (four total within one microfluidic device) for the complete design with the upper fluidic level (blue) and bottom fluidic level (red).

The key feature of this device design was the implementation of a centrifugo-pneumatic valve to allow for sample metering.[36] This valve architecture included the sample channel (3 mm width, 8 mm height, 124 μm depth), reagent chamber (3 mm width, 4 mm height, 348 μm depth), and narrow connecting channel (0.6 mm width, 124 μm depth) between the two sample and reagent features (features labeled in **Fig. 4-1**). Utilizing capillary action, sample solution added to the inlet filled the sample channels from left to right, displacing air towards the center of rotation for filling. A meniscus was formed at the narrow connecting channel preventing air from escaping the unvented reagent chamber.[36] The surface tension at the sudden 3D-expansion of the narrow connecting channel to the reagent chamber, 90° expansion angle assumed, kept the meniscus pinned. Once all sample channels were filled, excess sample solution within the inlet channel was centrifugally driven to the waster chamber after opening the laser valve as described previously.[34, 35] After excess sample was moved to the waste chamber, an equal volume of sample solution (3 μL) remained in each of the identical sample chambers. The metered sample volumes were released simultaneously into the reagent chamber by increasing the rotational frequency to allow the trapped air in the unvented reagent chamber to displace above the sample plug towards the center of rotation. Unlike printed hydrophobic valves used previously with polyester-toner devices[37], a centrifugo-pneumatic valve is based on surface tension of the solution and air compression, making it a suitable candidate for metering organic solvents, which is less-explored and otherwise challenging.

4.3.2 Translating Colorimetric Reactions to Microfluidic Devices

Each explosive of interest was broadly classified as either an inorganic or organic explosive for partitioning the colorimetric assay optimization. Organic explosives consisted of military explosives including TNT and DNT, a precursor to TNT, and Tetryl. For detection purposes urea nitrate (UN), considered an IED, was evaluated with this group of explosives as a high explosive. Inorganic explosives consisted of common oxidizer material, i.e., nitrate (NO_3^-), perchlorate (ClO_4^-), and ammonium (NH_4^+) (used to detect ammonium nitrate (AN), a common fertilizer based explosive). For detection purposes, a colorimetric reaction for H_2O_2, a peroxide-based explosive precursor, was evaluated with this group of explosives.

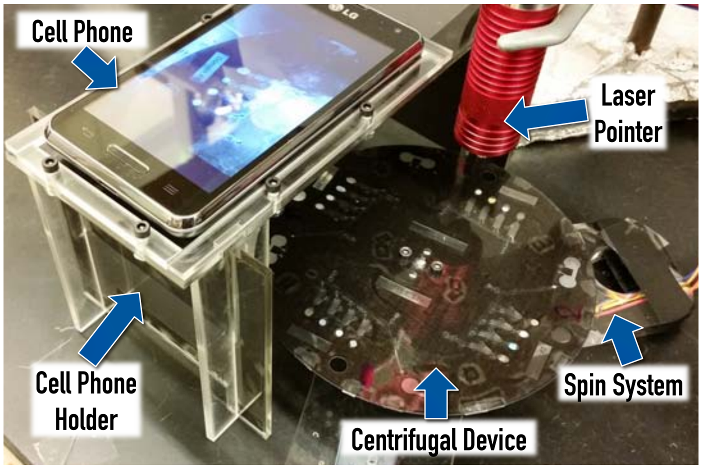

Figure 4-2. Image of the imaging setup with cell phone, cell phone holder (10 cm in height), device, spin system, and laser for valving labeled.

Initially, each colorimetric reaction was individually translated to the microfluidic device format. Each of the resulting color changes were analyzed by imaging the microfluidic device with a cell phone using a laser-cut PMMA holder for consistent imaging (**Fig. 4-2**). The images were analyzed for the color change within the device reagent chambers using ImageJ. Images were analyzed using both HSB and RGB color spaces to determine a method for implementing an objective and automated analysis scheme. The most appropriate image analysis parameter for detection was determined by analyzing the color change for various concentrations of each explosive. Quantitatively measuring the color response can be correlated to a qualitative 'yes or no' readout for determining the presence of an explosive material and discriminating between each explosive to provide additional information for safety of the user. Hue was the desired image analysis parameter for defining detection thresholds because color is represented by a single numerical value more closely related to the perceived color. Saturation, also within the HSB color model, was the desired secondary analysis parameter as it has potential for generating quantitative information based on color intensities. Although RGB was not the preferred analysis method, these results can be valuable for identifying problems with the analysis, verifying that the color is being correctly represented with the analysis, and for the detection of white and black colors. Since white contains all color, and black is the absence of all color, neither of these is defined as a particular shade of color and, therefore, not represented by any given hue value.

4.3.2.1 Organic Explosives

It is well-documented that polynitroaromatic compounds, i.e. TNT, DNT, and Tetryl, produce colored Meisenheimer complexes in alkaline solutions.[38] These Meisenheimer complexes are described as resonance-stabilized complexes and the red-colored product of the reaction between 1,3,5-trinitrobenzene and sodium methoxide is shown in **Figure 4-4**. A number of variations have been used for the detection of nitroaromatic explosives with changes in the alkali, organic base, and solvent compositions.[38-41] A 25% aqueous

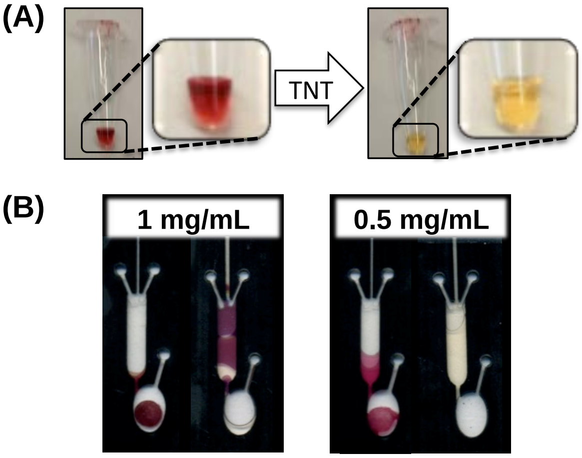

Figure 4-3. (**A**) Image of colorimetric reaction for 0.5 mg/mL TNT with tetramethylammonium hydroxide in-tube with zoomed-in inset for the red initial color (left) and yellow color after ~5 s (right). (**B**) Image of colorimetric reaction with tetramethylammonium hydroxide.

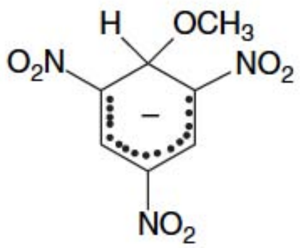

Figure 4-4. Resonance-stabilized Meisenheimer complex.

solution of tetramethylammonium hydroxide (TMAH) was used here as the colorimetric reagent for TNT, DNT, and Tetryl.[42] **Figure 4-3** shows the color change for 0.5 mg/mL TNT with TMAH in-tube. This colorimetric reaction has been reported to have a fast color change[40, 42] and is demonstrated in **Figure 4-3A,** where the red-colored product changed to yellow within ~5 seconds. When the TMAH reagent was transferred to the microfluidic device format using paper[29], the color was further stabilized at low TNT concentrations (**Fig. 4-3B**).

The polyester-paper device method (described in **Chapter 3**) was used to incorporate TMAH into the design described in **Figure 4-1**. TNT was added to the microfluidic device at various concentrations and analyzed using HSB and RGB color models. Due to the rapid color change, immediate image capture of the reaction

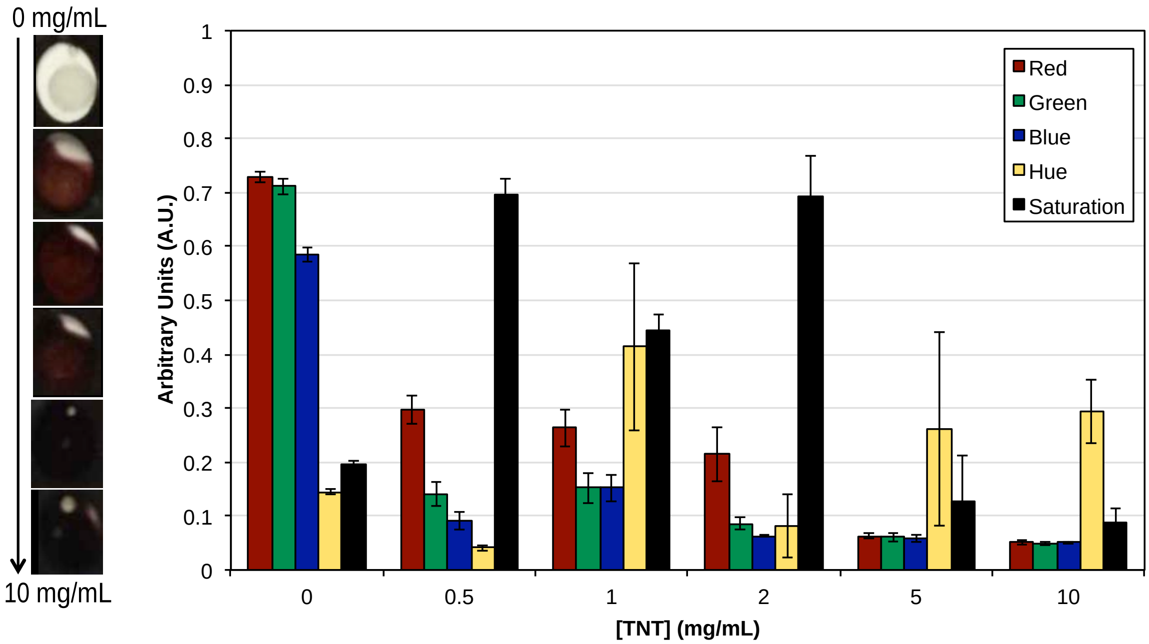

Figure 4-5. Image analysis results for R, G, B, hue, and saturation color responses of TNT and TMAH at varying concentrations from 0 – 10 mg/mL TNT, with exemplary images (left) of a reagent chamber for each color response.

chambers was performed after the centrifugal spin protocol was completed. The sample and reagent were mixed for 45 seconds during the device spin protocol before image capture. The device design allowed for n = 3 to perform initial assay evaluations, and **Figure 4-5** shows the image analysis for the color response of TNT and TMAH at varying concentrations from 0 – 10 mg/mL TNT with exemplary images for each color response. As the TNT concentration increased, the color response became darker. This was consistent with the decrease in RGB, each response <0.1 A.U., demonstrating that the color was too dark, or black, to discern the specific reaction color. This was also observed from the highly varied responses for hue and saturation that do not follow any particular trend.

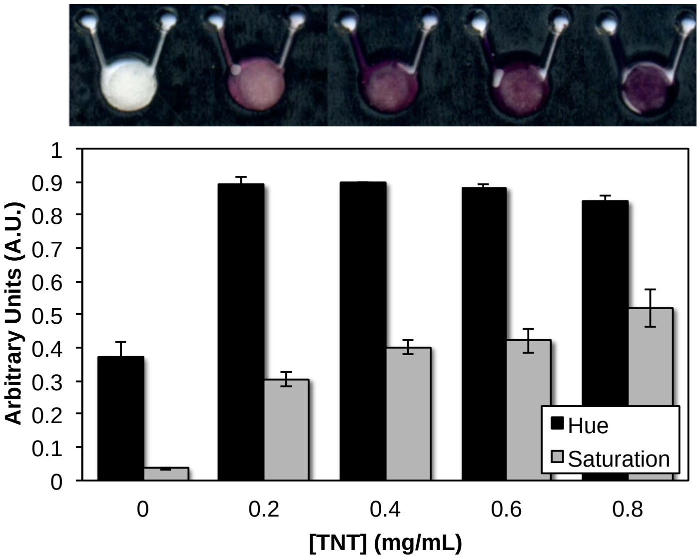

Figure 4-6. (**A**) Images of the corresponding color changes for TNT with TMAH at each concentration. (**B**) Image analysis results for color analysis using hue and saturation for TNT with TMAH at varying concentrations.

Since the analysis at higher TNT concentrations was problematic, lower concentrations from 0 – 0.8 mg/mL TNT with TMAH were analyzed using a microfluidic device with an array of chambers for controlled analysis with a desktop scanner. The hue and saturation results are shown in **Figure 4-6** with exemplary images of each color response above the respective data points. At lower concentrations of TNT, the saturation increased as expected with an increase in TNT concentration. Additionally, the hue response in the presence of TNT consistently remained in the purple hue value range demonstrating the shade of color for the reaction was similar at varying TNT concentrations. This was ideal for defining threshold values for the detection of TNT, where a positive detection range can be defined by +3σ of the negative hue response for 99.7% confidence that TNT is present based on hue analysis. This threshold value was found to be 0.521 A.U. using the microarray device and scanner analysis. These results demonstrated that lower concentrations of TNT, below 1 mg/mL, could be detected with color analysis while higher concentrations near 10 mg/mL may be problematic.

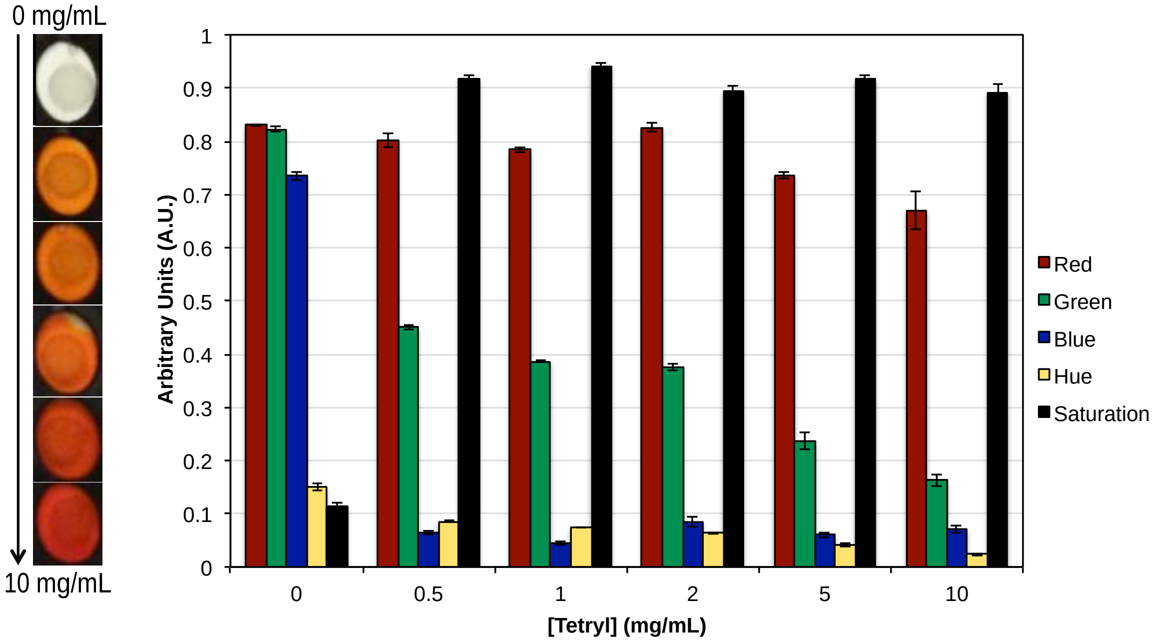

Figure 4-7. Image analysis results for R, G, B, hue, and saturation color responses of Tetryl and TMAH at varying concentrations from 0 – 10 mg/mL Tetryl, with exemplary images (left) of a reagent chamber for each color response.

Tetryl is both a polynitroaromatic and a nitramine compound due to the presence of a nitroamino group, and similar to TNT, a colored Meisenheimer complex is formed in alkaline solutions.[38, 41] While TNT forms a red-purple colored product with TMAH, Tetryl forms a red-orange color. As with initial TNT analysis, the described polyester-paper, toner-based device was used for evaluation of the color response with varying Tetryl concentrations from 0 – 10 mg/mL for n = 3. Image capture was taken immediately after the centrifugal spin protocol described, and the images were analyzed using HSB and RGB color models. The image analysis is shown in **Figure 4-7** with exemplary images for each of the color responses. Since the resulting color change was red in color, there was a greater red response in the presence of Tetryl than green or blue. The green response decreased with increasing Tetryl concentration due to the color changing from orange to red, and a high saturation response resulted for all Tetryl concentrations analyzed, and the hue response decreased as the Tetryl concentration increased due to an orange color response (~0.1 A.U.) at lower Tetryl concentrations and a red color response (<0.05 A.U.) at higher concentrations. The resulting hue trend was ideal for defining a threshold value for the qualitative detection of Tetryl, and a positive detection range can be defined as any value below 0.129 A.U., from -3σ of the negative hue response.

As shown in **Figure 4-3** with TNT, the color changed rapidly over 35 seconds within a microwell containing a 1:1 solution of TMAH and DNT. The images in **Figure 4-8** show the observed color change

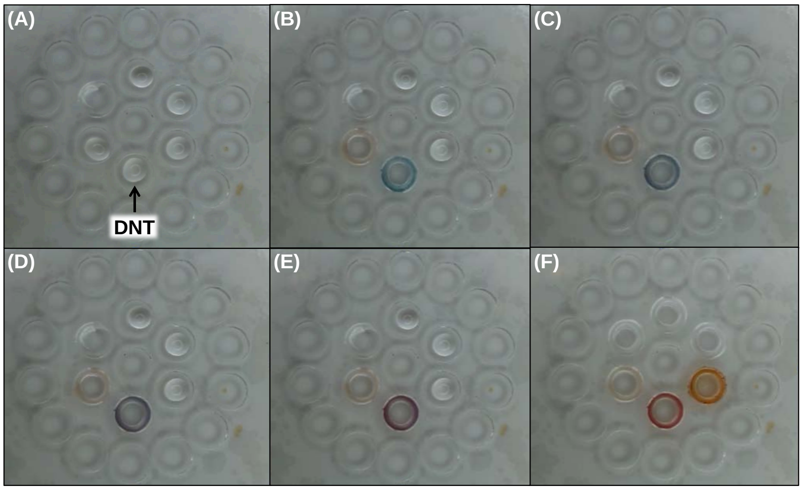

Figure 4-8. Images taken from a video showing the color change with DNT added to a chamber with TMAH (**A**) before the addition of DNT, (**B**) upon the addition of DNT, (**C**) 2.27 s, (**D**) 5.01 s, (**E**) 8.41 s, and (**F**) 33.25 s after the addition of DNT.

from shades of blue to shades of purple colors and finally to a red color. Performing this reaction with the microfluidic device, image capture was taken immediately after the centrifugal spin protocol for evaluation of the color response. The DNT concentration was varied from 0 – 10 mg/mL (n = 3) for initial image analysis using RGB and HSB color models, and the image analysis results are shown in **Figure 4-9** with exemplary images for each of the DNT concentrations. Due to the blue-green color change for DNT with TMAH, the blue and green color responses were greater than the red response at all DNT concentrations. Additionally, as the concentration of DNT increased, the saturation increased due to the darker color that was observed at concentrations near 10 mg/mL. The hue response also increased from ~0.3 A.U. to ~0.5 A.U. with increasing DNT concentration, as the color changed from blue-green to more blue colored. Based on the hue results, a threshold value defined at 0.155 A.U. can be used for qualitative detection of DNT.

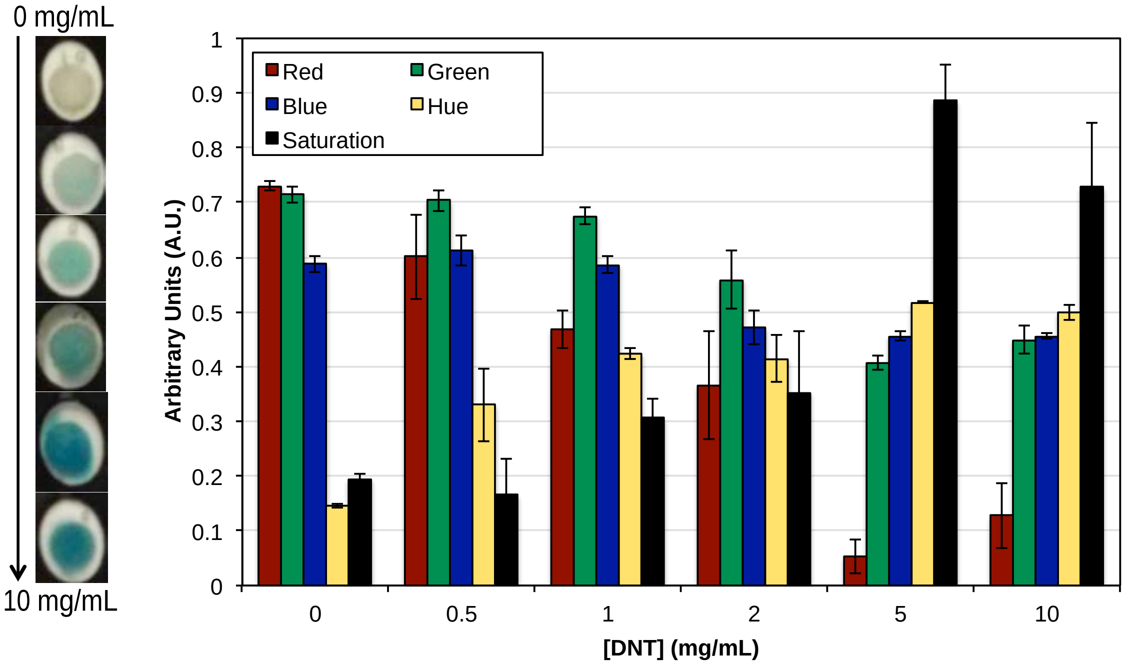

Figure 4-9. Image analysis results for R, G, B, hue, and saturation color responses of DNT and TMAH at varying concentrations from 0 – 10 mg/mL DNT, with exemplary images (left) of a reagent chamber for each color response.

concentrations was

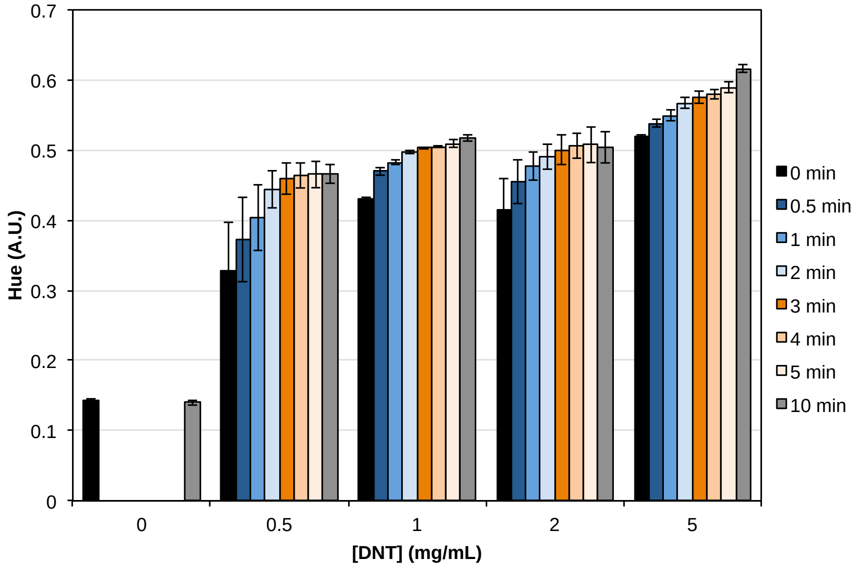

Figure 4-10. Hue analysis results for 0 – 5 mg/mL DNT with TMAH with image capture at 0, 0.5, 1, 2, 3, 4, 5, and 10 min time points for image analysis.

Since the hue response at 0.5 and 2 mg/mL DNT (**Fig. 4-9**) was more varied, or resulted in greater uncertainty, the color response at varying DNT assessed over time. The hue response from 0 – 5 mg/mL DNT over a number of time points including 0, 0.5, 1, 2, 3, 4, 5, and 10 min are shown in **Figure 4-10**. The hue response for 0.5 and 2 mg/mL DNT was still more varied, which is most likely due to subtle variations in color between the individual reagent chambers. The overall trend of increasing hue response with increasing time of the image capture was observed for each DNT concentration. The largest change in hue response was observed from 0 – 2 min, demonstrating that the color change was becoming a deep blue color (from an initial

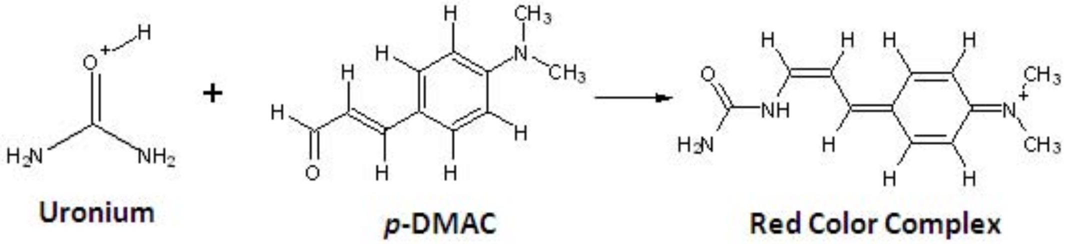

Figure 4-11. Reaction between uronium and *para*-dimethylaminocinnamaldehyde (*p*-DMAC) for a yellow to red color change with urea nitrate present.

blue-green color) over time. As a result of the negative hue response not changing over time, only the 0 and 10 min time points are shown in **Figure 4-10**. At any time point, the hue response did not fall below the defined threshold value (0.155 A.U.), allowing for image capture to be taken immediately to implement the fastest protocol for rapid detection.

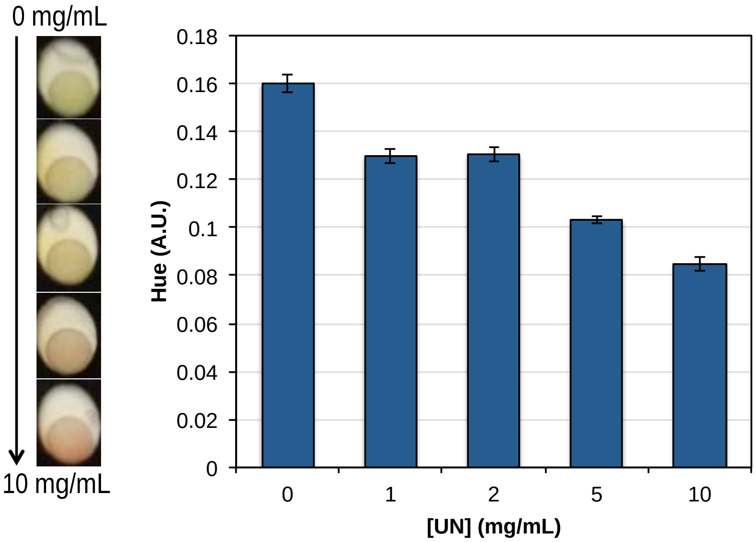

Figure 4-12. Initial hue analysis results for the reaction of 0.023 M *p*-DMAC with varying UN concentrations from 0 – 10 mg/mL.

Urea nitrate (UN) is not sold commercially but can be manufactured as an IED from urea fertilizer and nitric acid.[43] A colorimetric reaction between UN and *para*-dimethylaminocinnamaldehyde (*p*-DMAC) in ethanol produces a red-colored product. The hydrogen present with uronium (urea-like structure with an –OH group replacing the carbonyl group) protonates *p*-DMAC and allows for nucleophilic substitution in which uronium is added to *p*-DMAC with the loss of water (**Fig. 4-11**).[44] Previous work by Peters et al. demonstrated the use of 0.023 M *p*-DMAC for colorimetric detection of UN using a paper-based microfluidic device.[45] Initial tests using 0.023 M *p*-DMAC and varying UN concentrations from 0 – 10 mg/mL resulted in a subtle color change that was not consistent with the expected red color change (**Fig. 4-12**). The concentration of *p*-DMAC was increased to 0.046 and 0.069 M, with 0.069 M reaching the maximum solubility of *p*-DMAC in ethanol. Due to solubility constraints, *p*-DMAC at 0.069 M was spotted and overlaid onto filter paper three times (3X) for reagent storage to increase the amount of *p*-DMAC deposited onto the paper, rather than the originally reported 2X spots for this method.[29] The hue responses for the reaction of 10 mg/mL UN with each *p*-DMAC concentration over a number of time points including 0, 0.5, 1, 2, 3, 4, 5, and 10 min are shown in **Figure 4-13**, with exemplary images at each *p*-DMAC concentration for 0 and 10 min. The hue response varied the most over time at the lowest *p*-DMAC concentration (0.023 M) while the hue response varied the least at the highest *p*-DMAC concentration (0.069 M, 3X). Based on these results, 0.069 M, 3X-spotted *p*-DMAC was chosen as the optimal reagent concentration.

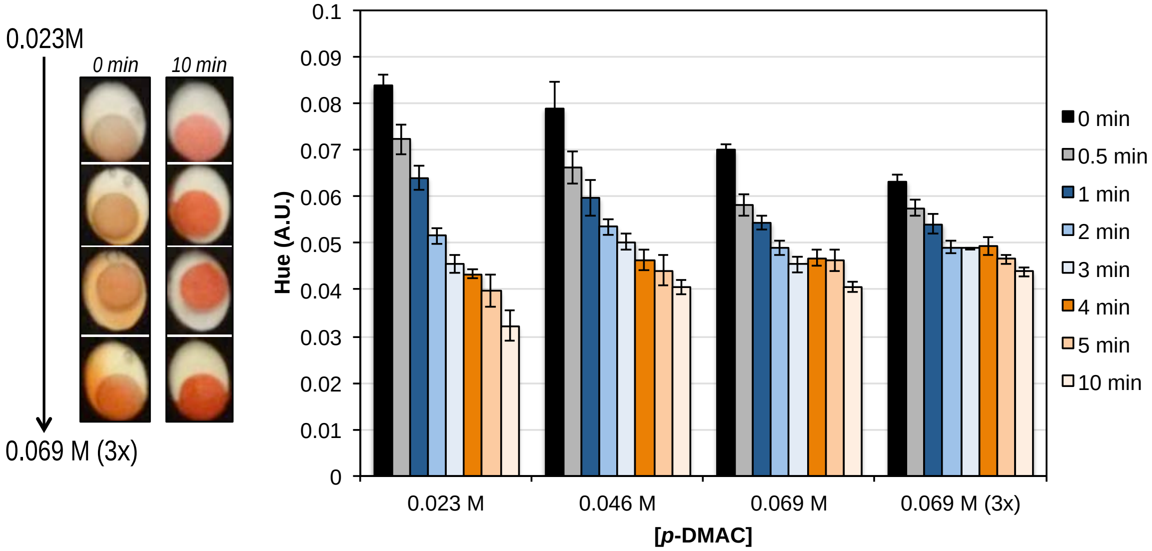

Figure 4-13. Hue analysis results for the reaction of 10 mg/mL UN and varying *p*-DMAC concentrations with image capture at 0, 0.5, 1, 2, 3, 4, 5, and 10 min time points for image analysis.

Image capture of the microfluidic device was taken immediately after the centrifugal spin protocol for image analysis using RGB and HSB color models at varying UN concentrations from 0 – 10 mg/mL (dilutions in methanol) for n = 3. The results from image analysis are shown in **Figure 4-14** with exemplary images for each UN concentration. The color change from yellow to red resulted with an increased red response compared to blue and green. As the UN concentration increased, the color change became more red-colored, resulting in a decreased green response at 5 and 10 mg/mL. Due to the natively yellow color of *p*-DMAC, the saturation at 0 mg/mL UN is higher than those responses seen previously with 0 mg/mL TNT, DNT, and Tetryl with TMAH. Although *p*-DMAC is colored, the saturation response still increased with UN present. The hue response decreased from ~0.15 A.U., a hue value indicative of a yellow color, to ~0.05 A.U. for a more red-colored product. Hue analysis can be used for detection with a threshold value defined at 0.149 A.U. for UN with *p*-DMAC.

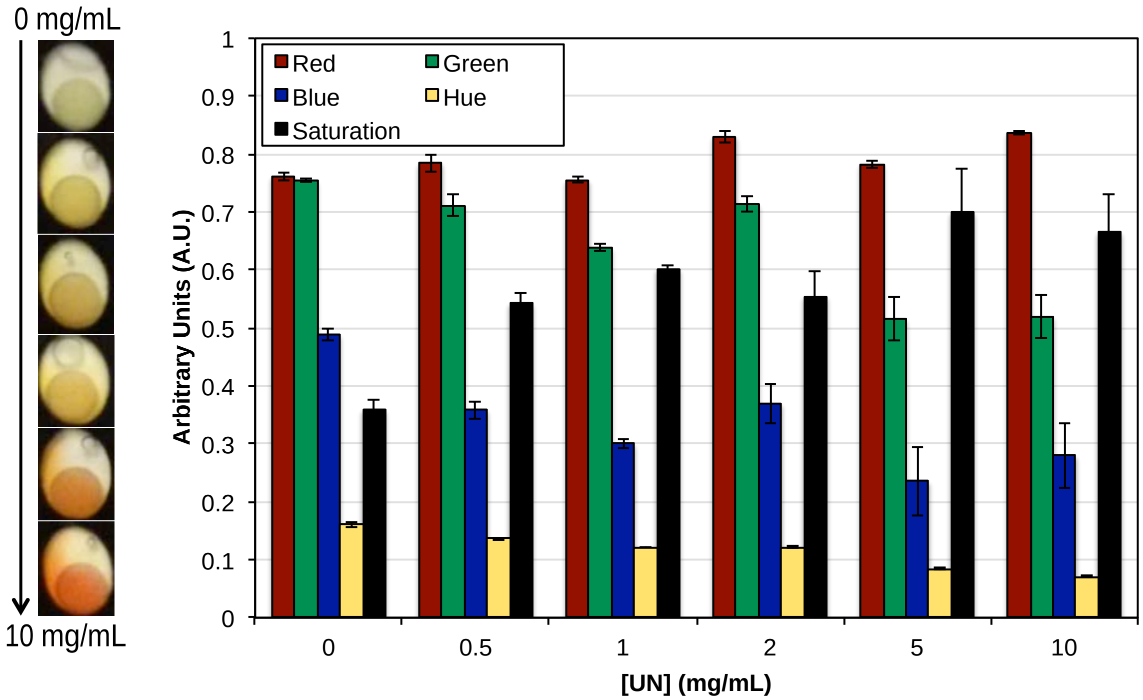

Figure 4-14. Image analysis results for R, G, B, hue, and saturation color responses of UN and 0.069 M (3X) *p*-DMAC at varying concentrations from 0 – 10 mg/mL UN, with exemplary images (left) of a reagent chamber for each color response.

4.3.2.2 Solvent Evaluation for Organic Explosives Detection

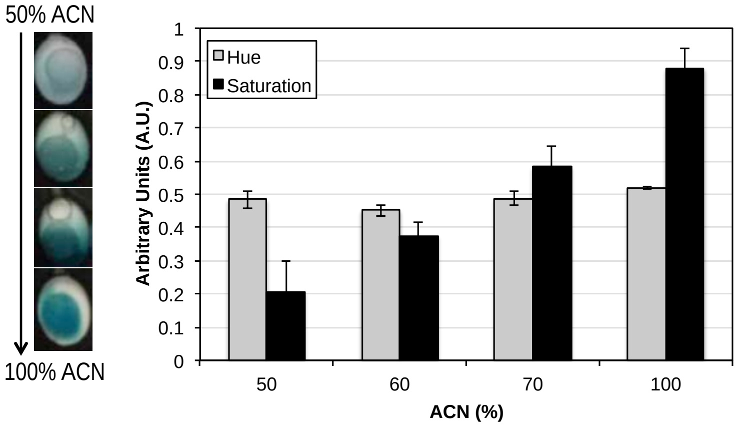

Figure 4-15. Hue and saturation analysis results for the reaction of 5 mg/mL DNT and TMAH with varying solvent compositions including 50%, 60%, 70%, and 100% acetonitrile (ACN) in methanol, with exemplary images (left) of a reagent chamber for each color response.

To decrease the number of sample processing steps, a solvent needed to be chosen for the dissolution of the organic explosives while maintaining a good colorimetric response. **Figure 4-15** shows the hue and saturation response for TMAH and 5 mg/mL DNT diluted in 50, 60, 70, and 100% acetonitrile (ACN) with methanol (MeOH). As the ACN concentration decreased, the saturation decreased due to a less intense blue color change, while the hue response did not change with decreasing ACN as the shade of the blue remained the same. Ideally, a solvent with the highest % ACN content should be used, however, UN does not dissolve readily in ACN and more readily dissolves in MeOH. To compromise between requiring both ACN and MeOH for analysis, a solution of 70% ACN and 30% MeOH was chosen (**Fig. 4-16**). The hue response for UN with 70% ACN from 0 – 3 mg/mL (constraints on UN concentrations used for analysis due to

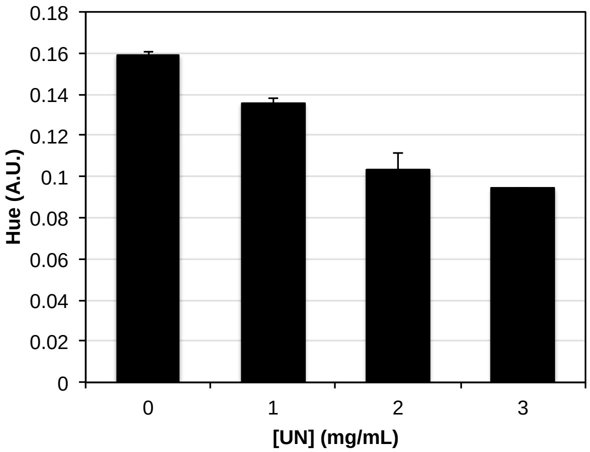

Figure 4-16. Initial hue analysis results for the reaction of 0.069 M (3X) *p*-DMAC with varying UN concentrations from 0 – 3 mg/mL in 70% ACN.

the purchased standard solution was in MeOH) resulted in a similar decrease in hue with increased UN concentration as observed with 100% MeOH.

4.3.2.3 Inorganic Explosives

The same device setup used for organic explosives analysis was used for the inorganic explosives. The described toner-based polyester-paper device (**Fig. 4-1**) was used for evaluation of each colorimetric reaction for n = 3 with image capture taken immediately after the centrifugal spin protocol was completed. The images were then analyzed using HSB and RGB color models.

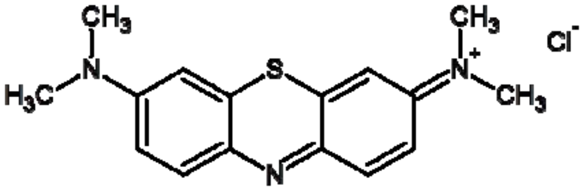

Figure 4-17. Methylene blue compound used for the blue to purple colorimetric reaction with perchlorate.

A simple color test for the detection of ClO_4^- has been reported utilizing dilute methylene blue (MB).[46] MB is natively blue-colored and when ClO_4^- is present it binds

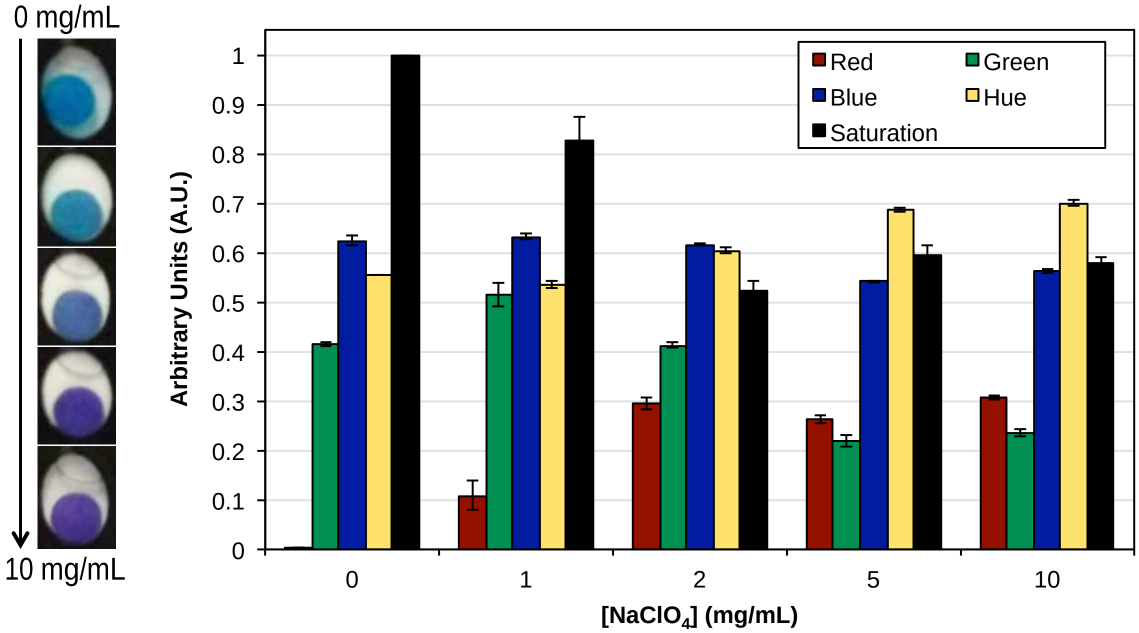

Figure 4-18. Image analysis results for R, G, B, hue, and saturation color responses for the reaction of $NaClO_4$ with MB at varying concentrations from 0 – 10 mg/mL $NaClO_4$, with exemplary images (left) of a reagent chamber for each color response.

with the MB complex, precipitating out a purple-colored product (**Fig. 4-17**). A dilute solution of 0.05% aqueous MB was used here for colorimetric detection of ClO_4^-. Varying concentrations of sodium perchlorate ($NaClO_4$) were added to the device, from 0 – 10 mg/mL, and analyzed for the color response with MB. The image analysis is shown in **Figure 4-18** with exemplary images for each concentration. Overall, the blue response was greater than red and green responses because blue was the predominant component of both the native MB color and the resulting purple-colored product in the presence of ClO_4^-. As the color changed to purple with ClO_4^-, the red response increased and the green response decreased. The native MB color resulted in a maximum saturation with a decreasing saturation response as ClO_4^- was added, and this was the only colorimetric reaction analyzed with this saturation trend. The hue response increased as ClO_4^- concentration increased, as the hue values from ~0.6 – 0.7 A.U. are associated with purple color. Hue analysis could be used for the qualitative detection of ClO_4^- with a threshold value defined as 0.558 A.U.

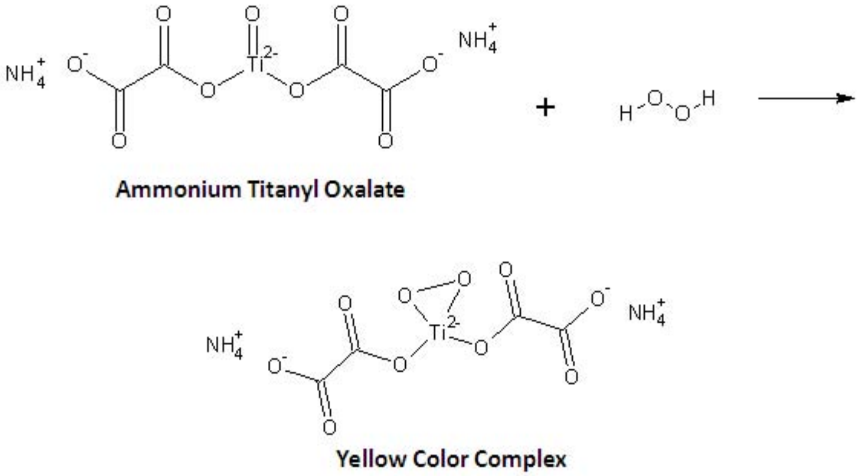

Figure 4-19. Reaction between hydrogen peroxide (H_2O_2) and ammonium titanyl oxalate (ATO) for a colorless to yellow colorimetric reaction.

Hydrogen peroxide (H_2O_2), a known constituent of peroxide-based IEDs, changes from a colorless to a yellow-colored product upon peroxide complexation with the Ti(IV) oxo moiety (**Fig. 4-19**) in the ammonium titanyl oxalate reagent (ATO).[43, 47] An aqueous solution of 1 M ATO was used here, and varying concentrations of H_2O_2 from 0 – 10 mg/mL were analyzed within the device. The image analysis is shown in **Figure 4-20** with exemplary images for each concentration. As the concentration of H_2O_2 increased, the blue response decreased. Alternatively, the saturation response increased with increasing concentrations due to the formation of a more saturated yellow color. Challenges occurred when hue was considered for the sole analysis parameter as there is no discrimination between the presence and absence of peroxide. This is due to all hue responses falling within the hue value range associate with a yellow color (~0.15 A.U.) requiring a different, or additional, image analysis parameter, i.e., saturation, for

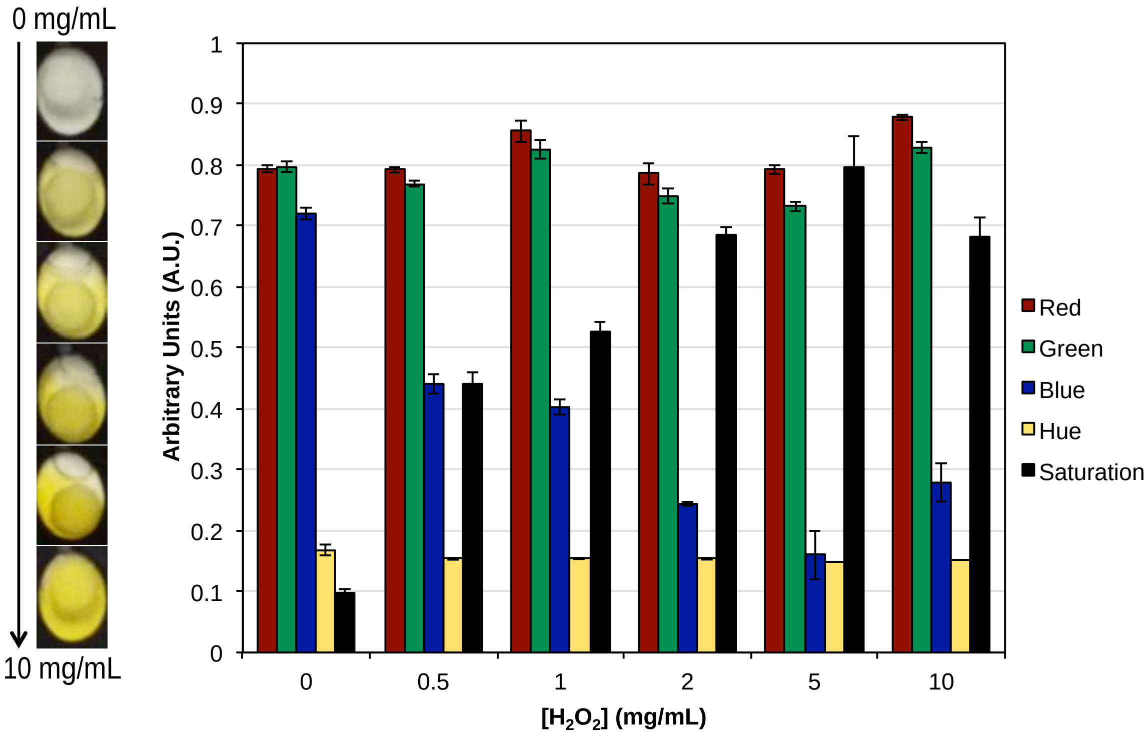

Figure 4-20. Image analysis results for R, G, B, hue, and saturation color responses for the reaction of H_2O_2 with ATO at varying concentrations from 0 – 10 mg/mL H_2O_2, with exemplary images (left) of a reagent chamber for each color response.

qualitative detection. This challenge results from the color white not able to be represented with hue, and consequently, the white paper results in a yellow-type hue value.

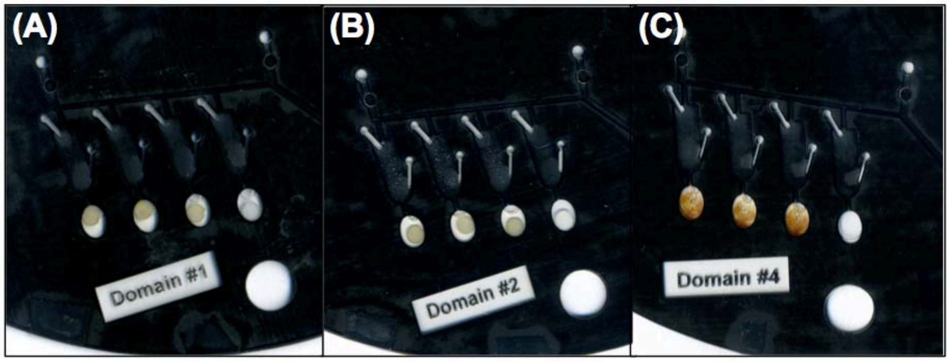

Figure 4-21. Images of Nessler's reagent stored within the microfluidic device on paper with (**A**) 0 mg/mL and (**B**) 10 mg/mL AN added, and images of Nessler's reagent pipetted directly onto the polyester device for storage for reaction with (**C**) 2.5 mg/mL AN.

Ammonium nitrate (AN) is commercially available and commonly used as an ammonium nitrate and fuel oil (ANFO) heterogeneous mixture IED.[43] For the colorimetric detection of AN, an ammonium (NH_4^+) test needed to first be implemented. The Nessler's reagent, containing potassium tetraiodomercurate (II) in an alkaline solution of potassium hydroxide (KOH), has been widely used for the determination of ammonium or ammonium nitrogen in different types of water (**Fig. 4-22**).[48-50] NH_4^+ is reduced to ammonia (NH_3) with KOH, and NH_3 reacts with Nessler's reagent (K_2HgI_4) to produce a brown color complex ($NH_2Hg_2I_3$).[51, 52] Due to the alkalinity needed for the Nessler's reagent, no reaction occurred with the reagent dried on paper for integration into the microfluidic device (**Fig. 4-21A,B**). Alternatively, when the reagent was pipetted onto the bottom polyester layer of the microfluidic device for storage, the colorimetric

$$2K_2HgI_4 + 2NH_3 \rightarrow NH_2Hg_2I_3 + NH_4I + 4KI$$

Figure 4-22. Chemical equation for the colorimetric reaction of ammonium with Nessler's reagent to produce a brown colored precipitate. Ammonia is produced from the reduction of ammonium with potassium hydroxide.

reaction with 2.5 mg/mL AN resulted in the characteristic brown precipitate (**Fig. 4-21C,D**). This was the only colorimetric reagent utilized that could not be stored in the polyester-paper device format. From these initial results, a reagent integration method was implemented where the reagent was added to the microfluidic device on the bottom polyester layer as a liquid with device layers 2 – 5 aligned and allowed to dry for ~10 min. Then, the capping polyester layer was added to the device and the device was bonded for use. Varying concentrations of AN from 0 – 10 mg/mL were added to this device format for reaction with Nessler's reagent, and the image analysis results are shown in **Figure 4-23** with exemplary images for each concentration. When AN was added, the blue response decreased by ~0.1 – 0.2 A.U. Although the saturation response increased with AN added, as the concentration of AN increased, the saturation response did not. This is most likely due to sedimentation of the free brown reaction precipitate in

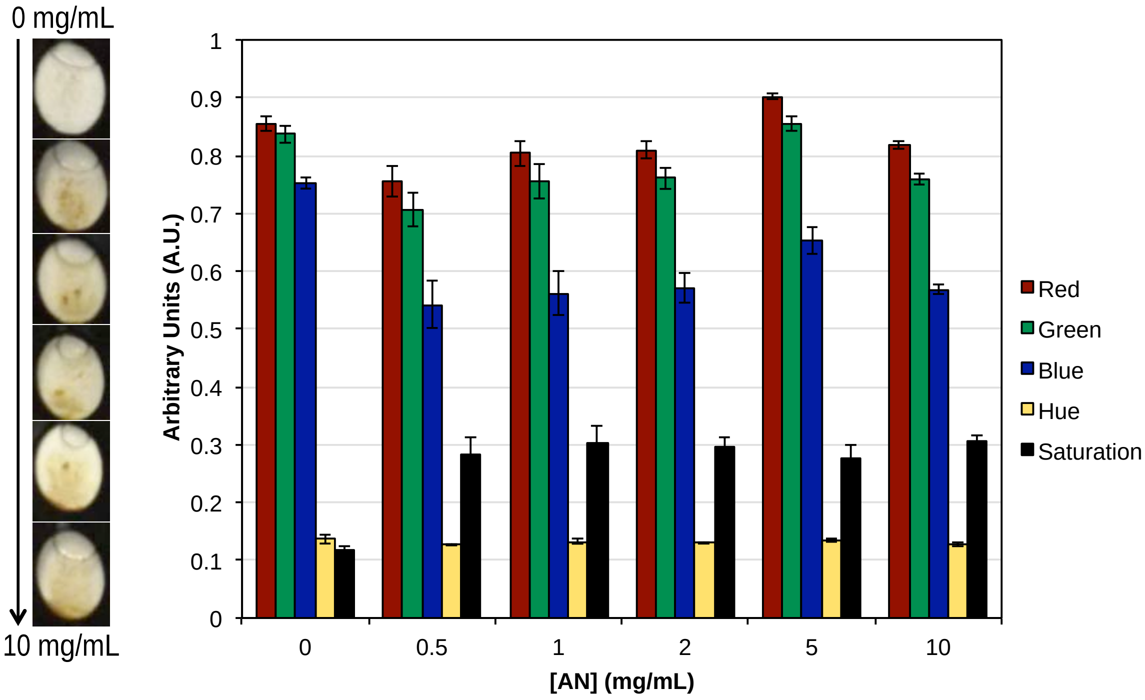

Figure 4-23. Image analysis results for R, G, B, hue, and saturation color responses for the reaction of AN and Nessler's reagent with liquid reagent storage at varying concentrations from 0 – 10 mg/mL AN, with exemplary images (left) of a reagent chamber for each color response.

solution to the bottom of the microfluidic reagent chamber during the centrifugal spin protocol. Additionally, due to the yellow-like color with AN present, all hue responses at each concentration resulted in ~0.15 A.U. providing no hue discrimination for qualitative analysis. Similar to the results observed for the H_2O_2 colorimetric reaction, ammonium detection would require a different image analysis parameter, i.e., saturation, for detection.

To facilitate detection of AN, and other explosives utilizing NO_3^- as an oxidizer, i.e., black powder, a colorimetric reaction for NO_3^- detection was required. The well-known Griess reaction was developed in 1879 and is used for the colorimetric detection of NO_3^- or nitrite (NO_2^-).[53] For this reaction, NO_2^- reacts with sulfanilic acid to form a diazonium cation which subsequently couples to 1-naphthylamine to produce a red-violet colored azo dye.[54] Due to the significant use and impact of the Griess reaction since development, a number of modifications to the original Griess assay have been made.[55-57]

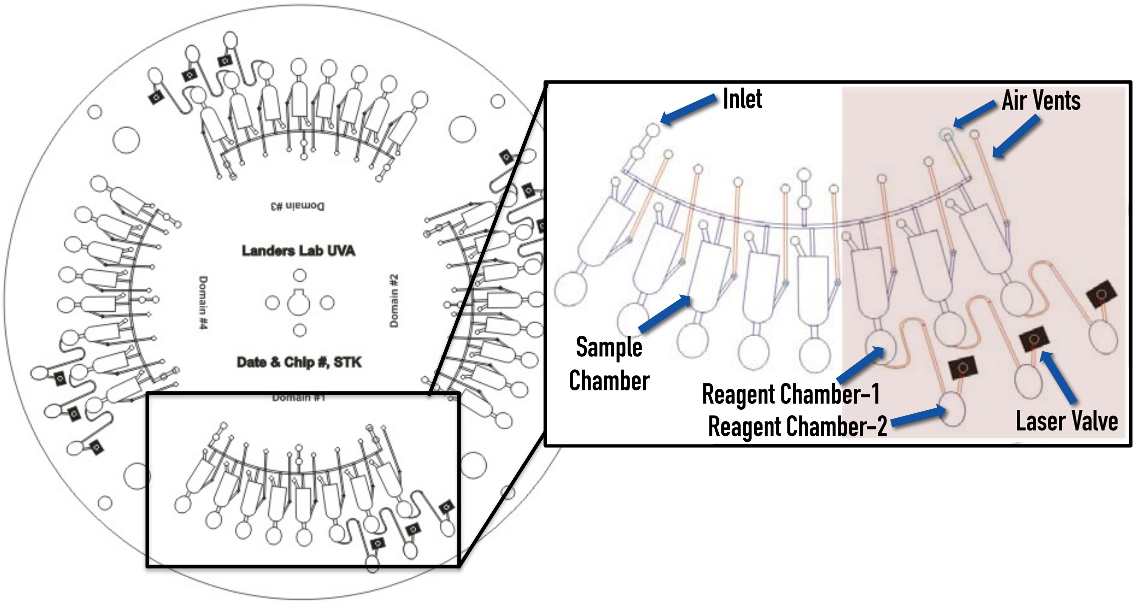

Figure 4-24. Device design optimized for multiplexed analysis from a single sample input to accommodate one- and two-step colorimetric reactions. The inset describes each feature of one domain (four total within one microfluidic device) for the complete design with the upper fluidic level (blue) and bottom fluidic level (red).

A modification of notable importance was by Bratton and Marshall replacing the use of carcinogenic 1-napthylamine with N-(1-naphthyl)ethylenediamine (NED) as a coupling component for sulfanilamide (**Fig. 4-25**).[58] This Griess reaction modification with NED resulted in a number of advantages for reproducibility, reaction time, and sensitivity, and has been the most commonly used Griess assay.[54]

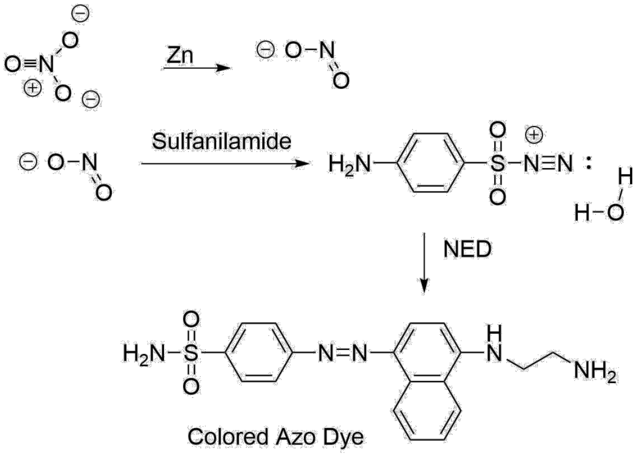

Figure 4-25. Modified Griess reaction for a colorimetric reaction between nitrate with sulfanilamide and N-(1-naphthyl)ethylenediamine (NED) reagents. Zinc powder was used to reduce nitrate to nitrite.

To implement the modified Griess reaction described using sulfanilamide and NED, the microfluidic device design needed to incorporate fluidic architecture capable of a two-step colorimetric reaction. The updated design is shown in **Figure 4-24** for the multiplexed analysis of each analyte from a single sample input, and the design included three additional channels for integration of the two-step modified Griess reaction for n = 3. Although the key features of the device design remained the same as originally discussed in **Figure 4-1**, small changes in the dimensions were made based on standard dye tests to assure precise fluidic movement and included: the sample channel width (3.5 mm), reagent chamber-1 width to allow for different sized paper punches to be evaluated when necessary (3.5 mm), and the narrow connecting channel width between the sample channel and reagent chamber-1 to allow for easier air displacement (0.7 mm). Changes in the air vent placement were made to move the vents to a position higher than the sample chambers to assure no sample spinout through the air vents occurred. The air vent started on the same fluidic layer (top layer) as the sample chambers (blue in **Fig. 4-24**) and was connected to the bottom fluidic layer (red in **Fig. 4-24**) by a circular port cut through both device fluidic layers (cyan port in **Fig. 4-24**). This allowed the vents to cross the fluidic architecture on alternate fluidic levels for no contact with the inlet channel. The topmost position of the tilted S-shaped channel used to connect the reagent chamber-1 to the reagent chamber-2 was utilized to assure that the pressure from the solution in reagent chamber-1 would not move the solution to the reagent chamber-2 until the device was spun. For additional fluidic control, a laser valve was positioned at the air vent of the reagent chamber-2 to prevent air displacement until the sample and reagent-1 were fully mixed.

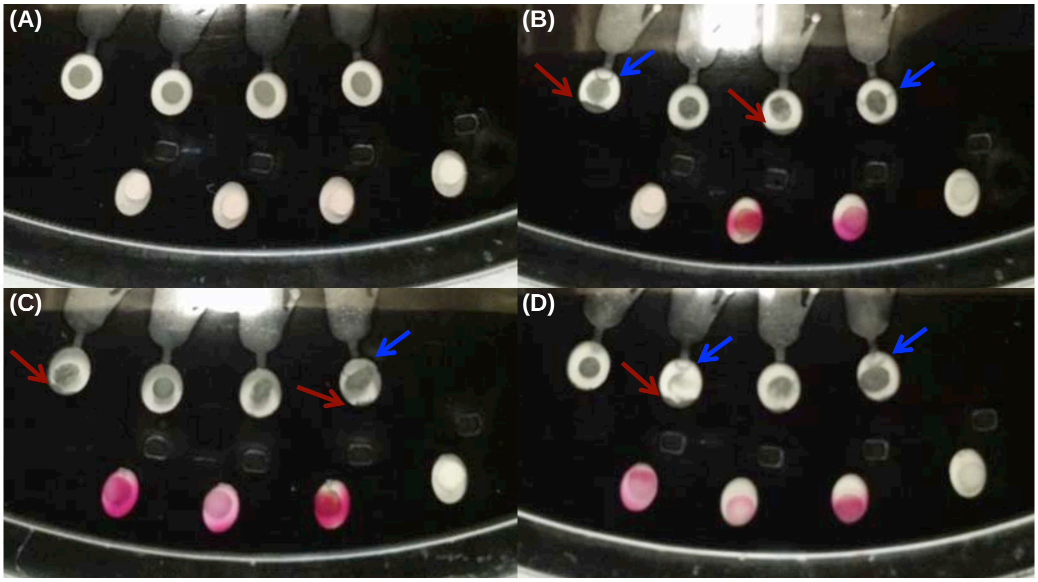

Figure 4-26. Images of zinc and NED reagent stored within a microfluidic device spotted in reagent chamber-1 and on paper in reagent chamber-2, respectively, without (**A**) and with (**B-D**) KNO_3 added. Red arrows highlight positions where zinc blocked fluidic channels and blue arrows highlight fluid menisci.

Once this integrated design was determined, the two-step architecture was isolated and used to fabricate a simplified device for optimization of the modified Griess reaction. Similar to initial tests for the one-step reactions, the device had four identical

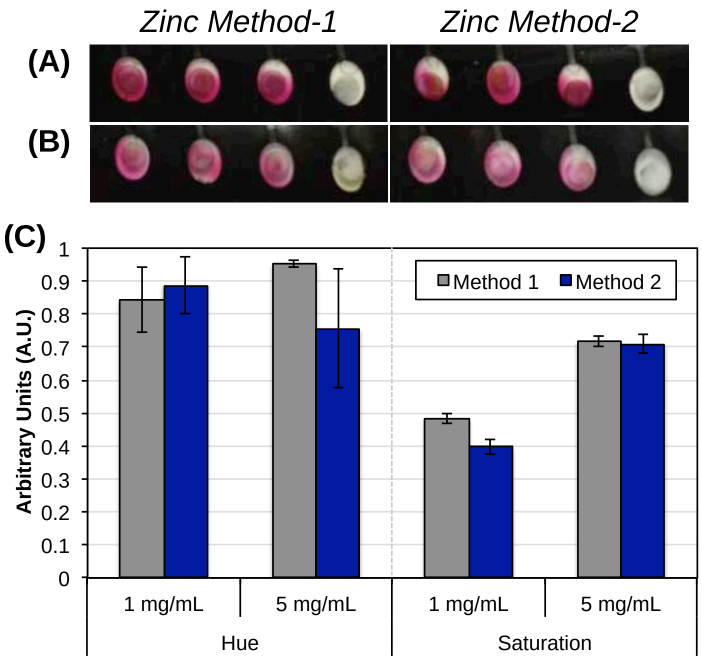

Figure 4-27. Images of the reaction between (**A**) 5 mg/mL and (**B**) 1 mg/mL KNO_3 with the modified Griess reagents stored using the one-step device design using two different zinc storage methods. (**C**) Hue and saturation analysis results for each corresponding image with both zinc storage methods.

sample channels to perform replicate (n = 3) analyses with an additional negative control chamber with no reagent added. To use the modified Griess reaction for NO_3^- detection, zinc powder was required to reduce NO_3^- to NO_2^- before the Griess reaction could proceed. A suitable method for integrating zinc powder into the microfluidic device was determined by using a 20% glycerol solution to control the zinc placement within the microfluidic device. For initial tests, zinc was spotted into the reagent chamber-1 (0.5 µL) and NED was added to the reagent chamber-2 using the polyester-paper device method. Potassium nitrate (KNO_3) was mixed with sulfanilamide off-chip and pipetted into the device to initially evaluate the color change. The images in **Figure 4-26** demonstrate the inconsistent color changes observed both within a single domain and within multiple domains (**Fig. 4-26B-D**). The hypothesis was that free zinc in solution sedimented and blocked the tilted S-shaped channel connecting the two reagent chambers during the centrifugal spin protocol. In many of the chambers where zinc was sedimented, a meniscus at the top of the reagent chamber was observed, indicating that the fluid movement to the reagent chamber-2 could not occur (blue arrows in **Fig. 4-26**).

To prevent the sedimentation effects from the zinc powder blocking the fluidic architecture, the one-step device design was utilized. A mixture of sulfanilamide and NED was added to paper for integration into the microfluidic device in the same chamber as the zinc. As a simple test to evaluate effects from the placement of the zinc in the chamber, two different zinc storage methods were implemented. Zinc method-1 incorporated zinc by spotting it on the bottom of the chamber (onto the polyester layer) and placing the reagent paper punch on top of this spot. Alternatively, the zinc method-2 was implemented by adding the zinc to the backside of the reagent paper punch in an attempt to stabilize the zinc placement in the chamber. It would be expected that when zinc was added to the reagent paper punch in the zinc method-2, the zinc spot would not sediment considerably. The comparison hue and saturation analysis from the two zinc integration methods is shown in **Figure 4-27**. Although variations were seen in the hue

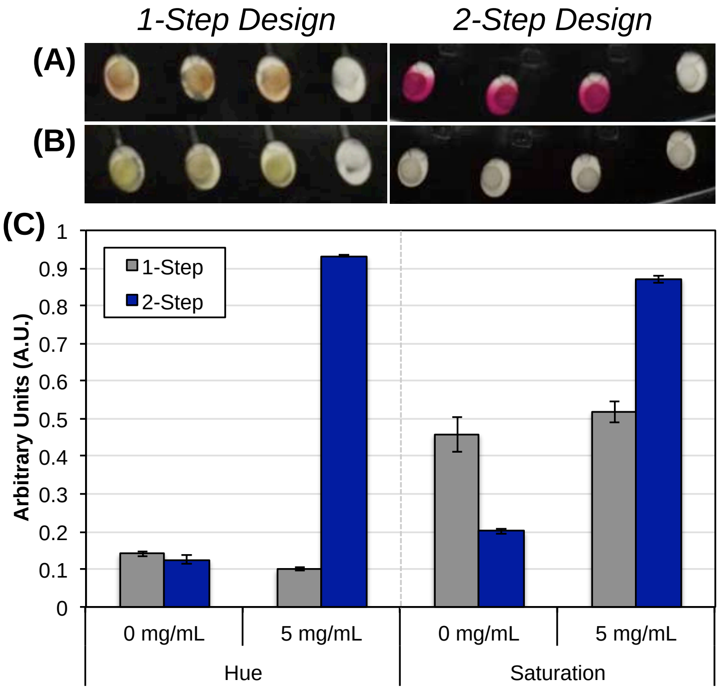

Figure 4-28. Images of the reaction between (**A**) 5 mg/mL and (**B**) 0 mg/mL KNO_3 with the modified Griess reagents stored over two weeks using the one-step and two-step device designs and zinc storage method-1. (**C**) Hue and saturation analysis results for each corresponding image for both device designs.

results for both zinc methods, the saturation response was increased for the zinc method-1 with 1 and 5 mg/mL KNO_3 added. The more saturated color change was ideal and likely due to increased reduction of NO_3^- to NO_2^- with the free zinc in the chamber not stabilized on paper. The zinc method-1 was applied for further studies comparing the one-step reaction method to the two-step method. Devices for each method (one- and two-step) were fabricated and stored at room temperature in the dark for two weeks. After the initial storage time, 0 and 5 mg/mL KNO_3 were added to the devices, and the hue and saturation results with exemplary images of the colorimetric reactions are shown in **Figure 4-28**. Although the one-step device design was ideal to simplify the fluidics, unfortunately, the reagents were not stable in this format when stored over time. The two-step approach was chosen for implementation of the modified Griess reaction for NO_3^- detection with the centrifugal microfluidic platform. Although color analysis was performed to evaluate the image analysis capabilities, future work optimizing the two-step device design was still needed.

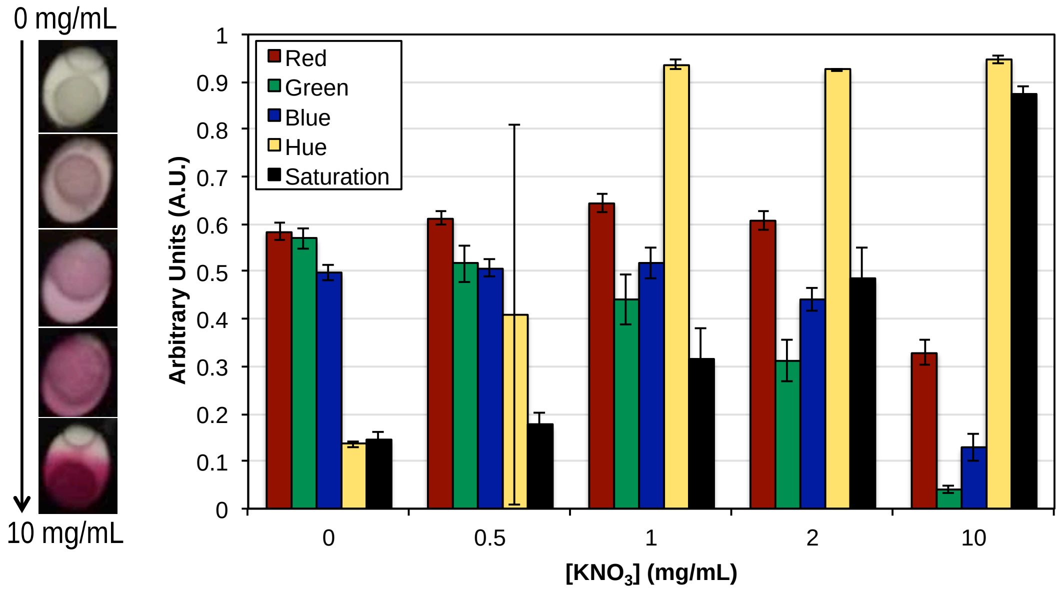

Figure 4-29. Image analysis results for R, G, B, hue, and saturation color responses for the reaction of KNO_3 with the zinc and the modified Griess reagents at varying concentrations from 0 – 10 mg/mL KNO_3, with exemplary images (left) of a reagent chamber for each color response.

Varying concentrations of KNO_3 from 0 – 10 mg/mL were added to the two-step device format for reaction with the modified Griess reagents. The image analysis results are shown in **Figure 4-29** with exemplary images for each concentration. The green and blue responses decreased as the NO_3^- concentration increased, due to the contribution of red in the resultant color. As expected, the saturation response increased as the concentration of NO_3^- increased. The hue response also increased in the presence of NO_3^-, but remained at ~0.95 A.U. as the shade of the color did not change over varying concentrations. The significant increase in hue was ideal for using hue for qualitative detection. A threshold value was defined as 0.157 A.U., but 0.5 mg/mL may result in a false negative due to the significant variation between replicate analyses.

The hue histograms using ImageJ for each 0.5 mg/mL KNO_3 replicate are shown in **Figure 4-30A-C**. A color bar representation was added to the bottom of the histogram in **Figure 4-30A**, to demonstrate the color association with each pixel hue value along the x-axis. Due to how the HSB color model is derived, a red color is associated with hue

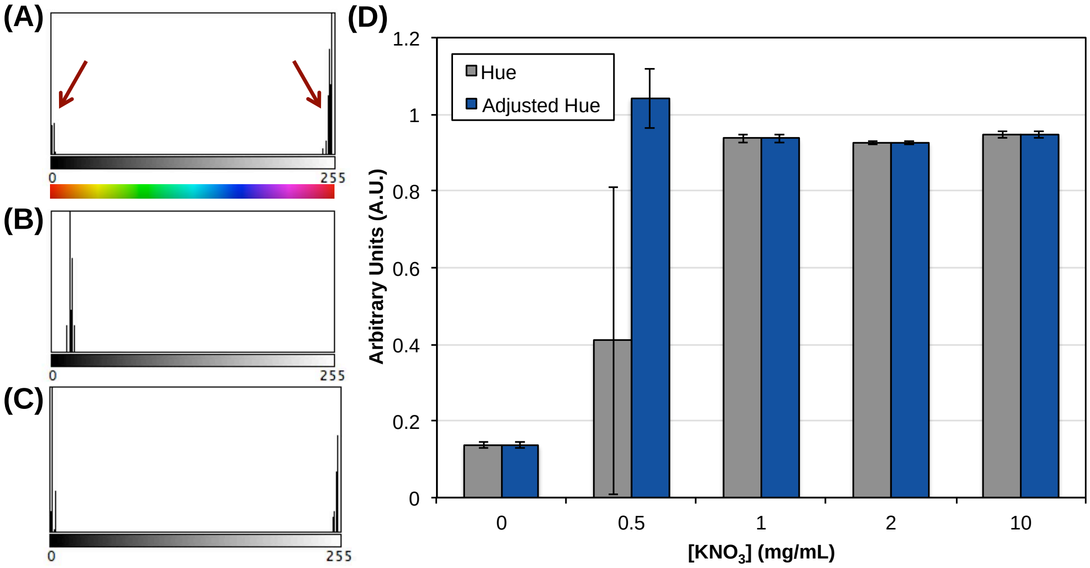

Figure 4-30. (**A-C**) Hue histograms using ImageJ for replicate 0.5 mg/mL KNO_3 responses, with the addition of a schematic color bar demonstrating the color representation for each pixel hue value. (**D**) Hue and adjusted hue analysis for varying concentrations from 0 – 10 mg/mL KNO_3.

values at both ends of the x-axis, which was converted to A.U. and represents 0 and 1 A.U. values on the y-axis of the image analysis plots. The histogram in **Figure 4-30B** has the majority of the pixel count at a pixel hue value of ~16, or 0.062 A.U. Alternatively, the histograms in **Figure 4-30A&C** have identical pixel counts, but the pixel hue values related to those counts result in two peaks at ~0 and 255, or 0 and 1 A.U. When the average pixel hue value from each histogram was averaged, and then averaged between three replicates, the result was significantly varied, as seen for 0.5 mg/mL in **Figure 4-29**. This limitation can be accounted for during hue analysis by adjusting the hue data. The pixel hue values from 0 – 255 were adjusted to 25 – 280, or 0.098 – 1.098 A.U. For example, a pixel count of 200 at the pixel hue value of 15 would be adjusted to a pixel hue value of 271 instead. The described adjustment would result in a single peak for each histogram in **Figure 4-30** at ~1 A.U. Since all of the pixel hue values associated with the pixel counts for the histogram in **Figure 4-30B** are between 13 – 20, this peak will now be positioned at pixel hue values 269 – 276, or 1.054 – 1.082 A.U. A comparison of the hue data and the adjusted hue is shown in **Figure 4-30D**. The adjusted hue did not change for any NO_3^- concentration other than 0.5 mg/mL because all of the

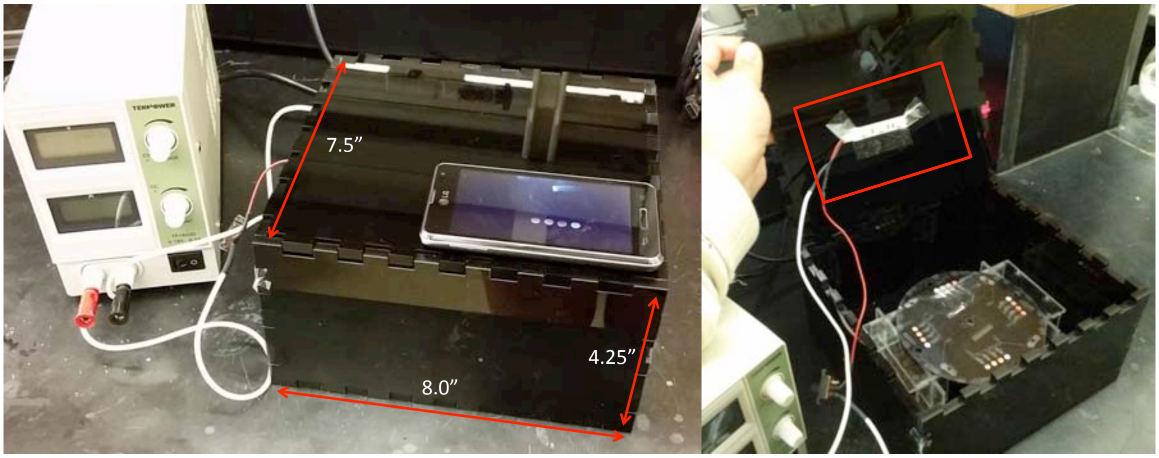

Figure 4-31. (**Left**) Image of the enclosure with cell phone and power supply for adjusting LED brightness. (**Right**) Image of the enclosure opened to show the device and three-LED strip positions.

hue values for concentrations from 1 – 10 mg/mL were above a 25 hue value, or 0.098 A.U. and, therefore, were not adjusted.

Figure 4-32. Image from the cell phone camera of the device without (**left**) and with (**right**) focus, with LED brightness adjusted using the power supply at 8.2 and 9 V, respectively.

4.3.3 Consistent Lighting for Image Analysis

The imaging setup described in **Figure 4-2** was utilized for initial analyses of each colorimetric reaction. Implementing a cell phone holder aided in imaging and analysis by allowing the cell phone to be in a consistent position for each image capture event. Once the initial analyses were performed, a new imaging setup was needed to have additional lighting control for analysis optimization. A simple PMMA enclosure was laser cut using a design generated with MakerCase (http://www.makercase.com/).

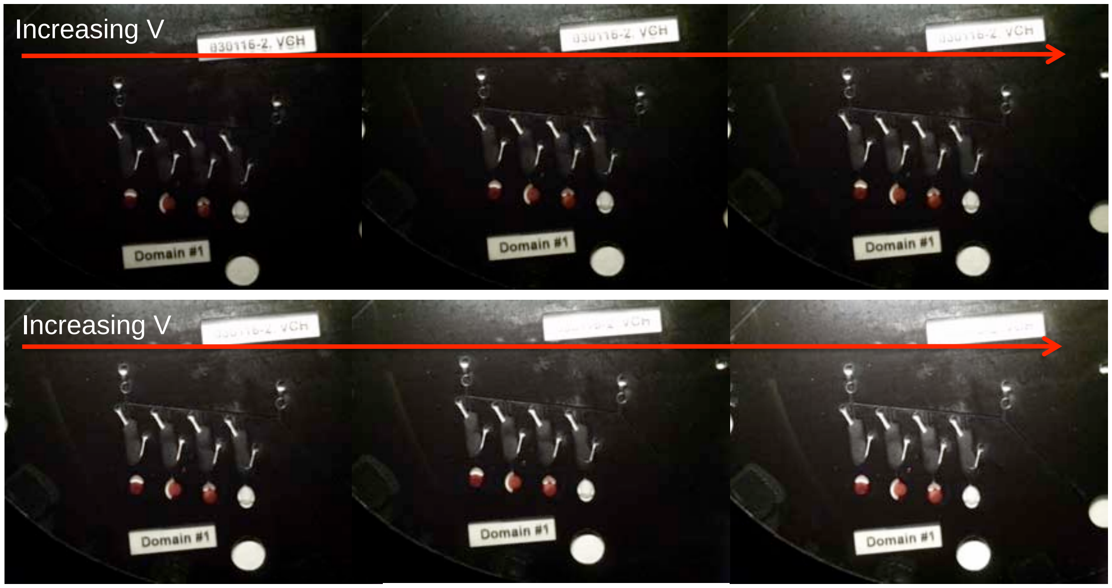

Figure 4-33. Replicate images from the cell phone camera of the device, with LED brightness adjusted using the power supply at 8.2, 8.5, and 8.8 V (top row), respectively, and 9.0, 9.2, and 10.0 V (bottom row), respectively.

This box generator website provides an easy platform for generating an enclosure of customizable size with finger-type edge joints. The assembled enclosure is shown in **Figure 4-31**, and a three-LED strip and power supply with adjustable voltage was implemented to control lighting. During initial optimization of the lighting position, the LED strip was simply attached to the enclosure with scotch tape. The microfluidic device was elevated off of the bottom of the enclosure using a PMMA stand to evaluate lighting from underneath the device. The cell phone was positioned to be 2.5” above the device for each device domain to be completely in view for imaging. Once an optimal LED position was determined to be above the device, positioned 4 cm below the cell phone camera hole for imaging, the LED strip was adhered to the lid using a more robust pressure-sensitive adhesive.

Once the position of the LED strip was determined, the brightness of the LEDs, controlled using voltage here, needed to be evaluated. The ability for the phone to auto-focus was important for automated imaging, and the images in **Figure 4-32** demonstrate that above 8.2 V the phone would consistently auto-focus, while below 8.2 V resulted in lighting that was not bright enough for the

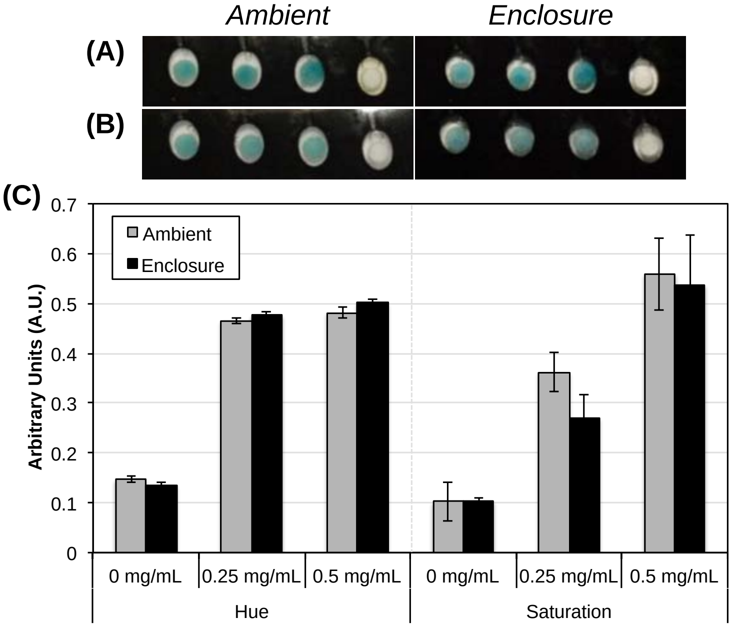

Figure 4-34. Images of the reaction between (**A**) 0.5 mg/mL and (**B**) 0.25 mg/mL DNT with TMAH using ambient and enclosure lighting. (**C**) Hue and saturation analysis results for each corresponding image for both lighting formats.

camera to acquire focus on the device. The effective range for lighting evaluation was defined as 8.2 – 10 V (**Fig. 4-33**), as >10 V would wash out the resulting color within the device reagent chambers. Initial attempts to optimize lighting further were comprised of reproducing the ambient lighting results using the PMMA phone holder with image analysis using the PMMA enclosure. Images were taken immediately after the centrifugal spin protocol with both ambient (using the setup from **Fig. 4-2**) and the enclosure lighting at 8.6 V for 0, 0.25, and 0.5 mg/mL concentrations of DNT and TNT. The hue analysis for DNT at each concentration resulted in similar values; however, the average hue results using the enclosure were slightly increased with DNT, indicating a slightly more blue color compared to blue-green (**Fig. 4-34**). Alternatively, the average hue results at 0 mg/mL DNT decreased slightly, resulting in a greater change in hue between a positive and negative DNT sample. The saturation analysis with DNT was varied with both ambient and enclosure analysis, and the saturation response for 0.25 mg/mL DNT decreased using the enclosure. The average hue results were similar for ambient and enclosure lighting with TNT (**Fig. 4-35**), and the saturation response increased consistently for TNT using the enclosure for analysis.

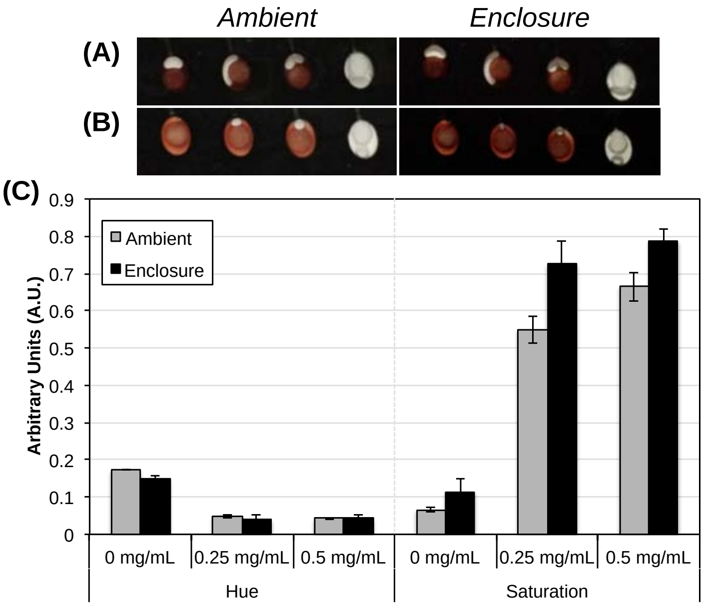

Figure 4-35. Images of the reaction between (**A**) 0.5 mg/mL and (**B**) 0.25 mg/mL TNT with TMAH using ambient and enclosure lighting. (**C**) Hue and saturation analysis results for each corresponding image for both lighting formats.

4.3.4 Color Manipulation Through Microdevice Tinting

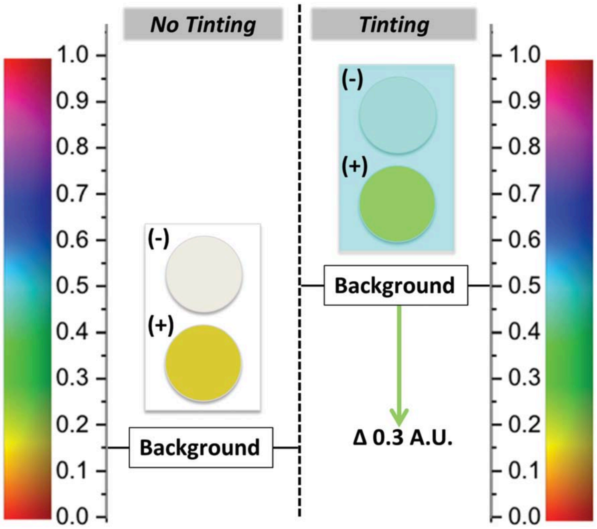

Figure 4-36. Schematic of the tinting method to manipulate color change. Color association with the y-axis for hue in arbitrary units (A.U.) is correlated with H_2O_2 colorimetric reaction with ATO as colorless to yellow (no tinting) and as cyan to yellow (tinting). Inset images of H_2O_2 reaction with and without tinting are shown.

Hue image analysis is advantageous for defining threshold values towards qualitative detection of explosives as color is represented by a single numerical value, rather than the sum of individual RGB values. Hue was utilized for defining threshold values for most of the colorimetric reactions described here, however, limitations were observed for analyzing H_2O_2 and NH_4^+ colorimetric reactions. Since hue analysis does not allow for the adequate detection of 'white', as it contains all colors (and is not associated with a particular shade of color), the post-reaction color of a reagent-saturated paper with sample without H_2O_2 or AN present is white. In the absence of 'tinting', a negative sample results in a hue value most closely associated with yellow, and since a positive sample for H_2O_2, for example, turns yellow with ATO, the reaction is essentially undetectable (**Fig. 4-36**). Fabricating devices from paper and polyester substrates allows for a variety of opportunities for colorimetric manipulation tinting such as dyeing paper, printing polyester, and applying colored light onto transparent detection areas. In order to evaluate the impact that each form of tinting has on an interpreted color change, the colorless-to-yellow color change from the reaction of H_2O_2 with ATO was utilized for development of each method.

4.3.4.1 Direct Dye Tinting of the Reagent-Saturated Paper

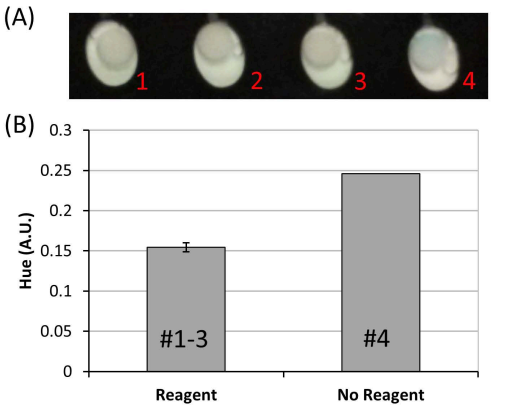

Figure 4-37. Tinting reagent paper with dye. (**A**) Images of paper tinted with erioglaucine before ATO reagent was added (1-3) and tinted without reagent added (4). (**B**) Hue response for the dye tinted punches in (A) with and without added reagent.

The first form of tinting involved altering the color of the paper substrate with dye. In theory, the background color can be tinted to shift the resultant color into a part of the spectrum that ultimately is more detectable. In **Figure 4-36**, without tinting, the negative and positive hue value for the white-to-yellow color change remain the same. If the background is then tinted cyan for the same white-to-yellow color change, the change in hue is now detectable as the native color change is combined with the tinted color, altering the overall color change to be cyan-to-green.

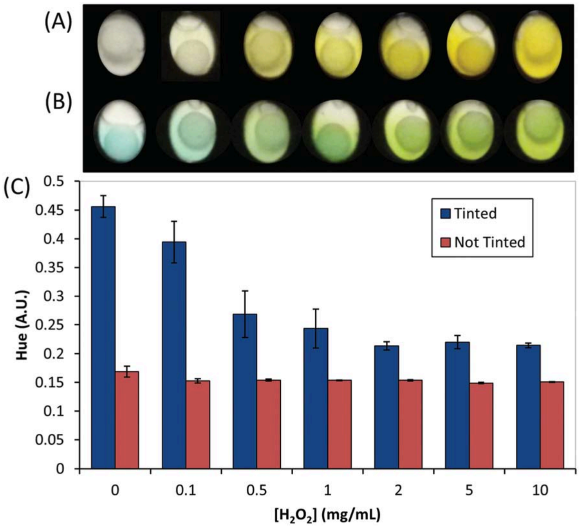

Figure 4-38. Tinting reagent paper with dye. (**A**) H_2O_2 colorimetric reaction with ATO reagent punches, changing from colorless to yellow. (**B**) H_2O_2 colorimetric reaction with ATO reagent punches tinted blue with dye, changing from blue to green-yellow with increasing H_2O_2 concentration. (**C**) Hue data analysis (n = 3) for each color change shown for punches in (A) and (B).

This was first trialled by pre-dying the reagent-saturated paper substrate containing ATO using a blue dye (erioglaucine). Attempts to dye the filter paper prior to reagent addition resulted in irreproducible shades of blue between paper punches with or without reagent (**Fig. 4-37**). However, when dying the paper following ATO addition, the difference in color between tinted and non-tinted paper was improved.

This is shown in **Figure 4-38** where, in the absence of tinting, the shade of yellow resulting from the presence of H_2O_2 over an order of magnitude concentration range (0 – 10 mg/mL) remained the same as indicated by no significant change in hue (**Fig. 4-38A&C**). In contrast, tinted substrate **(Fig. 4-38B**) allowed for a strong H_2O_2 concentration-dependent color change from blue (negative) to green, with a lower limit of detection (LOD) of 100 µg/mL (blue-green) and as high as 10 mg/mL H_2O_2 (green). With >2 mg/mL H_2O_2, the measured hue with tinted substrate tends to plateau as the reaction becomes reagent-limited. While this tinting method was simple for incorporating into device fabrication, it could result in dye-sample interactions within the detection chambers, affecting the colorimetric response. As a result, additional microchip tinting methods were explored.

4.3.4.2 Print-based Tinting of the Microdevice

An alternative to dyeing the reaction substrate was explored in the form of print-based tinting. During the fabrication of polyester-toner microdevices using the PCL technique, there are several steps that require printing toner on the polyester surface for either bonding or valving. As a result, tinting select areas of the microdevice with colored printer toner is a process that can be seamlessly integrated into the rapid PCL fabrication method. Additionally, a distinct advantage of print-based tinting was that it circumvented problems associated with chemical interference that may result from interaction between the dye and the

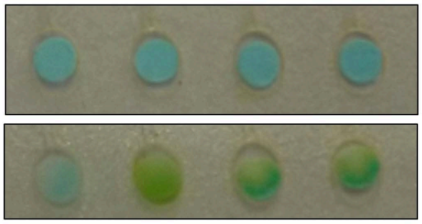

Figure 4-39. Images of tinting with dye on reagent paper punches. Images of H_2O_2 reagent punches tinted blue (**top**) and resulting heterogeneous color change with 10 mg/mL H_2O_2 added (**bottom**).

sample. For example, if the dye used to tint the paper is water-soluble, the resulting color of the paper punch can be heterogeneous in nature (**Fig. 4-39**).

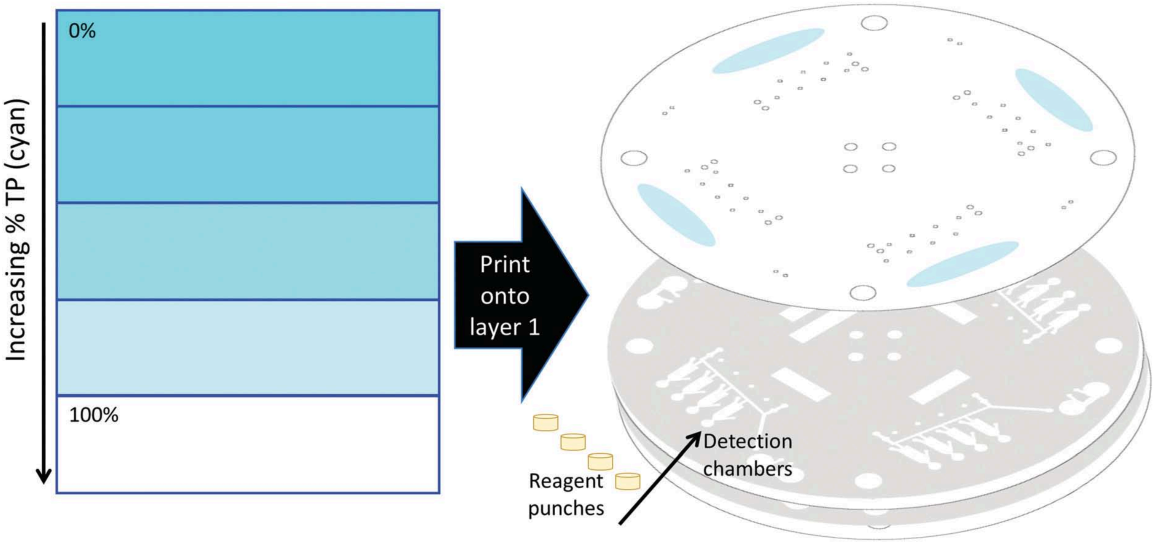

Figure 4-40. (**Left**) A schematic showing increasing % transparency (% TP) in a particular color (cyan here) as a form of gray scale to manipulate the print-based tinting intensity. (**Right**) Schematic of the device with print-tinting on layer 1 with paper punches added to device chambers below tinted regions.

In contrast, print-based tinting has remarkable bandwidth with respect to color selection, intensity and/or transparency of the color that can be directly embedded onto the polyester surface (**Fig. 4-40**). Additionally, other microfluidic devices utilize printable substrates that can be laminated, (e.g., paper-based devices[59]), and these can be tinted by printing onto the transparency sheet that is laminated. Printing colored toner is a simple method that provides considerable spatial control over the tint location and has flexibility in the tint color selection. This allows multiple tint colors, specific to different colorimetric reactions in a multi-reagent device, to be printed onto a single device layer. As a result, a LaserJet printer can be exploited to define architecture, print valves, and tint the surface of detection zones for colorimetric reaction detection.

To determine the effectiveness of this approach, four tinting colors – red, green, blue, and cyan – were printed above the detection zones, or reagent chambers of the one-

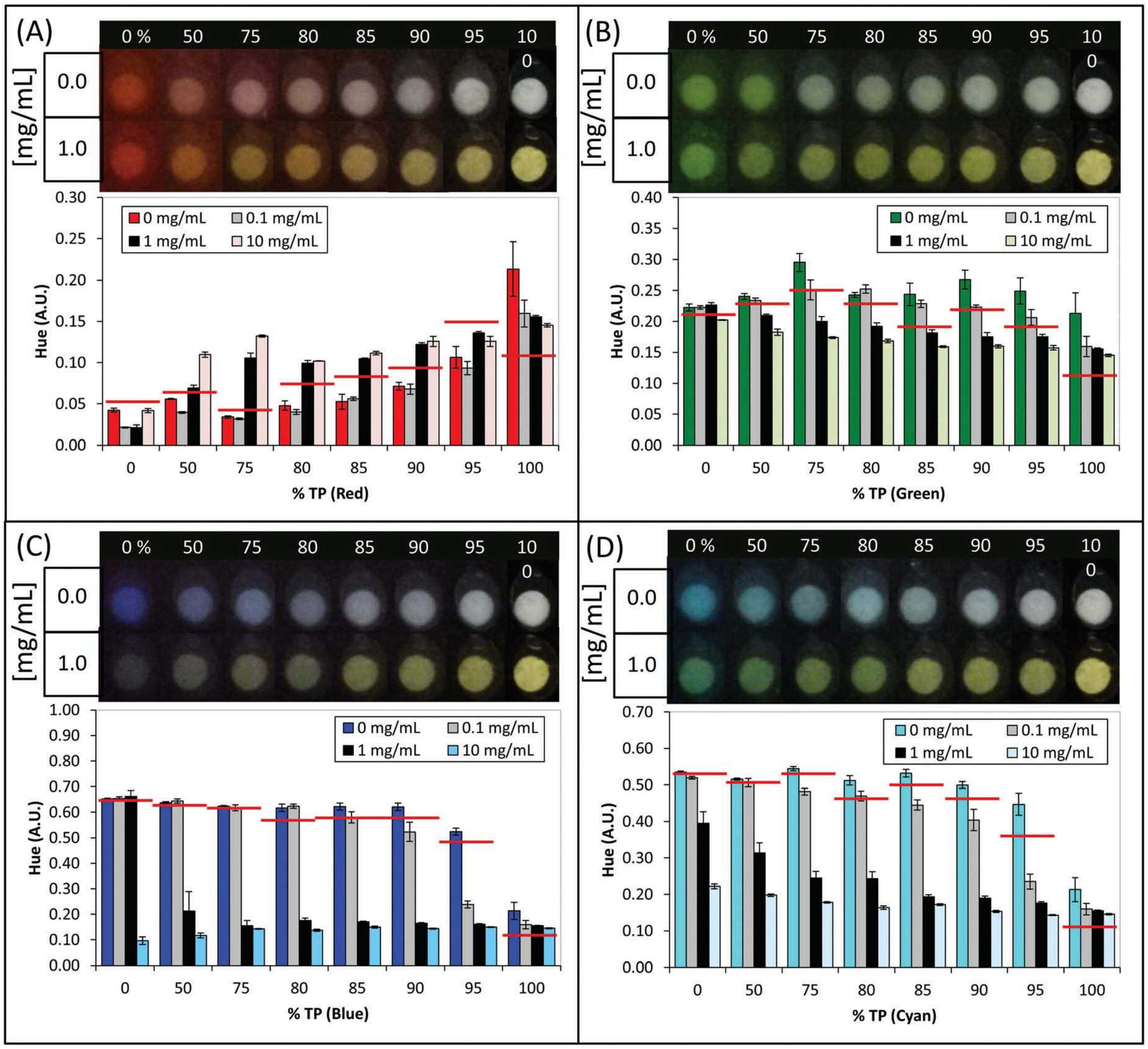

Figure 4-41. Hue analysis for print-based tinting with various colors (n = 3) for tinting blue (**A**), green (**B**), cyan (**C**), and red (**D**) over varying % TP for 0, 0.1, 1 and 10 mg/mL H_2O_2.

step device design, while varying the % transparency (% TP) values. **Figure 4-41** shows images for the H_2O_2 reaction chamber with the printing of each of the four colors over a 0 – 100% TP range; 100% TP indicates the complete absence of printed toner. The upper portion of each figure represent images obtained with the negative control and an H_2O_2 concentration of 1 mg/mL. The lower plots show the hue response corresponding to the images, with the inclusion of values for the 0.1 and 10 mg/mL H_2O_2 concentrations. The red solid line associated with the clustered hue values at each % TP setting represents the threshold value that explicitly distinguishes a sample positive or negative for H_2O_2, used for qualitative detection of H_2O_2. As the % TP of a printed color changes, the threshold value needs to be determined for that specific printed tint (**Table 4-1**). Depending on the tint color, and where that color is represented by hue values, a threshold value that is either plus or minus 3σ of the average 0 mg/mL H_2O_2 hue value can be defined for 99.7% confidence. With the exception of red tint, as the concentration of H_2O_2 increases, the hue value decreases. As a result, no tint (100% TP) and colored tints of green, blue, and cyan have defined threshold values of -3σ of the average 0 mg/mL H_2O_2. Any hue value below this threshold value can be considered as positive for the presence of H_2O_2. Red tinting has a defined threshold value plus 3σ of the average 0 mg/mL H_2O_2, and any hue value above this threshold is considered positive H_2O_2 detection.

Table 4-1. Threshold values for determining a positive sample of H_2O_2 using print-based tinting. Cyan, blue, and green thresholds are $[0]-3\sigma$. Red thresholds are $[0]+3\sigma$.

		% Transparency							
		0	50	75	80	85	90	95	100
Pe Tint Color	Red	0.05	0.06	0.04	0.07	0.08	0.09	0.15	0.31
	Green	0.21	0.23	0.25	0.23	0.19	0.22	0.19	0.11
	Blue	0.65	0.63	0.62	0.57	0.58	0.58	0.48	0.11
	Cyan	0.53	0.51	0.53	0.47	0.50	0.47	0.36	0.11

Using the defined thresholds, there is no discriminatory power between 0 mg/mL H_2O_2 and 10 mg/mL H_2O_2 without tinting. Red, green, and blue tinting at the darkest color (0% TP) is of limited value because the background is too dark to provide discrimination at low H_2O_2 concentrations. Additionally, red or green tinting in this format, at any % TP, showed a LOD of 1 mg/mL H_2O_2 for qualitative analysis based on the calculated threshold value. When tinting at 90 and 95% TP in blue and between 85 – 95% TP in cyan, the LOD was determined to be 0.1 mg/mL H_2O_2. These results indicate that print tinting provides an effective method for detection of the monochromatic H_2O_2

colorimetric reaction.

For each assay, potential tinting colors need to be defined. This often can be determined based on the native color change associated with the assay. A tinting color that is furthest from the native color represented on the hue scale (largest Δhue) can provide enhanced color discrimination. Although red and yellow are both primary colors that mix well, they have a lower Δhue than blue and yellow or blue and red. Once potential tint colors are chosen, % TP can be altered to optimize the tint for the desired LOD when using threshold values to unequivocally determine if the analyte of interest is present. The darkest tint color, 0% TP, is generated by printing the most toner droplets onto the polyester film. As the % TP increases, less toner droplets are printed resulting in droplets that are increasingly more spread out. At the optimized tint % TP, the printed toner droplets are sparse enough to allow the native color change to be detected at low concentrations. For the exemplary H_2O_2 reaction, optimized blue and cyan print-based tints allow detection of the light yellow color at 0.1 mg/mL and the light blue/cyan color when no analyte is present.

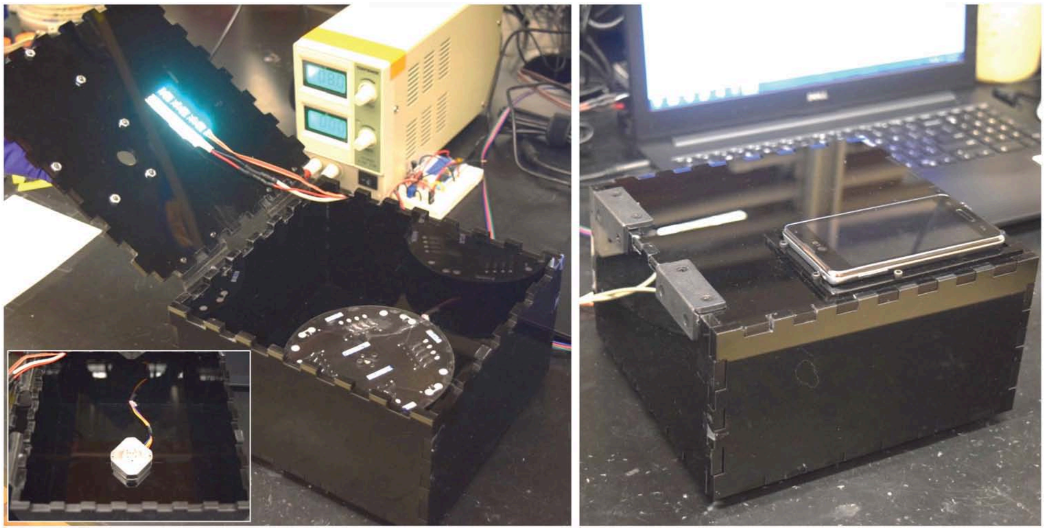

Figure 4-42. (**Left**) Image of PMMA enclosure with RGB and white LED strips on the lid with the microdevice for tinting; the inset shows the spin motor with no microdevice. (**Right**) Image of a cell phone holder on the lid of the imaging enclosure.

4.3.4.3 Tinting with External Light

Finally, background lighting was explored as a contactless form of tinting that does not involve altering the device fabrication process. RGB-tuneable LEDs combine red, green, and blue at individually set levels, by changing each RGB value, to produce a wide range of colors. These RGB LEDs were installed in order to provide tinting via selectively controlling background lighting during image capture. In this format, the desired tint colors (red, green, blue, and cyan) could be obtained using the RGB values

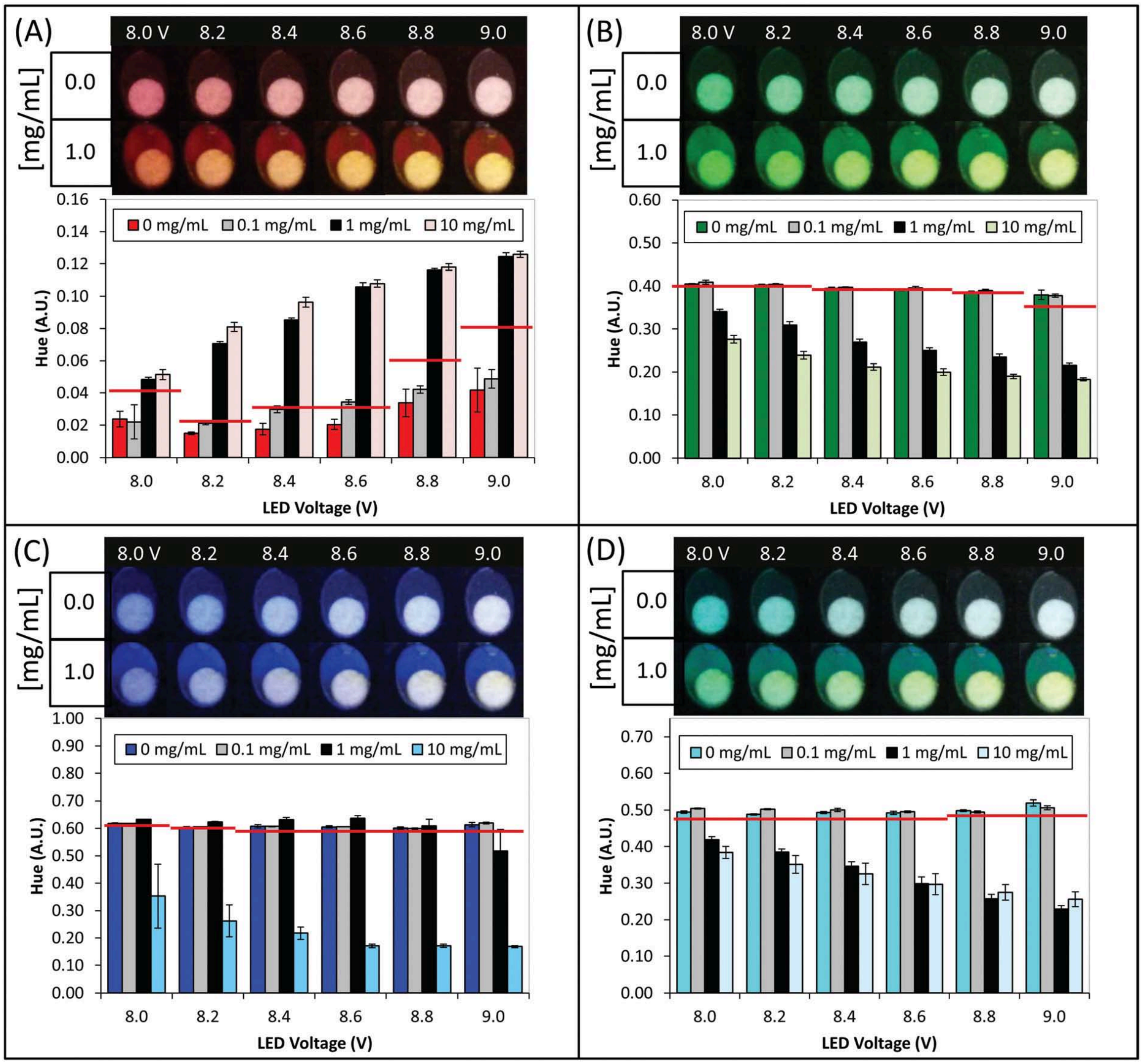

Figure 4-43. Hue analysis for external light tinting with various colors (n = 3) for tinting blue (**A**), green (**B**), cyan (**C**), and red (**D**) over varying white LED voltages for 0, 0.1, 1 and 10 mg/mL H_2O_2.

needed to generate each color, thus, defining a tinted environment for optical interrogation.

In contrast to dye and print-based tinting, this form of tinting is implemented during image analysis rather than during device fabrication. An RGB LED strip was used in combination with a white LED strip (**Fig. 4-42**), because RGB LEDs alone produced color that was too dark for colorimetric analysis. **Figure 4-43** displays images of the H_2O_2 reaction with LED tinting in red, green, blue and cyan. As with an earlier figure, H_2O_2 concentrations of 0 mg/mL and 1 mg/mL H_2O_2 were chosen for exemplary images, with hue plots shown for 0, 0.1, 1, and 10 mg/mL H_2O_2. Instead of utilizing % TP, the brightness of the white LED was varied using a bench top variable power supply from 8.0 – 9.0 V to optimize the tint intensity. This voltage range was chosen because 7.0 – 7.9 V was not bright enough to detect the colorimetric reaction while >9.0 V was too bright, washing out the image. The RGB LED brightness was kept constant, as the greatest impact on the image was seen with altering the white LED brightness. As described previously, the plotted red lines over clustered hue values at each voltage, and with each tint color, shown in **Figure 4-43** demonstrates the threshold value (99.7% confidence) for qualitative detection of H_2O_2, as present or not present. Any hue value either above (for red light-based tinting) or below (for green, blue, and cyan tinting) these

Table 4-2. Threshold values for determining a positive sample of H_2O_2 using external light tinting. Cyan, blue, and green thresholds are $[0]-3\sigma$. Red thresholds are $[0]+3\sigma$. All hue values are in A.U.

		Voltage					
		8.0	8.2	8.4	8.6	8.8	9.0
LED Tint Color	Red	0.04	0.02	0.03	0.03	0.06	0.08
	Green	0.40	0.40	0.39	0.39	0.38	0.35
	Blue	0.61	0.60	0.59	0.59	0.59	0.59
	Cyan	0.48	0.48	0.48	0.48	0.49	0.49

threshold values explicitly distinguish a positive H_2O_2 sample from a negative sample. Each threshold is specific to the RGB LED tint color, and white LED voltage applied (**Table 4-2**).

Light-based blue tinting had the worst sensitivity for H_2O_2 (highest LOD at 10 mg/mL; all voltages), green and cyan tints provided the best H_2O_2 sensitivity (LOD of 1 mg/mL; all voltages), and red tinting had LODs of 1 mg/mL H_2O_2 for 8.0 – 8.4 V and 8.8 – 9.0 V and 0.1 mg/mL for 8.6 V. Light-based tinting red at 8.6 V had the lowest LOD of 0.1 mg/mL H_2O_2, resulting in the most sensitive tinting parameter for H_2O_2 detection.

Table 4-3. Summary of advantages and disadvantages of each tinting method.

	Tinting Methods		
	Dye	Print	Lighting
Advantages	Simple method, only needs dye and pipette	Precise control over tinting with R,G,B values Minimal impact on fabrication time	Tinting method is independent of device fabrication Can use with more device types
Disadvantages	Interaction with sample and reagent Possible heterogeneous color change	Need external equipment (printer) Device needs to be amenable for printing	Requires external equipment (power source and software for controlling LEDs with R,G,B values)

4.3.4.4 Tinting Method Selection

All three tinting methods were effective for enhancing the colorimetric detection of H_2O_2 with hue analysis. Each tinting method has inherent advantages and disadvantages and these are summarized in **Table 4-3**. Dye and print-based tinting methods are advantageous because they can be implemented during microdevice fabrication, while light-based tinting is invoked externally during image capture and is independent of device fabrication. Despite the need for external hardware to power the LEDs, light-based tinting is simple and provides flexibility with multiple device types. This method also provides precise color control using RGB LEDs and voltage control.

Dye tinting is the simplest of the three methods, as it only requires a pipet and dye for drying the dye onto the device substrate prior to device use. This method is best used when no interactions between the dye and the sample or reagent can occur. Print-based tinting utilizes a commercial printer with precise color control using RGB values and is easily applied when device fabrication includes a printing step. If the device fabrication is not amenable for printing, a sheet of polyester or overhead transparency with the desired printed tint could be used as a cover layer during image capture. Here, each tinting parameter for the methods summarized in **Table 4-3** was optimized using the exemplary H_2O_2 colorimetric reaction. This reaction provides a benchmark for optimizing the described tinting methods for additional colorimetric assays.

4.3.5 Transitioning from PET to HSA Devices

The PCL fabrication technique has offered a number of advantages for inexpensive device fabrication, ideal for rapid prototyping. Additionally, this fabrication technique has proved to be especially advantageous for devices centered on centrifugal fluidic control. With a view towards field use, the strength and long-term stability of printed

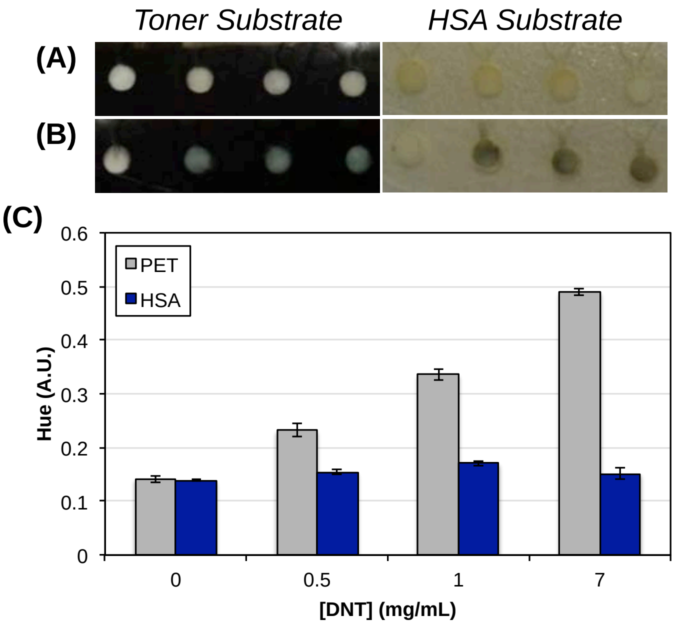

Figure 4-44. Images of the reaction between (**A**) 0 mg/mL and (**B**) 1 mg/mL DNT with TMAH using toner- and HSA-based devices. (**C**) Hue and saturation analysis results for each corresponding image for both device substrate formats.

toner for device bonding elicits concern.[33] An alternative to printer toner that can prevent delamination between the device layers and is stable over time is required. A number of adhesives can be used as a replacement to toner; however, many of these substrates complicate device assembly, negatively impacting the simplicity of PCL fabrication.

Commercial heat-sensitive adhesive (HSA) was implemented as an alternative to printer toner for device fabrication as described previously.[33] Due to the proprietary chemical composition of the HSA material used, inhibition of the colorimetric reactions needed to be evaluated. Negative effects on the color changes for the described colorimetric reactions for explosives detection did not occur for many of the reactions used, however, undesirable effects from chemical interactions with the HSA were seen for DNT and NH_4^+.

4.3.5.1 Colorimetric Detection of DNT with HSA Devices

Generally, the negative color observed (no explosive present) using an HSA-fabricated device with TMAH reagent was yellow in color rather than white-colored due to the filter paper as observed previously (**Fig. 4-44A**). Since white is not represented with hue, this effect from HSA is not problematic as the negative response already resulted in a yellow hue value (~0.15 A.U.). When DNT was added

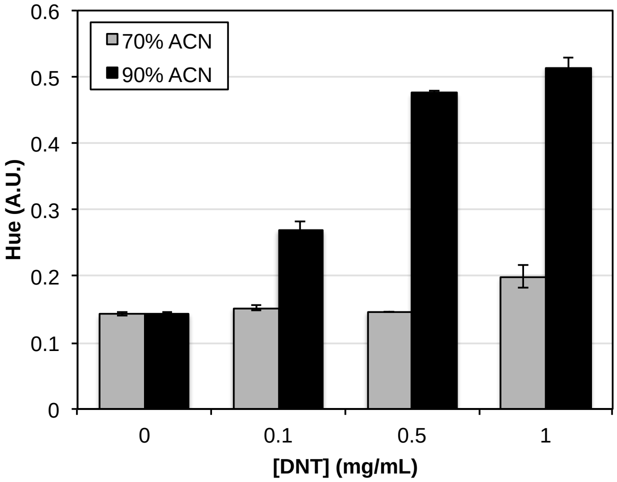

Figure 4-45. Hue and saturation analysis results for 0 – 1 mg/mL DNT with TMAH with 70% and 90% ACN solvent compositions.

to the device the color change was green in color rather than the expected blue color with toner-based devices (**Fig. 4-44B**). **Figure 4-44C** demonstrates that this color change has an overall negative effect on the ability to detect DNT colorimetrically with hue analysis. Although the change in hue values (Δhue) for a green and yellow color is lower than the change in hue values for blue and yellow, the hue response should still have a sufficient Δhue for qualitative analysis. The measured hue values reported in **Figure 4-44C** were not expected for a green color, i.e., ~0.3 A.U., making hue analysis problematic.

To address this analysis limitation caused by the HSA substrate, the dissolution solvent was altered from 70% to 90% ACN to increase the color response with DNT added. This change in solvent composition was based on initial solvent analysis with toner devices, where an increase in ACN content increased the reaction color intensity. **Figure 4-45** shows a significant increase in the hue response, resulting in a hue value more associated with blue (~0.5 A.U.). Additionally, the saturation response increased with increasing DNT concentration in 90% ACN, as expected for DNT analysis. To implement 90% ACN as the organic explosive solvent, subsequent evaluation of UN detection with 90% ACN was required. The hue analysis in **Figure 4-46** shows that UN was still detected qualitatively using 90% ACN, allowing for this

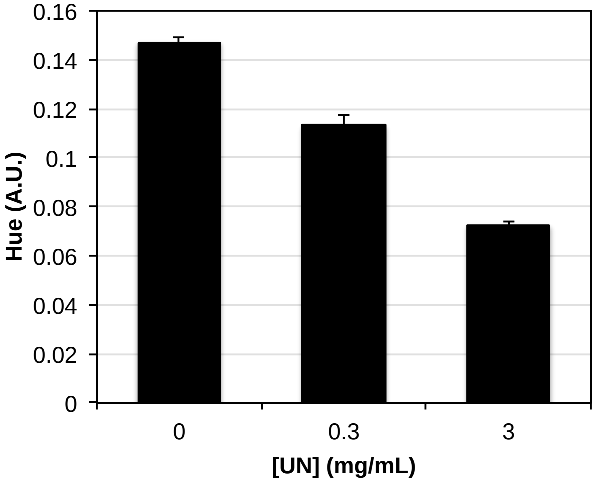

Figure 4-46. Hue analysis results for 0 – 3 mg/mL UN and *p*-DMAC with 90% ACN in methanol solvent.

solvent composition to be used with all organic explosives. The new threshold value was defined as 0.141 A.U. for UN detection.

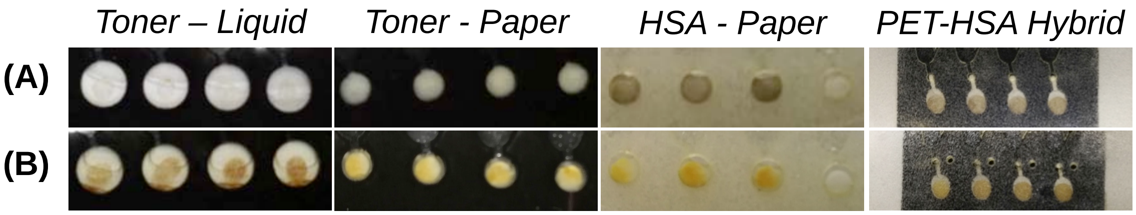

Figure 4-47. Images of the reaction between (**A**) 0 mg/mL (negative) and (**B**) positive NH_4^+ with Nessler's reagent using toner- and HSA-based devices.

4.3.5.2 Colorimetric Detection of NH_4^+ with HSA Devices

During initial analysis, the NH_4^+ colorimetric reaction with Nessler's reagent was the only reagent stored within the microfluidic device as a liquid and not using paper. Due to concerns with the stability of the liquid reagent for long-term storage, the reaction was optimized for use with paper, as follows. Since filter paper is slightly acidic (pH 5), a small amount of sodium hydroxide (0.5 µL, 2.5M NaOH) was added to the sample channel of the device to allow the sample solution to become alkaline before introduction

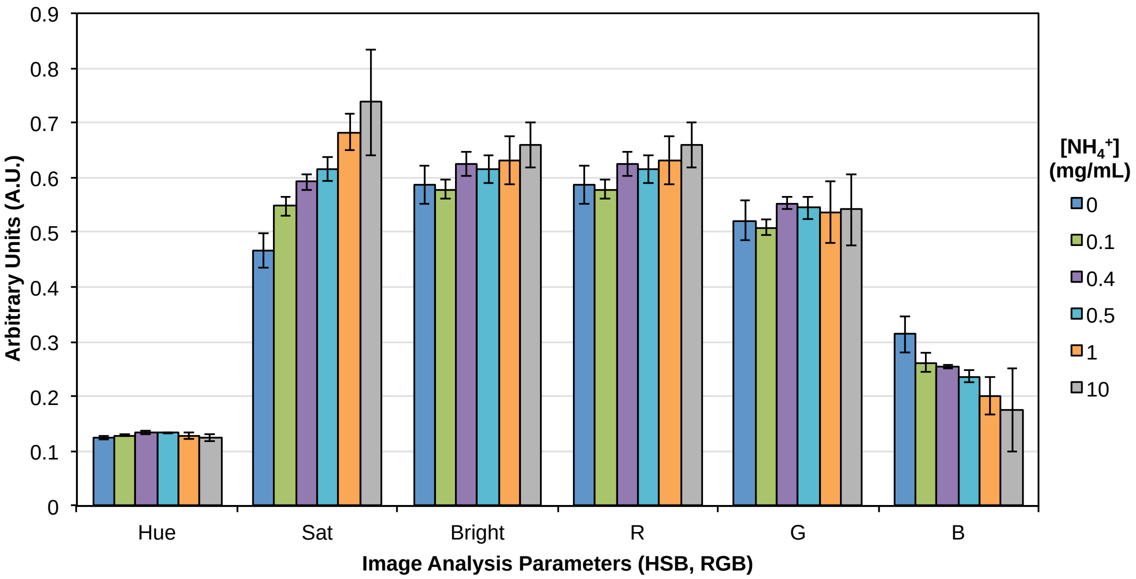

Figure 4-48. Image analysis results for hue, saturation (sat), brightness (bright), R, G, and B color responses for evaluation of each response for the reaction of NH_4^+ with the Nessler's reagent at varying concentrations from 0 – 10 mg/mL AN.

to the Nessler's reagent stored on paper within the reagent chamber. **Figure 4-47** shows a more homogenous color response on paper than without paper for printed toner devices.

Transitioning to an HSA device resulted in a change in the color for a negative sample without NH_4^+ present. The color change for 0 mg/mL AN using a toner device was white from a colorless solution on filter paper, however, the color change was now a brown color for HSA devices (**Fig. 4-47**). To address this limitation, a modular toner device was fabricated for storage of the Nessler's reagent while the rest of the device was fabricated using HSA. The sample solution could travel from the HSA device to the modular toner device using an access port on the top of the toner section and bottom of the HSA device. Unfortunately, this device arrangement had no positive effect on the 0 mg/mL NH_4^+ color change as shown in **Figure 4-47**.

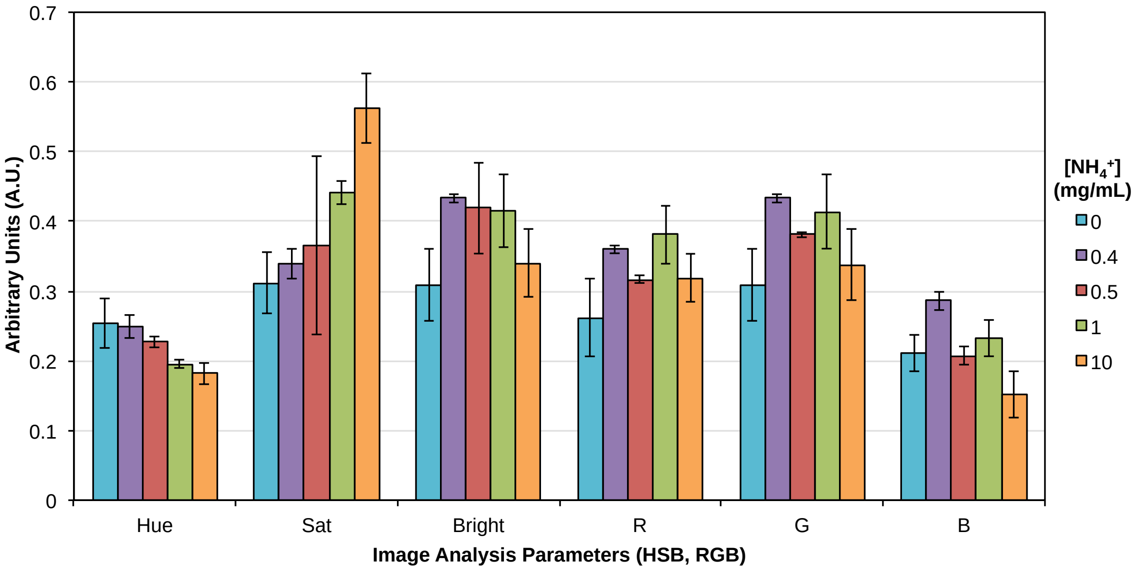

Figure 4-49. Image analysis results for hue, saturation (sat), brightness (bright), R, G, and B color responses for evaluation of each response for the reaction of NH_4^+ with the Nessler's reagent at varying concentrations from 0 – 10 mg/mL AN using print-based tinting in cyan at 75% TP.

Because this assay is inhibited by the HSA substrate, analysis with all image parameters was performed to see if an alternative analysis parameter to hue could be used for qualitative detection and threshold determination. The image analysis results are shown in **Figure 4-48** for AN concentrations from 0 – 10 mg/mL, and the saturation (HSB) and blue (RGB) responses changed with increasing NH_4^+ concentrations, however, the error bars were larger than those seen with hue analysis resulting in neither of these parameters being ideal for defining a threshold value. Alternatively, image analysis was performed with print tinting cyan at 75% TP, and the results are shown in **Figure 4-49**. Tinting with image analysis was also unable to provide an analysis scheme for defining a threshold value for detection.

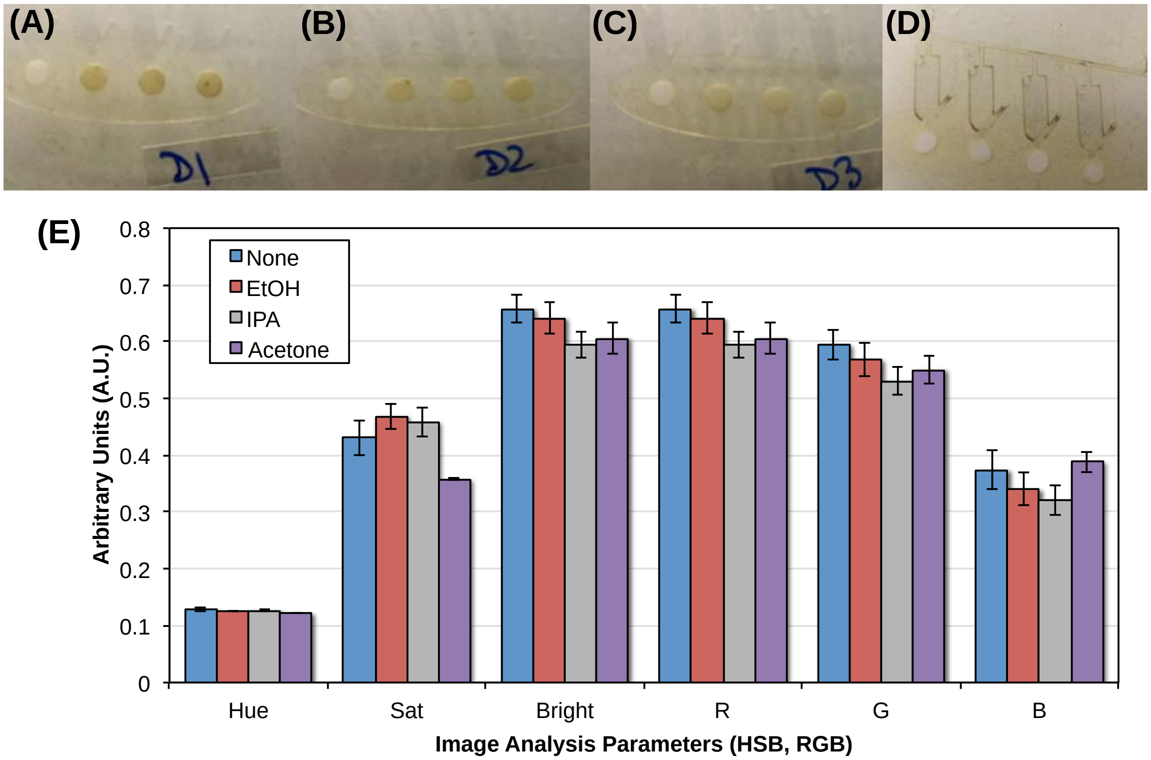

Figure 4-50. Images of 0 mg/mL AN reaction with Nessler's reagent with HSA-based devices after solvent-pretreatment with (**A**) ethanol, (**B**) isopropyl alcohol, and (**C**) acetone. (**D**) Image of Nessler's reagent pipetted into the sampling channels to show interaction at the laser-cut device architecture. (**E**) Image analysis results for hue, saturation (sat), brightness (bright), R, G, and B color responses for 0 mg/mL AN with Nessler's reagent to evaluate solvent pre-treatment with no wash (none), ethanol (EtOH), isopropyl alcohol (IPA), and acetone.

It was observed that the interaction between the HSA and Nessler's reagent occurred along the channel walls where the architecture was laser ablated during fabrication. To reduce the brown color formation with 0 mg/mL AN added, a number of

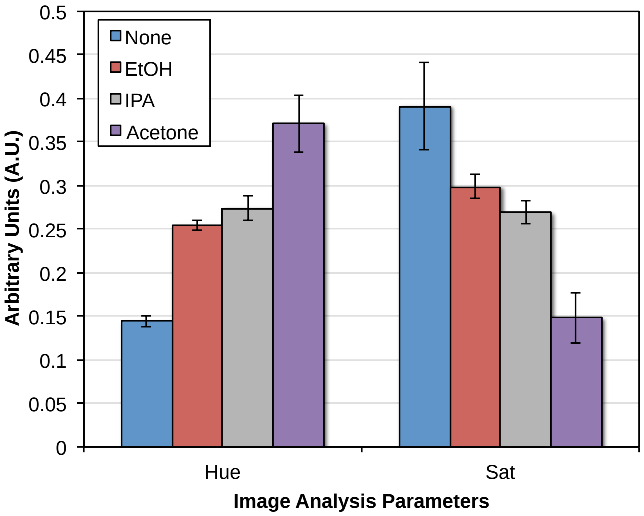

Figure 4-51. Hue and saturation (sat) analysis results for 0 mg/mL AN with Nessler's reagent to evaluate solvent pre-treatment with no wash (none), ethanol (EtOH), isopropyl alcohol (IPA), and acetone using print-based tinting in cyan at 75% TP for ananlysis.

washing protocols for the laser cut HSA layers were attempted. Ethanol, isopropanol (IPA), and acetone were chosen as volatile solvents with varying effects on the HSA, i.e., ethanol used as a mild solvent, IPA as a somewhat mild solvent, and acetone used as a harsh solvent. Care was taken when washing with acetone to not remove the HSA coating. Each wash had positive effects on the color response seen with 0 mg/mL AN, with acetone having the biggest impact on the color. Image analysis results in **Figure 4-50** show that although acetone analysis results generally provided the largest change in response compared to no wash step, no significant differences in hue were observed for any solvent wash method. Image analysis was then performed with print-based tinting cyan (75% TP) and the results for hue and saturation are shown in **Figure 4-51**. Considering any change in response compared to no wash, tinting with a solvent wash potentially provided a platform for NH_4^+ analysis with HSA devices. Acetone had the biggest change in hue and saturation for 0 mg/mL AN than without washing, however, the addition of an acetone wash to the fabrication process would be labor-intensive to assure the integrity of the device was not compromised during washing. Alternatively, IPA shows the next largest change in response compared to no wash and may be a viable option moving forward.

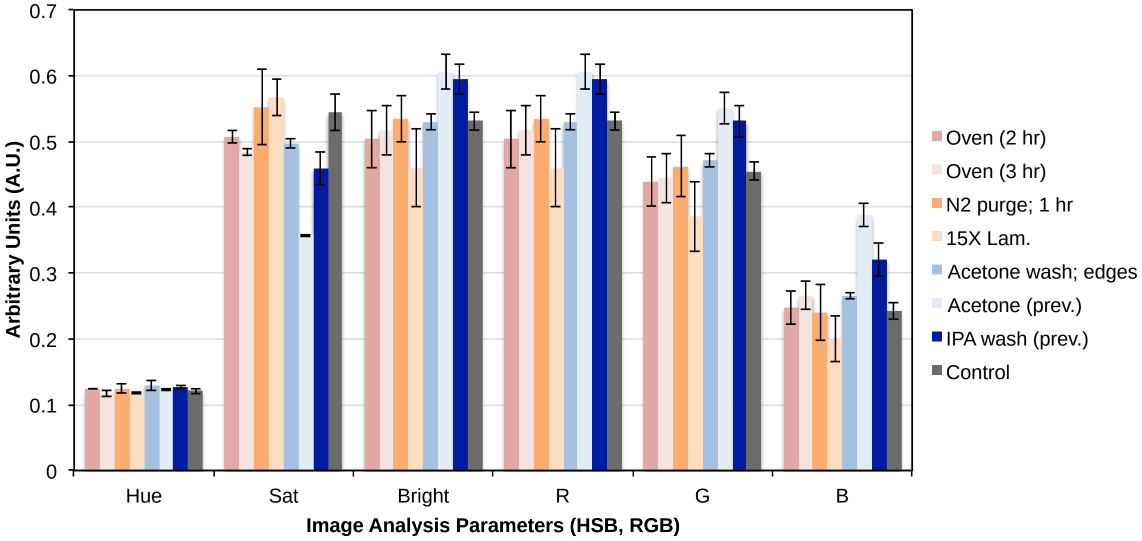

Figure 4-52. Image analysis results for hue, saturation (sat), brightness (bright), R, G, and B color responses for 0 mg/mL AN with Nessler's reagent to evaluate device without pre-treatment (control) and with pre-treatment using heat (oven and excess lamination, labeled 15X lam.), purging with inert gas (N_2), and solvent wash (IPA and acetone).

Additional approaches were also evaluated for treating the HSA device before use. The image analysis results for 0 mg/mL AN with each approach is shown in **Figure 4-52**, with the acetone and IPA wash from the previous results (labeled with 'prev.' in **Fig. 4-52**) utilized as ideal and comparative data. Applying additional heating time through baking the fabricated devices in an oven at >120 °C and using additional lamination steps was performed to assure that the HSA chemical reaction involved in device bonding was completed before use. Purging the device with N_2 was also performed as an alternative device treatment to heat. Since acetone solvent wash provided the best image analysis results, after the HSA layers were cut, the architecture was wiped down with acetone using a cotton swab along the edges (labeled 'acetone wash; edges' in **Fig. 4-52**) as a gentle method for acetone pre-treatment. The results in **Figure 4-52** demonstrate that heat and N_2 purge did not result in enhanced analysis. An IPA or acetone solvent wash still provided the greatest change in response compared to the control (no device treatment), however, the acetone wash along the edges of the architecture did not produce similar results to a complete acetone wash of the HSA layers.

IPA was chosen as a milder solvent pre-treatment method compared to acetone and was optimized for 70% IPA, providing improved results compared to 100% IPA (**Fig. 4-53**). A 70% IPA pre-treatment was evaluated with a positive AN sample, resulting in a large change in response compared to 0 mg/mL results and the control (no pre-treatment). **Figure 4-53 inset** shows 0 mg/mL responses (labeled '[0]') with and without 70% IPA treatment and for the 10 mg/mL response with 70% IPA treatment.

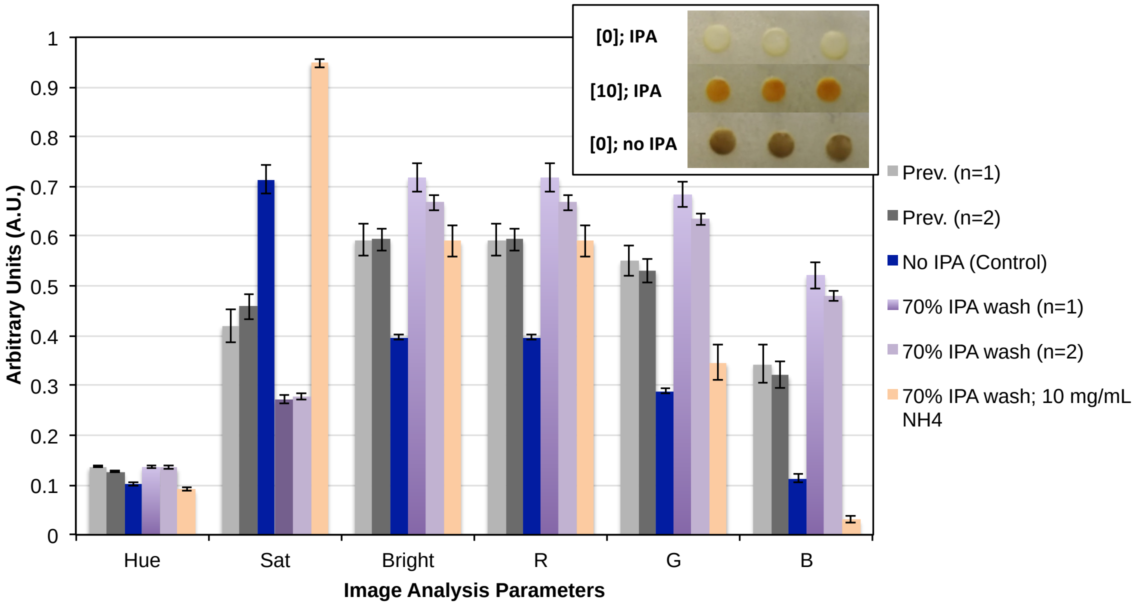

Figure 4-53. Image analysis results for hue, saturation (sat), brightness (bright), R, G, and B color responses for mostly 0 mg/mL AN with Nessler's reagent to evaluate device without IPA pre-treatment and with IPA pre-treatment using 100% (prev.) and 70% IPA content.

After the optimization of DNT and NH_4^+ detection using HSA, the LODs for each colorimetric reaction was empirically defined for the HSA-based devices. The LOD results are outlined in **Table 4-4**, including a comparison of these empirically-defined results to the LOD requirements defined for each explosive analyte by the funding source of this work through calculating the mass of analyte added based on the concentration and volume used. Each of the reported LODs using HSA devices exceeded the outlined specifications.

Table 4-4. Empirically defined detection limits for each explosive analyte, and a comparison to the detection limit specifications outlined. H_2O_2 and NH_4^+ results are based on tinting cyan with 75% transparency.

Explosive Material	Concentration (mg/mL)	Volume Added (µL)	Mass LOD (µg)	LOD Requirement (µg)
TNT	0.01	16	0.16	5
Tetryl	0.05	16	0.8	5
DNT	0.05	16	0.8	5
UN	0.3	16	4.8	30
ClO_4^-	1.5	16	24	100
H_2O_2	0.05	16	0.8	50
NH_4^+	0.1	16	1.6	30
NO_3^-	0.4	16	6.4	30

4.4 Conclusions

An enhanced method for presumptive colorimetric detection of multiple explosives for field-testing was developed using a centrifugal microfluidic device. First, colorimetric reactions for the detection of TNT, DNT, Tetryl, UN, NH_4^+, NO_3^-, ClO_4^-, and H_2O_2 were translated to the microfluidic device format with a reagent integration method that was advantageous for field use. Evaluation of each color change using a number of image analysis parameters for objective analysis with a cell phone was performed and optimized for hue analysis of all color reactions. Hue image analysis was advantageous for defining threshold values towards qualitative detection of explosives as color is represented by a single numerical value, rather than the sum of individual RGB values, providing a robust method for detection.

Three different tinting methods were developed for enhanced hue analysis through manipulating the color change from colorimetric reactions that result in subtle or monotonal color changes. Exploiting paper for reagent storage and polyester substrates for fabrication allowed for simple and inexpensive microfluidic devices. Additionally, each substrate allowed for inherent advantages for tinting that were complementary to the device fabrication. Dye tinting was used to change the paper substrate color and print-based tinting was used to color the cover polyester device layer. If a tinting method that was independent of device fabrication was desired, a light-based tinting method using RGB LEDs was applied. To demonstrate the effectiveness of each tinting method, the same H_2O_2 colorless-to-yellow color change with all three tinting methods was evaluated. After optimizing the tinting parameters, each method resulted in comparable LODs of 0.1 mg/mL. This demonstrates that each of these tinting methods was a viable solution for detecting a monochromatic color change. Overall, this technique allows for front-end color enhancement of colorimetric reactions on microfluidic devices using a method that integrates into fabrication techniques and offers advantages for various in situ analyses.

Towards a complete on-site analysis system, a device enclosure was fabricated for consistent, controllable lighting during image capture. Additionally, a device design for multiplexed analysis from a single sample input was developed for future use with additional studies towards complete device integration.

4.5 References

1. P. G. Rieger and H. J. Knackmuss, *Biodegradation of Nitroaromatic Compounds*, 1995, **49**, 1-18.

2. A. Hilmi, J. H. T. Luong and A. L. Nguyen, *Journal of Chromatography A*, 1999, **844**, 97-110.
3. J. C. Spain, *Annual Review of Microbiology*, 1995, **49**, 523-555.
4. J. S. Caygill, F. Davis and S. P. J. Higson, *Talanta*, 2012, **88**, 14-29.
5. R. G. Smith, N. D'Souza and S. Nicklin, *Analyst*, 2008, **133**, 571-584.
6. R. L. Wang, G. Yang, J. Q. Zhang, Q. Li, R. X. Fu, J. C. Ye, T. Z. Wang, Y. Lu, H. Zhou and G. L. Huang, *Analytical Methods*, 2014, **6**, 9628-9633.
7. *2011 Report on Terrorism*, The National Counterterrorism Center, Washington, DC 2012.
8. E. L. Izake, *Forensic Science International*, 2010, **202**, 1-8.
9. T. P. Forbes and E. Sisco, *Analytical Methods*, 2015, **7**, 3632-3636.
10. J. Almog and S. Zitrin, in *Aspects of Explosives Detection*, eds. M. Marshall and J. C. Oxley, Elsevier, Amsterdam, Netherlands, 2009, pp. 41-58.
11. D. L. Macadam, *Optical Engineering*, 1983, **22**, S116-S117.
12. J. Liu, Z. F. Shao and Q. M. Cheng, *Optics Letters*, 2011, **36**, 4821-4823.
13. A. W. Martinez, S. T. Phillips, E. Carrilho, S. W. Thomas, H. Sindi and G. M. Whitesides, *Analytical Chemistry*, 2008, **80**, 3699-3707.
14. S. K. Vashist, T. van Oordt, E. M. Schneider, R. Zengerle, F. von Stetten and J. H. T. Luong, *Biosensors & Bioelectronics*, 2015, **67**, 248-255.
15. T. Soga, Y. Jimbo, K. Suzuki and D. Citterio, *Analytical Chemistry*, 2013, **85**, 8973-8978.
16. N. Lopez-Ruiz, V. F. Curto, M. M. Erenas, F. Benito-Lopez, D. Diamond, A. J. Palma and L. F. Capitan-Vallvey, *Analytical Chemistry*, 2014, **86**, 9554-9562.

17. M. M. Mentele, J. Cunningham, K. Koehler, J. Volckens and C. S. Henry, *Analytical Chemistry*, 2012, **84**, 4474-4480.
18. L. Shen, J. A. Hagen and I. Papautsky, *Lab on a Chip*, 2012, **12**, 4240-4243.
19. K. Abe, K. Suzuki and D. Citterio, *Analytical Chemistry*, 2008, **80**, 6928-6934.
20. S. C. Kim, U. M. Jalal, S. B. Im, S. Ko and J. S. Shim, *Sensors and Actuators B-Chemical*, 2017, **239**, 52-59.
21. K. A. Oliveira, D. Damasceno, C. R. de Oliveira, L. A. da Silveira, A. E. de Oliveira and W. K. T. Coltro, *Analytical Methods*, 2016, **8**, 6506-6511.
22. C. L. M. Morais, A. C. O. Neves, F. G. Menezes and K. M. G. Lima, *Analytical Methods*, 2016, **8**, 6458-6462.
23. A. R. Gillespie, A. B. Kahle and R. E. Walker, *Remote Sensing of Environment*, 1986, **20**, 209-235.
24. J. S. Tyo, D. L. Goldstein, D. B. Chenault and J. A. Shaw, *Applied Optics*, 2006, **45**, 5453-5469.
25. J. S. Tyo, B. M. Ratliff and A. S. Alenin, *Optics Letters*, 2016, **41**, 4759-4762.
26. K. Cantrell, M. M. Erenas, I. de Orbe-Paya and L. F. Capitan-Vallvey, *Analytical Chemistry*, 2010, **82**, 531-542.
27. D. M. Cate, J. A. Adkins, J. Mettakoonpitak and C. S. Henry, *Analytical Chemistry*, 2015, **87**, 19-41.
28. B. L. Thompson, Y. Ouyang, G. R. M. Duarte, E. Carrilho, S. T. Krauss and J. P. Landers, *Nature Protocols*, 2015, **10**, 875-886.
29. S. T. Krauss, V. C. Holt and J. P. Landers, *Sensors and Actuators B-Chemical*, 2017, **246**, 740-747.

30. R. Schulte-Ladbeck, M. Vogel and U. Karst, *Analytical and Bioanalytical Chemistry*, 2006, **386**, 559-565.

31. R. Schulte-Ladbeck, P. Kolla and U. Karst, *Analytical Chemistry*, 2003, **75**, 731-735.

32. D. L. Lu, A. Cagan, R. A. A. Munoz, T. Tangkuaram and J. Wang, *Analyst*, 2006, **131**, 1279-1281.

33. C. Birch, J. A. DuVall, D. Le Roux, B. L. Thompson, A. C. Tsuei, J. Y. Li, D. A. Nelson, D. L. Mills, J. P. Landers and B. E. Root, *Micromachines*, 2017, **8**.

34. J. L. Garcia-Cordero, D. Kurzbuch, F. Benito-Lopez, D. Diamond, L. P. Lee and A. J. Ricco, *Lab on a Chip*, 2010, **10**, 2680-2687.

35. S. T. Krauss, T. P. Remcho, S. M. Lipes, R. Aranda, H. P. Maynard, N. Shukla, J. Li, R. E. Tontarski and J. P. Landers, *Analytical Chemistry*, 2016, **88**, 8689-8697.

36. D. Mark, T. Metz, S. Haeberle, S. Lutz, J. Ducree, R. Zengerle and F. von Stetten, *Lab on a Chip*, 2009, **9**, 3599-3603.

37. Y. W. Ouyang, S. B. Wang, J. Y. Li, P. S. Riehl, M. Begley and J. P. Landers, *Lab on a Chip*, 2013, **13**, 1762-1771.

38. J. Yinon and S. Zitrin, *The Analysis of Explosives: Pergamon Series in Analytical Chemistry*, Pergamon Press, Oxford, 1981.

39. J. V. Janowski and L. Erb, *Ber.*, 1886, **19**, 2155.

40. F. L. English, *Analytical Chemistry*, 1948, **20**, 745-746.

41. E. Dimitriu, S. C. Moldoveanu and E. E. Iorgulescu, *Russian Journal of Physical Chemistry A*, 2009, **83**, 1537-1541.

42. S. A. H. Amas and H. J. Yallop, *Analyst*, 1966, **91**, 336-337.

43. K. Yeager, in *Forensic Investigation of Explosions*, ed. A. Beveridge, CRC Press, Boca Raton, 2012, pp. 493-538.

44. J. Almog, A. Klein, T. Tamiri, Y. Shloosh and S. Abramovich-Bar, *Journal of Forensic Sciences*, 2005, **50**, 582-586.

45. K. L. Peters, I. Corbin, L. M. Kaufman, K. Zreibe, L. Blanes and B. R. McCord, *Analytical Methods*, 2015, **7**, 63-70.

46. R. Houghton, *Emergency Characterization of Unknown Materials*, CRC Press, Boca Raton, 2008.

47. M. A. Xu, B. R. Bunes and L. Zang, *Acs Applied Materials & Interfaces*, 2011, **3**, 642-647.

48. L. N. Demutskaya and I. E. Kalinichenko, *Journal of Water Chemistry and Technology*, 2010, **32**, 90-94.

49. H. Jeong, J. Park and H. Kim, *Journal of Chemistry*, 2013.

50. K. Kolacinska and R. Koncki, *Analytical Sciences*, 2014, **30**, 1019-1022.

51. J. Nessler, *Chem. Ztg.*, 1856, **27**, 538.

52. I. E. Kalinichenko and L. N. Demutskaya, *Russian Journal of General Chemistry*, 2004, **74**, 1-6.

53. P. Griess, *Berichte der deutschen chemischen Gesellschaft* 1879, **12**, 426-428

54. Q. H. Wang, L. J. Yu, Y. Liu, L. Lin, R. G. Lu, J. P. Zhu, L. He and Z. L. Lu, *Talanta*, 2017, **165**, 709-720.

55. D. Tsikas, *Journal of Chromatography B-Analytical Technologies in the Biomedical and Life Sciences*, 2007, **851**, 51-70.

56. M. Miro, A. Cladera, J. M. Estela and V. Cerda, *Analyst*, 2000, **125**, 943-948.

57. K. Niki, Y. Kiso, T. Takeuchi, T. Hori, T. Oguchi, T. Yamada and M. Nagai, *Analytical Methods*, 2010, **2**, 678-683.

58. A. C. Bratton and E. Marshall, *Journal of Biological Chemistry*, 1939, **128**, 537-550.

59. W. Liu, C. L. Cassano, X. Xu and Z. H. Fan, *Analytical Chemistry*, 2013, **85**, 10270-10276.

5. An Integrated Microfluidic Device for *Sample-In-Answer-Out* Explosives On-Site Detection

5.1 Introduction

The widespread use of explosives by terrorist groups has lead to an increased interest for developing portable sensing techniques for the detection and identification of explosives material.[1] It is imperative to evaluate contaminations, or residual material, transferred to the clothing, body, and surrounding surfaces from the handling or manufacturing of an improvised explosives device (IED) for rapid on-site screening.[2, 3] IEDs can be broadly categorized as fertilizers, inorganic oxidizers, and peroxides. A major cause of casualties from terrorist attacks derives from bombing events, with a number of incidents involving the use of IEDs. Previous incidents included the use of flash powder containing potassium chlorate during attacks on a popular Bali nightclub in 2002[4], fertilizer-based explosives containing urea nitrate were used in the first attack on the World Trade Center in 1993[2], and peroxide-based explosives were cause for bombings on public transportation in London during 2005[5]. To facilitate a rapid response to an explosives-related incident by first responders, a detection platform that is portable and automated, for ease-of-use, is needed.

Microfluidic technologies offer many potential advantages from the scaled-down size of devices including rapid analysis capabilities, low cost substrates and instrumentation, low reagent and sample consumption, automated sample processing, closed systems, and simple operating procedures. While there is a growing interest in microfluidics for forensics, considerable exploration is needed to equal the efforts reported for clinical and point-of-care applications. Early uses of microfluidics for explosives detection, through electrophoresis[6, 7], electrochemical[8, 9], and color based devices[10-13], have shown great promise for field analysis. Many of these reported devices, however, are plagued by the lack of multiplexed analysis for inorganic and organic explosive types, relevant real-world sampling methods, on-board sample processing, automation and portability for adaptation of a microfluidic device as an enhanced on-site screening technique.

The development of a fully-integrated, sample in-answer out microfluidic technology for explosives identification on-site requires integration of the following processes for automation and ease-of-use without basic laboratory equipment and consumables: sampling, sample processing, fluidic control, chemical reagent use, colorimetric analysis, and reporting results. Although certain microfluidic technologies are well-suited to address the issues of portability and automation, i.e. paper-based devices, there still remains a major challenge relating to the implementation of lab-on-a-chip devices from the requirement of external equipment for device operation, making commercialization problematic.[14] The centrifugal microfluidic platform offers advantages in portability and automation as a simple motor with programmable parameters such as rotation speed, direction, and duration is all that is needed to drive fluid flow and sample interrogation.[15, 16] External equipment including pneumatic pumps for fluid flow and signal acquisition devices are not required with the addition of a smartphone to the centrifugal microfluidic platform for analysis. Significant challenges for microfluidic devices that were initially overlooked relating to sample preparation, the lack of a relevant world-to-chip interface, and fully integrated, autonomous systems has more recently gained attention.[14, 17-19]

There are a variety of different approaches used in the field for interrogating surfaces for explosive residue collection. Handheld Raman spectrometers are an example of a noncontact sensing technique for analyzing explosives samples where a surface swab is not required for collection of sample before analysis is performed.[20] The majority of analysis techniques, however, utilize an indirect analysis technique where sample needs to be collected from the desired surface for explosive screening, followed by a subsequent analysis procedure.[21] Indirect analysis techniques are widely used in forensic analysis applications, and each analysis technique requires the use of relevant sample collection material, i.e., sexual assault evidence from buccal swabs[22] or crime scene analysis from collected fabric material[23].

Although reagent storage and colorimetric analysis have been thoroughly described in previous chapters, the development of a sampling platform that can interface with the small dimension of the microfluidic device platform is critical for on-site device use. A complete sampling method includes the swab material, swabbing protocol, swab-to-device interface, sample elution, and sample cleanup. Implementing a single, universal swab with the ability to process the presence of either organic or inorganic explosive residue from a surface is ideal for unknown analysis. The optimal swab-wetting and elution solvents differ for organic and inorganic explosives[24], similarly the solvents also differ for sample cleanup, i.e., extraction, purification and concentration, for both explosives types.[25] Centrifugal devices offer advantages with sampling processing by providing a method to centrifuge or filter contaminants, concentrate the sample, and perform extraction protocols.

This chapter describes the integration of techniques discussed in previous chapters with methods developed here for sampling, sample processing, and multiplexing for the detection of eight different explosive materials from a single surface swab. All developed methods remain compatible with the laser print, cut and laminate device fabrication method previously described.[26] First, the surface swab material was defined for optimal collection of sample from a surface with the capability for elevated sample recovery from the swab once added to the microfluidic device (on-chip elution). After the surface swab was implemented, limits of detection (LOD) for each explosive analyte of interest were empirically-define and the threshold values originally identified in **Chapter 4** were updated for detection. Once the fully integrated device design was defined, modifications were made to additional device processes for seamless automation of the device protocol. Additionally, the device enclosure system and Android cell phone application were adapted for use with the fully integrated devices. Finally, evaluation of the complete detection system with eight different explosive materials and thirteen contaminants was performed in the laboratory setting and additionally off-site with a participating agency.

5.2 Materials and Methods

5.2.1 Reagents

2,4,6-Trinitrotoluene (TNT), 2,4-dinitrotoluene (DNT), methyl-2,4,6-trinitrophenylnitramine (Tetryl), and urea nitrate (UN) were provided by Signature

Science (Austin, TX). Hydrogen peroxide (35%), phosphoric acid, sodium chloride, and isopropyl alcohol were purchased from Fisher Scientific (Waltham, MA). Nessler's reagent was purchased from La-Mar-Ka, Inc. (Baton Rouge, LA). Ammonium nitrate (AN), potassium nitrate, sodium perchlorate, glycerol, acetonitrile, methanol, ethanol, water, tetramethylammonium hydroxide (TMAH), methylene blue (MB), sulfanilamide, zinc powder, ammonium titanyl oxalate (ATO), N-(1-naphthyl)ethylenediamene dihydrochloride (NED), and 4-(dimethylamino) cinnamaldehyde (*p*-DMAC) were purchased form Sigma-Aldrich (St. Louis, MO).

Acetonitrile, methanol, ethanol, and water were purchased as high-performance liquid chromatography grade solvents. Tetramethylammonium hydroxide, methylene blue, and Nessler's reagent were used as is. A 1M aqueous solution of ammonium titanyl oxalate was prepared. For the Griess reaction, 8% sulfanilamide and 0.5% N-(1-naphthyl)ethylenediamene were prepared in 8.5% phosphoric acid either separately or combined.

5.2.2 Device Fabrication

Devices were fabricated using a method adapted from the laser print, cut, and laminate (PCL) protocol for devices generated from TRANSNS Copier/Laser transparency sheets purchased from Film Source, Inc. (Maryland Heights, MO) and heat-sensitive adhesive (EL-7970-39) from Adhesives Research (Glen Rock, PA).[26, 27] Devices were fabricated using five layers of polyester overhead transparency sheets, with adhesive-coated layers 2 and 4 for device bonding. Heat-sensitive adhesive (HSA) was bonded to both sides of a polyester layer simply using lamination for HSA-coated layers

(layers 2 and 4). Patches of printed toner for laser valving[28, 29] were generated by printing two layers of black toner onto each side of the device layer 3 using an HP LaserJet 4000 printer. Device architecture was cut out of each device layer using a VersaLASERVLS3.50 system (Scottsdale, AZ) with compatible CAD software. Reagents stored on Whatman filter paper, or reagent-saturated paper, were added prior to device bonding using a method previously described.[30] Devices were laminated at >160 °C for device bonding using an office laminator (Akiles UltraLam 250B).

5.2.3 Spin System Enclosures

The three spin system enclosures utilized for this chapter for microfluidic device operation had the following commonalities: the rotation system was composed of a FAULHABER Coreless Technology series 2232_SR motor controlled by a Pololu DRV8801 Single Brushed DC Motor Driver Carrier and aligned by a TT Electronics wide gap slotted optical switch. The lighting system was composed of a RadioShack three-light emitting diode (LED) Waterproof Flexi Strip.

The custom-made printed circuit boards (PBCs) were designed in Easily Applicable Graphical Layout Editor (EAGLE) and were comprised of the multicore microcontroller, motor drivers, laser diode drivers, N-Channel metal-oxide-semiconductor field-effect transistors (MOSFETs), high efficiency linear voltage regulators, and various passive electronic components and connectors. Control of the multipurpose microfluidic spin system was accomplished through the Parallax Serial Terminal (PST) program running on a Microsoft Windows based personal computer that was connected to the Parallax Propeller multicore microcontroller by a universal serial bus (USB) cable. The PST allowed the user to manually control all aspects of the system.

The spin system enclosures used for initial sampling optimizations and for initial integrated analysis contained the following variable laser system for valving: the laser system was composed of a Thorlabs 638nm red laser diode, a Thorlabs LT230260P-B laser diode focusing tube, a Thorlabs SR9F electrostatic discharge (ESD) protection and strain relief cable, a Thorlabs MTS50-Z8 motorized translation stage, and two Wavelength Electronics FL500 laser diode drivers. The simplified spin system used for sampling optimization was enclosed utilizing a custom PMMA support structure and spin system enclosure to immobilize the motor during rotation and permitted consistent imaging. The spin system used for analysis with the integrated microfluidic device was enclosed and operated within a custom-made 3D printed polylactic acid (PLA) support structure and permitted consistent imaging.

The final assembled spin system enclosure contained the following fixed laser diode system for valving: the laser system was composed of four Thorlabs 638nm red laser diodes, four Thorlabs LT230260P-B laser diode focusing tubes, four Zener diodes, four Schottky diodes, four N-Channel MOSFETs, and two Wavelength Electronics FL500 laser diode drivers. The final assembled spin system was enclosed and operated within a custom-made 3D printed acrylonitrile butadiene styrene (ABS) support structure and permitted consistent imaging. Additionally, two-way communication between the multicore microcontroller and the Huawei P9 Android phone was accomplished with this system through the Huawei P9 3.5mm Tip-Ring-Ring-Sleeve (TRRS) connector. This two-way communication allowed the user to start and stop fully automated runs and to conduct an automated system check directly from the Huawei P9 Android phone's capacitive touch screen.

5.2.4 Laser Valve Actuation

Two layers of black toner patches were printed onto the middle transparency layer prior to use. Briefly, these toner patches were used as a physical barrier between two channels for valving purposes, a method described previously by Garcia-Cordero et al. [28] A 700 mW, 638 nm laser diode (Thorlabs, Inc., Newton, NJ) below the microfluidic device was used to open each valve after 0.5 – 2 seconds of exposure.

5.2.5 Image Analysis

The reagent chambers within each microfluidic device were imaged using an Android cell phone positioned above the microdevice either on top of or incorporated into a spin system enclosure for consistent image capture. Resulting color changes observed in each image were cropped and analyzed with HSB or RGB color spaces in ImageJ, or using the developed Android cell phone application.

5.3 Results and Discussion

5.3.1 Determining a Surface Swab Material

Although studies have been performed previously on the evaluation of sampling material for efficient explosives recovery from a given surface[21, 31-33], cotton-based swabs still remain one of the most widely used material for forensic laboratories due to the low cost, availability, and ease of use for the material.[24] Swab materials of similar cost and

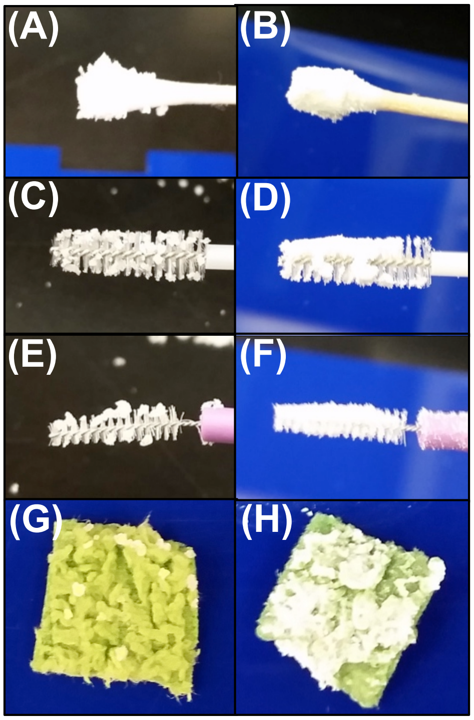

Figure 5-1. Images of various swab materials used to collect granular and powdered material. A cotton buccal swab used to collect (**A**) granular and (**B**) powdered material, a long-bristle swab used to collect (**C**) granular and (**D**) powdered material, a short-bristle swab used to collect (**E**) granular and (**F**) powdered material, and a Scotch-brite microfiber cloth used to collect (**G**) granular and (**H**) powdered material.

availability to cotton were explored here, using commercial and household materials to determine a compatible swab for the microfluidic device platform described in **Chapter 4**. Initially, swab materials most resembling cotton swabs (**Fig. 5-1A-F)** were evaluated for the ability to collect both granular and powdered material from a given surface. Challenges with sampling using cotton swab-type material were that sample would oftentimes be collected onto the handle of the swab and the collected material would easily fall off when the swab was moved. Scotch-Brite microfiber household cleaning cloth was then chosen as a material without a handle that had cloth fibers, similar to bristles, for trapping collected particles (**Fig. 5-1E,H**). The household microfiber cloth was cut into 1 cm^2 pieces for use and was able to completely collect 10 mg of both granular and powdered material without releasing the material during handling. This was advantageous as a collection material, and additional quantitative tests needed to be performed to determine the sample collection and elution (within the microfluidic device) efficiencies.

Although colorimetry has been used previously as a method for quantitative analysis, the dynamic range can be limited leading to challenges with utilizing this method for overall evaluation of swab performance. An alternative, simple method for determining collection and elution efficiencies for the swab material was needed. Conductivity measures the ability of a solution to pass electrical flow based on the concentration of ions, and a Vernier conductivity probe was used as a simple method for quantitation of the amount of ions collected or eluted from a specific swab material. Sodium chloride (NaCl) was utilized as a non-hazardous reference standard to determine the swab collection and elution efficiencies by comparing the resultant conductivity values to a standard curve. The advantage of using a non-hazardous standard was that safety considerations were not required during evaluation and optimization of swab performance; however, the disadvantage was the physical differences in NaCl crystals relative to explosive materials. The standard curve (linear, $R^2 = 0.9987$) for a range of concentrations including 0, 0.05, 0.1, 0.5, 1, and 5 mg/mL NaCl is shown in **Figure 5-2**. The concentrations could also be related to a mass amount of collected material for a more relevant understanding of the sampling capabilities.

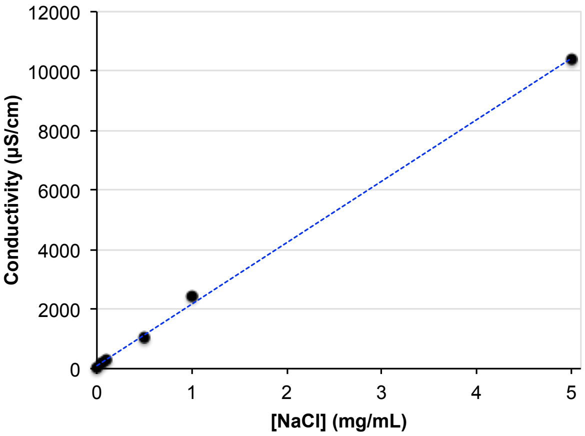

Figure 5-2. Standard curve for determining sample recovery from swab materials. A standard curve was generated associating the conductivity with the concentration for a given solution of NaCl.

The generated standard curve was used to determine the amount of sample collected with the household microfiber cloth by depositing 10 mg NaCl to a surface, a section of poly(methyl methacrylate) (PMMA) was used as the surface, and collection using 1 cm^2 laser cut microfiber pieces (**Fig. 5-3A,B**). Identical steps were used to determine the elution capabilities of the swab material within the microfluidic device by

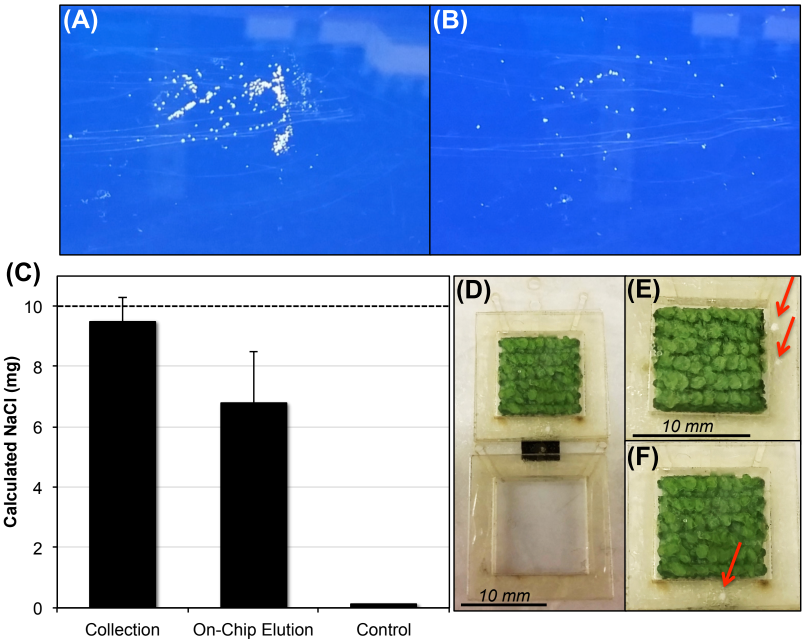

Figure 5-3. Scotch-brite household microfiber cloth used as a swab material. (**A**) Image of 10 mg NaCl deposited onto PMMA for collection using the Scotch-brite microfiber cloth. (**B**) Image of the PMMA surface with remaining NaCl not collected. (**C**) Results for calculated NaCl recovered from collection and on-chip elution using the Scotch-brite microfiber cloth. The cloth, with no sample added, was measured as a control. (**D**) Image of the overall microfluidic device used for on-chip elution studies with additional images (**E,F**) highlighting NaCl sample that was not eluted (red arrows).

collecting 10 mg NaCl onto the swab material with subsequent addition of the swab to a microfluidic device chamber. The device used for evaluation contained a series of chambers (sized to 1 cm^2), reinforced with PMMA (1.5 mm thickness), to enclose the swab with a polyester cover layer (**Figure 5-3D**). Water was used as the solvent (100 μL) to elute NaCl from the swab material with a simple centrifugal mixing protocol consisting of rotation in the clockwise and then counterclockwise direction for multiple replicate rotations. Once mixing was performed for dissolution of the sample, a laser valve was opened as previously described[28, 29, 34], to allow the sample solution to be centrifuged from the swab chamber into a subsequent chamber. The sample solution was removed from the subsequent chamber and measured for the conductivity. Additionally, a control swab with no sample was measured for the background conductivity. Collection and elution results for replicate swabs (n = 4) are shown in **Figure 5-3C**, and collection resulted in a greater amount of NaCl recovered than the elution, demonstrating a loss of sample during elution within the microfluidic device. The red arrows in **Figure 5-3E,F** show sample loss to the chamber seal within the adhesive (between the cover polyester layer and swab PMMA chamber) from addition of the swab to the microfluidic device that could account for the lower elution results.

Further consideration of the relevant sampling environment for collecting explosives residue, and the heightened interest in trace detection[35, 36], led to lower amounts of sample were utilized for additional swab analyses. To perform analyses of lower sample amounts, a new standard curve was generated (linear, R^2 = 0.9989) and is shown in **Figure 5-4**. The household microfiber cloth and additional materials including an electronics microfiber cloth, cotton swab (Q-tip), and filter paper (Whatman Grade 1) were evaluated for use as swab material. Difficulties occurred when collecting sample using dry swab material, especially with the cotton swab and filter paper (**Table 5-1**).

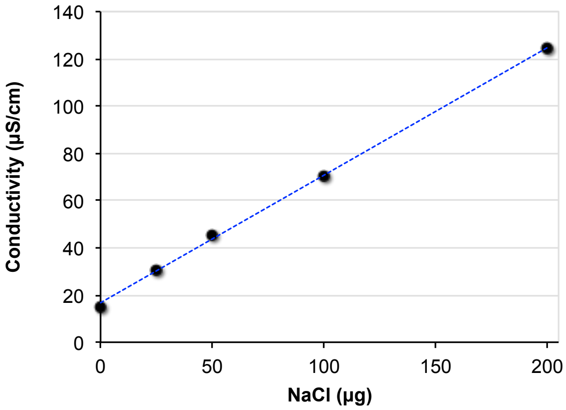

Figure 5-4. Standard curve for determining sample recovery from swab materials for trace amounts of sample. A standard curve was generated associating the conductivity with the concentration for a given solution of NaCl.

Table 5-1. Collection capabilities for 100 µg NaCl using various swab materials dry and with glycerol applied.

	Collected (µg)	
Swab Material	**Dry**	**Glycerol**
Microfiber cloth (electronics)	42.7	73.8
Microfiber cloth (housecleaning)	32.5	76.2
Cotton swab	--	134.0
Whatman 1 filter paper	--	60.1

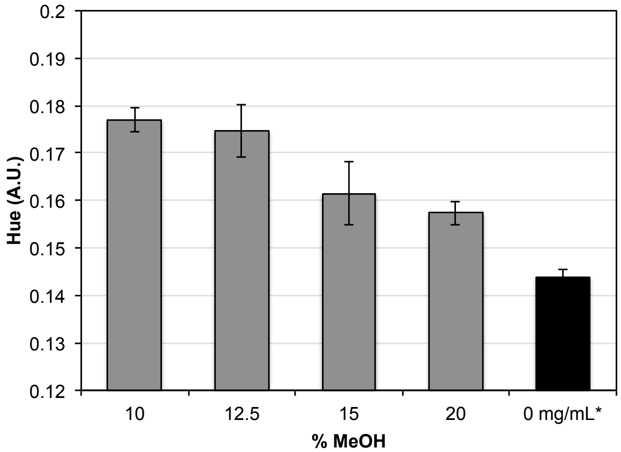

Figure 5-5. Varying solvent concentration with detection of DNT. The colorimetric detection of DNT with tetramethylammonium hydroxide was used to evaluate the use of methanol as a swab-wetting solvent. A 0 mg/mL solution was compared to the results for 0.05 mg/mL DNT with methanol between 10 – 20%.

Previous studies discuss the use of both organic solvents and water on swab material for collection of sample[24]; however, two different solvents were previously optimized for the broadly categorized organic and inorganic explosives colorimetric reactions to be used (**Chapter 4**). The two optimized solvents were 90% acetonitrile and 90% water solutions for the defined organic and inorganic groups, respectively. The only possible solvent component that could be compatible to wet the swab prior to sample collection was methanol, however, additional amounts of methanol resulted in negative effects on the colorimetric analyses. **Figure 5-5** demonstrates an example colorimetric reaction for DNT and tetramethylammonium hydroxide (TMAH), where an increase in methanol concentration resulted in a decrease in hue response with 0.05 mg/mL DNT (predefined limit of detection in **Chapter 4**). Additionally, the use of an organic solvent for wetting the swab prior to sample collection would require manual application of the solvent after the swab is opened from the packaging to avoid solvent evaporation.

Table 5-2. Evaluation of the background conductivities for various swab materials over time.

	Conductivity (μS/cm)		
Swab Material	**0 min**	**15 min**	**30 min**
Water (Control)	11.0	11.1	--
Microfiber Cloth (electronics)	11.3	11.0	--
Microfiber Cloth (housecleaning)	13.1	13.1	--
Cotton Q-tip	42.8	64.4	79.6
Whatman 1 filter paper	13.0	13.2	--

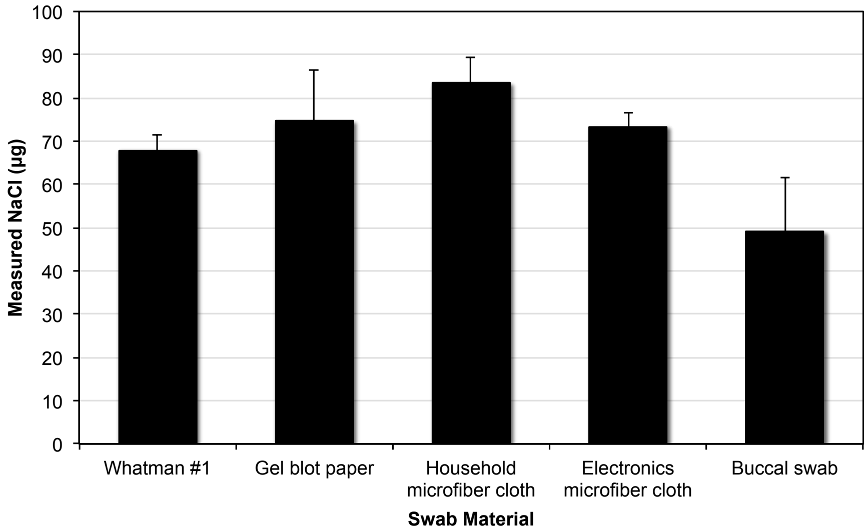

Figure 5-6. Comparison of various swab materials for collecting 100 µg NaCl from two microfiber cloths, a buccal swab, gel bot paper and filter paper (Whatman Grade 1).

An alternative swab-wetting solution was chosen as glycerol for the low volatility, allowing the swab material to be packaged with the glycerol already applied to the swab prior to use. The various swab materials were evaluated with glycerol applied to the surface of the swab for improved sample collection, and **Table 5-1** shows initial results of both dry and glycerol collection of 100 µg NaCl for two microfiber cloths, cotton swab, and filter paper. The amount of sample collected increased for both microfiber cloths coated in glycerol compared to dry. Additionally, both microfiber cloths resulted in more sample collected than the filter paper while the cotton swab, however, measured more sample collected than the amount deposited. Additional tests evaluating the background conductivity for each

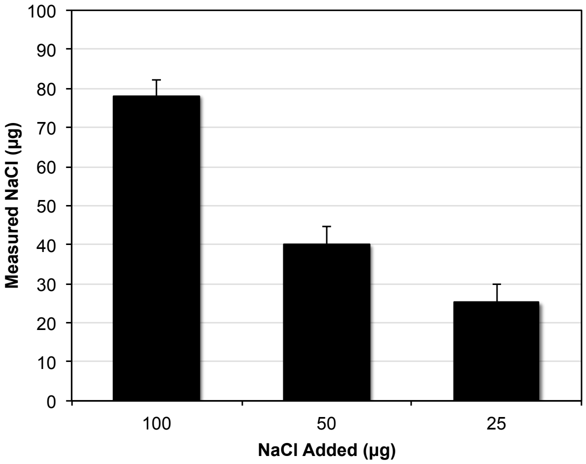

Figure 5-7. Recovery results for the collection of various amounts of NaCl using gel blot paper.

material confirmed that the conductivity from the cotton swab, with no sample, increased overtime due to the dissolution of the glue used to apply the cotton in solution (**Table 5-2**). A commercial cotton swab (Q-tip) was not considered further as a potential swab material; however, a cotton buccal swab and gel blot paper were evaluated as an alternative swab material due to the increased thickness of the woven cellulose fibers (0.8 mm) compared to the filter paper (11 μm). Results are shown in **Figure 5-6** from further evaluation of each swab material for the collection of 100 μg NaCl. Although the household microfiber cloth was able to collect the highest amount of NaCl, gel blot paper was the easiest to use and to customize the geometry with the laser cutter. Additional collection studies using the gel blot paper were performed for various amounts of sample including 25, 50, and 100 μg NaCl for n = 3, and resulted in a relatively linear relationship (R^2 = 0.9396), as expected (**Figure 5-7**). Frequently, evaluation of the gel blot paper for collecting 25 μg NaCl resulted in a measured mass >25 μg due to the sensitivity of the Vernier conductivity probe at this concentration range.

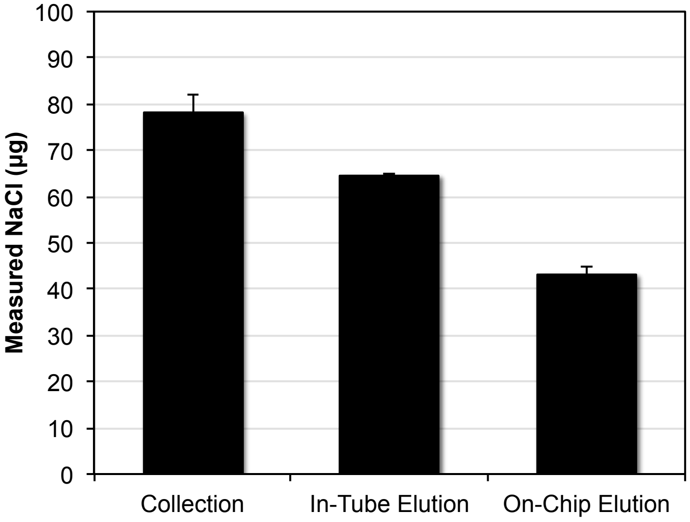

Figure 5-8. Comparison of the measured NaCl recovered from collection, in-tube elution, and on-chip elution of 100 μg NaCl deposited using gel blot paper.

A comparison of the collection, in-tube elution, and on-chip elution results for the gel blot paper as a swab material is shown in **Figure 5-8**. A significant decrease in the recovery of NaCl was observed between collection and on-chip elution, with in-tube elution providing increased recovery compared to on-chip. This revealed that an optimized on-chip elution method was required. Gel blot paper was used to collect 100 µg NaCl and the conductivity was measured prior to and immediately following a 5-second mix using a benchtop vortex. **Figure 5-9** shows that there was a ~2X increase in the response after the solution was mixed using the vortex. Implementing an enhanced mixing protocol on-chip should increase the on-chip elution results.

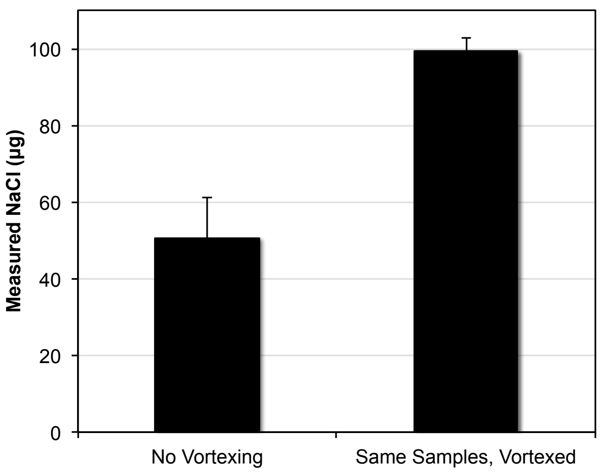

Figure 5-9. Results for the collection of 100 µg NaCl using gel blot paper with and without mixing the solution using a benchtop vortex before measuring the conductivity.

5.3.2 Surface Swab Fabrication and Use

A surface swab compatible with the microfluidic device was developed to optimize a microfluidic mixing protocol for improving the on-chip elution. The gel blot paper was adhered to PMMA (0.5 mm thickness) to fully extend the swab into the device chamber for complete submersion of the swab surface

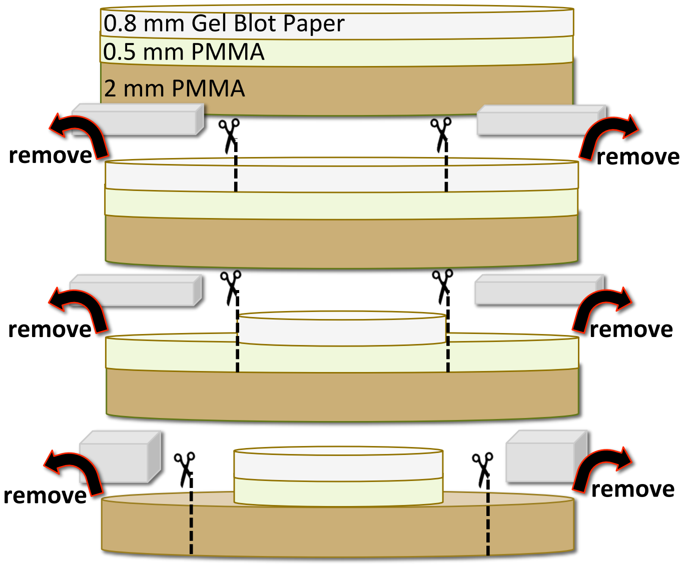

Figure 5-10. Schematic of the fabrication process for the single-swab compatible with the microfluidic device.

into the elution solvent (**Fig. 5-10**). An additional piece of PMMA (2.0 mm thickness) was adhered to the 0.5 mm PMMA piece for use as a rigid backing support for handling the swab. The three materials were adhered and then laser cut to remove unnecessary material around the swab area, and a schematic of the fabrication process is shown in **Figure 5-10**. Once the swab was fabricated, it was inserted into the swab chamber on the underside of layer five of the device (**Fig. 5-11**). A pressure-sensitive adhesive seal on the outside of the chamber allowed for attachment of the swab using the rigid PMMA backing piece, enclosing the gel blot paper within the device. After the swab was sealed, the device was rotated (vertically, 180°) for use (**Fig. 5-11D**).

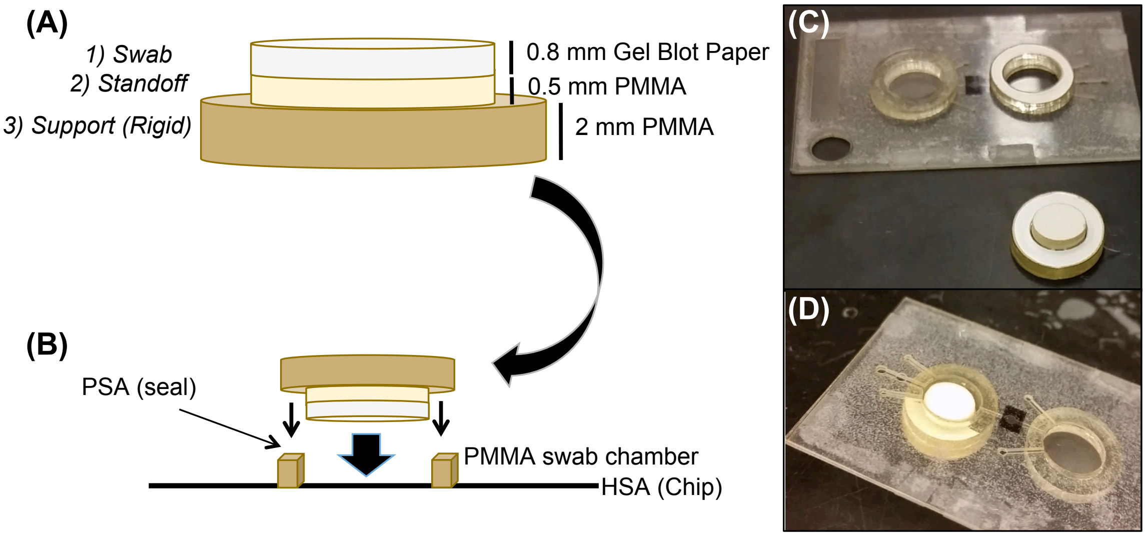

Figure 5-11. Schematic describing application of the single-swab to the microfluidic device with images. (**A**) A schematic of the fabricated single-swab for use. (**B**) Schematic describing the application of the surface swab to the microfluidic device using a complimentary device chamber. Image of the swab (**C**) before and (**D**) after Insertion into the microfluidic device.

To simulate a vortex mixing motion on-chip, the sample chamber was pushed on manually to move the solvent in the z-direction, or vertically, within the chamber. Additionally, the amount of elution solvent needed to be defined to get an optimal vortex motion within the ~1.5 mm (height) swab chamber, and ideally, would be the minimum amount of solvent necessary to elute all sample collected from the swab to reduce sample

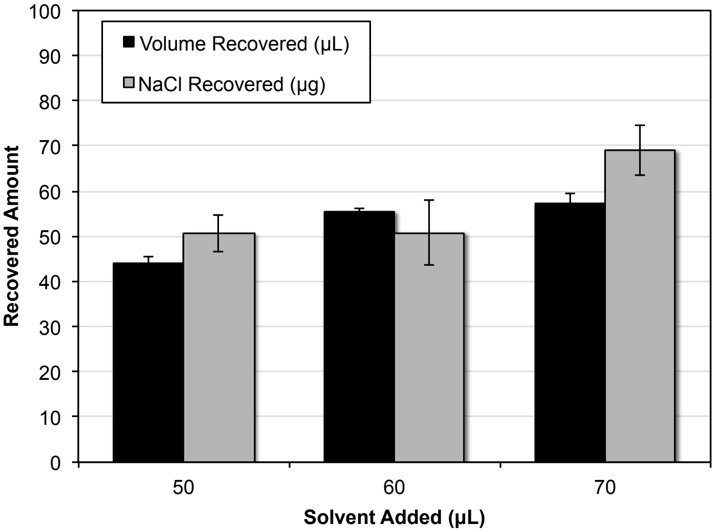

Figure 5-12. Results for the volume recovered and the amount of NaCl that was eluted using manual mixing from the microfluidic device with various amounts of solvent added.

dilution prior to detection. Solvent amounts from 50 to 70 µL (n = 3), water used in **Figure 5-12**, were utilized with manual mixing for elution of the sample. After the sample was collected onto the swab and eluted on-chip, the sample solution was removed from the device for conductivity analysis. The amount of volume and sample recovered from the device are shown in **Figure 5-12**, and as the amount of solvent increased, the amount of NaCl recovered also increased.

The NaCl recovery with manual and centrifugal mixing was compared using 70 µL (n = 4) and the results are shown in **Figure 5-13**. The amount of NaCl recovered using 70 µL with both manual and centrifugal mixing was an improvement from the initial on-chip elution analysis shown in **Figure 5-8**, however, there was still a significant improvement using manual mixing compared to centrifugal mixing. Applying a manual mixing step to the final device protocol would negatively affect the ability to fully automate the device protocol. Although manual

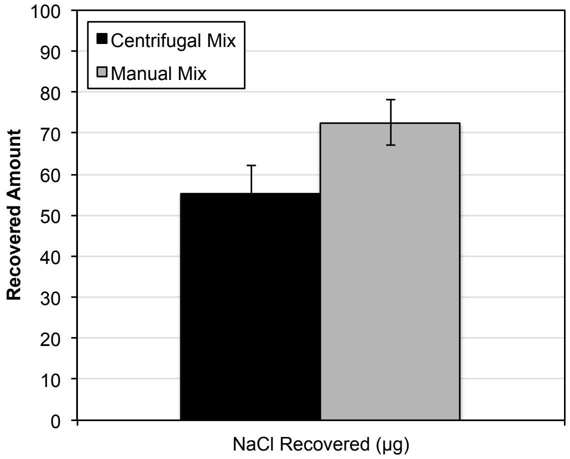

Figure 5-13. Comparison of the recovered amounts of NaCl using manual and centrifugal mixing for on-chip elution with 100 µg NaCl deposited.

mixing provided a significant improvement to the sample recovery, an additional elution protocol was considered to determine a potential automated mixing protocol. The integration of a sonication event after the swab was added to the device would agitate the collected sample particles on the swab surface and readily dissolve the collected sample into the elution solvent. Sonication was applied to the device chamber by touching the top of the device swab chamber to the edge of a beaker within the sonication bath (**Fig. 5-14A**). Various mixing protocols including sonication only, sonication with manual mixing, and all mixing options (sonication, manual, and centrifugal) were applied to the device (n = 3) using 70 μL elution solvent and results are shown in **Figure 5-14B**. Sonication provided the most varied response and was not a significant increase compared to centrifugal mixing with 70 μL solvent (**Fig. 5-13**), however, additional mixing using manual and centrifugal combined with sonication provided consistent and improved sample recoveries. Unfortunately, concerns for the overall device system during sonication and limitations for incorporating a piezo for sonication with

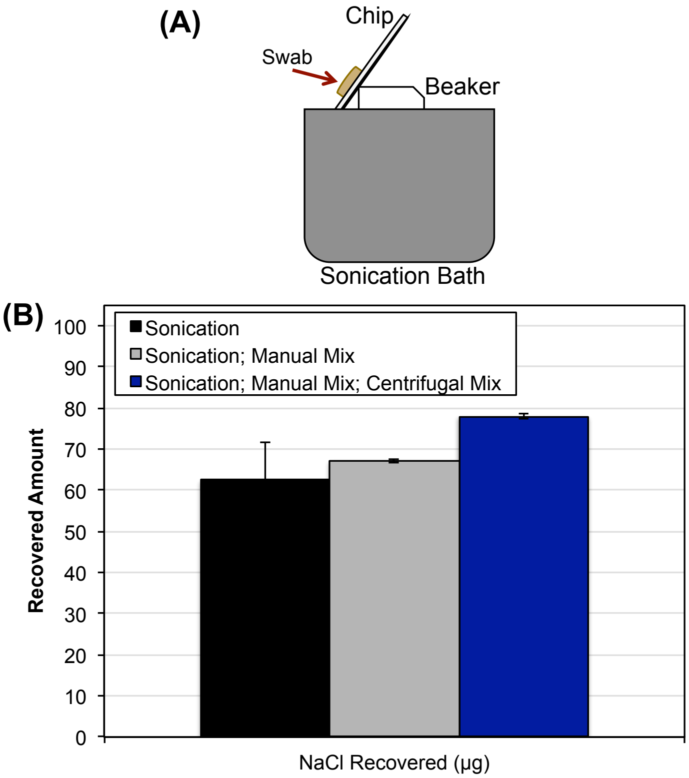

Figure 5-14. Effects from various methods on the on-chip elution recovery from 100 μg NaCl deposited. (**A**) A schematic describing the device setup used for sonication of the swab chamber. (**B**) Comparison of the various methods on the on-chip elution recovery.

elastomeric polyester material prevented the use of sonication for on-chip sample elution.

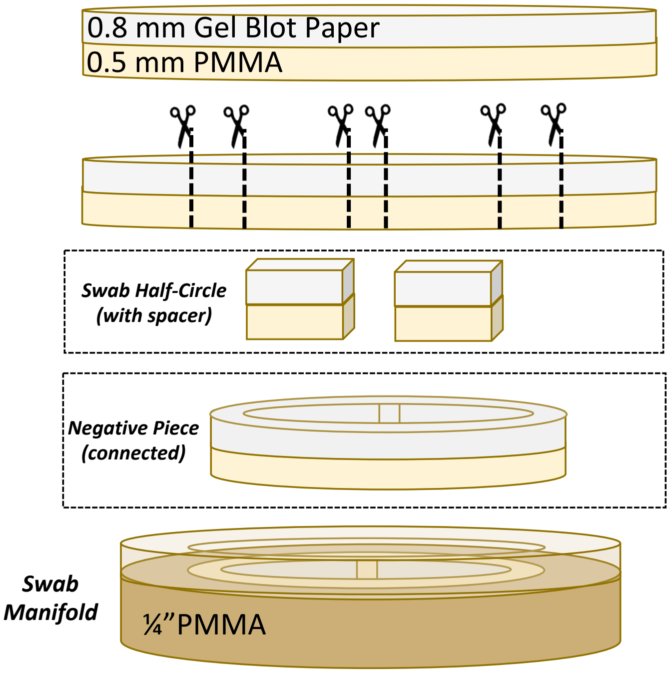

Figure 5-15. Schematic of the fabrication process for the split-swab and swab mold used for fabrication.

For continued sampling studies, a new swab design and complimentary fabrication technique were utilized to account for the sampling of both inorganic and organic explosives material. Two different solvents were optimized for the organic and inorganic explosives colorimetric reactions, and a split-swab was determined as the optimal swab design for the implementation of both elution solvents. This allows a single swab to be used for sampling instead of requiring two separate sampling events and individual swabs. A simple fabrication procedure described in **Figure 5-15** was applied; where the two swab pieces for the split-swab were laser cut from gel blot paper adhered to PMMA. A manifold for swab assembly was generated using the complementary cut pieces reinforced with PMMA. The split-swab assembly is shown in **Figure 5-16** where the two swab pieces were added to the manifold with pressure-sensitive adhesive facing upwards. The cover layer for the adhesive was removed to apply a rigid PMMA backing piece, similar to the single-swab fabrication described in **Figure 5-11**. An image of the assembled swab and manifold are shown in **Figure 5-16**, displaying the split-swab with two half circle-type swab pieces. A pressure-sensitive adhesive seal on the device swab chamber allowed for attachment of the swab using the rigid PMMA backing, enclosing the two gel blot paper swab pieces within two divided sections (completely separated) of the device chamber. After the swab was sealed, the device was rotated (vertically, 180°) for use.

Defining a swabbing protocol for a split-swab was critical for assuring an equal amount of sample was collected on each swab half. Various swabbing protocols including swabbing to the right, to the left, in a zig-zag motion, and in a swirl motion were evaluated with each motion described in **Figure 5-17**. Initial results in **Table 5-3** show the amount of NaCl recovered after on-chip elution, from 100 μg NaCl deposited and swabbed from the PMMA surface using each of the described motions. As expected, a swabbing motion to the right and to the left collected the majority of the sample on the leading swab half (denoted by an asterisk symbol '*' in **Table 5-3**). The leading swab was opposite of the

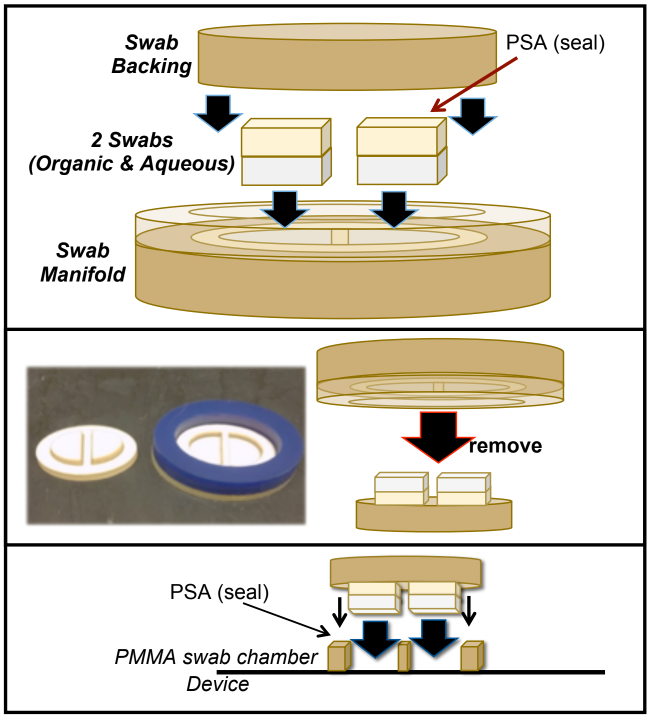

Figure 5-16. Schematic describing application of the split-swab to the microfluidic device with images. (**A**) Schematic of the swab mold used for the final swab fabrication step. (**B**) Schematic showing the completed swab with image of the swab and swab mold (blue). (**C**) Schematic describing the application of the split-swab to the microfluidic device using a complimentary partitioned chamber.

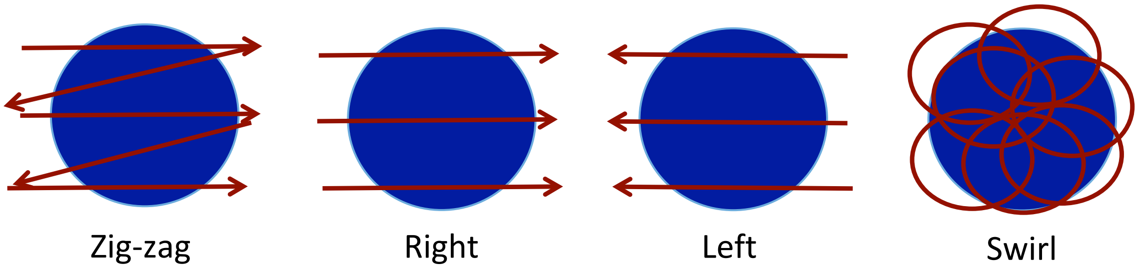

Figure 5-17. Schematic describing the various swabbing protocols evaluated using the split-swab, including swabbing to the right, to the left, in a zig-zag motion, and in a swirl motion.

swab motion applied due to the orientation of the swab when added to the microfluidic device from the bottom before use. The zig-zag swab motion provided the most even amount of sample collected onto both swab halves, although initial results show the swirl motion collected more sample overall. Since the desired motion would have an equal distribution of sample to both swab halves, the zig-zag motion was chosen for the defined swabbing protocol.

Table 5-3. Results for the amounts of NaCl collected using the various swabbing motions for the split-swab after on-chip elution. The leading swab half is denoted by an asterisk '*' symbol.

Sample #	Amount NaCl (µg)	Combining Left and Right Swab Halves (µg)
Zig-zag (L)	30.5	64.9
Zig-zag (R)	37.0	
Right (L)*	50.2	57.5
Right (R)	9.3	
Left (L)	9.9	56.9
Left (R)*	49.0	
Swirl (L)	56.7	69.9
Swirl (R)	16.1	

5.3.3 Modification of the Device Design for Integration

The device design originally proposed in **Chapter 4** for multiplexed analysis from a single sample input, with inclusion of both the one-step and two-step colorimetric reactions, was optimized for integration of the split-swab. Fluidic movement using the updated design is demonstrated with dye in **Figure 5-18**. The design required a chamber for each swab half with a laser valve below the chamber to allow fluid movement once the sample was completely dissolved from the swab. After the valves were opened, the sample solution would move from the swab chambers into separate inlet channel architecture using capillary action (**Fig. 5-18B**). Once the sample channels were filled, a laser valve was opened to allow centrifugal movement of excess sample in the inlet channel to a waste chamber for consistent metering of the sample solution (**Fig. 5-18C**). Finally, the sample solution could be centrifugally moved to the reaction chambers for colorimetric detection (**Fig. 5-18D**). The two sides of the fluidic architecture demonstrate the organic and inorganic explosives groups identified in **Chapter 4**.

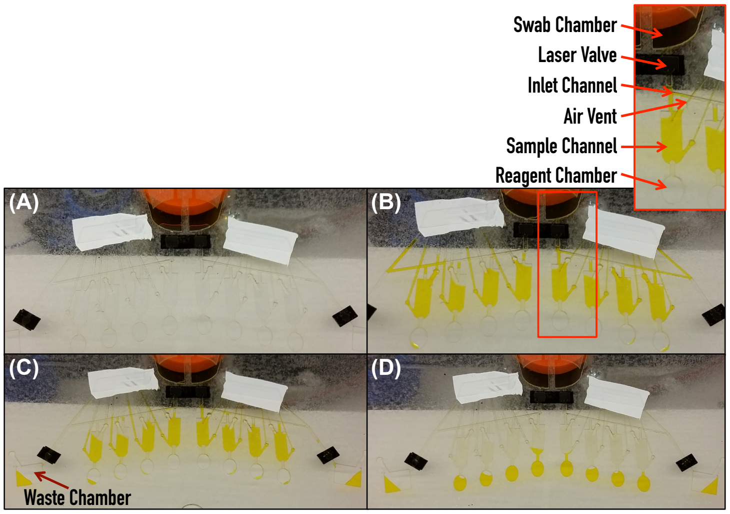

Figure 5-18. Images showing fluidic movement with dye. (**A**) Image with no dye. (**B**) Movement of dye from swab chambers into separate inlet and sample channels using capillary action. Inset describes each design feature. (**C**) Excess dye in the inlet channel was centrifugally moved to waste. (**D**) Metered sample solution was centrifugally moved into each reagent chamber.

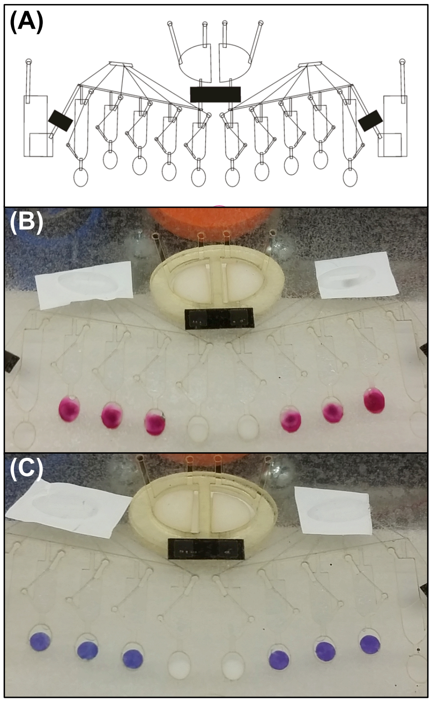

Figure 5-19. Device design and split-swab utilized with explosives. (**A**) Modified device design to conserve device size. Split-swab was used to collect (**B**) KNO_3 and (**C**) $NaClO_4$ explosive samples.

Before the device design was evaluated using explosive standards, the inlet channel was altered to conserve the device size (**Fig. 5-19A**). After replicate

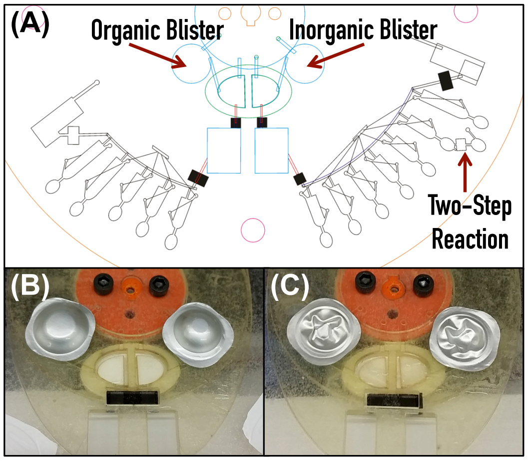

Figure 5-20. Integration of blister pouches for solvent delivery. (**A**) Modified device design for complete integration of sampling. Images of the microfluidic device with blisters (**B**) unused and (**C**) used for delivering solvent to the swab chambers.

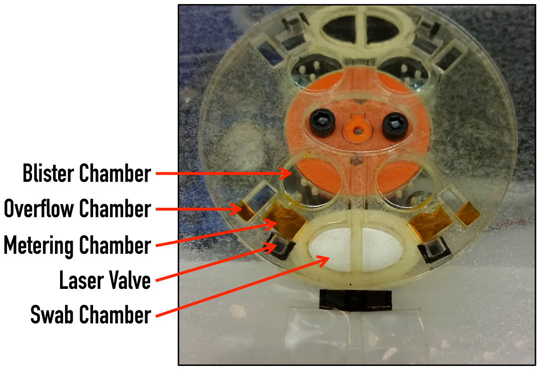

Figure 5-21. Image of the microfluidic device, with labeled features, for dye added to the blister chambers to demonstrate solvent metering.

dye studies to evaluate the fluidic architecture, this design was utilized for initial tests with sampling explosive material. The split-swab was used to collect 0.8 mg KNO_3 and 0.8 mg $NaClO_4$ deposited for two different surface sampling events (**Fig. 5-19B,C**). Moving towards integration of all device processes, the inlet of the device was altered for incorporating blister pouches to replace manual pipetting of solvent, and the inorganic explosives architecture (right portion of the design) was updated to include the two-step modified Griess reaction (**Fig. 5-20**). The commercial blister pouches were sized for 100 and 50 µL volumes with less than 100% volume recovery (~80% recoveries reported[37]). To account for these reported recoveries, a metering chamber was utilized within the device design for consistent delivery of 50 µL of solvent from a 100 µL blister pouch (**Figure 5-21**). Due to the split-swab use, an elution solvent volume of 50 µL was utilized for one swab half instead of 70 µL. The metering chambers were positioned below each blister chamber, and utilized an overflow waste chamber for the excess solvent volume. Once the volume was metered from the blister pouches, a laser valve was opened to allow the metered solvent to enter into each swab-half chamber for sample elution. **Figure 5-21** demonstrates the metering design using dye, where 80 μL of dye was pipetted into the blister chamber to simulate the use of a blister pouch. The fluidic architecture needed to be fully evaluated before utilizing purchased blister pouches. The overall multiplexed device design with blister and metering architecture is shown in **Figure 5-22** for one half of the centrifugal device. A duplicate design of the multiplexed architecture was added to the other half of the device, to perform two replicates on a single centrifugal device. The described design also included all of the colorimetric reactions and a sample cleanup chamber to centrifugally sediment environmental contaminants.

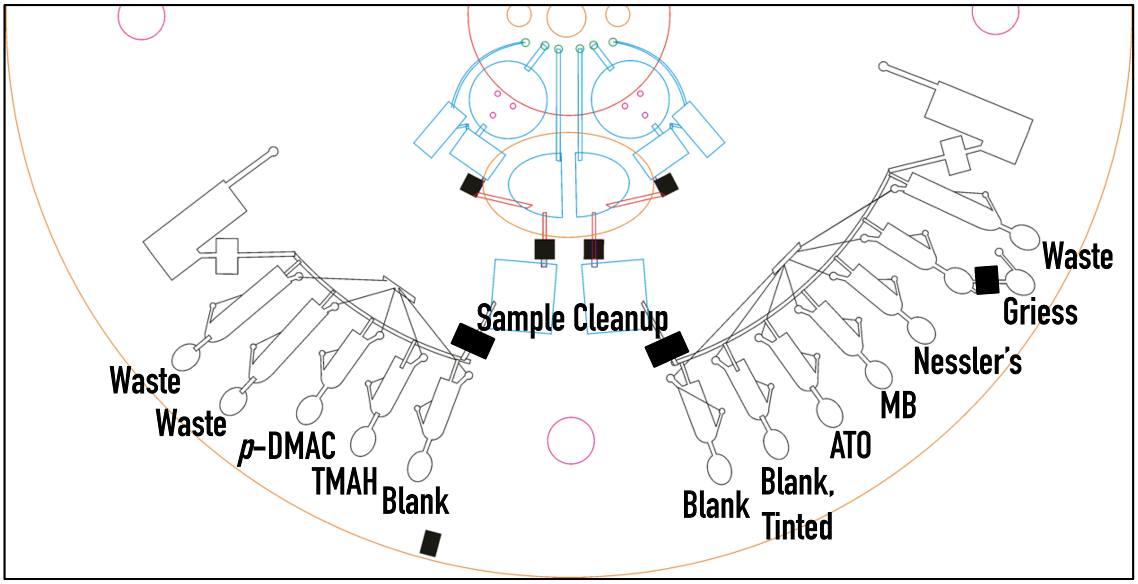

Figure 5-22. Device design modified for metering of solvent released from the blister pouches, describing each reagent chamber use.

It was critical to determine an initial, fully integrated design (blister, swab, sample preparation, and colorimetric detection) to understand the limitations of the design for making design optimizations. To fully integrate sampling into the microfluidic device, manual application of the swab to the device needed to be capable of straightforward operation for decreased user error. A swab handle and a handle adapter were 3D-printed

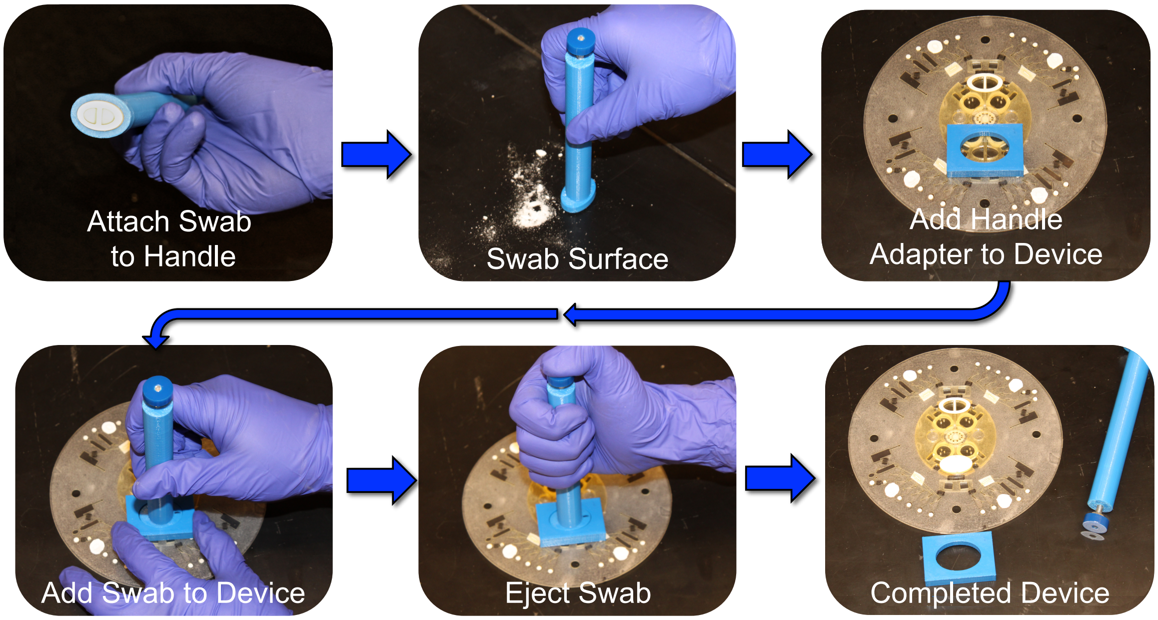

Figure 5-23. Images describing the swab protocol utilizing the 3D-printed swab handle and microfluidic device adapter for alignment of the swab.

for use of the swab and for alignment of the swab to the microfluidic device chamber. **Figure 5-23** describes the stepwise procedure for using the handle and adapter. After the surface is sampled using the swab added to the handle through a pressure-fit seal, the adapter is added to the device for alignment of the swab to the microfluidic device chamber. The 3D-printed adapter has a complimentary geometry to the PMMA piece adhered to the bottom of the microfluidic device for correct alignment of the adapter to the device. The swab handle is inserted into the adapter to guide each swab half into a device swab chamber. The swab handle can only rotate 180° to fit within the adapter, and either orientation will allow for correct insertion of the swab. A pressure-sensitive adhesive on the outside of the device swab chamber is used to seal the swab to the microfluidic device, enclosing the swab. The end of the swab handle is then manually triggered to eject the swab from the handle to generate the final device with sample added.

The ability of the fully integrated device described in **Figure 5-22** for sample preparation was evaluated using the developed swab protocol. The surface swab was utilized to collect the maximum amount of environmental contaminant, dirt used here, and evaluate the sample cleanup protocol within the device (**Fig. 5-24A**). **Figure 5-24B** shows an image of the swab applied to the device with dirt collected prior to operation of the device centrifugal protocol. Once the sample was eluted from the right swab-half using the aqueous-based solvent for the inorganic explosives defined in **Chapter 4**, a laser valve was opened to allow movement of the sample solution into the sample preparation chamber. The diameter of the laser valve hole (80 μm) was sufficient for filtering a majority of the contaminant from the sample solution as observed in **Figure 5-24C**. After the sample solution was centrifuged from the swab chamber and filtered, the contaminant that remained in the solution was centrifugally sedimented to the bottom of the chamber. The placement of the subsequent laser valve and device channel was utilized to siphon the clean sample from the top of the chamber, leaving a layer of the sedimented contaminant at the bottom of the sample preparation chamber (**Fig. 5-24D,E**).

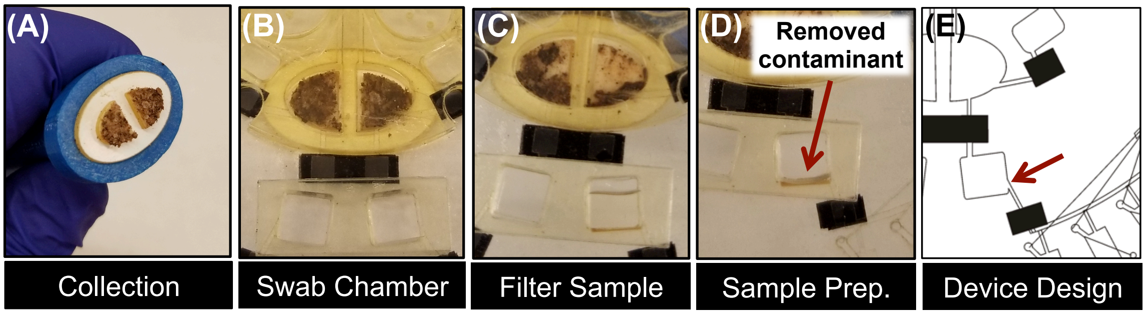

Figure 5-24. Images describing sample cleanup of environmental contaminants within the microfluidic device. (**A**) A significant amount of dirt was collected onto the swab for demonstration of the sample cleanup method. (**B**) The swab with contaminant was added to the microfluidic device and solvent was delivered for sample dissolution. (**C**) The laser valve filtered a majority of the contaminant and the remaining dirt was centrifugally sedimented in the sample preparation chamber. (**D**) Clean sample was siphoned from the top of the sample preparation chamber, device architecture shown in (**E**), for downstream analysis.

5.3.4 System Enclosure for Automated Analysis

Collaborators at TeGrex Technologies (Charlottesville, VA) generated a system enclosure for automated device operation (**Fig. 5-25**), and a number of spin functions could be performed in an automated manner using this system, including: homing the device ('H'), returning to the home position ('R'), open laser valves ('Z'), single manual spin step ('M'), series of automated spin steps ('A'), and centrifugal mixing protocol ('X'). The alignment functions, homing and return to home, were critical for aligning the device to open laser valves and for device imaging. The device position in which the alignment marking, or patch of printed toner at the edge of the device, is at the left edge between the optical switch (**Fig. 5-25C inset**) is considered 'home' for the device, and all other positions are relative to this 'home' position. When the alignment mark passes the optical switch it impedes the light from passing through the device to the receiving end of the sensor, denoting the device 'home' position.

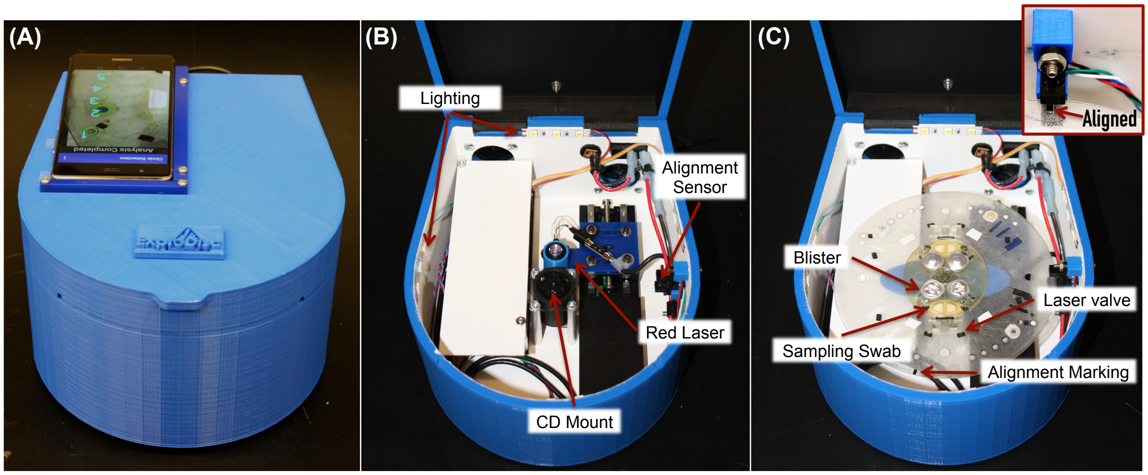

Figure 5-25. Images of the device enclosure system used for device operation. (**A**) Image of the closed device system with cell phone for analysis. Image of the device opened showing features for device operation (**B**) without and (**C**) with a microfluidic device added.

This alignment systems allows for consistent opening of laser valves, where each valve is opened two times, separated by 1° for the angular position on the device to account for any random error that could result in unsuccessful opening of a laser valve. The laser diode used for opening these valves is placed on a linear actuator that controlled the radial position of the laser, or distance from the center. There were four different laser valve positions (radial from the center) that needed to be actuated, or opened. This linear actuator allowed for minor adjustments during device prototyping in the position of the laser valves and would later be replaced by a fixed laser system (four different individual laser diodes at different radial positions rather than one laser diode on a linear actuator). The device protocol for the fully integrated device described is shown in **Table 5-4**. The overall device spin protocol time was ~4.5 min (aqueous protocol), not including the time for imaging, to home the device before moving to specific angular positions, and move the laser diode on the linear actuator for valving, while the complete protocol time from start to finish was 8.5 min.

Table 5-4. The complete device protocol for the fully integrated device described.

		Centrifugal Protocol (Aqueous-based Solvent)			Centrifugal Protocol (Organic-based Solvent)			Valve Protocol	
Protocol Step	Function Code	Speed (RPM)	Time (s)	Spin Replicates	Speed (RPM)	Time (s)	Spin Replicates	Radial Distance (cm)	Angle Relative to Home Position (°)
Solvent Metering	M	2000	15		2000	5			
Home device	H								
Return to Home Position	R								
Open Metering Valves (Domain 1)	Z = 4							25	258, 259; 315, 316
Open Metering Valves (Domain 2)	Z = 4							25	77, 78; 135, 136
Spin Solvent to Sampling Chambers	M	2500	15		2500	5			
Centrifugal Mix for Sample Dissolution	X	3000	1	3	3000	1	3		
Open Sampling Valves (Domain 1)	Z = 4							30	279, 280; 291, 292
Open Sampling Valves (Domain 2)	Z = 4							30	100, 101; 111, 112
Elute Sample Solution	M	2500	15		2500	5			
Centrifuge Sample Solution	M	3300	120		3300	10			
Open Sample Preparation Valves (Domain 1)	Z = 4							42	272, 273; 299, 300
Open Sample Preparation Valves (Domain 2)	Z = 4							42	92, 93; 119, 120
Fill Sampling Channels	M	700	20		700	10			
Fill Reagent Chambers	M	2500	35		2500	15			
Centrifugal Mix for Reagent Chamber-2	X	3000	1	3					

5.3.5 Image Capture and Analysis using Smartphone Application

The cell phone utilized for image capture in **Chapter 4** was the discontinued LG Optimus F3 (LG Electronics) and consisted of small size and relatively inexpensive cost. This cell phone was compared to other models in **Table 5-5** to determine a potential benefit for sacrificing the size and cost to upgrade to a newer phone model with additional functionalities and better quality images. The most expensive cell phone model considered was the Huawei P9 (HUAWEI Technologies), however, this model was reported to have excellent image quality and a small focal distance. The smallest focal distance was desired for imaging as the closer the phone could be to the microfluidic device, the smaller the height requirement would be for the entire portable system. The LG G2 (LG Electronics) was a compromise between the LG Optimus F3 and the Huawei P9 with respect to quality and cost. Ultimately, the Huawei P9 was chosen for further development of the image analysis and Android application with the potential for an alternative cell phone to be used in the future, if necessary, after initial development of the completed system.

Table 5-5. Comparison of the specifications for different cell phones to use with colorimetric analysis.

Specifications	LG Optimus F3	Huawei P9	LG G2
MP	5	12 (x2)	13
Size	116.1 x 62 x 10.1 mm	145 x 70.9 x 6.95 mm	138.5 x 70.9 x 8.9 mm
Display	4.0”	5.2”	5.2”
RAM	1 GB	4 GB	2 GB
Price	$50	$450	$190
Other	--	2 cameras	--

An initial comparison between an image taken with both the LG Optimus F3 and Huawei P9 cell phones for colorimetric reaction of 10 mg/mL H_2O_2 and ammonium titanyl oxalate (ATO), with and without tinting is shown in **Figure 5-26**, and demonstrates differences between the two photos through the analysis. The Huawei P9 cell phone was able to better differentiate between a positive and negative result without tinting, for the yellow and white color responses, respectively. Additionally, the tinting response for a negative sample from an image taken with the Huawei P9 phone had an increased hue value compared to the LG Optimus F3. This result is advantageous as a hue result between 0.4 – 0.45 A.U. is more indicative of a cyan color, which was the chosen tint color used here.

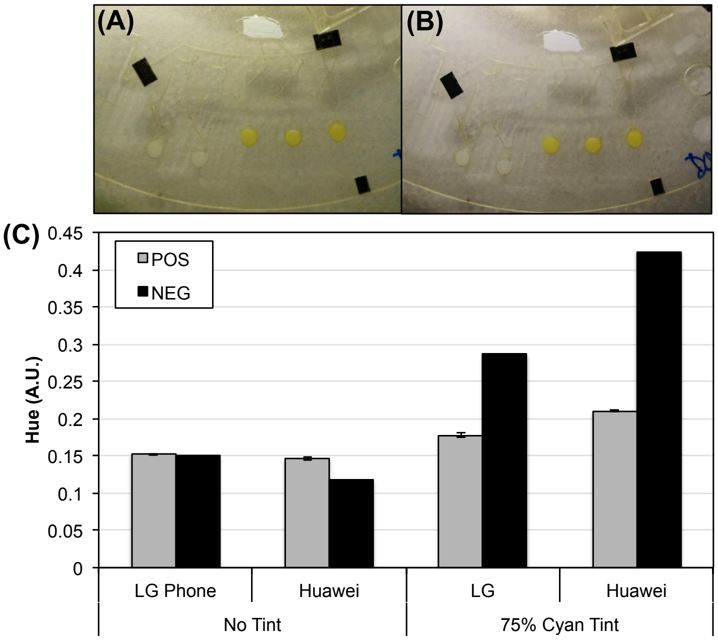

Figure 5-26. Analysis comparison of the LG Optimus F3 and Huawei P9 cell phones for the colorimetric reaction of hydrogen peroxide with ammonium titanyl oxalate. Images of the device for the colorimetric detection of H_2O_2 using the (**A**) LG Optimus F3 and (**B**) Huawei P9 cell phones. (**C**) Comparison of the hue results for a positive and negative H_2O_2 sample with and without tinting applied.

An Android cell phone application, compatible with the Huawei P9 cell phone, was developed in collaboration with the Department of Computer Science at the University of Virginia (Charlottesville, VA). The initial cell phone application used for colorimetric detection of cocaine and methamphetamine with the LG Otimus F3 cell phone (discussed in **Chapter 2**) required significant user operation. Although the simplicity of this application was ideal for straightforward use, the user was required to align the cell phone with the device, capture an image of the device within the application, crop the area for analysis, and select the correct threshold value to apply (labeled as 'cocaine' or ‘methamphetamine’). Ultimately, image capture, cropping of the image, and applying threshold values would all be programmed for automation of the analysis protocol without user intervention.

Each imaging event would be programmed during assembly of the final device enclosure system to automate positioning the device and image capture. Cropping or isolating the reaction chambers for color analysis within the image can be performed using pixel coordinates or detection markings. Although the device should be in the same position during each image capture event, subtle variations in the device position or the use of a different cell phone in the future would limit the ability for pixel locations to define analysis regions within the images. Alternatively, detection markings were implemented to locate each of the detection regions, or reagent chambers, for performing the colorimetric analysis. Since printing is inherent in the laser print, cut, and laminate (PCL) fabrication process, detection markings were printed onto the cover layer of the device to locate the detection regions using the Android application. The detection chambers were ordered, or numbered, from the top of the image to the bottom of the

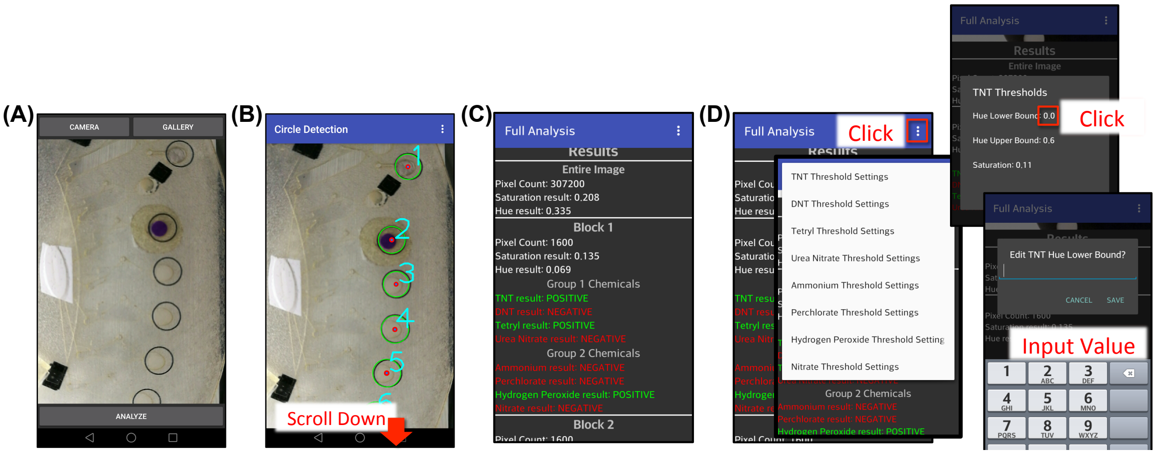

Results

Entire Image

Pixel Count: 307200
Saturation result: 0.208
Hue result: 0.335

Block 1

Pixel Count: 1600
Saturation result: 0.135
Hue result: 0.069

Group 1 Chemicals

TNT result: POSITIVE
DNT result: NEGATIVE
Tetryl result: POSITIVE
Urea Nitrate result: NEGATIVE

Group 2 Chemicals

Ammonium result: NEGATIVE
Perchlorate result: NEGATIVE
Hydrogen Peroxide result: POSITIVE
Nitrate result: NEGATIVE

Block 2

Pixel Count: 1600

TNT Thresholds

Hue Lower Bound: 0.0
Hue Upper Bound: 0.6
Saturation: 0.11

Edit TNT Hue Lower Bound?

Figure 5-27. Step-wise images of the microfluidic device image analysis process using the Android application. (**A**) Image of the device is taken within the Android application (‘app.’). (**B**) The reagent chambers are detected and labeled within the app. for automated analysis. (**C**) Threshold values are applied for detection at each labeled location, and (**D**) thresholds can be modified easily within the app.

image for determining which threshold values to apply for each analysis location. **Figure 5-27** describes the stepwise operation of the Android application where the image is first captured and the detection markers around each reaction chamber are instantaneously identified (green circles in **Fig. 5-27B**) and numbered. The image analysis is then performed within the detection region (small red circles in **Figure 5-27B)** and the image analysis results are reported for each numbered detection region (**Fig. 5-27C**). The number of pixels used for averaging can be defined within the application by changing the radius setting to increase or decrease the radius from the center of the detection circle to perform the analysis within (**Fig. 5-28A**). Initial evaluation of the size of the analysis region is shown in **Figure 5-28B** and resulted in no change in hue analysis based on the number of pixels averaged. The radius setting of 0.2, associated with ~729 pixels, was chosen for analysis to account for any variations within the device fabrication that could affect the analysis regions, i.e., misalignment of the top device layer.

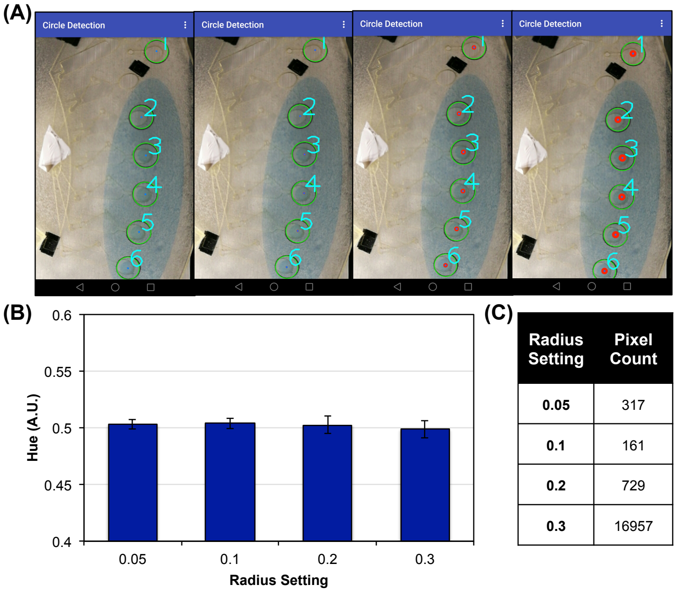

Radius Setting	Pixel Count
0.05	317
0.1	161
0.2	729
0.3	16957

Figure 5-28. Choosing a pixel count to use within the Android application for analysis. (**A**) The number of pixels analyzed can be readily changed within the Android application. (**B**) Increasing the number of pixels averaged for analysis did not affect the hue results. (**C**) Correlation between the arbitrary radius setting and the number of pixels used for analysis.

For initial use of the Android application, the user is only required to capture the photo to perform the analysis. The steps following the image capture are automated by the Android application and the user can scroll down on the screen to see the results. Threshold values can be programmed for analysis of each explosive material by selecting the toggle at the top right within the application **(Fig. 5-27D)** and inputting the predefined upper and lower threshold values.

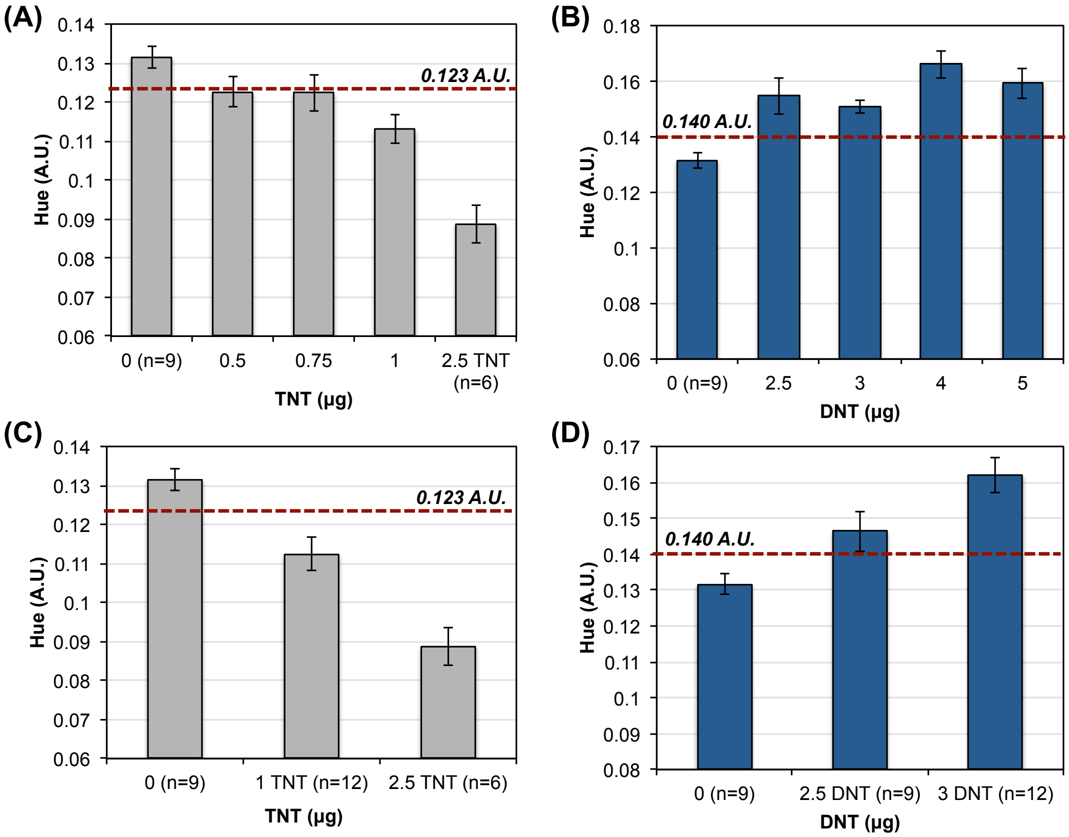

Figure 5-29. Reevaluation of the detection limits and threshold values used for detection with TNT and DNT as exemplary colorimetric reactions with tetramethylammonium hydroxide. Initial analyses for determining the detection limit for (**A**) TNT and (**B**) DNT colorimetric analysis. Final analyses of the detection limit for threshold determination to use for detection of (**C**) TNT and (**D**) DNT. Threshold values are shown as red dashed lines.

5.3.6 Defining Limits of Detection and Threshold Values

The limit of detection (LOD) and threshold values for each explosive analyte using the colorimetric reaction defined in **Chapter 4** was reevaluated using the updated device design, developed surface swab, and new detection scheme with the Android application and Huawei P9 cell phone. It was expected that the LODs determined using the surface swab would be higher than those defined previously in **Chapter 4**, due to the loss of sample to the swab during on-chip elution. To assure a consistent amount of analyte would be added to the swab, each explosive standard solution was pipetted onto the surface of the swab for analysis instead of swabbing solid material from a given surface. The mass of explosive analyte deposited onto the swab could be calculated from the explosive concentration used and the on-chip elution volume. First, a range of concentrations was evaluated for each analyte to empirically determine the LOD, and **Figure 5-29A**,**B** shows an example of this analysis for TNT and DNT. Once the LOD was determined, additional analysis of a sample without explosive (0 mg/mL), the defined LOD, and a concentration slightly higher than the LOD were analyzed with additional replicates to define threshold values to use for detection (**Fig. 5-29C,D**). Each threshold value was then defined by +/- 3σ (dependent on the color change for each reaction) of the negative hue response for 99.7% confidence in the detection of each explosive analyte, and this process was repeated for all of the target explosives analytes.

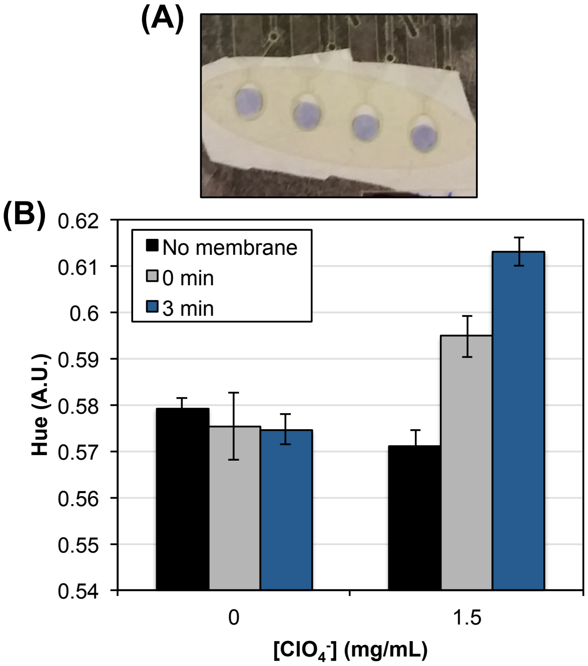

Figure 5-30. Pre-concentration of perchlorate within the reagent chamber for enhanced colorimetric analysis. (**A**) Image of reagent chambers sealed with PTFE. (**B**) Hue results for perchlorate with methylene blue with and without the PTFE, and analyzed overtime with PTFE.

Two of the target explosives analytes, perchlorate (ClO_4^-) and urea nitrate (UN), needed additional optimization before threshold values could be defined. The required LOD for ClO_4^- specified by the Department of

Defense was 100 µg, and this detection limit was not met using the updated device design, developed surface swab, and new detection scheme. A method for concentrating the sample within the reagent chamber was implemented to allow for increased detection of ClO_4^- at low concentrations. This method minimally altered the device fabrication and consisted of sealing the MB reagent chamber from underneath the device using a PTFE membrane filters (0.2 µm pore size) allowing for the solvent to evaporate (aqueous-based solvent consisting of 10% methanol). As the solvent evaporates, the sample becomes more concentrated within the reagent chamber, resulting in a more purple color change indicative of increased ClO_4^- concentration. An image of PTFE-sealed MB reagent chambers with ClO_4^- present is shown in **Figure 5-30A**, and immediate image capture after the device protocol was completed resulted in an increased hue response compared to no membrane (PTFE) sealed chambers (**Fig. 5-30B)**.

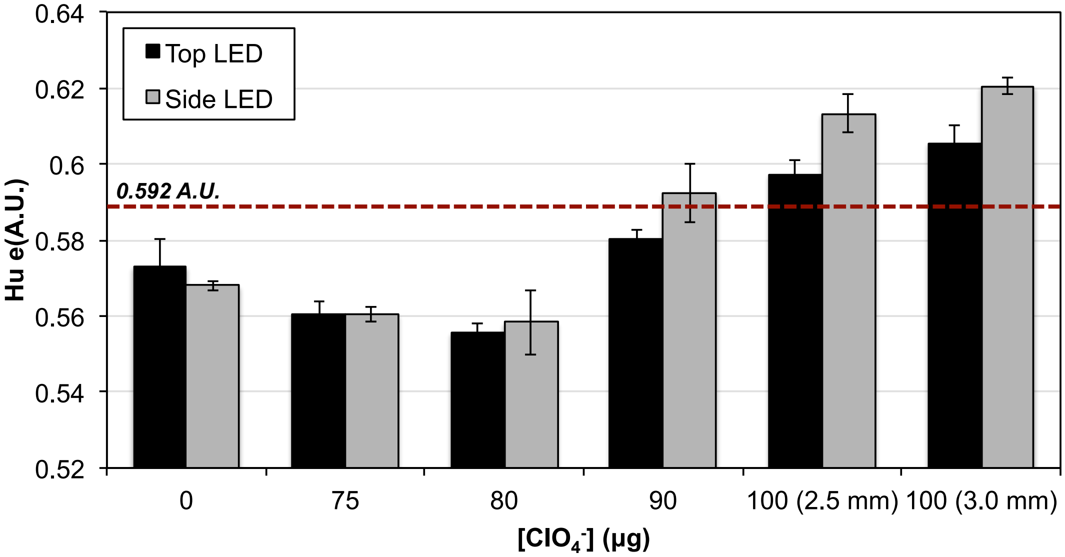

Figure 5-31. Comparison hue results for perchlorate with methylene blue using lighting on the top and side of the device enclosure system. The threshold value is shown as a red dashed line.

Although the PTFE-sealed membrane concentrated ClO_4^- within the reagent chamber, a method to further enhance the detection of ClO_4^- was explored. Each of the

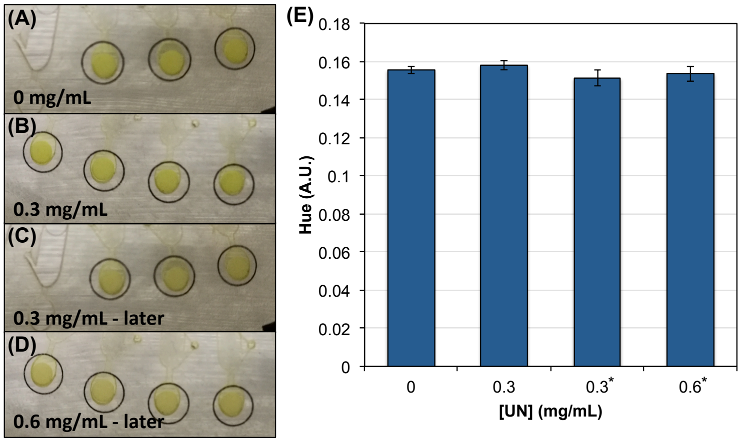

Figure 5-32. Reevaluation of urea nitrate reaction with *p*-DMAC for detection limit and threshold value determination. Images of (**A**) 0 mg/mL, (**B**) 0.3 mg/mL, (**C**) 0.3 mg/mL imaged 2 min. later, and (**D**) 0.6 mg/mL imaged 2 min. later for urea nitrate detection. (**E**) Hue analysis for each corresponding image with results from images taken 2 min. later denoted with an asterisk

colorimetric reactions were imaged with white LED lights positioned on the lid of the system, as described in **Chapter 4**, however, the detection of ClO_4^- was improved with lighting on the sides of the system for imaging (side lighting shown in **Fig. 5-25**). The advantage of a fully automated system is that the lighting can be customized for each individual colorimetric reaction, if necessary. An additional image capture event can be simply programmed into the device protocol where the side LEDs turn on as the top LEDs turn off to image for the detection of ClO_4^-. Then, the data from multiple images throughout the device protocol can be compiled before reporting the final results to the user. The results in **Figure 5-31** demonstrate the increased detection capability with a side LED strip for imaging the reaction of ClO_4^- with MB.

Analyzing the reaction of UN and *para*-dimethylaminocinnamaldehyde (*p*-DMAC) with the updated device, detection scheme, and surface swab, resulted in difficulties for detection as the previously defined LOD in **Chapter 4** and 2X the previously defined LOD could not be detected. Each of the color changes looked identical (**Fig. 5-32A-D**) and the resulting hue values were indistinguishable between varying concentrations (**Fig. 5-32E**). From previous evaluation of this reaction, the color change should become darker red-colored over time, and this was not observed for 0.3 or

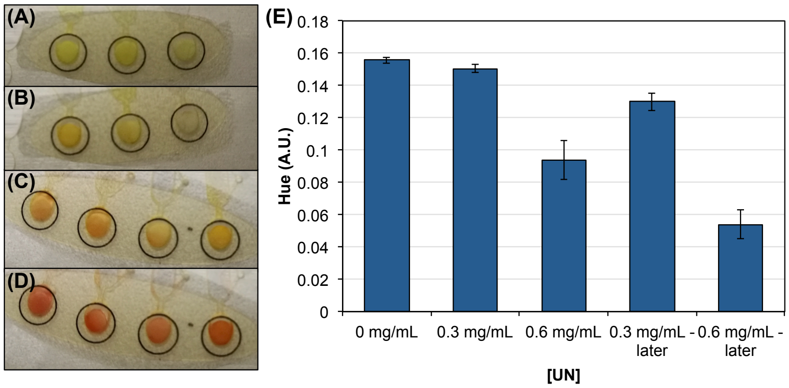

Figure 5-33. Evaluation of urea nitrate reaction with *p*-DMAC using PTFE-sealed reagent chambers. Images of (**A**) 3 mg/mL, (**B**) 0.3 mg/mL imaged 5 min. later, (**C**) 0.6 mg/mL and (**D**) 0.6 mg/mL imaged 5 min. later for urea nitrate detection. (**E**) Hue analysis for each corresponding image with results from images taken 5 min. later denoted with 'later'.

0.6 mg/mL UN imaged ~2 min after the device protocol was completed (images in **Fig. 5-32C,D** and results denoted by '*' in **Fig. 5-32E**). The method used to concentrate ClO_4^- within the reagent chamber with a PTFE-sealed chamber was also applied for UN detection. It was expected that PTFE-sealed chamber would be advantageous for UN detection because the organic solvent used for elution would evaporate more readily. Both 0.3 and 0.6 mg/mL UN concentrations were analyzed with PTFE-sealed chambers for images taken immediately (**Fig. 5-33A, C**) and 5 min after (**Fig. 5-33B,D**) the device protocol. The hue results from these images are shown in **Figure 5-33E** with the subsequent images (5 min) denoted as 'later'. Although the hue response for 0.6 mg/mL UN could be differentiated from the 0 mg/mL response immediately, the subsequent images for both 0.3 and 0.6 mg/mL resulted in enhanced UN detection.

Since 0.3 mg/mL UN detection required image capture 5 min after the device protocol was complete, doubling the overall protocol time, additional studies were performed without the PTFE-sealed chambers to determine the source for the increased LOD using the updated device design, detection scheme, and swab. A concentration of 0.3 mg/mL UN (or 15 µg) was evaluated without the swab, with the swab (no glycerol on the swab), and with the swab (including glycerol). The results in **Figure 5-34A** show that the swab material is effecting the colorimetric reaction downstream within the device, while glycerol seemed to have no negative effect on the color change. Because the swab material did not have a similar negative effect on the other colorimetric reactions, implementing a PTFE-covered chamber for UN detection with an additional 30 second centrifugal mixing protocol was implemented (as an alternative to image capture 5 min later). The hue results for 0, 9, and 15 µg of UN are shown in **Figure 5-34B** with analysis performed immediately after the device protocol, and with the additional 30 second mix prior to image capture. Because the hue response for 0 mg/mL UN was more varied with the additional mixing step, this step was not added to the device protocol. Using the PTFE-covered chambers, the LOD was defined as 15 µg UN and the threshold values could be determined for hue analysis.

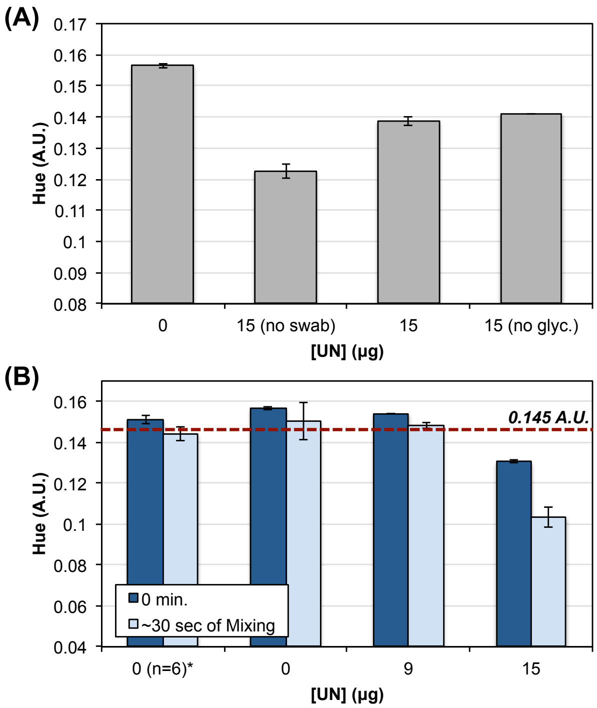

Figure 5-34. Reaction of urea nitrate with *p*-DMAC for detection limit and threshold value determination. (**A**) Evaluation of 15 µg urea nitrate without a swab, with the swab (no glycerol), and with the swab (including glycerol). (**B**) Comparison of hue results from an image taken immediately and after 30 seconds of mixing with PTFE-sealed chambers, red dashed line denotes threshold value for time point 0 min.

Table 5-6 shows the empirically defined LOD for each explosive analyte, the amount of standard solution added to the swab, and the threshold values defined from the hue results for 99.7% confidence in the detection. These threshold values were included in the Android application for future studies. A different LOD requirement was defined for each of the explosive analytes of interest by the funding source of this work (Department of Defense), and each of the defined LODs met these specifications.

Table 5-6. Empirically defined detection limits for each explosive analyte, the amount of standard solution added to the swab, and the defined threshold values for hue analysis. H_2O_2 and NH_4^+ results are based on tinting cyan with 75% transparency.

Explosive Material	Empirical LOD (µg)	Added to Swab	LOD Requirement (µg)	Lower Threshold Value (A.U.)	Upper Threshold Value (A.U.)
TNT	1	1 µL, 1 mg/mL	5	0	0.123
Tetryl	2.5	2.5 µL, 1 mg/mL	5	0	0.123
DNT	2.5	2.5 µL, 1 mg/mL	5	0.140	0
UN	15	1.5 µL, 10 mg/mL	30	0	0.130
ClO_4^-	100	10 µL, 10 mg/mL	100	0.592	1
H_2O_2	2.5	2.5 µL, 1 mg/mL	50	0	0.419
NH_4^+	20	2 µL, 10 mg/mL	30	0	0.357
NO_3^-	20	2 µL, 10 mg/mL	30	0.427	1

5.3.7 Multistep Image Analysis for TNT and Tetryl Discrimination

The defined threshold value both for TNT and Tetryl was 0.123 A.U., and all hue values below this are considered positive for either TNT or Tetryl. Alternatively, the threshold value defined for DNT was 0.140 A.U., and all hue values above this are considered positive for DNT. Although the color changes for TNT, Tetryl, and DNT with tetramethylammonium hydroxide (TMAH) differ, red-purple, red-orange, and blue, respectively, the defined threshold values cannot discern between the presence of TNT and Tetryl (**Fig. 5-35**). To explicitly identify the presence of

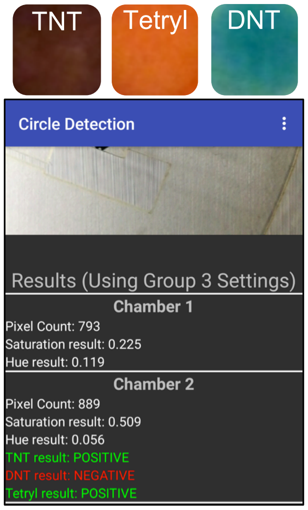

Results (Using Group 3 Settings)

Chamber 1

Pixel Count: 793
Saturation result: 0.225
Hue result: 0.119

Chamber 2

Pixel Count: 889
Saturation result: 0.509
Hue result: 0.056
TNT result: POSITIVE
DNT result: NEGATIVE
Tetryl result: POSITIVE

Figure 5-35. Cannot discriminate TNT and Tetryl with TMAH using hue analysis and threshold values 0 – 0.123 A.U., and TNT was added here.

either TNT or Tetryl, additional analysis was explored.

The hue values between 0 – 0.123 A.U. could potentially be partitioned further to define a range of hue values associated with the different color changes for TNT and Tetryl over a range of concentrations (**Fig. 5-36A**). Unfortunately, the color response for both high and low concentrations of TNT and Tetryl vary, making it difficult for defining an explicit range for each analyte. The hue responses from a range of concentrations including 2.5, 5, 10, and 100 μg for both TNT and Tetryl were plotted in **Figure 5-36B,** and although the hue response at the same concentration of TNT and Tetryl never resulted in identical hue values, significant sections of the plotted data overlap limiting analysis for an unknown sample of unknown concentration.

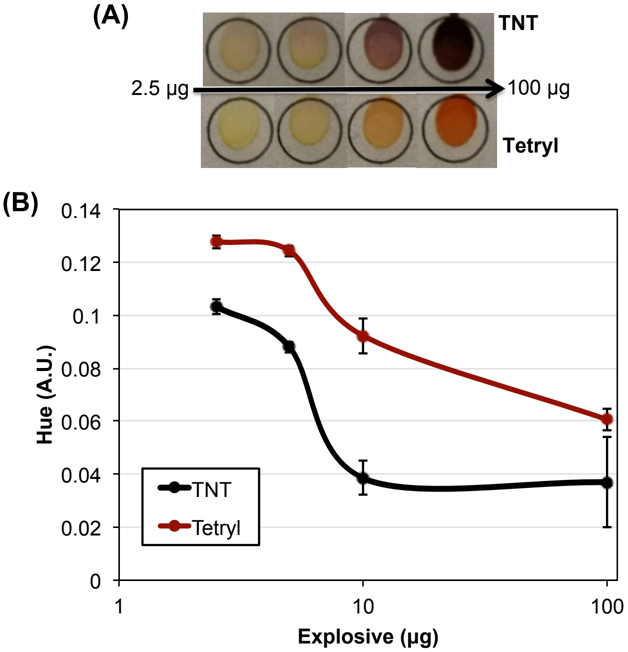

Figure 5-36. Hue analysis of TNT and Tetryl for various concentrations. (**A**) Images of TNT and Tetryl colorimetric reactions with TMAH from 2.5 – 100 μg of analyte. (**B**) Hue analysis results corresponding each of the images for various TNT and Tetryl concentrations.

Hue was not an ideal image analysis parameter for identifying either TNT or Tetryl; however, a different image analysis parameter could be sufficient. After evaluating additional image analysis parameters (RGB and HSB color models), red analysis from RGB was chosen as the most advantageous parameter, and the red responses for TNT and Tetryl over a range of concentrations from 0 – 100 μg are shown in **Figure 5-37**. Although the red responses overlap for a low concentration of TNT and a high concentration of Tetryl, the majority of the red responses do not overlap at any given concentration. Overall, a red response below 0.480 A.U. is indicative of TNT and a red response above 0.520 A.U. is indicative of Tetryl. This information can be used in combination with hue, to determine a multi-level analysis protocol for discriminating between a sample of either TNT or Tetryl. An overview of the proposed analysis protocol is described in **Table 5-7**. The first step of the analysis for the TMAH reaction would be to determine if the sample is negative, contains DNT, or contains either TNT or Tetryl using hue analysis. The TNT/Tetryl threshold value was adjusted from 0.123 A.U. to 0.120 A.U. based on the additional analyses performed here. If the hue value is above 0.140 A.U., the sample is positive for DNT and the analysis is completed, however, if the hue value is between 0.120 – 0.140 A.U., then the sample is negative for TNT, Tetryl, and DNT and the analysis is completed for this reaction chamber. Alternatively, if the hue response is less than 0.120 A.U. then either TNT or Tetryl is present and an additional analysis step is required for identification. The second form of analysis is the red response associated with the same reaction chamber (TMAH). As described, a red response less than 0.480 A.U. can be sued to indicate the presence of TNT and greater than 0.520 A.U. for Tetryl. If the red response falls within either of those ranges, then the analysis is complete and the explosive is identified using the second

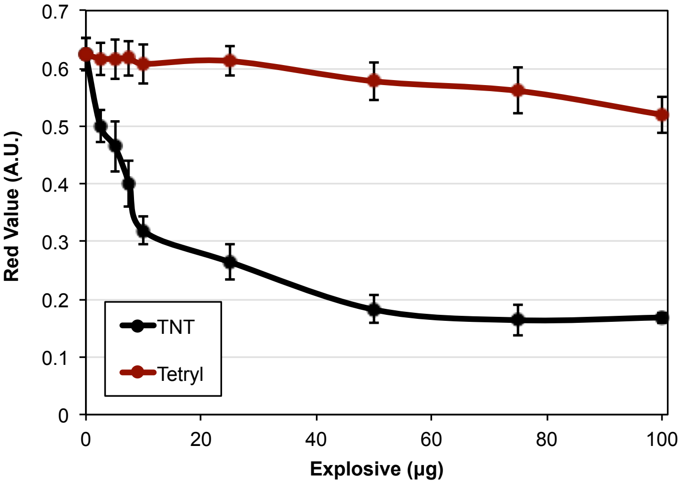

Figure 5-37. Red analysis for varying concentrations of TNT and Tetryl from 0 – 100 µg.

analysis parameter, and if the red response is between 0.480 – 0.520 A.U. then the result is inconclusive for either TNT or Tetryl and a third analysis step is needed. The third analysis can use hue analysis again, because any red response between 0.480 – 0.520 A.U. can only be from a low concentration of TNT or a high concentration of Tetryl. Using the hue analysis results in **Figure 5-36**, a low TNT concentration corresponds to a hue value of ~0.1 A.U. and a high Tetryl concentration corresponds to ~ 0.06 A.U. The third analysis would be defined as a hue value above 0.060 A.U. indicates TNT present and a hue value below 0.060 A.U. indicates the presence of Tetryl. For either of these results the analysis is completed using the third analysis step and the explosive is identified.

Table 5-7. Multilevel analysis protocol for the identification of TNT or Tetryl with TMAH.

Analysis Steps	Analysis Parameter	Result	Analysis Protocol
1	Hue > 0.140	DNT	Complete
	0.140 > Hue > 0.120	NEG	Complete
	Hue < 0.120	TNT and/or Tetryl	Continue to Red (R, RGB) Analysis
2	R < 0.480	TNT	Complete
	R > 0.520	Tetryl	Complete
	0.520 > R > 0.480	TNT and/or Tetryl	Continue to Secondary Hue Analysis
3	Hue < 0.060	Tetryl	Complete
	Hue > 0.060	TNT	Complete

5.3.8 Analysis of TNT and DNT at High Concentrations

Significant effort was spent analyzing low concentrations of each explosive material to account for the common scenario where residual material, from handling bulk explosives, is used for detection. Oftentimes, the source bulk material is not sampled directly for the identification of an explosive, however, evaluation of the developed system (swab, device, and analysis) was performed with the intent of sampling bulk sample incase this scenario is encountered in the field. Difficulties did not occur for the majority of explosive analytes evaluated at high concentrations (maximum concentration that could be obtained was 10 mg/mL), with the exception of TNT and DNT. At high concentrations of TNT and DNT, the resultant color change was a very dark, near black color change creating a challenge for analysis. **Figure 5-38** shows an example of the color changes for TNT at a low concentration and a high concentration, with the associated hue histograms (using ImageJ). The histogram for TNT at a high concentration does not display an expected distribution of pixels compared to the histogram for a low concentration, although both histograms have identical pixel counts. Since black is not a color represented with hue analysis, the results are inconsistent for a higher concentration.

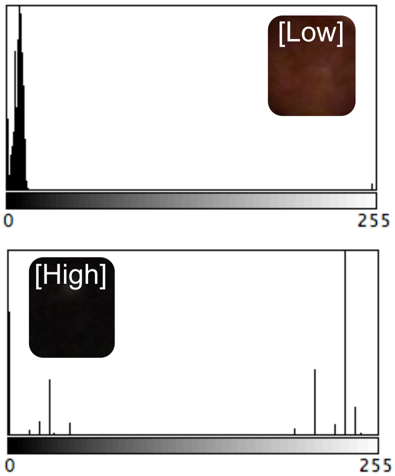

Figure 5-38. Exemplary hue histograms for TNT at a low and high concentration, with associated images (insets).

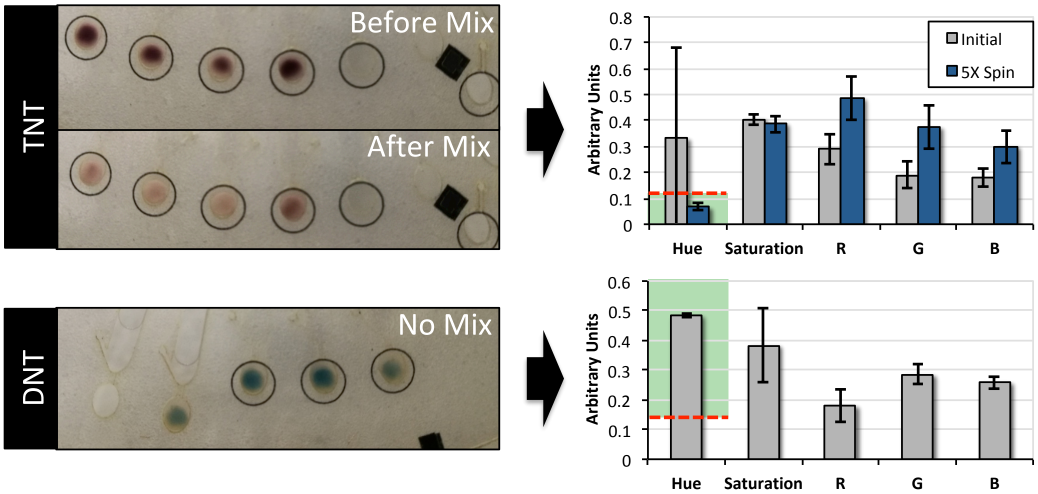

Figure 5-39. Analysis of TNT and DNT with 25% and 75% tetramethylammonium hydroxide, respectively, with associated hue analyses. Threshold values are denoted using red dashed lines.

Analysis utilizing various TMAH dilutions was performed to account for high concentrations of TNT and DNT, and a 25% TMAH solution (diluted with methanol) produced a purple color change with a high concentration of TNT, instead of a black

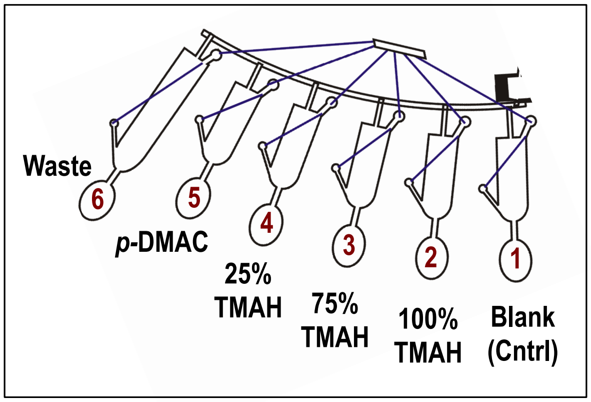

Figure 5-40. Device design for detection of the organic explosives group with additional reagent chambers for inclusion of tetramethylammonium hydroxide reagent dilutions.

color change. Consequently, a 25% TMAH solution was too dilute for detecting DNT and an additional solution of 75% TMAH was required for analysis of both TNT and DNT (**Fig. 5-39**). For high concentrations of TNT, an additional centrifugal mixing step resulted in a lighter color change (pink-colored) that produces a more consistent hue response. However, to implement a method for the detection of TNT and DNT at high concentrations, additional reactions chambers were required. **Figure 5-40** describes the device design for detection of the organic explosives group with additional reagent chambers for additional TMAH analysis. The 100% TMAH solution was still required for Tetryl analysis and detection of TNT and DNT at low concentrations. Although the device design was modified, a method for determining when to perform analysis at subsequent 75% and 25% TMAH chambers was needed.

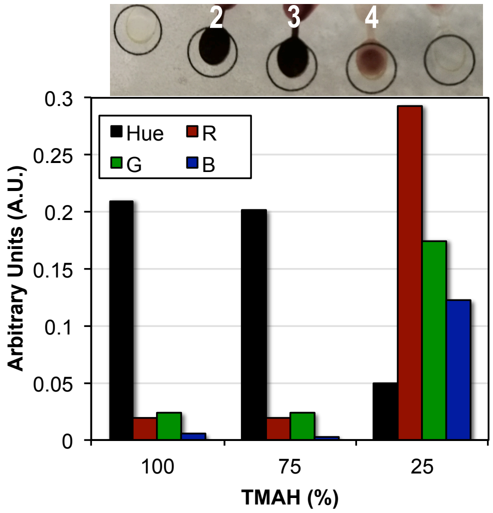

Figure 5-41. Analysis of a high concentration of TNT after an additional centrifugal mixing step with associated image labeled for 100%, 75%, and 25% TMAH as 2, 3, and 4, respectively.

Although black color is not represented using hue, black is represented by the RGB color model and these parameters were explored for identifying a high concentration of TNT or DNT. The image in **Figure 5-41** is labeled for 100%, 75%, and 25% TMAH with 2, 3, and 4, respectively, and analysis was performed after an additional centrifugal mixing step for a high concentration of TNT added. The hue results for 100% and 75% TMAH are not indicative of TNT and would result in a false positive result for DNT if analysis was performed in this manner. Alternatively, the hue result for 25% TMAH is indicative of a positive result for TNT, with a hue value less than 0.120 A.U. To assure that the analysis is performed at reaction chamber-4 in this scenario, RGB can be used to determine a color that is too dark for analysis (inconclusive) that needs to be analyzed using an alternative method (TMAH dilution). If RGB is considered 'too low' for analysis, or below 0.050 A.U., the analysis will be performed at the subsequent chamber (reaction chamber-3 here). Moreover, if the RGB response is too low at chamber-3 as well, then the analysis will be performed at reaction chamber-4 for TNT detection. If the RGB response is not below 0.050 A.U. at chamber-3, then the analysis will be performed at chamber-3 for DNT detection and subsequent analysis at chamber-4 is not required.

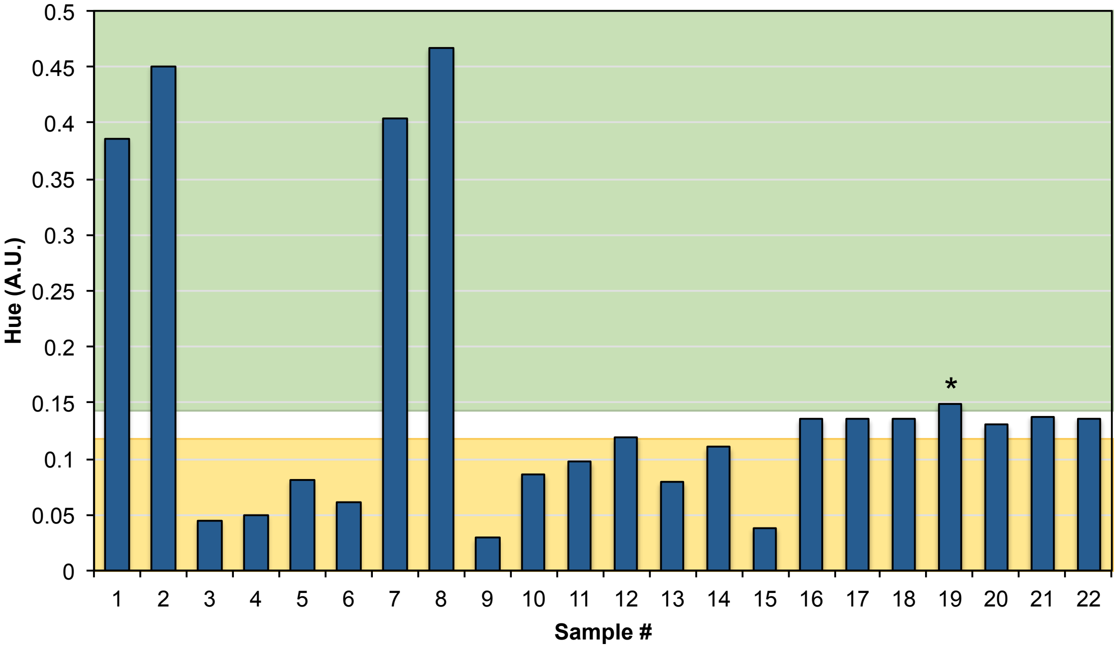

Figure 5-42. Evaluation of the analysis methods for detecting a negative sample, the presence of DNT, or the presence of either TNT or Tetryl with hue analysis.

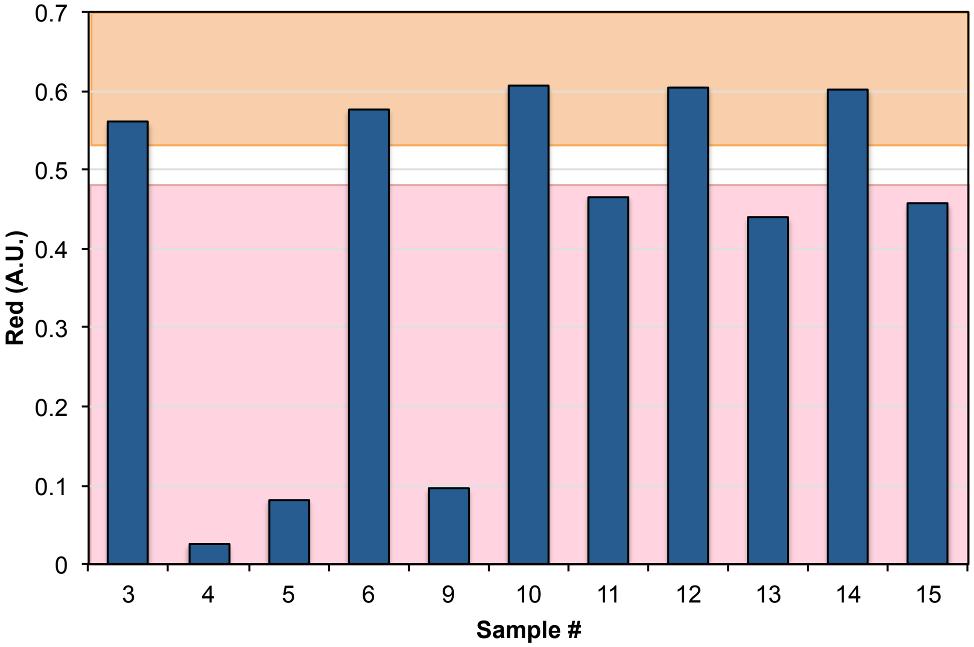

Figure 5-43. Evaluation of the red analysis for discriminating between TNT and Tetryl. A result between 0.480 – 0.520 A.U. would require additional analysis.

The Android application was updated with the described analysis changes and threshold value modifications for TNT, Tetryl, and DNT. To verify these new analysis methods, a series of sample solutions were evaluated. The first evaluation was for the ability to detect a negative sample, the presence of DNT, or the presence of either TNT or Tetryl with hue analysis. The main component of this analysis was comprised of first evaluating the TMAH reaction chambers for an RGB response below 0.050 A.U., to either perform the analysis with the 100%, 75%, or 25% TMAH chamber. There was a 95% success rate (21/22 samples correctly identified) and the hue results are shown in **Figure 5-42**. Samples 1, 2, 7, and 8 contained DNT and were correctly identified in addition to samples 3 – 6 and 9 – 15 for containing either TNT or Tetryl using hue. Samples 16 – 23 were negative samples containing a blank solution (no explosive) or a UN sample. Sample 19 was the only incorrect call, with a false positive result for 15 µg UN added (previously defined LOD). The red responses for samples 3 – 6 and 9 – 15 shown in **Figure 5-43** resulted in 100% success for identifying each sample as either TNT or Tetryl, and none of the responses were between 0.480 – 0.520 A.U. requiring additional hue analysis. Samples 4, 5, 9, 11, 13, and 15 were correctly identified as TNT and samples 3, 6, 10, 12, and 14 were correctly identified as Tetryl. Due to the incorrect call for sample 19, additional samples containing either a blank solution (no explosive) or UN were analyzed using hue with the *p*-DMAC reaction chamber (**Fig. 5-44**). Analysis for the detection of UN resulted in a 72% success rate (8/11 samples correctly called). Although samples 16 – 18 and 20 – 22 were correctly identified during analysis at the TMAH reaction chambers, only 5 of the 6 samples were correctly identified and sample 19, which was incorrect during TMAH analysis, was also incorrect during analysis with *p*-DMAC. Samples 17, 20, 21, 24, and 26 were blank solutions with no explosive present and samples 16, 18, 19, 22, 23, 25 contained UN. All samples that contained 15 μg UN

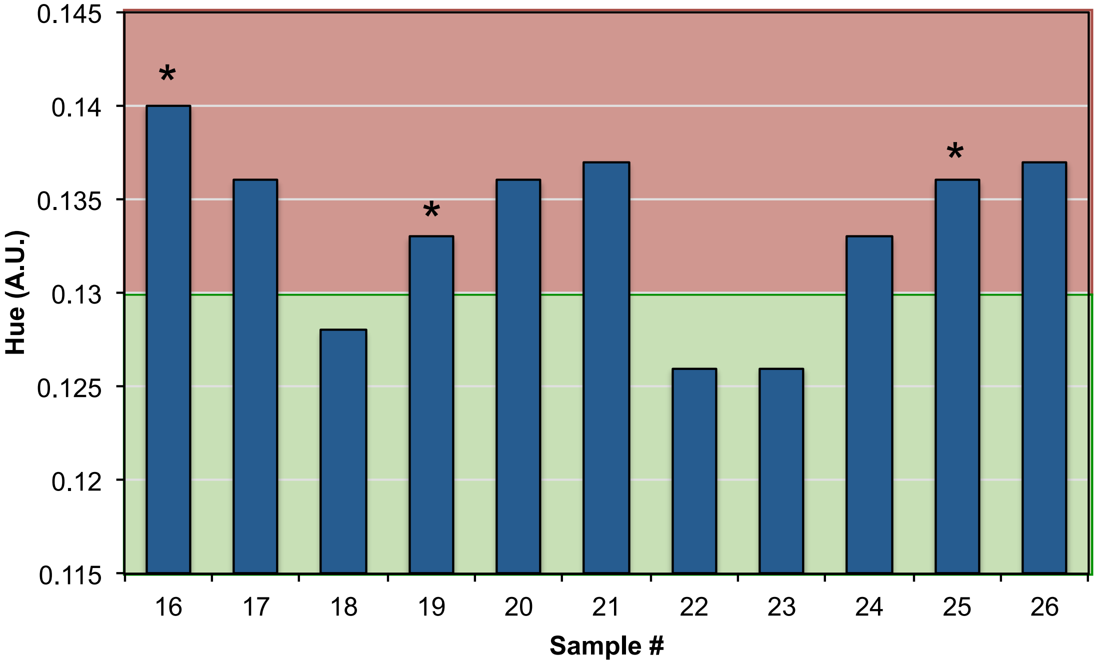

Figure 5-44. Additional samples containing either a blank solution (no explosive) or urea nitrate were analyzed using hue with the *p*-DMAC reaction chamber. The three incorrect identification results leading to false negative responses (denoted by asterisk symbol '*') were the lowest urea nitrate concentrations analyzed at 15 μg (detection limit).

(LOD), samples 16, 19, and 25, were incorrectly called as a blank sample with no explosive present. The number of incorrect calls concerning UN detection were a result of the additional reaction chambers added to the device design for 75% and 25% TMAH, negatively effecting the ability for the sample solution to fill the last reaction chamber in the series (the *p*-DMAC reagent chamber). The metering chamber for the blister pouch containing organic solvent for the elution of sample was modified to meter 55 µL volume instead of 50 µL (each additional sample channels holds 3 µL sample). This resulted in consistent filling of the *p*-DMAC reaction chamber with sample.

5.3.9 Integration of Capillary Ampules for Reagent Storage

The detection of NH_4^+ with the Nessler's reagent for partial identification of ammonium nitrate (AN), with inclusion of NO_3^- detection for complete AN identification, was optimized in **Chapter 4** for incorporation into the microfluidic device. Initial reagent storage tests determined that the Nessler's reagent was not stable within the device prior to use over a short period of time. The custom capillary ampule method described in **Chapter 3**, however, demonstrated the potential for on-chip liquid reagent storage. The ampules containing Nessler's reagent were sealed with PTFE to provide a faster method for device fabrication than epoxy-sealed ampules, and these ampules were integrated into the final microfluidic device. Once the reaction chambers were each filled with metered sample containing 10 mg/mL AN, a color change within the Nessler's reagent chamber was indicative of NH_4^+ present (**Fig. 5-45A**). After the sequential centrifugal mixing protocol was completed, the precipitate brown-colored complex ($NH_2Hg_2I_3$) indicative of NH_4^+ present had sedimented to the bottom of the chamber (**Fig.**

5-45B). The laser valves were then opened to move sample solution into the second reagent chamber for NO_3^- detection prior to a final centrifugal mixing protocol. At this point, a color change indicative of NO_3^- present with the modified Griess reaction was produced, however, the brown colored product from reaction of NH_4^+ with Nessler's reagent was no longer visible (**Fig. 5-45C**). Alternatively, when the identical procedure was performed with a lower concentration of NH_4^+ (0.5 mg/mL), the brown-colored product was observed after the final centrifugal mixing protocol (**Fig. 5-45D**). To account for analysis of both high and low concentrations of NH_4^+, two images were incorporated into the final device protocol for detecting NH_4^+. The first image was used to detect higher concentrations of NH_4^+ from bulk sample from image capture before the NO_3^- laser valves are actuated (opened). If there was no NH_4^+ present or NH_4^+ was present at low concentrations, the brown-colored product would not be present in the image. The additional image would be used to detect lower concentrations of NH_4^+ after the overall device protocol was completed as shown with **Figure 5-45D.** The compilation of these two images would provide complete detection of NH_4^+ for both a high and low concentration scenario.

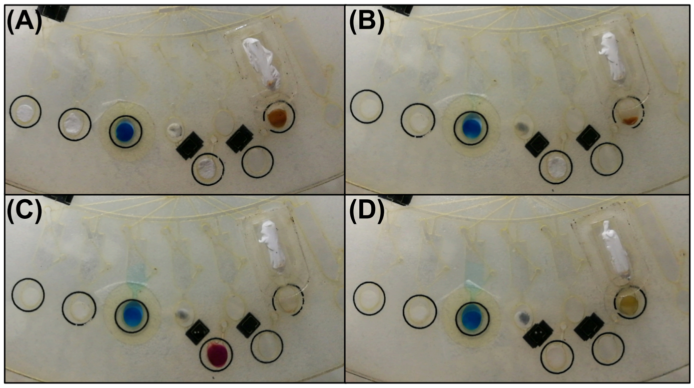

Figure 5-45. Images for the detection of ammonium nitrate with the Nessler's reagent integrated using capillary ampules. Images for 10 mg/mL ammonium nitrate with sample (**A**) initially added to reagent chambers, (**B**) centrifugally mixed with reagent, and (**C**) at the end of the completed device protocol. (**D**) Image at the end of the completed protocol for 0.5 mg/mL ammonium nitrate.

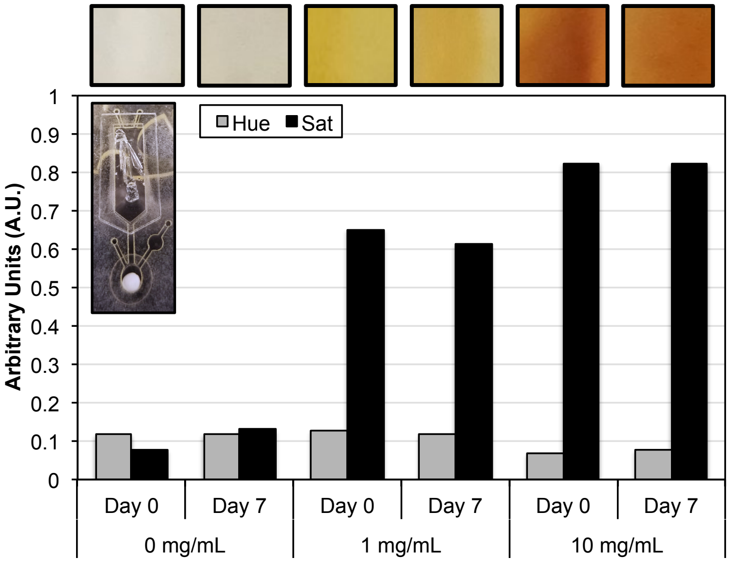

Figure 5-46. Image analysis for storage of Nessler's reagent within epoxy-sealed ampules over 1 week with varying ammonium concentrations. Exemplary images for each data point are shown above, with an inset image of the ampule broken within the storage test device.

Attempts to store fabricated microfluidic devices containing the PTFE-sealed ampules with Nessler's reagent were ineffective after storage over one week. Additional storage tests were attempted with epoxy-sealed ampules containing Nessler's reagent and the results shown in **Figure 5-46** demonstrate the potential for an improved reagent storage method after one week of device storage prior to use. Following three weeks of device storage with epoxy-sealed ampules containing Nessler's reagent, the ampules were still effective for NH_4^+ detection (**Fig. 4-47**). Of the eight ampules that were stored over three weeks, six ampules remained viable for use (**Fig. 5-47A**) and two contained degraded reagent, observed by the yellow-colored Nessler's reagent enclosed (**Fig. 5-47B**). The

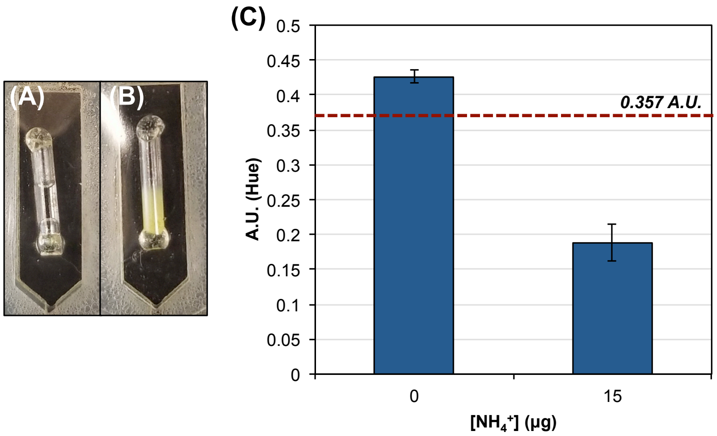

Figure 5-47. Analysis of Nessler's reagent stored within epoxy-sealed ampules over 3 weeks. Images of ampules after storage that were either (**A**) viable or (**B**) degraded. (**C**) Hue analysis with tinting for 0 and 15 µg ammonium using stored ampules containing Nessler's reagent, with the threshold value shown by a red dashed line.

six viable ampules were used to evaluate 0 and 15 μg NH_4^+ for n = 3 and the results are shown in **Figure 5-47C** with the previously defined threshold value in red, demonstrating successful use of the stored Nessler's reagent. The two reagents that had degraded were likely from error during fabrication or breakage of the ampule within the chamber during storage.

A simple method to activate, or break, the Nessler's reagent-filled capillary ampule that is user-friendly and seamlessly incorporated into the device operation was needed. A ~2 cm diameter circle was laser cut into the top piece of the device holder, used to secure the device during transportation, to guide the user to the location of the capillary ampules (**Fig. 5-48A)**. Additionally, a section of PMMA was added to the bottom piece of the device holder to allow a flat surface to rest against the bottom of the ampule during the breaking event (**Fig. 5-48B)**. An extrusion was added to the back of the swab handle to use for consistent capillary ampule breakage (**Fig. 5-48C)**, and the diameter of the circle added to the top holder piece was the same diameter as the swab handle (**Fig. 5-48D)**. The dimension of the extrusion was varied between

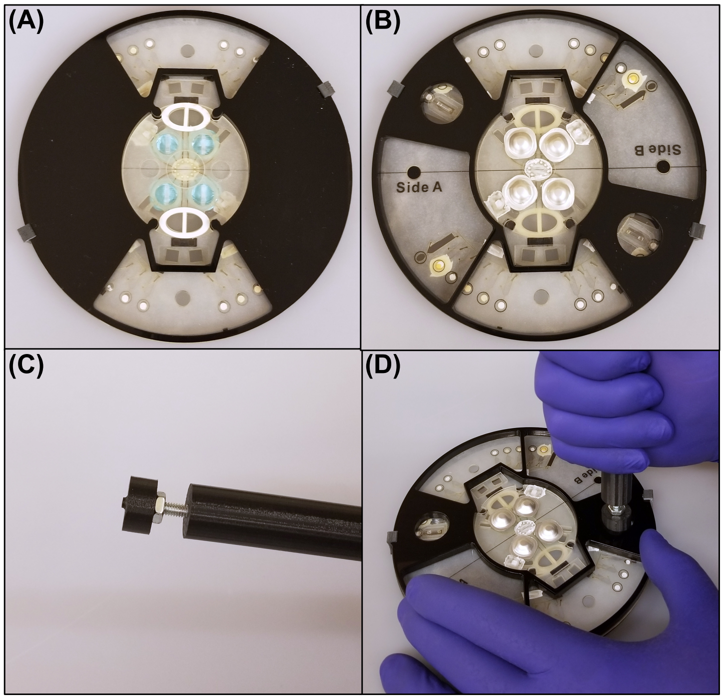

Figure 5-48. Method for integration and use of Nessler's reagent ampules. Images of the (**A**) bottom and (**B**) top device holder pieces, modified for application of the ampules by the user. (**C**) Image of the swab handle with the extrusion on the end for breaking the ampule with image of using the swab handle (**D**).

1 – 3 mm in length (consistently 3 mm in diameter), with 1.25 mm in length chosen for optimal use.

5.3.10 Integration of Blister Pouches for Aqueous and Organic Solvents

Blister pouches are a commercial method for storing liquid reagents within foil packets, and puncturing the pack mechanically releases the contents.[38, 39] Blisters are an ideal method for storing dissolution solvents, where the pouches prevent solvent evaporation during storage and can accommodate volumes between 50 μL and 0.5 mL from microfluidic ChipShop GmbH (Jena, Germany). Although blisters have been reported previously for use with microfluidic in point-of-care and forensic DNA-based applications[40, 41], the use of organic solvent blisters for microfluidics is less explored.

Due to the low surface tension of organic solvents, fluidic control was difficult for blisters containing the 90% acetonitrile (ACN) solvent, optimized in **Chapter 4**, for use with the identified organic explosives. A pressure sensitive adhesive (IS-7876-84) from Adhesives Research (Glen Rock, PA) was chosen for use with organic solvents due to initial difficulties adhering the organic solvent blisters to the device without

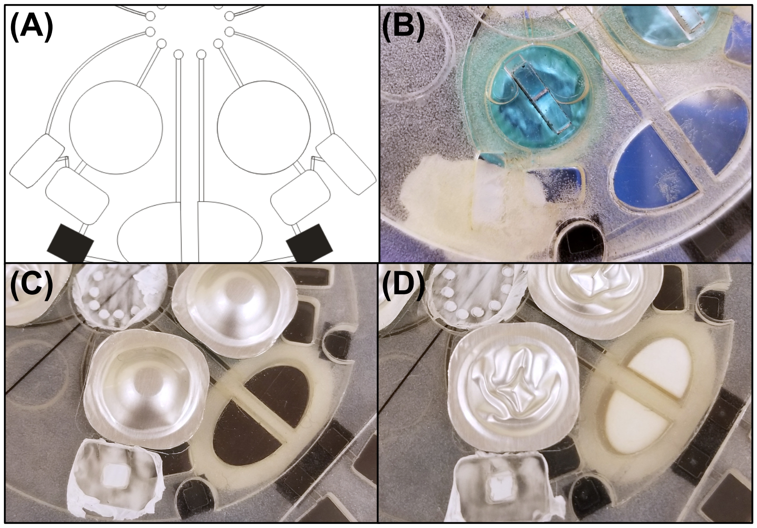

Figure 5-49. Integration of blister pouches for both the aqueous and organic solvents. (**A**) Device design used for the blister chambers. (**B**) Image of an ideal release of solvent from the blister pouch into the blister chamber within the device. (**C**) unused and (**D**) used blister pouch images.

removal during release of the solvent. Additionally, PTFE membrane filters (0.2 μm pore size) were added to each air vent outlet within the fluidic architecture to prevent the organic solvent from leaking due to the pressure applied when releasing the blister contents and to create a completely closed system once the swab is added.

Manual pressure was used to pierce the bottom of the blister with a PMMA piece (that comes to a sharp point) within the blister chamber to release the solvents. The majority of the solvent volume stored within the blister was released into the blister chamber below when the foil was flattened against the device **(Fig. 5-49)**. For preferential movement of the organic solvent towards the solvent metering chamber as opposed to movement towards the air vents at the center of the device, an open waster chamber sealed with PTFE was applied to the excess solvent chamber (for waste) attached to the metering chamber. The open chamber acts as an additional air vent for air displacement from the microfluidic architecture once the blister is opened. This open waste chamber design is not required for the aqueous blister as the surface tension of the solvent is higher

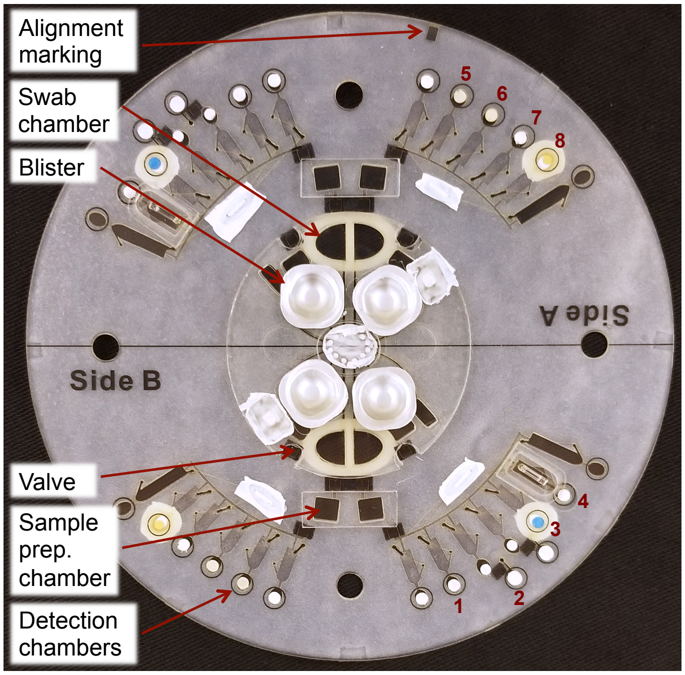

Figure 5-50. Image of the final, fully integrated centrifugal microfluidic device for sampling (surface swab, sample elution, and sample cleanup) and multiplexed analysis of a single sample for eight different explosive materials. Each critical reagent chamber is labeled for ATO (1), modified Griess reaction (2), MB (3), Nessler's reagent (4), 100% TMAH (5), TMAH dilutions (6,7), and *p*-DMAC (8). All other unlabeled chambers were either controls or waste chambers.

resulting in filling of the blister chamber due to pressure generated when puncturing the blister. The remaining solvent within the blister that was not released during the blister puncture event is removed using centrifugal force during the device protocol.

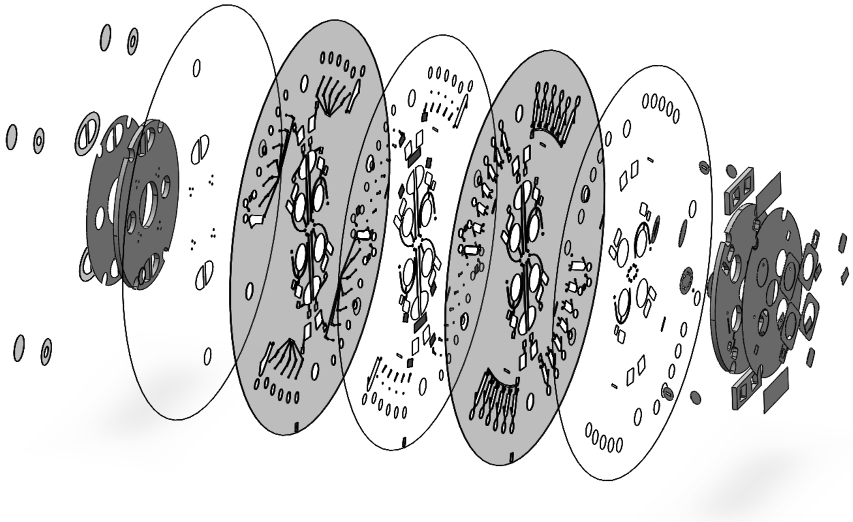

Figure 5-51. Expanded view of the final device design comprised of five polyester layers, six adhesive layers, two PMMA layers, and three PTFE membrane layers.

5.3.11 Validation of the Fully-Integrated Device and Portable Systems

An image of the final, fully integrated centrifugal microfluidic device for sampling (surface swab, sample elution, and sample cleanup) and multiplexed analysis of a sample for eight different explosive materials is shown in **Figure 5-50**. The final device was comprised of five polyester layers, six adhesive layers, two PMMA layers, and three PTFE membrane layers (**Fig. 5-51**). Once a sample was added to the device using the protocol described in **Figure 5-23**, the user manually applied pressure on both blister pouches (aqueous and organic) to release the solvents in addition to using the swab handle to break the capillary ampule containing Nessler's reagent. Once this procedure was complete, the user added the device to the device enclosure system, closed the lid, and locked the lid into place so it cannot be opened during the device procedure. In addition to a mechanical lock on the outside of the system for assuring the lid remains closed during operation, a magnetic safety interlock was also added to the system (**Figure 5-52**). If the lid was opened during the device procedure, the procedure stopped to assure that the user could not be harmed by the laser diodes used during operation of the laser valves.

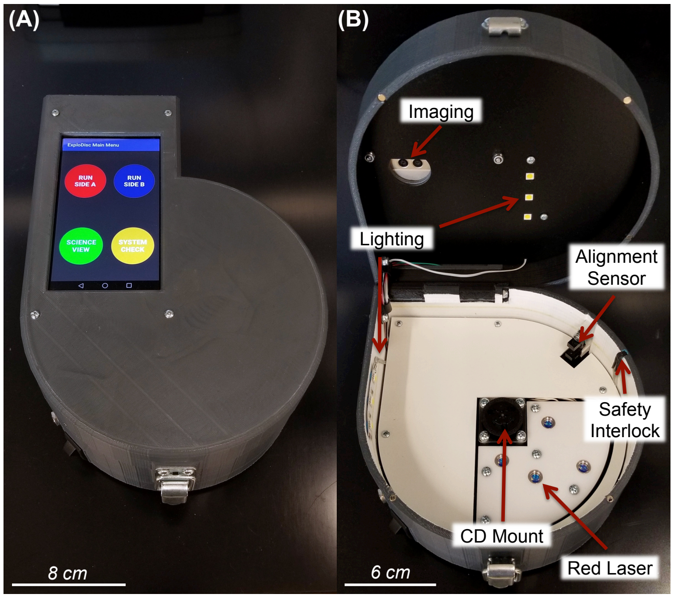

Figure 5-52. Images of the final device enclosure system used for device operation. (**A**) Image of the closed device system with cell phone integrated for analysis, and (**B**) image of the device opened showing features used for device operation.

Once the device was added to the enclosure and the lid was closed, the user chose to operate either ‘Side A’ or ‘Side B’ on cell phone interface (**Fig. 5-52A**). At this point, the user had no further interaction with the system as the device centrifugal spin protocol, imaging protocol, and analysis protocol were programmed and automated. The overall (final) device procedure was completed in ~ 7 min with a total of 17 spin steps, 7 laser valves, and 6 image capture events. The final device protocol is outlined in **Table 5-8**, and the associated image analysis protocol is described in **Table 5-9**.

Three replicate device system enclosures were fabricated by TeGrex Technologies (Charlottesville, VA) in accordance with the specifications outlined by the Department of Defense. At the conclusion of the grant timeline these systems, with 45 microfluidic devices for processing 90 samples, were brought to collaborators at the

Defense Forensic Science Center (DFSC) for evaluation with relevant explosive samples.

Table 5-8. The final device protocol used with the final assembled system with optimized angular valve positions each of the three systems for use with the fixed laser diodes. Before every 'go to angle' step, the device home position was found to assure correct alignment.

	Centrifugal Protocol			Angle Relative toHome Position (°)		
Protocol Step	Speed (RPM)	Time (s)	Replicates	System 1	System 2	System 3
Solvent Metering	3000	5				
Go to Angle and Activate Laser 1				Side A: 121.25, 177.75 Side B: 301.50, 358.00	Side A: 123.16, 179.75 Side B: 302.99, 359.94	Side A: 122.71, 179.68 Side B: 302.58, 359.21
Spin Solvent into Swab Chambers	3000	4				
Centrifugal Mix for Sample Dissolution	3000, -3000	1	3			
Go to Angle and Activate Laser 2				Side A: 55.00, 66.50 Side B: 234.25, 246.00	Side A: 55.11, 66.83 Side B: 235.25, 246.69	Side A: 54.38, 66.00 Side B:234.38, 245.92
Spin Sample into Prep. Chamber	2500	3				
Centrifuge Sample from Swab Chamber	3000	3	2			
Go to Angle and Activate Laser 3				Side A: 106.33 Side B: 286.50	Side A: 108.08 Side B: 287.58	Side A: 107.25 Side B: 286.96
Fill Sampling Channels (Organic)	700	5				
Fill Sampling Channels – Additional Spin	900	5				
Fill Reagent Chambers	2500	5				
Fill Reagent Chambers – Additional Spin	3300	5				
Go to Angle For Picture-1 and Capture Photo (Top LED)				Side A (Organic): 202.00; Side B (Organic): 22.00		
Centrifugal Mix Sample and Reagent	3000, -3000	1	3			
Go to Angle For Picture-2 and Capture Photo (Top LED)				Side A (Organic): 202.00; Side B (Organic): 22.00		
Go to Angle and Activate Laser 3				Side A: 133.75 Side B: 313.75	Side A: 135.11 Side B: 314.87	Side A: 134.29 Side B: 313.89
Fill Sampling Channels (Aqueous)	700	15				
Go to Angle For Picture-3 and Capture Photo (Top LED)				Side A (Aqueous): 279.00; Side B (Aqueous): 99.00		
Fill Sampling Channels – Additional Spin	900	15				
Fill Reagent Chambers	2500	20				
Fill Reagent Chambers – Additional Spin	3300	15				
Go to Angle and Activate Laser 4				Side A: 123.75 Side B: 303.50	Side A: 124.82 Side B: 304.47	Side A: 124.17 Side B: 304.00
Fill Reagent Chamber-2	2500	5				
Centrifugal Mix Sample and Reagent	3000, -3000	1	3			
Go to Angle For Picture-4 and Capture Photo Photo (Top LED)				Side A (Aqueous): 279.00; Side B (Aqueous): 99.00		
Centrifugal Mix Sample and Reagent	3000, -3000	1	3			
Go to Angle For Picture-5 and Capture Photo (Top LED)				Side A (Aqueous): 279.00; Side B (Aqueous): 99.00		
Capture Photo Additional Photo, Picture-6 (Side LED)						

Before the systems were transported, an in-house validation of each system was required in a laboratory setting for defining success rates in a controlled environment using explosive standards. The final detection limits were reported as the Department of Defense requirements, which were intentionally more conservative than the LODs reported in **Table 5-6**. A concentration 2X greater than the detection limit reported for each explosive analyte were used for evaluation of the three device enclosure systems, and the final detection threshold values implemented into the Android application are outlined in Table **Table 5-10**.

Table 5-9. Overview of the final imaging protocol with explosive and reagent listed for each image for compiled analysis. Only picture-6 was taken with side lighting, all other images were taken with lighting from the top. In the final protocol, picture-5 was not utilized but still taken during the protocol.

		Chamber #					
	Picture #	1	2	3	4	5	6
Organic Solvent	1	Control	TNT, Tetryl, DNT; 100% TMAH	DNT; 75% TMAH			
	2				TNT; 25% TMAH	UN; *p*-DMAC	
Aqueous Solvent	3	Control	High [NH_4^+]; Nessler's reagent				
	4		Low [NH_4^+]; Nessler's reagent			NO_3^-; Modified Griess	H_2O_2; ATO
	5						
	6			ClO_4^-; MB			

Systems 1 and 2 were each evaluated with 20 samples and system 3 was evaluated with only 11 samples due to complications encountered during evaluation. Evaluation of systems 1 and 2 included n = 3 analysis for each explosive analyte and 13 different negatives or contaminants of interest (outlined with collaborators) including sugar (n = 2), Equal commercial sweetener, Sweet n' Low commercial sweetener, an environmental contaminant (dirt), ethanol, methanol, isopropanol, water, salt (NaCl), and a true blank (n = 3). An outline of the samples and results for each system evaluation are shown in **Tables 5-11, 5-12, and 5-13** for systems 1, 2, and 3, respectively.

Table 5-10. Conservative detection limits reported for each explosive analyte with 2X the detection limit concentrations recommended for evaluation of final device system enclosures. Defined threshold values for hue analysis are also reported with H_2O_2 and NH_4^+ results based on tinting cyan with 75% transparency.

Explosive Material	Demonstrated LOD (µg)	Recommended for System Evaluation (µg)	Lower Threshold Value (A.U.)	Upper Threshold Value (A.U.)
TNT	5	10	0	0.116
Tetryl	5	10	0	0.116
DNT	5	50	0.144	0
UN	30	60	0	0.130
ClO_4^-	100	200	0.625	1
H_2O_2	50	50	0	0.419
NH_4^+	30	200	0	0.300
NO_3^-	30	60	0.427	1

Table 5-11. Outline of the samples and results for evaluation of system 1.

System 1

Sample #	**Explosive Material**	**Amount Added (µg)**	**Experimental Readout**	**Correct Call?**
1	None	N/A	All Clear	Yes
2	Sugar	5000	DNT Detected	No
3	Equal (Sweetener)	4800	All Clear	Yes
4	Dirt	4900	All Clear	Yes
5	H_2O_2	50	H_2O_2 Detected	Yes
6	$NaClO_4$	200	ClO_4^- Detected	Yes
7	KNO_3	60	NO_3^- Detected	Yes
8	NH_4NO_3	200	NH_4^+, NO_3^- Detected	Yes
9	TNT	10	TNT Detected	Yes
10	Tetryl	10	Tetryl, UN, NH_4^+ Detected	No
11	DNT	50	DNT Detected	Yes
12	UN	60	UN, NO_3^- Detected	Yes
13	NH_4NO_3	200	NO_3^- Detected	No (Partial)
14	Ethanol	*(15 µL)*	All Clear	Yes
15	$NaClO_4$	200	ClO_4^- Detected	Yes
16	UN	60	UN, NO_3^- Detected	Yes
17	NH_4NO_3	200	NH_4^+, NO_3^- Detected	Yes
18	Isopropanol	*(15 µL)*	All Clear	Yes
19	None	N/A	All Clear	Yes
20	Sugar	5300	All Clear	Yes

From the 20 samples evaluated using system 1, three samples had incorrect results during the evaluation including samples 2, 10, and 13. For sample 2, sugar was added and the expected result was ‘all clear’, however, the experimental readout resulted in ‘DNT detected’. The threshold range predefined for the detection of DNT using hue analysis at the 100% TMAH reagent chamber was 0.144 – 1 A.U. Unfortunately, the hue result from the sugar added was 0.145 A.U., a value just within the positive detection range for DNT. Because this was strictly an analysis error likely due to an outlier data point, all samples were reevaluated using a new DNT threshold range for detection (0.146 – 1 A.U.) after complete analysis of each system. This change in the threshold for a positive DNT result (+0.002 A.U.) did not result in any false negative results from a positive DNT sample with a hue value that was within 0.144 – 0.145 A.U. that would be incorrectly identified using the new threshold values. Since all of the data was reevaluated using the updated threshold, this in correct call could be considered a correct call for the overall system evaluation, resulting in an overall success rate of 90% (18/20 samples correctly identified) for system 1. The source of the incorrect call from sample 10 was not clear, leaving this sample as a truly negative call. Alternatively, sample 13 was correctly identified for NO_3^- present, but did not identify the presence of NH_4^+. This was likely due to a fabrication error incorporating the capillary ampules that contain Nessler's reagent as previously observed. Unfortunately, the fragile nature of the ampules for easy release of the reagent contents can impart challenges for sealing the ampules within the device chambers without breakage that can result in reagent degradation.

System 2 performed similarly to system 1, resulting in three samples that were incorrectly identified from the 20 samples evaluated, and included samples 7, 10, and 17. Sample 7 resulted in an incorrect call due to no solvent entering the organic explosive analysis portion of the device from a blister pouch manufacturing error, where the organic solvent blister added to the device was empty from a hole in the pouch, allowing solvent to leak or evaporate prior to use. Since this error was from the blister pouch manufacturer, we chose to not take this sample into consideration for the overall

Table 5-12. Outline of the samples and results for evaluation of system 2.

System 2

Sample #	Explosive Material	Amount Added (µg)	Experimental Readout	Correct Call?
1	None	N/A	All Clear	Yes
2	H_2O_2	50	H_2O_2 Detected	No
3	$NaClO_4$	200	ClO_4^- Detected	Yes
4	KNO_3	60	NO_3^- Detected	Yes
5	NH_4NO_3	200	NH_4^+, NO_3^- Detected	Yes
6	TNT	10	TNT Detected	Yes
7	DNT	50	All Clear	No
8	DNT	50	DNT Detected	Yes
9	Tetryl	10	Tetryl Detected	Yes
10	Tetryl	10	Tetryl, UN Detected	No
11	UN	60	UN, NO_3^- Detected	Yes
12	H_2O	*(15 µL)*	All Clear	Yes
13	H_2O_2	50	H_2O_2 Detected	Yes
14	KNO_3	60	NO_3^- Detected	Yes
15	NaCl	5000	All Clear	Yes
16	Sweet n' Low	5200	All Clear	Yes
17	TNT	10	Tetryl, UN, NH_4^+ Detected	No
18	Methanol	*(15 µL)*	All Clear	Yes
19	TNT	10	TNT Detected	Yes
20	DNT	50	DNT Detected	Yes

evaluation of our developed systems and methods, resulting in an overall success rate of ~90% (17/19 samples correctly identified) for system 2. The incorrect call for sample 10 was perceived as a fluidic error, where some of the resultant orange color for a positive Tetryl sample was carried into the UN detection chamber, altering the hue value within the positive detection range for UN (0.127 A.U.). The incorrect call for sample 17, however, was relatively unclear and the presence of a device fabrication error could have potentially been the cause. Centrifugal spinout residue of the sample solution from the swab chamber was observed along the device, which could result in loss of sample or not enough sample solution to enter each reagent chamber and negatively impact the results.

System 3 did not perform as well as systems 2 and 3, however; only 11 samples were evaluated using this system due to timing towards the end of the evaluation studies. Although all three systems were assembled to be identical, the laser power outputs (used for laser valving) were individually optimized for each system as 505, 408, and 432 mW for systems 1, 2, and 3, respectively. System 3 required to most amount of time to optimize the laser power output, as a setting too high would easily burn a hole through the device allowing a lose of sample solution through the hole and a setting too low would not open the valve at all. Once the laser power was finally optimized to product no valve failures during trial tests, there was limited time left in the project before the systems needed to be delivered to DFSC. Of the 11 samples that were evaluated using system 3 with the remaining time left in the research grant, samples 6 and 8 were incorrectly identified. All of the reagent chambers for the inorganic explosives portion of the device for sample 6 were not filled, however, the source of the sample loss was unclear. Without sample in the reagent chamber for NO_3^- detection, the result consistently provides a false positive reading. Sample 8 also resulted in partial identification of the sample as NO_3^- was detected and UN was not. This error was due to a hole in the organic solvent metering valve that caused a loss of sample solution during the centrifugal spin protocol, resulting in only reagent chambers 1-3 were filled with sample on the organic explosive side (associated with a control, 100% TMAH, and 75% TMAH reagent chambers).

Table 5-13. Outline of the samples and results for evaluation of system 3.

System 3

Sample #	Explosive Material	Amount Added (μg)	Experimental Readout	Correct Call?
1	None	N/A	All Clear	Yes
2	$NaClO_4$	200	ClO_4^- Detected	No
3	H_2O_2	50	H_2O_2 Detected	Yes
4	KNO_3	60	NO_3^- Detected	Yes
5	NH_4NO_3	200	NH_4^+, NO_3^- Detected	Yes
6	DNT	30	DNT, NO_3^- Detected	No (Partial)
7	TNT	10	TNT Detected	Yes
8	UN	60	NO_3^- Detected	No (Partial)
9	UN	60	UN, NO_3^- Detected	Yes
10	Tetryl	10	Tetryl Detected	No
11	Dirt	5200	All Clear	Yes

Overall, only systems 1 and 2 were given to DFSC with 45 devices for off-site evaluation using relevant explosives samples. The success rate of these systems in a laboratory setting was ~90%, from 35 out of 39 samples correctly identified, which met the success rate requirement outlined by the Department of Defense. The errors associated with the incorrectly identified samples were as follows: one fluidic error, two device fabrication errors, and one unclear error that could have also been fluidic-based. Additionally, during the evaluation of systems 1 and 2, a total of 156 blisters were manually actuated (punctured to release contents) without solvent leaking, a total of 273 laser valves were opened automatically during the device procedure without any valve failures, and a total of 78 ampules were manually actuated (using the swab handle to release the contents). After an hour of training at DFSC with the three device enclosure systems, system 3 was returned to the Landers Lab to use for assessment of any potential challenges that may be encountered during off-site testing with systems 1 and 2.

5.4 Conclusions

A simple method was determined for the development of a custom, laser-ablated surface swab for the collection of explosive residues from surfaces for integration into a microfluidic device. Initially, different commercial materials were assessed for the ability to collect material from a given surface, including cotton buccal swabs, microfiber cloths, filter paper, and blotting paper. Overall collection efficiencies were determined for each potential swab material using conductivity detection of a nonhazardous reference standard. Gel blot paper was chosen for further studies due to the ability for both trace and macro sample collection and the ability to easily integrate this material into the PCL fabrication method and interface with the microfluidic device. Different microfluidic mixing protocols were assessed to increase sample elution efficiencies once added to the microdevice, however, the centrifugal mixing protocol compatible with automation only resulted in ~50% recoveries. A final split-swab was developed for explosives screening using the blotting paper.

Final spin system enclosures were assembled and evaluated with the fully-integrated microfluidic device for determining success rates of each system. Two of the three assembled systems resulted in ~90% success rates for a total of 39 samples. Of the incorrectly identified samples, one was a fluidic error, two were device fabrication-based, and the source of the last error was inconclusive. In the future, the errors resulting from the device fabrication process could be addressed by considering additional methods for reinforcing the ampule chambers to assure no breakage of the capillary ampules. Additionally, if the described fully integrated device were to be commercialized and mass manufactured, inconsistencies in fabrication could be monitored and a method for quality control could be assessed. Although system 3 required additional evaluation due to time constraints for this project, the incorrect sample identification resulting from samples 6 and 8 both produced a partial correct result that could still be used to identify the presence of an explosive material.

5.5 References

1. S. Singh, *Journal of Hazardous Materials*, 2007, **144**, 15-28.
2. K. Yeager, in *Forensic Investigation of Explosions*, ed. A. Beveridge, CRC Press, Boca Raton, 2012, pp. 493-538.
3. M. E. Staymates, J. Grandner and J. R. Verkouteren, *Ieee Sensors Journal*, 2013, **13**, 4844-4850.
4. M. Marshall and J. C. Oxley, in *Aspects of Explosives Detection*, eds. M. Marshall and J. C. Oxley, Elsevier, Amsterdam, Netherlands, 2009, pp. 11-26.
5. M. Marshall and J. C. Oxley, in *Aspects of Explosives Detection*, eds. M. Marshall and J. C. Oxley, Elsevier, Amsterdam, Netherlands, 2009, pp. 1-10.
6. M. Pumera, *Electrophoresis*, 2006, **27**, 244-256.
7. M. Ueland, L. Blanes, R. V. Taudte, B. H. Stuart, N. Cole, P. Willis, C. Roux and P. Doble, *Journal of Chromatography A*, 2016, **1436**, 28-33.
8. M. Pumera, *Talanta*, 2007, **74**, 358-364.
9. J. Wang, *Talanta*, 2002, **56**, 223-231.
10. R. V. Taudte, A. Beavis, L. Wilson-Wilde, C. Roux, P. Doble and L. Blanes, *Lab on a Chip*, 2013, **13**, 4164-4172.

11. M. O. Salles, G. N. Meloni, W. R. de Araujo and T. Paixao, *Analytical Methods*, 2014, **6**, 2047-2052.
12. A. Pesenti, R. V. Taudte, B. McCord, P. Doble, C. Roux and L. Blanes, *Analytical Chemistry*, 2014, **86**, 4707-4714.
13. K. L. Peters, I. Corbin, L. M. Kaufman, K. Zreibe, L. Blanes and B. R. McCord, *Analytical Methods*, 2015, **7**, 63-70.
14. M. I. Mohammed, S. Haswell and I. Gibson, *Proceedings of The 1st International Design Technology Conference, DESTECH2015*, 2015, **20**, 54-59.
15. M. Madou, J. Zoval, G. Y. Jia, H. Kido, J. Kim and N. Kim, in *Annual Review of Biomedical Engineering*, Annual Reviews, Palo Alto, 2006, vol. 8, pp. 601-628.
16. R. Gorkin, J. Park, J. Siegrist, M. Amasia, B. S. Lee, J. M. Park, J. Kim, H. Kim, M. Madou and Y. K. Cho, *Lab on a Chip*, 2010, **10**, 1758-1773.
17. R. Mariella, *Biomedical Microdevices*, 2008, **10**, 777-784.
18. M. Hitzbleck and E. Delamarche, *Chemical Society Reviews*, 2013, **42**, 8494-8516.
19. C. D. Chin, V. Linder and S. K. Sia, *Lab on a Chip*, 2012, **12**, 2118-2134.
20. E. L. Izake, *Forensic Science International*, 2010, **202**, 1-8.
21. E. L. Robinson, E. Sisco, M. E. Staymates and J. A. Lawrence, *Analytical Methods*, 2018, **10**, 204-213.
22. K. M. Horsman, S. L. R. Barker, J. P. Ferrance, K. A. Forrest, K. A. Koen and J. P. Landers, *Analytical Chemistry*, 2005, **77**, 742-749.

23. M. Stangegaard, B. B. Hjort, T. N. Hansen, A. Hoflund, H. S. Mogensen, A. J. Hansen and N. Morling, *Forensic Science International-Genetics*, 2013, **7**, 384-388.

24. N. Song-im, S. Benson and C. Lennard, *Forensic Science International*, 2012, **222**, 102-110.

25. N. Song-Im, S. Benson and C. Lennard, *Forensic Science International*, 2012, **223**, 136-147.

26. B. L. Thompson, Y. Ouyang, G. R. M. Duarte, E. Carrilho, S. T. Krauss and J. P. Landers, *Nature Protocols*, 2015, **10**, 875-886.

27. C. Birch, J. A. DuVall, D. Le Roux, B. L. Thompson, A. C. Tsuei, J. Y. Li, D. A. Nelson, D. L. Mills, J. P. Landers and B. E. Root, *Micromachines*, 2017, **8**.

28. J. L. Garcia-Cordero, D. Kurzbuch, F. Benito-Lopez, D. Diamond, L. P. Lee and A. J. Ricco, *Lab on a Chip*, 2010, **10**, 2680-2687.

29. S. T. Krauss, T. P. Remcho, S. M. Lipes, R. Aranda, H. P. Maynard, N. Shukla, J. Li, R. E. Tontarski and J. P. Landers, *Analytical Chemistry*, 2016, **88**, 8689-8697.

30. S. T. Krauss, V. C. Holt and J. P. Landers, *Sensors and Actuators B-Chemical*, 2017, **246**, 740-747.

31. J. C. Oxley, J. L. Smith, E. Resende, E. Pearce and T. Chamberlain, *Journal of Forensic Sciences*, 2003, **48**, 334-342.

32. R. Waddell, D. E. Dale, M. Monagle and S. A. Smith, *Journal of Chromatography A*, 2005, **1062**, 125-131.

33. A. Zeichner, S. Abramovich-Bar, T. Tamiri and J. Almog, *Forensic Science International*, 2009, **184**, 42-46.

34. B. L. Thompson, S. L. Wyckoff, D. M. Haverstick and J. P. Landers, *Analytical Chemistry*, 2017, **89**, 3228-3234.

35. L. Senesac and T. G. Thundat, *Materials Today*, 2008, **11**, 28-36.

36. J. S. Caygill, F. Davis and S. P. J. Higson, *Talanta*, 2012, **88**, 14-29.

37. S. Smith, R. Sewart, K. Land, P. Roux, C. Gartner and H. Becker, San Francisco, CA, 2016.

38. M. Focke, D. Kosse, C. Mueller, H. Reinecke, R. Zengerle and F. von Stetten, *Lab on a Chip*, 2010, **10**, 1365-1386.

39. http://www.thinxxs.com/main/produkte/microfluidixxs/blister-on-a-chip.html, (accessed 8 February 2018).

40. S. Smith, R. Sewart, H. Becker, P. Roux and K. Land, *Microfluidics and Nanofluidics*, 2016, **20**.

41. B. L. Thompson, C. Birch, D. A. Nelson, J. Y. Li, J. A. DuVall, D. Le Roux, A. C. Tsuei, D. L. Mills, B. E. Root and J. P. Landers, *Lab on a Chip*, 2016, **16**, 4569-4580.

6. Final Remarks

6.1 Conclusions

This dissertation has focused on the development of portable sample-in-answer-out microfluidic systems for on-site colorimetric detection of target analytes, i.e., explosives and illicit drugs. The work described in **Chapter 2** demonstrated the evaluation of an objective colorimetric analysis method for use with a cell phone application towards presumptive on-site testing of illicit drugs using inexpensive centrifugal microfluidic devices. Colorimetric detection of cocaine and methamphetamine were utilized for optimization of the image analysis method, and resulted in empirically determined detection limits of 0.25 and 0.75 mg/mL for cocaine and methamphetamine, respectively, when analyzed using a smartphone. Using the defined analysis method, a total of 30 unknown samples were correctly identified for the presence of cocaine and methamphetamine in the presence of other uncontrolled substances using developed microfluidic device and analysis.

The implementation of various chemical reagent storage methods compatible with polyester-based centrifugal microfluidic devices were performed in **Chapter 3** to aid in complete device integration. The reagent storage methods utilized inkjet printing, custom glass capillary ampules, and hybrid device substrates for the addition of the reagents necessary to perform various proof-of-principle colorimetric reactions for clinical, forensic, and environmental applications. All three methods were effective for colorimetric reagent storage with inherent advantages and disadvantages for different device applications. The inkjet printing-based reagent storage method was advantageous for an automated device fabrication protocol, where reagents are incorporated using a commercial office inkjet printer, however, corrosive reagents can damage components of the printer. Paper- and capillary ampule-based reagent storage methods demonstrated a more simplistic fabrication approach for storing reagents in either dry (paper) or liquid form (ampules), where the only requirement is basic laboratory equipment.

The described reagent storage techniques in **Chapter 3** were utilized in **Chapters 4** and **5** for developing a centrifugal microfluidic system to colorimetrically detect explosives using single-use, disposable, and inexpensive devices with on-board reagent storage. The focus of **Chapter 4** was the evaluation and optimization of the resultant color changes within microfluidic devices for the detection of 8 different explosive compounds, including TNT, DNT, Tetryl, UN, NH_4^+, NO_3^-, ClO_4^-, and H_2O_2. Hue image analysis was advantageous for defining threshold values towards qualitative detection of explosives for implementation into a cell phone application as color is represented by a single numerical value, providing a robust method for detection of various color changes. Additionally, three different tinting methods complimentary to the microfluidic device format were developed for enhanced analysis of subtle color changes.

The focus of **Chapter 5** was to fully integrate the initial developments in **Chapter 4** for a more portable and automated device format to perform analysis of the 8 different explosives from a single sample input. A split-swab with 3D-printed handle and microdevice adapter was developed for sampling residue from a given surface and to facilitate both organic and aqueous based chemistries. Additional analysis optimizations were performed for complete automation of the detection method using a cell phone application for different sampling scenarios, i.e., bulk and trace sampling. The final fully integrated systems exhibited 90% success rates for 39 samples, utilizing a ~7 min automated protocol (per sample) with a total of 17 spin steps, 7 laser valves, and 6 image capture events.

6.2 Future Directions

Many of the experiments and results presented in this dissertation demonstrate the development of an on-site analysis platform incorporating centrifugal microfluidic devices to perform colorimetric assays for detection and spin system enclosures for device operation. A sampling split-swab and method was developed for integration into the microfluidic device to account for real-world application and sampling environments for explosives residues. At the end of this initial work, the sampling method only resulted in a ~50% on-chip elution recovery of sample collected onto the swab. Additional work would be advantageous to increase the sample recovery by altering the swab material or exploring additional microfluidic mixing methods. Grumann, et al. presented a method for utilizing the batch-mode centrifugal mixing protocol with the addition of magnetic beads into the mixing chamber within the device for a 6X decrease in the necessary mixing time.[1] The beads were easily pulled through the mixing chamber using a set of external permanent magnets to attract the beads radially inward and outward, which is the opposite direction of the centrifugal mixing. In this proposed format, once the sample was thoroughly mixed with dissolution solvent using magnetic beads in combination with centrifugal mixing, the laser valve below the swab chamber could be used to filter the beads from the sample as demonstrated in **Chapter 5** with collected environmental contaminants. Additionally, evaluation of the radial position of the swab chamber would impact the sample elution efficiencies, as increasing the radial position of the chamber radially outward, towards the perimeter of the device, would increase the centrifugal force on the solution.[2]

The requirement of sample dissolution from the developed swab contributed to the overall protocol time for the fully-integrated device design. A method for enhanced sample recovery from the swab once added to the microfluidic device would decrease the amount of centrifugal mixing utilized within the spin protocol. Overall, there are two separate spin protocols for the organic and aqueous solvents used. Once the initial protocol diverges for the two separate protocols (at ~ 30 sec) the organic spin protocol is ~ 30 sec and the aqueous protocol is 1.5 min. Various aspects of the automated protocol generate the remainder of the sample processing time including: spin deceleration, image capture, 'homing' the device, and actuating the laser valves. The reduction in any of these steps would contribute to lowering the overall analysis time. Additionally, modifications to the image capture protocol would allow for the separate organic and aqueous centrifugal spin protocols to be performed simultaneously.

For complete unknown sample screening with the described portable microfluidic system, the implementation of colorimetric reactions for both explosives and illicit drugs within a single centrifugal device would be advantageous. A proof-of-concept microfluidic device was demonstrated for the detection of cocaine and methamphetamine analytes. Later, a reagent storage method capable of integrating harsh acids and volatile reagents was developed and proof-of-principle reactions were performed, however, to generate a fully integrated detection system, as demonstrated for explosives, additional colorimetric assays need to be implemented for complete drug screening. Other colorimetric reagents for future evaluation would include Duquenois-Levine and Fast blue B, Mecke, and Mandeline's reagents for detection of cannabinoids in cannabis, opium alkaloids, and amphetamines, respectively.[3] Additional evaluation of the Marquis reagent to empirically determine detection limits for the various opium alkaloids and amphetamines with the reagent stored using the described capillary ampule method would be needed. Both the paper and capillary ampule reagent storage methods described in this dissertation are currently the best options for complete reagent storage and can be altered for enhanced use, i.e., altering the paper material used for reagent storage.

Finally, while the core of the PCL fabrication technique provides a simple and inexpensive method for rapid prototyping, the complexity of the final fully-integrated centrifugal device for explosives detection resulted in additional time necessary for device fabrication. The overall fabrication time for a single microfluidic device including preparing the polyester and coated-polyester layers, laser ablating all device layers and materials, adding the reagents for each colorimetric assay, and assembling all device components totaled 116 minutes. The final device was comprised of five polyester layers, six adhesive layers, two PMMA layers, and three PTFE layers and required a significant amount of hands-on assembly. With considerations of manufacturing and mass production of these developed devices, the number of layers and individual components will need to be reduced to eliminate the hands-on nature of the device assembly. If laser-assisted wax valves were implemented into the device design, only one fluidic layer would be necessary for the described device design, which would simplify the complexity of the current device and allow other device fabrication options to be considered towards mass production, i.e., injection molding and embossing.

An alternative method for decreasing the fabrication time contribution would be to modify the design for processing more than two samples on a given device. By decreasing the microfluidic design dimensions to allow for decreased sample metering volumes, additional space within the device would become unused to apply replicate architecture for additional sample processing. For example, the channel widths could be decreased from 3 mm to 1.5 mm to meter half of the volume of sample (1.5 μL). Since there are 13 individual metering chambers within the device, this change in channel dimensions would conserve at least 20 mm. Overall the microfluidic design uses 10.5 cm of the circumference of the device for processing one sample and 21 cm for two samples, however, 13 cm of the circumference of the device remains unused. If the current device design could be altered to generate an additional unused 4 cm of the device circumference, then there should be enough space within the microfluidic device (14.5 cm in diameter) for processing four separate samples.

Alternatively, if processing more than four samples were desired on a single device, or the application of additional colorimetric reactions, a more significant change in the device design would be required. Current commercial colorimetric kits utilize a sequential reaction-processing scheme, and adopting this method would conserve a significant amount of the circumference of the design by adding radially to the design. Adapting this format would also allow for the implementation of additional colorimetric tests within the described device, i.e., sample could be introduced to reagent for detecting nitroaromatic compounds (TNT, DNT, and Tetryl), once the color change is evaluated with the described image analysis platform a laser valve could be activated to move the reacted sample radially into an additional reagent chamber. At this second reagent chamber position, the sample can be introduced to reagent used for detecting nitrate esters (nitroglycerin), and after that resultant color change is evaluated, the sample would be reduced and the Griess reaction can be performed for nitrate compounds in sequential chambers. The proposed reagent storage methods would be amenable for this sequential-type sample processing scheme utilizing a single aliquot of sample.

6.3 Summation

Microfluidic devices used in the field, whether for clinical or forensic applications, offer many advantages for translating conventional instrumentation to a portable, field-deployable platform. The scaled-down size of these devices offer advantages for rapid analysis, low cost substrates and instrumentation, low reagent and sample consumption, automated sample processing, and simple operating procedures. A core requirement of field technology is that the analysis technique can be performed with minimal training by the user and independently of a centralized facility. With continued study of the methods described in this dissertation, the developed microfluidic platform could be utilized for on-site, sample-in-answer-out screening for analytes of interest.

6.4 References

1. M. Grumann, A. Geipel, L. Riegger, R. Zengerle and J. Ducree, *Lab on a Chip*, 2005, **5**, 560-565.
2. O. Strohmeier, M. Keller, F. Schwemmer, S. Zehnle, D. Mark, F. von Stetten, R. Zengerle and N. Paust, *Chemical Society Reviews*, 2015, **44**, 6187-6229.
3. M. Philp and S. L. Fu, *Drug Testing and Analysis*, 2018, **10**, 95-108.